AUSTRALIAN NATIONAL UNIVERSITY

Optical imaging of dendritic spikes in apical oblique dendrites of layer 5 pyramidal neurons

by

Michael Lawrence Garcia Castañares

A thesis submitted for the degree of Doctor of Philosophy of The Australian National University

20/02/2020

Student Declaration

I hereby declare that this thesis contains no material that has been submitted, whether in part or full, for the award of another degree at this university or any other institution. To the best of my knowledge, this thesis contains no material previously published or written by another person except where due reference is made.

Michael Lawrence G. Castañares, 20/02/2020

Preface

All experiments in this thesis were performed at the Australian National University. Procedures conformed to the Australian National Health and Medical Research Council (NHMRC) and Australian Research Council (ARC) codes of practice for the use and care of animals, and institutional animal care and ethics committees at the Australian National University.

Some materials in the chapters have been published with me as the main author (and co-author in collaborative works) during my PhD candidature:

Castanares, M. L., Stuart, G. J. & Daria, V. R. 2019. Holographic Functional Calcium Imaging of Neuronal Circuit Activity. *In:* KAO, F.-J., KEISER, G. & GOGOI, A. (eds.) *Advanced Optical Methods for Brain Imaging.* Singapore: Springer.

Castanares, M. L., Gautam, V., Drury, J., Bachor, H. & Daria, V. R. 2016. Efficient multi-site two-photon functional imaging of neuronal circuits. *Biomedical Optics Express,* 7**,** 5325-5334.

Go, M. A., Mueller, M., **Castanares, M. L.**, Egger, V. & Daria, V. R. 2019. A compact holographic projector module for high-resolution 3D multi-site two-photon photostimulation. *PLoS One,* 14**,** e0210564.

Some of the results described in this thesis have appeared in the following abstracts:

Castanares, M. L., Ma, H., Stuart, G. J. & Daria, V. R. 2018. Non-linear Ca^{2+} events along apical obliques of layer 5 cortical pyramidal neurons. Neuroscience 2018. the Society for Neuroscience. San Diego, CA, United States of America.

Castanares, M. L., Gautam, V., Bachor, H. A. & Daria, V. R. 2016. Efficient holographic multi-site two-photon fluorescence for functional calcium imaging of neuronal circuits. Digital Holography and Three-Dimensional Imaging 2016. Heidelberg, Germany.

Castanares, M. L., Drury, J., Bachor, H. A. & Daria, V. R. 2015. Improving holographic multi-site fluorescence excitation via temporal gating. Australian and New Zealand Conference on Optics and Photonics. Adelaide, Australia

In this thesis, **V. R. D.** and **G. J. S.** conceptualized the problem on the oblique dendrites. **V. R. D.** and I designed and built the combined single- and two-photon holographic microscope. **V. R. D.** and I evaluated the generation of oblique spike in the model. **G. J. S.** gave critical comments in the numerical modelling and experimental design. I performed the electrophysiology and imaging experiments.

Acknowledgements

I dedicate this thesis to mom and dad who have always been supportive in my pursuit in science.

To my main supervisor, Vince, thank you for always being hands-on in troubleshooting the optical system, assessing the direction of the thesis, and teaching me to be clear and concise in writing. I will treasure all the things that you have taught me in science and in life.

To my co-supervisor, Greg, thank you for always being critical in assessing the quality of my work and data.

To my adviser, Hans, thank you for giving helping me to look at the bigger perspective of my work.

To members of my supervisory panel, Brian and John, for their inputs on the feasibility of the study. Thank you, Brian, for also giving me the post-doc opportunity to work with your group.

To my two best friends here at John Curtin, Suraj and Conrad, thank you for accompanying me in the "ups" and "downs" of Ph.D. life. Thank you for believing and pushing me to be better.

To my friends and colleagues here at ANU namely: Muriel, Ronnie, Eliezer, Peter, Chris, and many more, who welcomed me and be my second home here in Canberra.

To Sarah, thank you for giving me a fresh inspiration to see this thesis through.

Abstract

Dendrites have active properties capable of generating dendritic spikes that could boost the impact of distal synaptic inputs. The strong passive filtering of the membrane and generation of local dendritic spikes enable different dendritic regions to function as independent computational compartments. While there is a wealth of information about cortical processing in apical tuft and basal dendrites, the functional role of apical oblique dendrites of layer 5 pyramidal neurons (L5PNs) are less understood. In this thesis, I aim to understand to functional role of thin apical oblique dendrites of L5PNs in the cortex. Using a previously published multi-compartment model of a L5PN, I first investigated the excitability of apical oblique dendrites and the extent of action potential (AP) back-propagation. In the model, I found that a 2-AP train at $f > 35$ Hz elicited an *oblique branch spike* in certain dendrites. The spike is mediated by activation of voltage-gated sodium and voltage-gated calcium channels. In addition, oblique branch spikes manifest as after-depolarizing potentials (ADP) at the soma. I then experimentally verified the generation of spikes by imaging the dendritic activity of oblique branches of L5PNs from the somatosensory cortex *in vitro*. I used our custom-built two-photon (2P) holographic microscope to perform functional calcium imaging on thin oblique branches of L5PNs *in vitro*. Oblique branch spikes are evoked at a critical frequency of $f_c = 57\pm5$ Hz (from calcium imaging) and $f_c = 72\pm4$ Hz (from ADP measurements) of a 2-AP train. Generation of spikes in oblique dendrites could establish their role as independent computational compartments that could boost coincident synaptic inputs. To further improve optical recording along dendrites, I proposed novel optical recording techniques to enhance the signal-to-noise ratio (SNRs) of the detected signals. A 4-fold improvement in the SNR was obtained with temporal gating for multi-site holographic calcium imaging, while a 6-fold increase in SNR was obtained for voltage imaging when using scattered photons to excite voltage indicators. These two novel SNR enhancement techniques can facilitate experiments that require imaging of activity in thin dendrites.

Table of Contents

Chapter 1. Introduction 11

1.1 Structure and function: a guiding theme to study how the brain works 11
1.2 Cerebral Cortex 13
1.3 Pyramidal Neurons 16
1.4 Dendritic spikes 17
1.5 Optical recording of dendritic spikes 22
1.5.1 Functional calcium imaging 22
1.5.2 Historical overview of chemical and protein derived calcium indicators 24
1.5.3 Functional voltage imaging 25
1.5.4 Promising fluorescent voltage indicators 27
1.6 Microscopes used for recording dendritic spikes 28
1.7 Optical probing of dendritic spikes in apical oblique dendrites 31
1.7.1 Properties of apical oblique dendrites of CA1 PNs 31
1.7.2 Properties of apical oblique dendrites of cortical L5PNs 35
1.8 Summary and general aim of this thesis 37
1.9 Overview of chapters 39

Chapter 2. Numerical evidence of putative dendritic spikes in oblique dendrites 41

2.1 Introduction 41
2.2 Chapter aims 43
2.3 Methods 44
2.3.1 Active properties of the dendritic tree of the L5PN model 44
2.3.2 Implementing the critical frequency protocol in the model 46
2.3.3 The program flow of the script and defined functions in *NEURON* 46
Pre-run 47
Stimulus setup 48
Run 48
Oblique tracing routine 48
Branch dendrotomy 49
Removal of conductance in an oblique branch 49
2.3.4 Numerical quantification of linear and non-linear responding oblique dendrites 49
2.4 Results 50
2.4.1 105 Hz critical frequency for generating Ca^{2+}-AP at the nexus of the apical tuft 50
2.4.2 Shifts in the critical frequency in the model with the amplitude and pulse-width of the injected current 51
2.4.3 Invasion of a 4-AP train in the dendritic tree 52
2.4.4 Dendritic spike in oblique dendrites evoked at low-frequency burst of bAPs 55
2.4.5 Classifying oblique branches that exhibit linear and non-linear membrane potential response with 2-AP train 55
2.4.6 Conductance analysis of the dendritic oblique spike 56
2.4.7 Dendrotomy at oblique dendrites in the L5PN model 60
2.5 Summary 61

Chapter 3. General Methods Section: Two-photon holographic multi-site detection system and sample preparation 63

3.1 Introduction 63
Background 63
3.2 Chapter aims 66
3.3 Methods 67
3.3.1 Phase-only holographic projection 67
3.3.2 2P multi-site fluorescence detection 69
3.3.3 Sample preparation 70
Salt solutions 70
Slice preparation 71
Culture preparation 73
3.3.4 Electrophysiology and 2P calcium imaging 73
3.4 Results 75
3.5 Summary 76

Chapter 4. Experimental evidence of oblique branch spikes in oblique dendrites of L5PNs *in vitro*	78
4.1 Introduction	78
4.2 Chapter aim	79
4.3 Methods	79
4.3.1 Analysis of calcium response and the after-depolarizing potential (ADP)	79
4.3.2 Classification of linear and non-linear responses in Ca_{21} and ADP	79
4.3.3 Quantification of the recorded sites	80
4.3.4 Laser dendrotomy	80
4.3.5 Analysis	80
4.4 Results	81
4.4.1 Calcium imaging at oblique branches of L5PNs	81
4.4.2 Morphologies of the responding neurons and the location of the recorded sites	84
4.4.3 The influence of oblique branch spike to the ADP	86
4.4.4 Targeted Pruning of thin oblique dendrites	90
4.5 Discussion and summary	92
Chapter 5. Development of techniques to enhance calcium and voltage imaging on dendrites	95
5.1 Introduction	95
5.2 Chapter aims	96
5.3 Temporal gating for efficient calcium imaging	96
5.4 Method for implementing multi-site functional calcium imaging with temporal gating	97
5.4.1 Mathematical basis for fluorescence enhancement with temporal gating	97
5.4.2 Holographic 2P microscope with an acousto-optic modulator (AOM)	98
5.4.3 Calibration with Fluorescein dye	100
5.4.4 Calcium imaging on cultured hippocampal neurons	100
5.4.5 Data Analysis	101
5.5 Preliminary results showing improved fluorescence yield and SNR with temporal gating	101
5.6 Voltage imaging using single-photon excitation via scattered photon illumination (1PESP)	104
5.7 Methods for implementing 1PESP	103
5.7.1 Intracellular loading of JPW-1114 voltage indicator	105
5.7.2 Integrated 2P and 1P holographic microscope	108
5.8 Preliminary results showing improved SNR with 1PESP	109
5.8.1 Signal-to-noise ratio with different regions-of-interests (ROIs)	109
5.8.2 Improvement of SNR in the optical voltage recordings by 1PESP (Preliminary results)	111
5.8.3 Multi-site 1PESP	114
5.8.4 Optical recordings at thin oblique and basal dendrites	114
5.9 Discussion	116
5.9.1 Multi-site functional calcium imaging with temporal gating	116
5.9.2 Voltage imaging with 1PESP	120
5.10 Summary	120
Chapter 6. General discussion and future directions	122
6.1 Summary	122
6.2 Discussions of specific findings	122
6.3 Implications of my results	127
6.4 Limitations of the study	131
6.5 Future Directions	132
6.6 Conclusion: The role of apical oblique dendrites in information processing	133
References	136

Figure and table captions

Figure 1.1 The cortex and its laminar organization
Figure 1.2 Pyramidal neurons from different brain regions
Figure 1.3 Sodium, calcium, and NMDA spikes
Figure 1.4 Dendritic-somatic patch clamp and fluorescence calcium imaging configuration for the critical frequency protocol
Figure 1.5 Ca^{2+} dynamics during neuronal activity
Figure 1.6 Recorded calcium transients during burst firing of primary hippocampal culture neurons
Figure 1.7 The spectral shift in excitation and emission spectra of electrochromic VSDs due to a voltage transient
Figure 1.8 A summary of single-photon (1P) and two-photon (2P) microscopes used to perform high-speed fluorescence detection.
Figure 1.9 Evidence of synaptic contacts and active properties of oblique dendrites of CA1 PNs
Figure 1.10 Evidence of synaptic contacts and active properties of oblique dendrites of L5PNs
Figure 1.11 Illustration on how oblique dendrites and their properties affect forward and back-propagating spikes

Figure 2.1 Dendritic morphology shapes action potential firing properties of neurons
Figure 2.2 Active dendritic properties of the model
Table 2.1 List of parameters used in the published L5PN model
Table 2.2 Script implemented in NEURON
Figure 2.3 The generation of Ca^{2+}-AP in the L5PN model
Figure 2.4 The shifts in the critical frequency with the amplitude and pulse width of the injected current in the Shai et al. (2015) model
Figure 2.5 Snapshots of the invasion of bAPs in the dendritic tree taken at different times
Figure 2.6 The invasion of AP train along the trunk and oblique dendrites in the L5P neuron model
Figure 2.7 The multi-compartment model of L5PN captures an oblique branch spike in oblique dendrites
Figure 2.8 Classification of linear and non-linear responding oblique dendrites of a L5PN multi-compartment model
Figure 2.9 The conductance analysis of branches exhibiting the putative oblique spike
Figure 2.10 Influence of blocking a conductance in a single branch to neighbouring oblique dendrites
Figure 2.11 The initiation/removal of dendritic oblique spikes with changes in conductance of specific oblique branches
Figure 2.12 Dendrotomy in the *NEURON* model

Figure 3.1 Common microscope modalities to perform functional calcium imaging
Figure 3.2 Phase-only holographic projection
Figure 3.3 Intensity distribution and optical throughput
Figure 3.4 Schematic diagram of our custom-built two-photon laser scanning and holographic microscope
Table 3.1 ACSF solution used for slice incubation and recording
Figure 3.5 Surgery and slice preparation
Figure 3.6 The interleaving protocol to measure the differences in the calcium influx between single and two AP train
Figure 3.7 A summary of 1P and 2P microscopes used to perform high-speed fluorescence detection

Figure 4.1 Variable calcium influx on different oblique branches
Figure 4.2 Pooled summary of the recorded responses from oblique dendrites
Figure 4.3 The calcium transients versus frequency with the sigmoid fit from neurons that exhibited an oblique branch spike
Figure 4.4 Representative two-photon images of neurons loaded with Cal-520 and Alexa-Fluor 488 indicators
Table 4.1 L5PNs recorded in calcium imaging experiment

Figure 4.5 Measured after-depolarising potentials in neurons at different frequencies for 2- and 4-AP train
Figure 4.6 Summary of the critical frequencies of large neuronal sample and the effect of APV with the ADP with an oblique branch spike
Table 4.2 Recordings in the ADP experiment
Figure 4.7 The effect of cutting oblique dendrites with the after-depolarizing potentials
Figure 4.8 Critical frequency responses at different dendritic regions

Figure 5.1 A two-photon holographic microscope with an acousto-optic modulator for temporal gating
Figure 5.2 The increase in fluorescence yield from holographic sites with temporal gating
Figure 5.3 Enhancement of SNR with temporal gating
Figure 5.4 An illustration of the 1PESP
Figure 5.5 Comparison of the extent of loading of calcium and voltage indicators
Figure 5.6 The single-photon holographic attachment integrated with our existing two-photon holographic and laser-scanning microscope
Figure 5.7 The recovered optical transients and the SNR of the spike and hyperpolarization for different regions-of-interest
Figure 5.8 The signal-to-noise ratio with different ROIs
Figure 5.9 Differences in the fluorescence signal from apical trunk of a neuron loaded with VSDs with beam positions
Figure 5.10 The optically recorded voltage spikes from different beam positions
Figure 5.11 SNR enhancement with 1PESP
Figure 5.12 Multi-site 1PESP
Figure 5.13 Back-propagating action potentials reliably invades trunk, oblique dendrites and basal dendrites
Figure 5.14 Sample optical voltage recordings at oblique dendrites

Figure 6. Role of apical oblique dendrites of L5PNs

Chapter 1: Introduction

1.1 Structure and function: a guiding theme to study how the brain works

The interplay between structure and function is a common feature in biology. Nature shows us many clever examples of structural designs that underlie important functions. For example, Japan's "Shinkansen" bullet train engineers integrated bird parts into the train design such as: the beak of a king fisher, wings of an owl, and the belly of a penguin. As a result, Japan's bullet train efficiently travels at high-speed through tunnels while keeping the aerodynamic noise low for the nearby residents (Eiji Nakatsu, Shinkansen 500-series, Japan Railway Company, 1997). Thus, taking inspiration from nature's design and understanding their structure-function relationship will help researchers create better products and processes (Benyus, 2002).

The theme "structure and function" has driven our efforts to understand the brain. With the invention of the microscope, biologists and neuroanatomists started to study the structure of the brain under high magnification (for a historical account, see Shepherd (2015a)). Camillo Golgi invented a staining technique (also called the "black reaction"), which revealed the structure of nerve cells, showing that they consist of a cell body, protoplasmic prolongations from the cell body, and an axis cylinder (now known as the axon). An account of Golgi's work can be found in his 1906 noble lecture (Golgi, 1906). Ramón y Cajal then used Golgi's staining method to trace the structural development of cells in the nervous system. In 1889, Ramón y Cajal introduced the new term "dendrites" to refer to the complex prolongations that extend from the cell body (Cajal, 1889). An English translation of Cajal's work introducing the new term dendrites is described in the book by Shepherd (2015b), and I quote,

> "As a particular meaningful result, I consider the initial one-sided [unipolar] development of all central nerve cells. Each neuroblast gives rise to an axis cylinder [axon] which from its cell of origin pushes out toward a certain target area. Considerably later it begins the generation of new extensions which with increasing branching spread out in the region of the cell. *Dendrites-fibers*, or *dendrites*, we can call them, in contrast to the axis fibers, in order not to need an adjective each time to describe them (Shepherd, 2015b)."

Ramón y Cajal, the father of modern neuroscience and an artist himself, produced detailed illustrations of the structure of neurons with their elaborate dendrites that puzzle scientists as

to their underlying function to this very day (Mel, 1994; Shepherd, 2015b; Swanson and Newman, 2016). Ramón y Cajal proposed two ideas that give insight into brain function: the neuron doctrine and the law of dynamic polarisation. The neuron doctrine states: "The neuron is the basic anatomical and physiological unit of the nervous system (Shepherd, 2015a)." The neuron doctrine points out that a neuron with its complex branching patterns is a finite unit. Cajal also proposed the law of dynamic polarisation, which states: "The transmission of nervous impulses is always from the dendritic branches and the cell body to the axon or functional processes (Shepherd, 2015a)." Synaptic transmission describes the conduction of impulses from one neuron to another. In a synaptic event, axon terminals of pre-synaptic neurons release neurotransmitters such as acetylcholine (Dale, 1906; Fishman, 1972; Todman, 2008), and glutamate (Watkins and Evans, 1981). These neurotransmitters diffuse at the synaptic cleft at a given time course (Clements et al., 1992), bind to neurotransmitter receptors on the post-synaptic membrane, and activate ion channels generating post-synaptic potentials (Brock et al., 1952; Eccles, 1972).

Indeed, the brain is a complex organ containing billions of cells with different cell types defined by their geometry, chemical, and molecular composition. At the same time, the brain is a powerful computing system capable of processing multi-sensory inputs and performing cognitive functions such as reasoning and storing memories. The complexity of the brain requires studies that involve imaging brain structures and activity at different scales ranging from: brain regions, network of neurons, single neurons, dendrites, synapses, ion channels, proteins, down to signalling molecules (Lichtman and Denk, 2011).

In this thesis, I aim to understand how the brain works by focusing on the functional role of a specific set of dendrites, the apical oblique dendrites of layer 5 pyramidal neurons (L5PNs) in the cortex. I investigated the generation of putative dendritic spikes in thin oblique branches. I utilized three approaches namely: (1) use of multi-compartment model; (2) single-cell electrophysiology; and (3) fluorescence calcium imaging. I built a microscope that uses two-photon multi-site holographic excitation to enable simultaneous recording of calcium activity at different sites along the neuron's dendritic tree. Using these techniques, I present evidences that apical oblique dendrites generate dendritic spikes during low-frequency burst of back-propagating action potentials (bAPs). I refer to these dendritic spikes as "***oblique branch* spikes**." The active nature of somatic action potentials (APs) to back-propagate into the dendritic tree provides a retrograde signal that activates voltage-gated channels in the dendrites (Stuart and Sakmann, 1994). In addition, we propose two techniques that can be used to optical record these oblique branch spikes with voltage imaging namely: temporal gating and "single-

photon excitation by scattered photons (1PESP)" to improve the signal-to-noise ratio (SNR) of the optically recorded voltage and calcium transients. I provide preliminary experiments demonstrating the efficacy of these techniques. I conclude by pointing to possible future experiments that would investigate how oblique branch spikes play a role in in dendritic integration.

1.2 Cerebral Cortex

The cerebral cortex processes most sensory information, apart from olfaction (see **Figure 1.1a** for cross-sections of the rat brain showing the cortex). The cortex is organized in a columnar manner with six layers (Mountcastle, 1997). Specific layers receive different thalamic projections. For example, in the whisker-barrel system, layers in the barrel cortex receive axon terminals in an organized fashion via the lemniscal and paralemniscal pathways. Axons of VPM neurons follow the lemniscal pathway terminating at layer 4 and layer 6 of the cortical column (**Figure 1.1b**). On the other hand, neurons in the posterior medial nucleus (POm) from the thalamus project their axons to the primary (S1) and secondary somatosensory cortex (S2) via the paralemniscal pathway. Axons in this pathway terminate to layer 1 and layer 5a of the cortical column.

In 1991, Felleman and Van Essen proposed that the cortex connectivity consists of feed-forward and feedback streams of information (Felleman and Van Essen, 1991). The feed-forward stream includes neurons: in the thalamus, in the supragranular layer (layers 1-2/3), and in the infragranular layers (layer 5-6) of the cortex with axons that terminate to layer 4. On the other hand, the feedback stream of information is carried by neurons from the thalamus and in the infra- and supra-granular layers of the cortex with axons that terminate to layer 1 and layer 6. In addition, a fraction of neurons in layer 5 form uni- and bidirectional connections among themselves (Markram et al., 1997; Markram et al., 2015).

The layers of the cortex are populated with neurons of different cell types, densities, and morphologies. Excitatory and inhibitory neurons populate all layers in the cortical column. Each neuron type exhibits diverse morphology and serves different functions (**Figure 1.1b**) (for comprehensive summaries, see Jiang et al., 2015; Markram et al., 2015; Rojo et al., 2016).

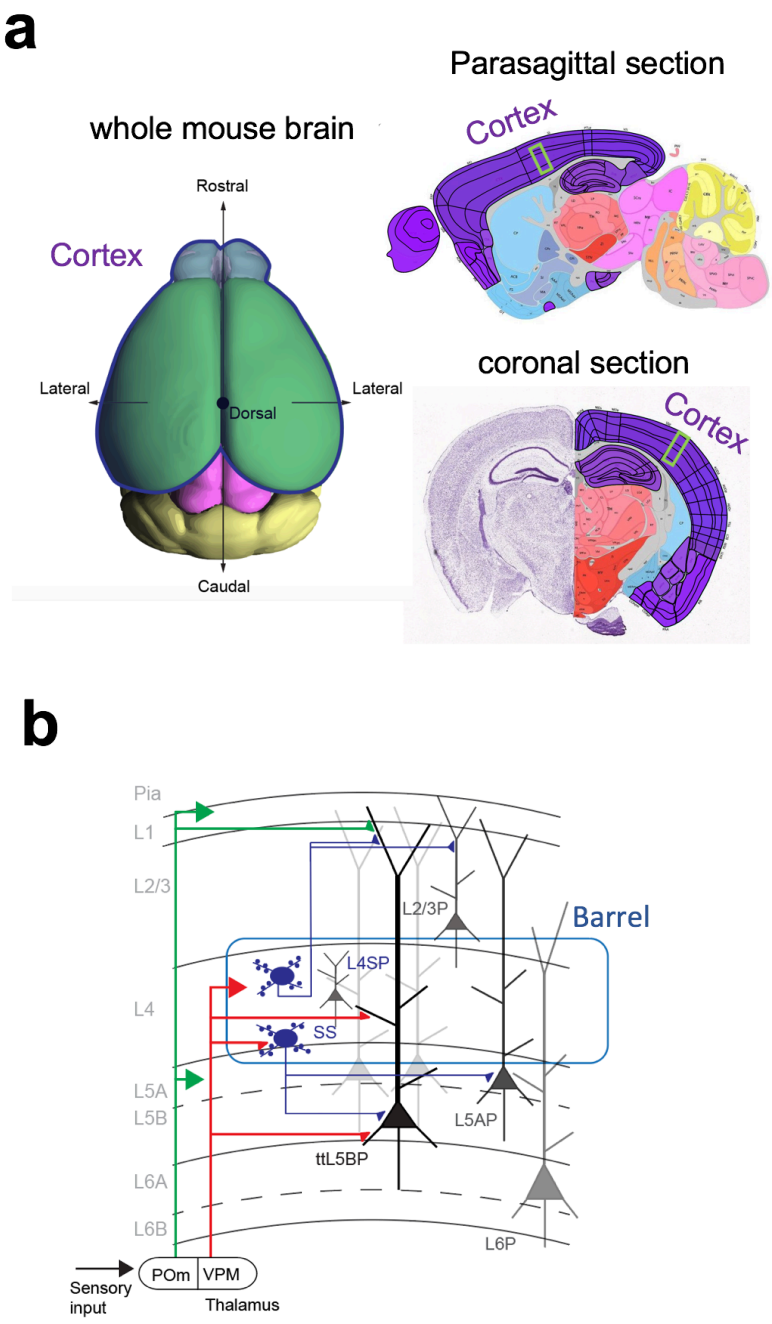

Figure 1.1 The cortex and its laminar organization. **a,** The whole-brain and cross-sectional view (i.e. parasagittal and coronal sections) of a mouse brain with the cortex, highlighted in purple), occupying the upper-half of the brain. **b,** A patch of membrane (indicated by the green box in **Figure 1.1a**) showing axonal projections arriving at different layers in the Somatosensory cortex. Axons from POm (green) and VPM (red) neurons in the thalamus terminate at layer 4 (lemniscal pathway) forming discrete barrels or at layer 4 and layer 1 (paralemniscal pathway). Within the cortical column, inputs to layer 4 are received by inhibitory somatostatin (SS) interneurons and layer 4 star pyramidal neurons, which interconnects with excitatory pyramidal neurons across different layers and modulates the output of L5PNs. **Figure 1.1a** is taken from the mouse brain atlas of the Allen Brain Institute (http://atlas.brain-map.org/). **Figure 1.1b** is adapted from Petersen (2007).

In this study, I focused on cortical pyramidal neurons in the somatosensory or barrel cortex. Layer 1 is the input layer where most of the axons from the POm terminate. This layer contains mostly inhibitory cells (e.g. neurogliaform cells). Layers 2 and 3 contain excitatory layer 2/3 pyramidal neurons and interneurons. Layer 4 is the input layer of the barrel cortex where afferents from the VPM terminates. This layer contains spiny stellate neurons, basket cells and layer 4-star pyramidal neurons (L4SP), with a strong overlap of the axons and dendrites of these neurons (Lubke et al., 2000; Egger et al., 2008). Layer 5 consists of pyramidal neurons (L5PNs), the output neurons of the cortex, with an apical trunk that extends up to layer 1 (Groh et al., 2010; Oberlaender et al., 2011; Oberlaender et al., 2012) and with axons that project back to the thalamus (Hattox and Nelson, 2007).

L5PNs can be further categorised into layer 5a (L5aPNs) and layer 5b pyramidal neurons (L5bPNs). The upper portion of layer 5 consists of slender tufted L5aPNs with a thin apical trunk but elaborate apical tuft dendrites in layer 1. The bottom portion of layer 5 contains thick-tufted L5bPNs, which have thick apical trunks and elaborate apical oblique dendrites in layer 4 and tuft dendrites in layer 1. With its dendritic tree crossing all layers, L5PNs are hypothesized to play a vital role in coupling feed-forward and feedback streams of information (Larkum, 2013). Feed-forward inputs arrive in layer 4 and layer 1 of the cortex, which activate inhibitory somatostatin (Som) interneurons and L4SP neurons. These neurons then modulate the output of L5aPNs and L5bPNs. *In vivo* recordings have shown that slender-tufted L5aPNs fire during active whisking task while the thick-tufted L5bPNs repetitively fire and are more involved during passive whisker touch (de Kock et al., 2007; de Kock and Sakmann, 2009). Layer 6 contains L6 pyramidal neurons, which have apical trunks that extend only up to layer 4, with a few short apical tuft branches (Ferrer et al., 1986; Ledergerber and Larkum, 2010). While different cell types populate different layers, recent studies that combined 3D anatomical reconstruction of neurons with thalamic axon innervation *in vivo* show that locations of different cell types do not necessarily match with independently defined cell layer borders (Oberlaender et al., 2011; Oberlaender et al., 2012). In particular, layer 5 exhibits a mixed distribution of L5aPNs and L5bPNs, except for a narrow zone at the borders of layers 4/5 and layers 5/6, where L5aPNs and L5bPNs are homogenously distributed, respectively.

1.3 Pyramidal Neurons

Pyramidal neurons are the primary excitatory neurons in the brain (for reviews, see DeFelipe and Farinas (1992), and Spruston (2008)). They populate brain regions that are involved in cognitive processes such as: the cerebral cortex, the hippocampus, and the amygdala. Like other neuronal types, pyramidal neurons exhibit diverse dendritic branching morphologies (**Figure 1.2**) and it is a growing interest to uncover the role of dendrites in information processing (Mel, 1993; Mel, 1994).

Pyramidal neurons have pyramid-shaped cell bodies with dendritic projections at the base and apex of the cell body (Spruston, 2008). At the base of this cell are thin projections from the soma called the basal dendrites. Another long thick branch stems out at the top of the soma and extends towards the brain surface, known as the main apical trunk. Layer 4 and layer 2/3 pyramidal neurons have short (~200 μm) apical trunks while L5PNs have long apical trunks (~800 μm), which span across all layers of the cortical column. At the end of the main apical trunk is a bifurcation point from which forms the nexus of a set of dendrites referred to as the apical tuft dendrites.

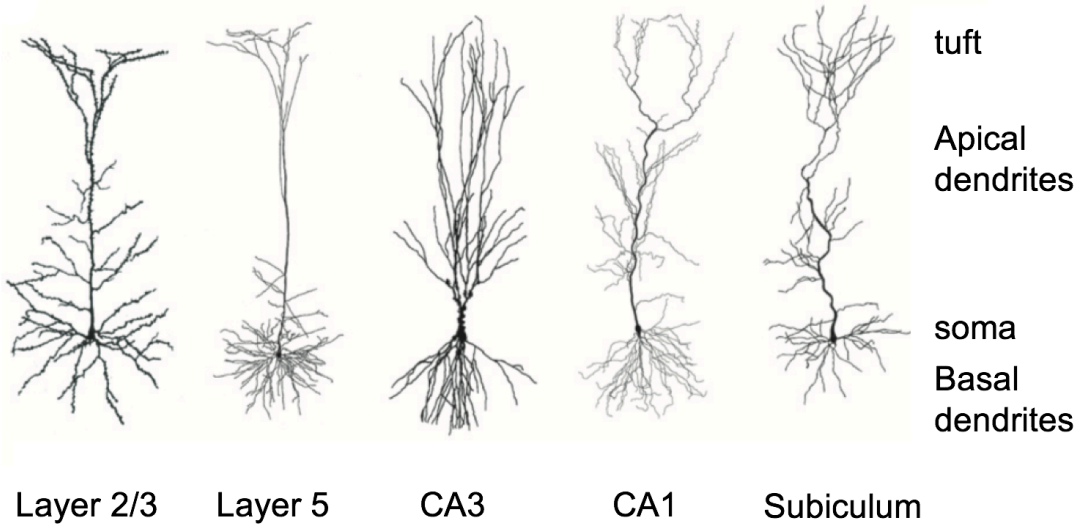

Figure 1.2 Pyramidal neurons from different brain regions. Morphological reconstructions of pyramidal neurons from different cortical areas. Each neuron has a soma, basal, apical, and apical tuft dendrites. Each neuron also has a distinct dendritic arborisation. For example, CA1 and CA3 neurons in the hippocampus have dense apical dendrites as compared to Layer 2/3 and L5PNs. **Figure 1.2** is taken from (Spruston, 2008).

Dendrites receive inputs from different layers. As discussed in the previous section, each dendritic region (i.e., basal, and apical dendrites) carries different streams of synaptic information from other neurons. At the synaptic connection, the synaptic cleft physically separates the axon terminal of a pre-synaptic neuron and the spine head or dendrite of the post-synaptic neuron. When a pre-synaptic neuron fires an AP, its axon terminals (or boutons) release neurotransmitters (e.g., acetylcholine, glutamate, and GABA) to the extracellular space and specifically to spine heads of dendritic branches of a receiving neuron. The extracellular space between a bouton and a spine forms a synaptic cleft between the firing neuron (pre-synaptic) and the receiving neuron (post-synaptic). Once released, the neurotransmitters bind to the receptor sites of different ligand-gated channels (e.g., AMPA and GABA receptors) on the membrane of the post-synaptic neuron generating a post-synaptic potential (for a review of different ion channels, see Purves (2004)). The soma and the axon receive inhibitory GABA-ergic synaptic inputs while the apical tuft dendrites receive excitatory synaptic inputs.

Dendrites act as low-pass filters, which help segregate synaptic inputs coming from distal dendrites and proximal dendrites. As recorded from the soma, distal inputs are strongly attenuated and delayed compared to proximal inputs. Triple electrode recordings, at the soma and two sites along the apical trunk of L5PNs, showed an exponential drop of the excitatory post-synaptic potential (EPSP) amplitude from the distal site (>40-fold) to the soma (Williams and Stuart, 2002). This strong passive filtering of the membrane requires more distal synapses to be activated in order to fire an AP at the soma. Somatic impact of distal synaptic inputs can be boosted with the recruitment of local dendritic spikes (reviewed in Etherington et al. (2001)).

1.4 Dendritic spikes

Synaptic potentials suffer attenuation and broadening as they propagate to the soma, reducing their capacity to bring the neuron to reach the threshold for firing APs (Stuart and Spruston, 1998). One way to boost the somatic impact of distal synaptic inputs is by the recruitment of regenerative events called dendritic spikes.

Over 60 years of studies now show that dendrites have active properties, which can transform and boost synaptic inputs (for reviews, see London and Hausser (2005), Major et al. (2013), and Stuart and Spruston (2015)). Dendritic spikes are regenerative potentials that arise from the activation of voltage-gated channels in the dendrites. The unique conditions required for activation of dendritic spikes *in vitro* imply that dendrites themselves are capable of

performing complex dendritic computation such as coincidence detection, logical and-or operation, and temporal discrimination (London and Hausser, 2005). With the advancement of genetically encoded calcium and voltage indicators that optically reports membrane activities of dendrites, scientists are now beginning to unravel how dendritic spikes play a role in sensory perception *in vivo* (Lavzin et al., 2012; Xu et al., 2012; Smith et al., 2013; Palmer et al., 2014; Manita et al., 2017).

There are three types of dendritic spikes, namely: sodium, calcium, and NMDA spikes (**Figure 1.3**). These spikes exhibit distinct temporal profiles arising from the kinetics of the channels that mediate them (as indicated by blue arrows in **Figure 1.3a-c**). Heterogeneous expression of these channels across the dendritic tree forms local dendritic spike domains (**Figure 1.3d**). Sodium spikes show fast activation of ~2 ms duration and have been recorded in thin apical oblique branches (Golding and Spruston, 1998; Kamondi et al., 1998; Losonczy and Magee, 2006).

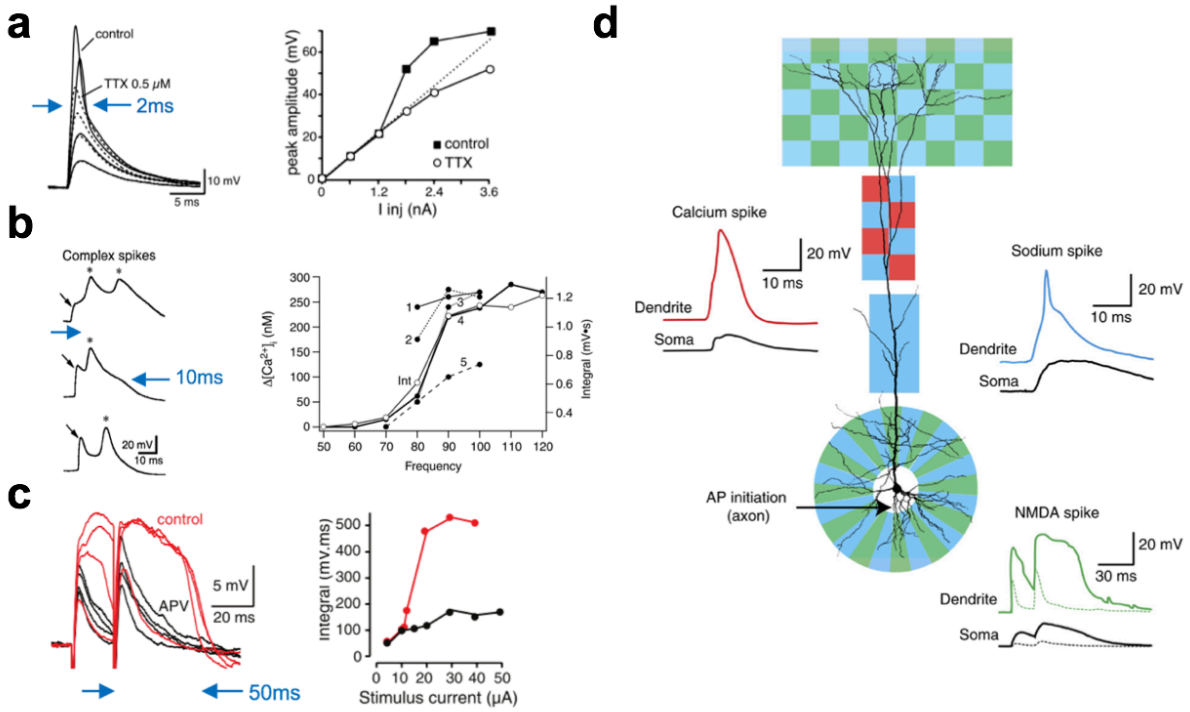

Figure 1.3 Sodium, calcium, and NMDA spikes. a, The generation of fast (~2 ms) sodium spike by injecting currents at a dendrite. The membrane voltage a non-linear increase in the peak amplitude at a certain current injection, which is abolished by bath application of sodium channel blocker (0.5 µM Tetrodotoxin, TTX). **b,** The generation of calcium spike (~10 ms depolarization) by a train of bAPs via the critical frequency protocol resulting to a non-linear increase in the intracellular calcium and total charge. **c,** The generation of broad (>50 ms) NMDA spikes with an extracellularly injected current, which non-linearly increases the total charge and is blocked by NMDA receptor antagonist, APV. **d,** The non-uniform distribution

of voltage-gated sodium and calcium, and NMDA receptors along the dendritic tree give rise to location-specific dendritic spikes. (Golding and Spruston, 1998; Golding et al., 1999; Larkum et al., 1999a; Golding et al., 2002; Stuart and Spruston, 2015)

Calcium spikes are mediated by the activation of voltage-gated calcium channels at the nexus of the apical trunk causing a long (50 ms) and wide-spread depolarization of the dendritic tree (Amitai et al., 1993; Schiller et al., 1997; Golding et al., 1999; Larkum et al., 1999a; Larkum et al., 2007). A train of bAPs above a critical frequency can provide sufficient depolarization in the dendritic tree to recruit calcium spikes in the distal apical trunk (Larkum et al., 1999a). The critical frequency protocol (which will be discussed in Chapters 2 and 4) provides a systematic approach to characterize the frequency of bAP train to recruit calcium spikes (Larkum et al., 1999a). NMDA spikes results from regenerative activation of NMDA receptors leading to plateau potentials that last more than 100 ms (Schiller et al., 2000; Major et al., 2008; Larkum et al., 2009; Antic et al., 2010a). NMDA receptors are ligand-gated channels expressed at excitatory synapse, but are intrinsically voltage-dependent due to internal block by magnesium ion at resting membrane potentials (Schiller et al., 2000; Major et al., 2008). A combination of these different types of spikes can also be evoke under strong synaptic inputs. For example, multiple synaptic inputs to the apical tuft dendrites of L5PNs can generate NMDA spikes, which can generate enough depolarization at the nexus of the apical tuft to cause the generation of a global Ca^{2+} spike (Larkum et al., 2009).

Recently, dendritic patch-clamp recordings and two-photon calcium imaging at tuft dendrites of L5PNs and layer 2/3 pyramidal neurons showed that global calcium spikes (Xu et al., 2012; Ranganathan et al., 2018) and local NMDA spikes (Lavzin et al., 2012; Smith et al., 2013; Palmer et al., 2014) are recruited *in vivo*. Dendritic spikes were observed when animals are performing an active-sensing whisker task (Xu et al., 2012; Ranganathan et al., 2018) or given a visual (Smith et al., 2013) or hind paw sensory stimulus (Palmer et al., 2014). In addition, NMDA spikes were recorded in layer 4 spiny stellate neurons in the barrel cortex and *in vivo*. These NMDA spikes are thought to contribute to angular tuning of whisker deflection (Lavzin et al., 2012).

Probing dendritic spikes along thin dendrites is challenging. Investigating whether thin dendrites (such as the basal dendrites) can generate dendritic spikes requires a combination of electrophysiology and imaging. For example, several studies coupled patch-clamp techniques with laser-uncaging and fluorescent voltage and calcium imaging to induce and record

dendritic activity in basal dendrites of L5PNs (Schiller et al., 2000; Antic, 2003; Kampa and Stuart, 2006; Nevian et al., 2007; Branco et al., 2010). Early work using glutamate-uncaging with UV lasers combined with a somatic patch showed that basal dendrites support the generation of NMDA spikes (Schiller et al., 2000). Functional calcium imaging studies of thin basal dendrites showed the local generation of regenerative calcium spikes (Kampa and Stuart, 2006). On the other hand, voltage imaging (Antic, 2003) and dendritic patch-clamp recordings (Nevian et al., 2007) provided evidences that support the generation of sodium and NMDA but not calcium spikes in basal dendrites. With the capacity of basal dendrites to generate dendritic spikes, scientists have hypothesized that basal dendrites can act as separate integrative compartments favouring two integration modes: (1) sub-threshold, location-dependent summation, and (2) local amplification of incoming spatiotemporally clustered information through dendritic spike generation (Branco et al., 2010). Moreover, excitatory inputs to proximal basal dendrites sum linearly over a narrow time window, while distal inputs were amplified and integrated over a broader time window (Branco et al., 2010). Multi-compartment models showed asymmetric membrane potential responses in basal dendrites with proximal synaptic inputs driving stronger responses than distal inputs (Behabadi et al., 2012).

A systematic approach to determine the condition required for generation of dendritic spikes evoked by bAPs is the critical frequency protocol. This protocol involves using a series of brief somatic current pulses (I = 3-4 nA, $\Delta\tau = 2$ ms) at a range of frequencies ($10 \leq f \leq 200$ Hz) to elicit a train of APs that back-propagates into the dendrites initiate non-linear regenerative dendritic activity (Larkum et al., 1999a). The critical frequency protocol can be performed with just somatic patch-clamp recording alone or in combination with dendritic recording or fluorescence calcium imaging (Larkum et al., 1999b; Kampa and Stuart, 2006; Barth et al., 2008; Ledergerber and Larkum, 2010; Shai et al., 2015) (see **Figure 1.4**).

With dendritic and somatic patch configuration, the somatic recordings are aligned at the peak of the last AP in the train. Then, the dendritic voltage (taken at a time point where maximum depolarization is observed at the highest frequency) is measured for different frequencies of the bAP train. The dendritic voltage is plotted with the frequency of the bAP train and the curve is fitted with a sigmoid function (see **Figure 1.4b-c**). The critical frequency, understood as the minimum frequency of the AP train that evokes a dendritic spike, is taken from the inflection point of the sigmoid fit from the relation of dendritic voltage with frequency of the AP train. With just the somatic patch-clamp recording, the critical frequency can be determined from the after-depolarizing potential (ADP) at the soma (**Figure 1.4b**). Alternatively, with functional fluorescence calcium imaging, the peak amplitude of dendritic

calcium transients associated with the bAPs can be measured (see **Figure 1.4d-e**). There is no need to align the optical calcium traces with the last bAP as the decay time of the fluorescence signal are long (~100 ms) relative the time-course of a single bAP (~1 ms).

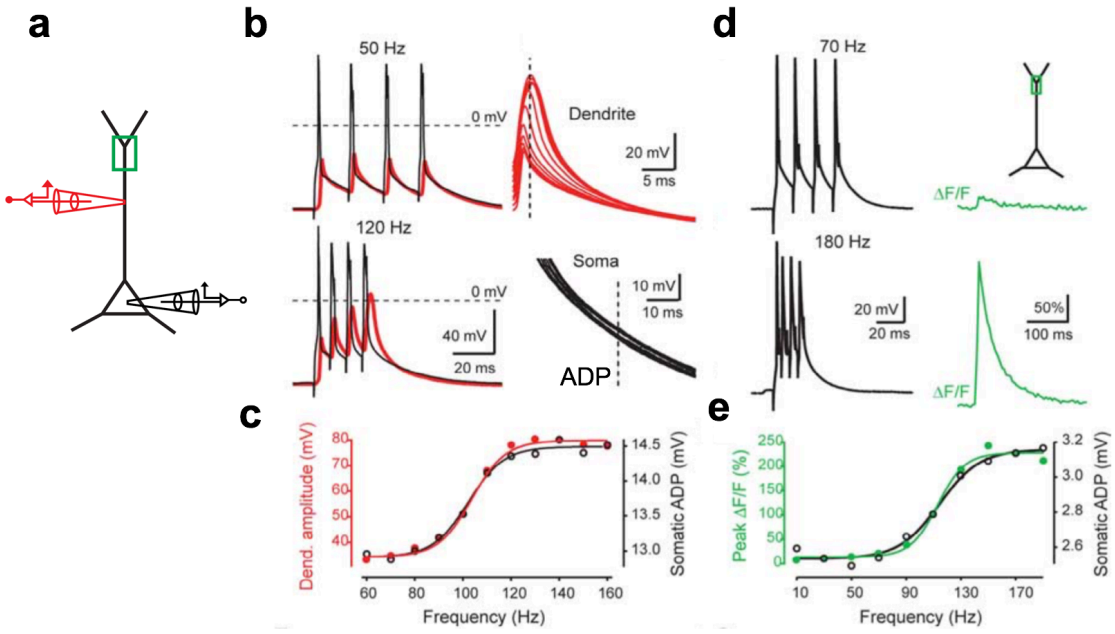

Figure 1.4 Dendritic-somatic patch clamp and fluorescence calcium imaging configuration for the critical frequency protocol. a, Schematic of sites for patch clamp electrodes at the apical trunk (red), soma (black), and imaging at the nexus of the apical tuft (green box) used in the critical frequency protocol. **b,** The recordings from the soma (black) and dendrite (red) during a 4-bAP train at 50 Hz and 120 Hz. The somatic and dendritic recordings were aligned to the last bAP in the train. **c,** The dendritic amplitude (red) and the after-depolarizing potential (black) at the soma across frequencies. The data were fitted with a sigmoid function. **d,** The somatic recordings of the bAP train and the associated calcium transients at the nexus of the apical tuft. **e,** The peak amplitude of the fluorescence calcium transient with the frequency of the bAP. The curve was fitted with a sigmoid function. Figure taken from Ledergerber and Larkum (2010).

Functional differences in dendritic spike generation between apical and basal dendrites have also been reviewed (Antic et al., 2010b). Dendritic NMDA spikes, generated in the apical tufts, can maintain a sustained dendritic depolarization critical for synaptic modification of distal synapses (Golding et al., 2002). In contrast, dendritic NMDA and Ca^{2+} spikes initiated at proximal locations in basal dendrites can bring the neuron into a sustained depolarized state, which resembles a cortical up-state (Milojkovic et al., 2004). Dendritic spikes can thus create conditions for causal interactions of active synaptic inputs setting up long-term synaptic

modifications in synaptic strength, as occurs during long-term potentiation (Bliss and Collingridge, 1993; Antic et al., 2010b; Gambino et al., 2014).

1.5 Optical recording of dendritic spikes

Dendritic spikes were first recorded using electrophysiological techniques. However, optical recording methods have been useful in probing spikes especially in thin dendritic domains. Optical recording using functional imaging with voltage and calcium indicators allow wide-field and non-invasive readout of the membrane activity (Hausser, 2014; Daria and Bachor, 2015). In the succeeding sections, I review the development and mechanisms behind calcium and voltage indicators, which enables optical recording of dendritic spikes.

1.5.1 Functional calcium imaging

Functional calcium (Ca^{2+}) imaging is now an indispensable tool in neuroscience since calcium activity can be correlated with fundamental neuronal processes. The transport of calcium between the extracellular and intracellular space is via ion channels such as: voltage-gated calcium channels (VGCCs), NMDA channels, AMPA channels among others (Catterall, 2000; Clapham, 2007; Higley and Sabatini, 2008; Grienberger and Konnerth, 2012). The expression and distribution of these channels in neurons have been extensively studied (Hille, 2001). The majority of Ca^{2+} influx occurs via VGCCs (Miyakawa et al., 1992; Markram and Sakmann, 1994; Christie et al., 1995) with Ca^{2+} pumps actively extruding Ca^{2+} ions to maintain a constant intracellular Ca^{2+} concentration (Carafoli, 1991). Also, intracellular organelles (e.g., endoplasmic reticulum and mitochondria) act as Ca^{2+} stores and contribute to Ca^{2+} homeostasis, as well as other functions (Berridge et al., 2000). Internal Ca^{2+} stores both buffer excess Ca^{2+} and act as a source of intracellular Ca^{2+} (Verkhratsky and Petersen, 1998). **Figure 1.5** shows how the intracellular Ca^{2+} concentration changes in response to the firing of an AP (bottom trace). At resting state, Ca^{2+} channels and pumps stay inactive keeping the internal calcium concentration at about 50-100 nM (Berridge et al., 2000). When a neuron receives excitatory synaptic inputs, the excitatory post-synaptic potentials propagate to the soma inducing a depolarization. As the neuron depolarizes to the threshold for an AP generation, VGCCs activate allowing Ca^{2+} ions to flow into the cell. Ca^{2+} influx via VGCCs also initiates neurotransmitter release in presynaptic terminals (Smith and Augustine, 1988).

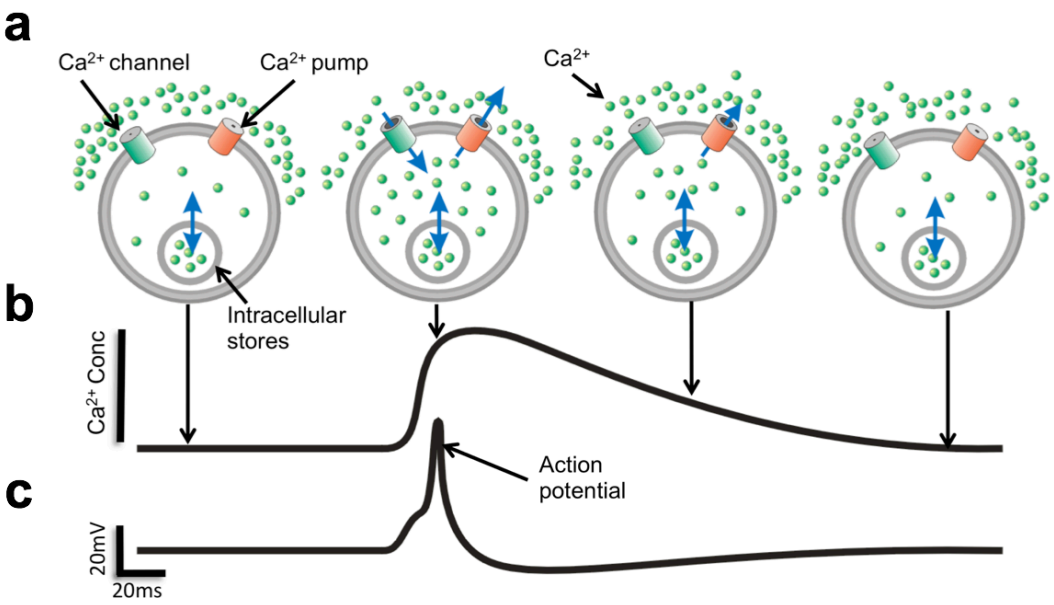

Figure 1.5 Ca^{2+} dynamics during neuronal activity. a, Schematic of a neuron with voltage-gated Ca^{2+} channels (green), Ca^{2+} pumps (orange) and internal Ca^{2+} stores. **b,** Internal Ca^{2+} concentration versus time. **c,** Voltage versus time. When a neuron fires an action potential Ca^{2+} influx via voltage-gated Ca^{2+} channels increases the internal Ca^{2+} concentration. Intracellular Ca^{2+} level returns to the resting state by extrusion of Ca^{2+} from the cytoplasm by Ca^{2+} pumps and buffering by internal Ca^{2+} stores. Figure taken from Castanares et al. (2019).

Chemical calcium indicators are synthesized with calcium binding sites and a fluorophore attached to it. The spectral properties (i.e., excitation and emission spectra) of the chemical fluorescent indicator determine the efficiency of the conversion of excitation photons to fluorescence photons. The common fluorescent calcium indicators (e.g., Fura-2, OGB-1) are excited with ultra-violet (UV) or blue light. When free intracellular calcium ions dock to the calcium binding sites, the dye molecules undergo a conformational change in their structure leading to changes in the spectral properties (excitation and emission) of the dye molecule (Tsien, 1980; Grynkiewicz et al., 1985). In addition, calcium indicators have characteristic calcium binding affinity constant, dissociation constant, and resting fluorescence. The dissociation time constant is the rate of which the bound calcium ion unbinds from the indicator (i.e., a shorter dissociation constant results in faster fluorescence decay time). Helmchen and Tank (2015) established a single-compartment approach to model the calcium dynamics relating the intracellular calcium concentration with the increase in fluorescence relative to the resting fluorescence, $\Delta F/F$. **Figure 1.6** shows a sample recording (at 100 frames per second using Andor Zyla 4.2 camera) of primary hippocampal cultures loaded with calcium indicator

(Cal-520 AM). Bath application of 1mM KCl triggered a synchronous burst activity in the network as observed by the calcium transients at the somas and dendrites of the neurons.

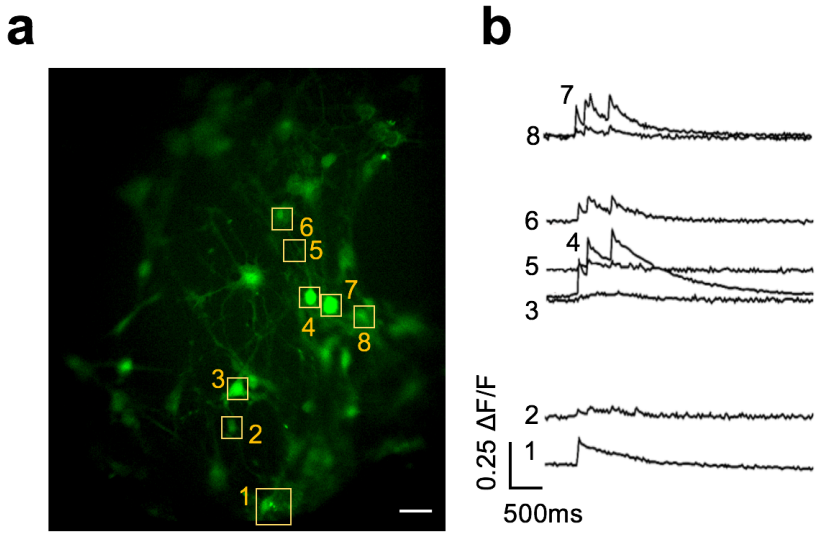

Figure 1.6 Recorded calcium transients during burst firing of primary hippocampal culture neurons. a, Epifluorescence single-photon image of the fluorescently labelled cultures with a calcium indicator. Regions of interest were drawn over the responding sites. **b,** The time-series fluorescence response of the ROIs after stimulating the cultures with a drop (~100-200µL) of 1 mM potassium chloride (KCl) in the bath. Figure modified from Castanares et al. (2019). Scale bar in Panel **a** is 40µm. Figure taken from Castanares et al. (2019).

1.5.2 Historical overview of chemical and protein derived calcium indicators

Tsien (1980) synthesized the first calcium dye indicator, which was modified from the selective Ca^{2+} chelator ethylene glycol tetraacetic acid (EGTA) to form 1,2-bis(o-aminophenoxy) ethane-N,N-N',N'-tetraacetic acid (BAPTA). At that time, the major issue in the design of the indicator was to make it selective between Mg^{2+} and Ca^{2+} (quinolinic derivative Quin-2) as well as its capacity to be loaded into cells without disrupting the membrane (Quin-2 acetoxymethyl or AM esters) (Tsien, 1981; Tsien et al., 1982). The next generation of Ca^{2+} indicators was based on Fura-2 which greatly improved the fluorescence yield by 30-fold by a larger blue-shift in the excitation/emission spectra with increasing Ca^{2+} concentration (Grynkiewicz et al., 1985). However, the application was limited since Fura-2's working wavelength is in the UV range, which can be phototoxic to the cells. Later on, visible-wavelength Ca^{2+} indicators, based on rhodamine (Rhod-2) and fluorescein (Fluo-2/Fluo-3), were developed (Minta et al., 1989). Another recently developed calcium indicator is Cal-520 which is a new BAPTA-based calcium indicator with a better signal-to-noise ratio (SNR ~ 2-

fold) and faster decay time (0.2 s slow-component) compared to oregon green bapta-1(OGB-1) (Tada et al., 2014). Cal-590, a red-shifted version of Cal-520, has been successfully used to image calcium activity of deep layer 5 and layer 6 pyramidal neurons *in vivo* (Tischbirek et al., 2015). These chemical calcium indicators are loaded into cells using methods such as: whole-cell patch (Tank et al., 1988; Eilers and Konnerth, 2009), electroporation (Haas et al., 2001; Nevian and Helmchen, 2007; Judkewitz et al., 2009; Dempsey et al., 2015), and multi-bolus loading (Stosiek et al., 2003; Barreto-Chang and Dolmetsch, 2009; Tischbirek et al., 2015; Cameron et al., 2016).

In 1997, Roger Tsien's group revolutionized calcium imaging with the development of genetically encoded calcium indicators (GECIs) referred to as 'Cameleons' (Miyawaki et al., 1997). These sensors are derived from a concatenation of recombinant calcium binding domain, Calmodulin, with a GFP-derived fluorescent protein pair (Whitaker, 2010). Later, the sensor was improved with the use of just single-GFP derived molecule which is now known as GCamp (Nakai et al., 2001). GCamp indicators have undergone several improvements, and its recent versions (i.e., GCamp6s and GCamp6f) are now widely used in experiments *in vivo* (Tian et al., 2009; Akerboom et al., 2012; Chen et al., 2013). These GECIs can be expressed in cells using methods such as:, AAV viral injection (Tian et al., 2009), and use of transgenic mouse lines (Heim et al., 2007; Zeng and Madisen, 2012). GECIs are useful in recording calcium activity at the cell bodies and dendrites while the animal receives sensory inputs or performs a behavioural task (Xu et al., 2012; Palmer et al., 2014).

1.5.3 Functional voltage imaging

Imaging the electrical activity of neurons is regarded as the holy grail in neuroscience(Emiliani et al., 2015; Bando et al., 2019). The cell membrane that separates the intracellular and extracellular space has a thickness of about 4nm. The membrane acts as a capacitor, where an electric field (~10^7-10^8 V/m) arises due to the separation of ions by the membrane. Voltage indicators (VIs) rely on detecting the changes in the electric field across the membrane (for review see (Peterka et al., 2011)). There are several mechanisms that facilitate reporting of the changes in electric field or equivalently the membrane potential such as: redistribution (Waggoner et al., 1977), reorientation, electrochromism (Loew et al., 1979), Förster energy transfer (FRET) and second-harmonic generation (Moreaux et al., 2002; Dombeck et al., 2005). In the next section, I will focus the review on electrochromism which is the mechanism observed by the voltage indicator (i.e., JPW-1114) used in this work.

Electrochromic voltage indicators rely on the direct interaction of the chromophore with the electric-field without involving any chromophore movement (Loew et al., 1979; Fluhler et al., 1985). These VIs, derived from styryl and hemicyanine dyes, are polar and lipophilic. These dyes also emit bright fluorescence when bound to a lipid membrane. When the membrane experiences a voltage transient, the membrane-bound chromophores are subjected to a change in the electric field, which induces linear shifts in the spectral excitation and emission properties otherwise known as the Stark effect. For example, **Figure 1.7** illustrates the spectral shift for the case of an electrochromic dye (JPW-1114) where a change in the membrane potential, ΔV, shifts the excitation (blue curve) and emission (red curve) spectra to the right (dotted curve). The shift increases the absorption efficiency (at 532 nm excitation) resulting in more "red" fluorescence photons emitted. The choice of excitation wavelength determines the sensitivity of the recording. Illuminating at the peak of excitation spectrum yields the maximal fluorescence yield but it results in a minimal sensitivity, *dF/F*, or SNR. Using an excitation wavelength at the rising or falling gradients of the excitation spectrum (w_{left} and w_{right} in **Figure 1.7**), provides higher sensitivity (Zhou et al., 2007; Loew, 2010). One issue with electrochromic VIs is the translocation of the dye molecules between the inner and outer leaflet of the membrane resulting to a reduction of the sensitivity (Moreaux et al., 2000). With dye molecules binding to either the inner and outer leaflet of the membrane, the Stark effect effectively cancels out resulting in low sensitivity. Such phenomena is otherwise referred to as "flip-flop," which was addressed by synthesizing dyes to be hydrophilic and hydrophobic at either ends (e.g. di-8-ANEPPS) (Loew et al., 1992).

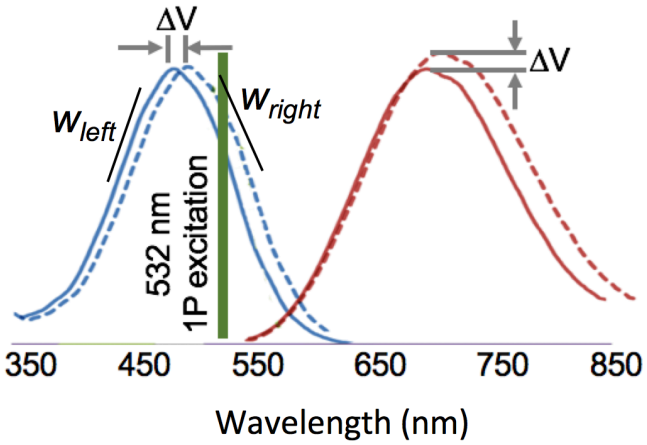

Figure 1.7 The spectral shift in excitation and emission spectra of electrochromic VSDs due to a voltage transient. This small rightward spectral shift with membrane depolarization, ΔV, increases the excitation coefficient at that band of wavelength (~532 nm), which further increases the number of emitted fluorescence photons.

1.5.4 Promising fluorescent voltage indicators

Several voltage sensors are commercially available such as the oxonol and hemicyanine dyes. Other novel voltage sensors can be obtained by communicating with the people who synthesize them. In this section, I highlight some of the reliable and recently synthesized voltage indicators that can be used to detect dendritic spikes in single neurons.

One of the commonly used dyes to probe neuronal activity is the JPW-1114 (or its di-methyl analogue JPW-3028) which belongs to the class of hemicyanine or styryl dyes (Loew, 2011). JPW-1114 is commercially distributed as Di-2-ANEPEQ (ThermoFisher catalogue no. D6923). This dye is water-soluble making it suitable for loading onto single cells by intracellular injection with a patch pipette (Popovic et al., 2012). This dye has been used to detect subthreshold and supra-threshold membrane potentials at the axon-initial-segment (Palmer and Stuart, 2006; Foust et al., 2010; Popovic et al., 2011), soma (Berger et al., 2007), apical trunk, thin oblique and basal dendrites (Antic, 2003; Zhou et al., 2008b; Holthoff et al., 2010; Zhou et al., 2015), as well as dendritic spines (Palmer and Stuart, 2009; Popovic et al., 2014). Combining voltage and calcium indicators allows simultaneous recording of fluorescence voltage and calcium activity. For example, using JPW-1114 and Calcium Green can be excited at 488 nm (exciting at the JPW-1114 at the rising gradient of its excitation spectrum) while a proper dichroic mirror can separate the detection of their respective fluorescence (Bullen and Saggau, 1998).

Fluorinated voltage-hemicyanine dyes are improved versions of the hemicyanines dyes and exhibit better sensitivity (Loew, 2011; Yan et al., 2012). Fluorination is done by adding fluorine substituents on the dye chromophore that allows fine-tuning of the excitation and emission spectra of the dyes (Yan et al., 2012) for single- and multi-photon excitation. The fluorinated di-2-AN(F)EPPTEA was used to record back-propagating action potentials at oblique dendrites and apical tuft dendrites of neurons using a two-photon microscope (Acker et al., 2011). ANNINE-6 and ANNINE-6P, a variant of the styryl dyes with a rigid "annelated" ring framework is promising particularly for two-photon application in vitro (Kuhn et al., 2004; Fromherz et al., 2008) and more recently *in vivo* (Roome and Kuhn, 2018). The ANNINE-6P has good solubility in water and has a high voltage sensitivity and SNR when excited by a narrow band light source at 488 nm (for single-photon) and 976 nm (for two-photon) (Kuhn et al., 2004).

An example of a hybrid FRET indicator is the DiO/dipycrilamine (DPA) sensor, which showed considerably large voltage sensitivity from *in vitro* recordings (Bradley et al., 2009). DiO is a lipophilic green fluorescent particle which specifically binds to the cellular membrane;

while, DPA exhibit strong absorption with "green" photons. When the neuron fires an action potential, the change in the electric field draws the DPA molecules close to the DiO particles and quenches its "green" fluorescence photons. As a result, the fluorescence signal decreases for every action potential. While FRET sensors are bright, their time-constants are slower (~μs) than the electrochromic dyes (~ns). In addition, the acceptor DPA increases the membrane capacitance, which broadens the width of the optical trace of the action potential (Bradley et al., 2009). The DiO/DPA voltage-sensor has been demonstrated to be compatible with two-photon excitation (Fink et al., 2012; Tran-Van-Minh et al., 2016).

Genetically encoded voltage indicators (GEVIs) are a recent development in optical voltage reporters (Kralj et al., 2012; Gong et al., 2014; Hochbaum et al., 2014; St-Pierre et al., 2014; Carandini et al., 2015; Gong et al., 2015). GEVI designs utilize voltage-sensing fluorescent proteins, Forster energy transfer FRET, or the use of opsins (for review see, Antic et al., 2016). A few notable ones are the ASAP (St-Pierre et al., 2014; Chamberland et al., 2017), VSFP-Butterfly (Akemann et al., 2012; Akemann et al., 2014; Carandini et al., 2015), Quasars (Hochbaum et al., 2014) and Ace1Q-mNeon/Ace2N-mNeon (Gong et al., 2015).

1.6 Microscopes used for recording dendritic spikes

The development of calcium and voltage indicators drives new designs of optical microscopes that can acquire dynamic changes in fluorescence with high temporal and spatial resolution. Optical recording of dendritic spikes is performed by acquiring the changes in fluorescence, *dF/F*, from either calcium or voltage indicators. To record dendritic spikes (20-100ms), voltage indicators can be used with the sampling rates of at least 100Hz. Slower acquisition times with calcium indicators can also be used but with additional interpolation techniques. The fluorescence from these indicators can be acquired using microscopes operating in either single-photon (1P) or two-photon (2P) excitation (see **Figure 1.8**).

Wide-field (Epifluorescence) 1P microscopes use high-energy photons (e.g. blue) to excite fluorophores in a wide area of the sample. The fluorescence signal from the illuminated region is captured via a camera (or multi-channel detector). Electron multiplying CCD cameras (EMCCD cameras; e.g., from Andor & Photometrics) have high sensitivity (i.e., ~90% quantum efficiencies at 600-800 nm), large dynamic range (up to 200,000e− well depth), and high sampling rates up to 4 kHz. For neuronal cultures, 1P wide-field microscopy with an EMCCD camera enables the recording of action potentials from VSDs and GEVIs (Zhou et

al., 2008a; Kralj et al., 2012). For tissue samples, several studies have utilized confocal microscopes coupled with an EMCCD to record dendritic spikes (Kampa and Stuart, 2006; Canepari et al., 2007), membrane potentials in dendrites (Antic, 2003; Popovic et al., 2015), fast APs in axons (Palmer and Stuart, 2006; Popovic et al., 2011) and bAPs in spine heads (Popovic et al., 2014). However, 1P excitation exhibits low resolution along the optical axis and can introduce strong photo-bleaching of the fluorescent indicators. Also, the capacity of 1P illumination to work *in vivo* is very limited due to poor tissue penetration.

On the other hand, a 2P laser-scanning microscopes use non-linear absorption of two photons with energies half of those required for 1P absorption to excite the same fluorophore. A 2P microscope typically uses a near-infrared femtosecond pulsed laser that is focused on the sample via a high numerical aperture objective lens (NA ~0.8-1.0). With non-linear excitation, the fluorescence is only emitted within the diffraction-limited focal volume of ~0.1 μm^3 (Zipfel et al., 2003) where there is a high probability of simultaneous two photon absorption by the fluorophore. To record the fluorescence across multiple regions of the sample, the focused laser beam is scanned in a point-to-point manner (e.g., 100 Hz to 1 kHz) (Katona et al., 2011; Katona et al., 2012; Grewe et al., 2014; Schuck et al., 2018). The beam is steered using a mechanical (e.g., galvanometric mirrors, resonant scanners) or crystal based instruments (e.g., acousto-optic deflectors (AODs)). A single-channel detector such as a photomultiplier tube or photodiode collects the fluorescence signal at each point. Then, a 2D fluorescence image is reconstructed from the set of single time point recordings.

Several laser-scanning modes are utilized to tune the spatio-temporal resolution of the acquisition and minimize the stress on the beam steering device. These laser scanning modes include raster-scan, line-scan, minimal-inertia trajectories and random-access scans (Katona et al., 2011; Katona et al., 2012; Grewe et al., 2014; Schuck et al., 2018). The raster scan is a common mode wherein the laser spot sweeps the image region in a zig-zag motion. Raster-scan imaging is implemented using galvanometric mirrors (GMs) and resonant scanners at rates of up to 100 Hz. Mechanical inertia in galvanometric mirrors limits the spatial range and temporal resolution of the recordings. Minimal-inertia beam trajectories, beam paths that pass only the sites of interest, can further increase the temporal resolution of the acquisition. An optimization algorithm can be implemented to pre-calculate the best beam trajectory that passes the cell bodies while minimizing the mechanical inertia of the GMs (Schuck et al., 2018). Line scans, which uses the fast-scan of the resonant scanning mirrors, can achieve ~5 kHz acquisition rates. Line scans along a dendritic segment proves to be fast enough to detect bAPs and spike (Acker et al., 2011; Tran-Van-Minh et al., 2016; Roome and Kuhn, 2018).

Our approach to record dendritic spikes is via a multi-site, multi-channel recording using the holographic projection technique. This technique allows projection of the multiple excitation foci "at the same time" with changes in fluorescence captured by a camera (see ★ in **Figure 1.8**). The temporal resolution of the recording is dictated by the maximum frame rate of the camera for a given imaging area (e.g., ~2 kHz for Red Shirt Imaging, or in our hands, 0.4 kHz for Andor Ixon 897 EMMCD camera with 128x128 pixels).

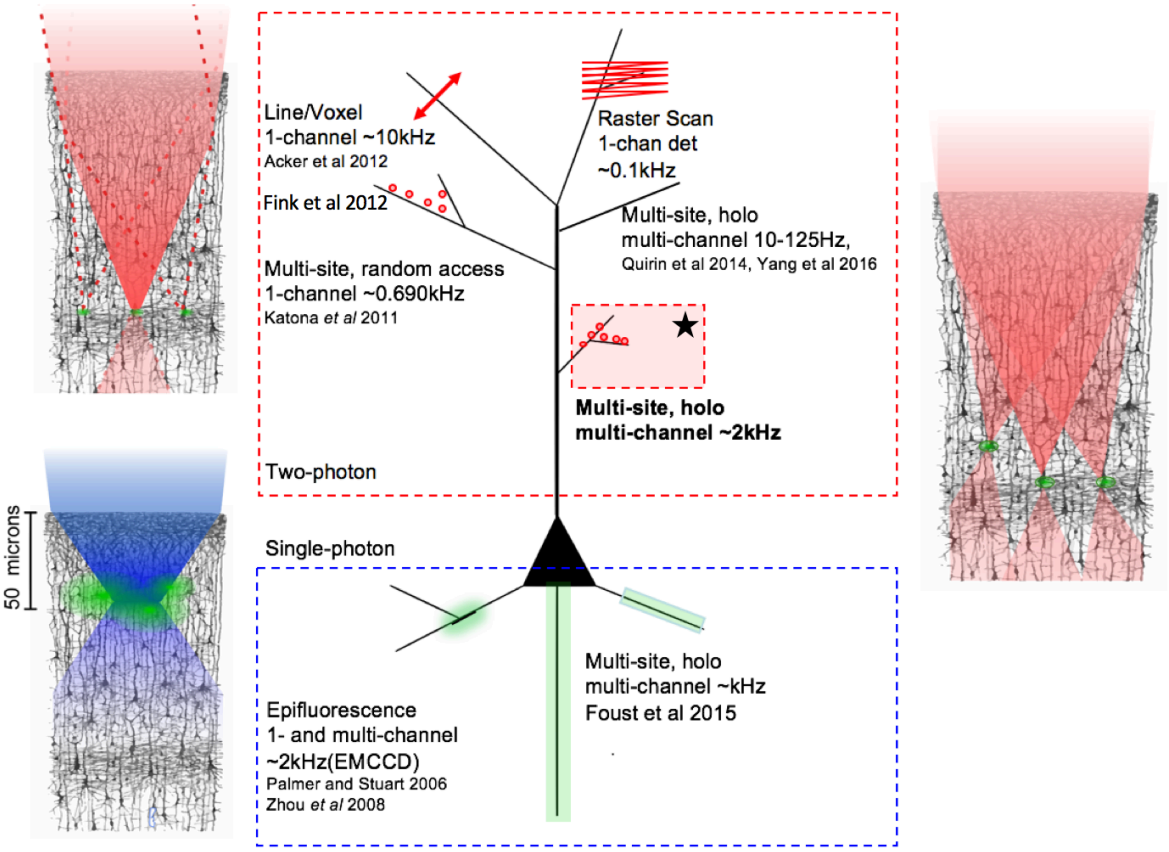

Figure 1.8 A summary of single-photon (1P) and two-photon (2P) microscopes used to perform high-speed fluorescence detection. 1P microscopy allows wide-field illumination of the sample that are <50 μm deep. On the other hand, two-photon microscopy allows deeper penetration on the tissue. Several modes of beam-scanning and beam-shaping are capable to readout fluorescent activity from multiple sites of the sample at high frame rates.

1.7 Optical probing of dendritic spikes in apical obliques dendrites

In the previous sections, I discussed a general overview of the brain down to the structure and function of PNs in the cortex. I also covered dendritic spikes in different dendritic domains (tufts and basal) of PNs and the optical techniques to probe them. However, the main question I pose in this thesis is to understand spikes in a specific dendritic domain of L5PNs, the **apical oblique dendrites**. Oblique dendrites are thin branches that bifurcate from the main apical trunk. Most studies on thin oblique branches were done in hippocampal CA1 PNs while there are only a handful of studies done in L5PNs. To gain a better perspective on my main research question, this section reviews some findings on oblique dendrites in CA1 PNs and L5PNs.

1.7.1 Properties of apical obliques dendrites of CA1 PNs.

CA1 PNs have numerous thin oblique dendrites, which receive approximately 80% of the synaptic input from the Schaeffer collaterals (Frick et al., 2003) (**Figure 1.2**). Several studies have assessed how thin oblique dendrites affect forward and back-propagation of action potentials and dendritic spikes *in silico* (Vetter et al., 2001; Migliore et al., 2005; Ferrante et al., 2013), *in vitro* (Gasparini et al., 2004; Canepari et al., 2007; Gasparini et al., 2007) and *in vivo* (Kamondi et al., 1998). In addition, a few notable works have assessed how the interaction of somatic AP with EPSPs leads to increased levels on calcium in oblique dendrites and the induction of long-term potentiation (LTP) (Magee and Johnston, 1997; Losonczy and Magee, 2006; Canepari et al., 2007).

In silico studies showed that dendritic morphological characteristics (i.e., number of branch points, diameter of the dendrites, and branch point morphology) and dendritic ion channel densities influence the efficacy of bAP invasion of the dendritic tree (Vetter et al., 2001; Migliore et al., 2005). Goldstein and Rall (1974) reported that the efficacy of bAP propagation was dependent on the impedance mismatch measured as the geometric ratio ($GR = \sum_j {d_j}^{3/2} / {d_a}^{3/2}$, where d_j is the diameter of the *j*th daughter branch and d_a is the parent branch where the action potential is propagating). A lower *GR* will result to a decrease or failure in the AP conduction. Furthermore, numerical calculations predict that the peak of the AP increases as it conducts from the branch point to the sealed end tip (Goldstein and Rall, 1974). Using multi-compartmental modelling of morphological reconstructions of different neuronal cell types, Vetter et al. (2001) observed that dendritic morphology and voltage-gated sodium and potassium channel densities act together to generate a diverse extent of AP propagation in different neurons. Furthermore, Migliore et al. (2005) showed that in CA1 pyramidal neurons,

bAPs invade the oblique branches in an "all-or-nothing" fashion tuned by the distribution of A-type potassium and hyperpolarization-activated cyclic nucleotide-gated (HCN or Ih) channels. The increase in Ih densities at oblique branches facilitates bAPs while the increase in the A-type potassium channel density from trunk to oblique branches limits bAP invasion.

CA1 PNs show that apical oblique dendrites exhibit active properties and voltage-gated ion channels (e.g., voltage-gated calcium, sodium, A-type potassium, calcium-activated SK channels, NMDA and AMPA receptors) (Frick et al., 2003; Canepari et al., 2007; Gasparini et al., 2007). Calcium influxes associated with single bAP or a train of bAPs in apical obliques of CA1 pyramidal neurons were observed (Frick et al., 2003; Gasparini et al., 2007). Frick et al. (2003) hypothesized that an increase in the surface-volume (s/v) ratio of small diameter oblique dendrites at the branch point compared with the main apical trunk would yield a larger Ca^{2+} signal in the oblique branches (if the bAP amplitude, calcium channel density, calcium channel type, and calcium buffering-extrusion were constant). However, Frick et al. (2003) observed that the amplitude of the calcium signals remained constant from the main apical trunk and up to ~40 μm along the oblique branches (**Figure 1.9c**). This calcium signal normalisation was due to an increased density of A-type potassium channels from the main apical trunk to the oblique branches as blocking the channels with 2-4 mM 4-aminopyridine (4-AP) in the bath solution resulted in a larger bAP-associated calcium signals in the oblique dendrites. Gasparini et al. (2007) further showed that the calcium influx in the oblique dendrites associated with bAP trains follows a biphasic response were the calcium signal increased along the proximal oblique segments then progressively decreased at the distal oblique segments. The distance-dependent decrease of the calcium signal in the distal oblique segments was reduced by the application of $BaCl_2$, another A-type potassium channel blocker, in the bath. Pairing bAP trains with asynchronous synaptic stimulation boosted the calcium influx in distal oblique segments (Canepari et al., 2007; Gasparini et al., 2007). Combined voltage and calcium imaging showed that synaptic activation of NMDA receptors via extracellular stimulation was enough to recruit large calcium influx in the oblique branches where the calcium influx seems not to affect the membrane potential profile at the soma (Canepari et al., 2007). The increased levels of intracellular calcium with synchronous activation of synapses and bAP trains may cause local changes in the ionic conductance and can be a mechanism for a branch specific plasticity proposed by Alkon (1999). The activation of voltage-gated sodium channels and/or AMPA and NMDA receptors led to the generation of dendritic oblique spikes as recorded *in vitro* and *in vivo* (Kamondi et al., 1998; Losonczy and Magee, 2006). Kamondi et al. (1998) showed that apical obliques of CA1 PNs can exhibit a large amplitude fast spike (LAS),

possibly a sodium spike, and a putative calcium spike *in vivo* (**Figure 1.9a**). In a later study, Losonczy and Magee (2006) confirmed that sodium spikes are recruited in oblique dendrites by synchronous activation of spines (with AMPA and NMDA receptors) within a 6-ms integration window (**Figure 1.9b**). This fast sodium spike was accompanied with a large calcium influx suggesting the presence of voltage-gated calcium channels in the oblique dendrites.

Several computer modelling studies have assessed the propagation of bAPs and dendritic oblique spikes with the morphology of CA1 PNs (Migliore et al., 2005; Ferrante et al., 2013). Bernard and Johnston (2003) reported a distance dependent sodium spike threshold along an oblique branch. The threshold of the sodium spike in oblique branches is influenced by the branch-point tapering (e.g., husky, lanky, and regular) with a husky branch-point taper resulting to the convergence of dendritic and AP spike threshold (Ferrante et al., 2013). In addition, oblique sodium spike seldom reaches the soma determined by the unfavourable impedance mismatch (large GR >1, from oblique branch to the main apical trunk) and the distance of the stimulation site (Migliore et al., 2005). However, an oblique spike with sustained dendritic activity (~10 mV) can influence the soma. This sustained activity can be through synchronous supra-threshold activation of neighbouring oblique branches.

Overall, recordings from CA1 pyramidal neurons show that apical oblique dendrites express ion channels (i.e., voltage-gated sodium, calcium, A-type K channels and calcium-activated SK channels) and AMPA and NMDARs that enable them to actively participate in dendritic integration. Indeed, there is sufficient evidence that oblique dendrites in CA1 pyramidal neuron participate in dendritic integration.

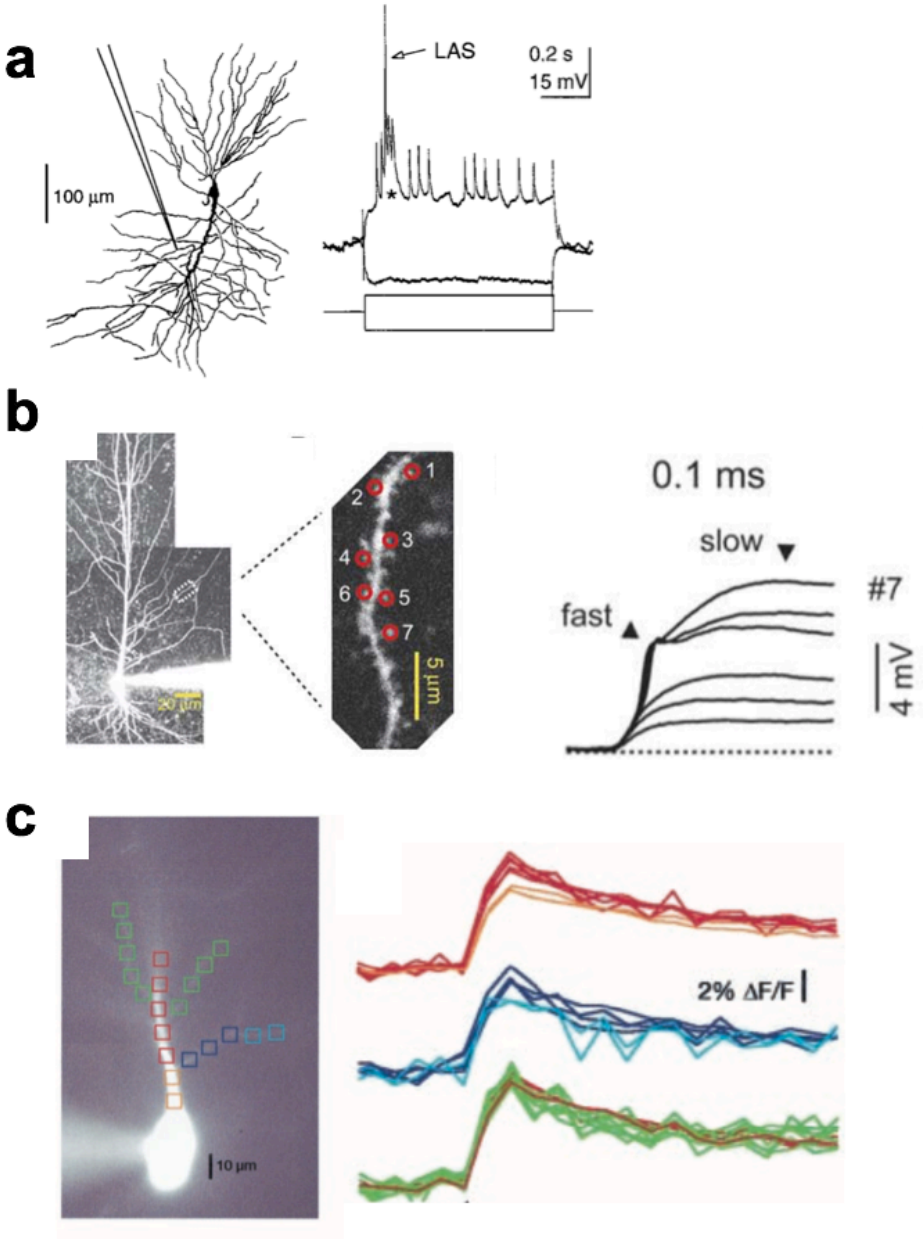

Figure 1.9 Evidence of synaptic contacts and active properties of oblique dendrites of CA1 PNs. a, Biocytin reconstruction of the recorded CA1 PN *in vitro* with a dendritic patch recording at an oblique dendrite. The membrane potential response with a step current showed a large amplitude spike (LAS) followed by a putative calcium spike (∗). **b,** 2P reconstruction of a CA1 PN with the uncaging sites targeting the spines at an oblique dendrite. The synchronous activation of the 7 spines led to the recruitment of a fast sodium spike which added fast 4 mV depolarization to the EPSP at the soma. **c,** The calcium transients along the oblique dendrites relative to the main apical trunk. Figures **1.8a-c** are taken from Kamondi et al. (1998), Losonczy and Magee (2006), and Frick et al. (2003), respectively.

1.7.2 Properties of apical oblique dendrites of cortical L5PNs

In contrast to CA1 PNs, L5PNs in the cortex have a fewer number of oblique dendrites. Biocytin reconstructions under high magnification light microscope showed uni- and bi-directional connections among L5PNs (Markram et al., 1997). Majority (63.2%, 56/106) of the total synaptic contacts were found at the basal dendrites while a considerable fraction (27.4%, 29/106) were observed at the oblique branches (Markram et al., 1997) (**Figure 1.10a**). A computer modelling study reveals that the distribution and number of oblique dendrites branching out from the apical trunk of L5PNs influence the capacity of somatic APs to evoke Ca^{2+}-AP in the nexus (Schaefer et al., 2003).

There are few findings suggesting that apical oblique dendrites of L5PNs exhibit active properties. Studies performing voltage imaging in cortical L5PNs show that bAPs invade the apical oblique dendrites with less filtering (maintained width of bAP) compared to what is expected in passive cable theory (Antic, 2003; Zhou et al., 2015) (**Figure 1.10b**). In addition, bAPs failed to invade select distal oblique dendrites when propagating along branch points (Zhou et al., 2015). Using calcium imaging, Schiller (2002) reported non-uniform calcium influx along the dendritic tree during associated with an inter-ictal paroxysymal depolarization shift (PDS) responses in L5PNs (**Figure 1.10c**) with the largest calcium influx in an apical oblique branch (see ★ in **Figure 1.10c**). These calcium influxes indicate that voltage-gated calcium channels are expressed in oblique branches of L5PNs.

Quadruple-paired somatic recordings of L5PNs with AP-EPSP pairing protocol generated LTP at proximal (<200 μm from the soma) L5PN-L5PN synaptic connections as estimated from the 2.2 ± 0.2 ms EPSP rise time (Sjostrom and Hausser, 2006). The frequency of the AP train used was 50 Hz, a frequency well below the critical frequency of evoking Ca^{2+} spikes at the nexus of the apical tufts (Larkum et al., 1999a). The results suggested that the mechanism of LTP induction could not be explained by recruitment of Ca^{2+} spikes at the nexus via coincidence of bAPs and EPSPs proposed by Larkum et al. (1999b). The induction of LTP with AP trains indicated that oblique dendrites of L5PNs allowed bAP invasion (via voltage-gated sodium channels) and calcium influx (possibly via AMPA and NMDA receptors) which are precursors for activity-dependent synaptic plasticity (Koester and Sakmann, 1998; Sjostrom et al., 2001) or meta-plasticity (Abraham and Bear, 1996).

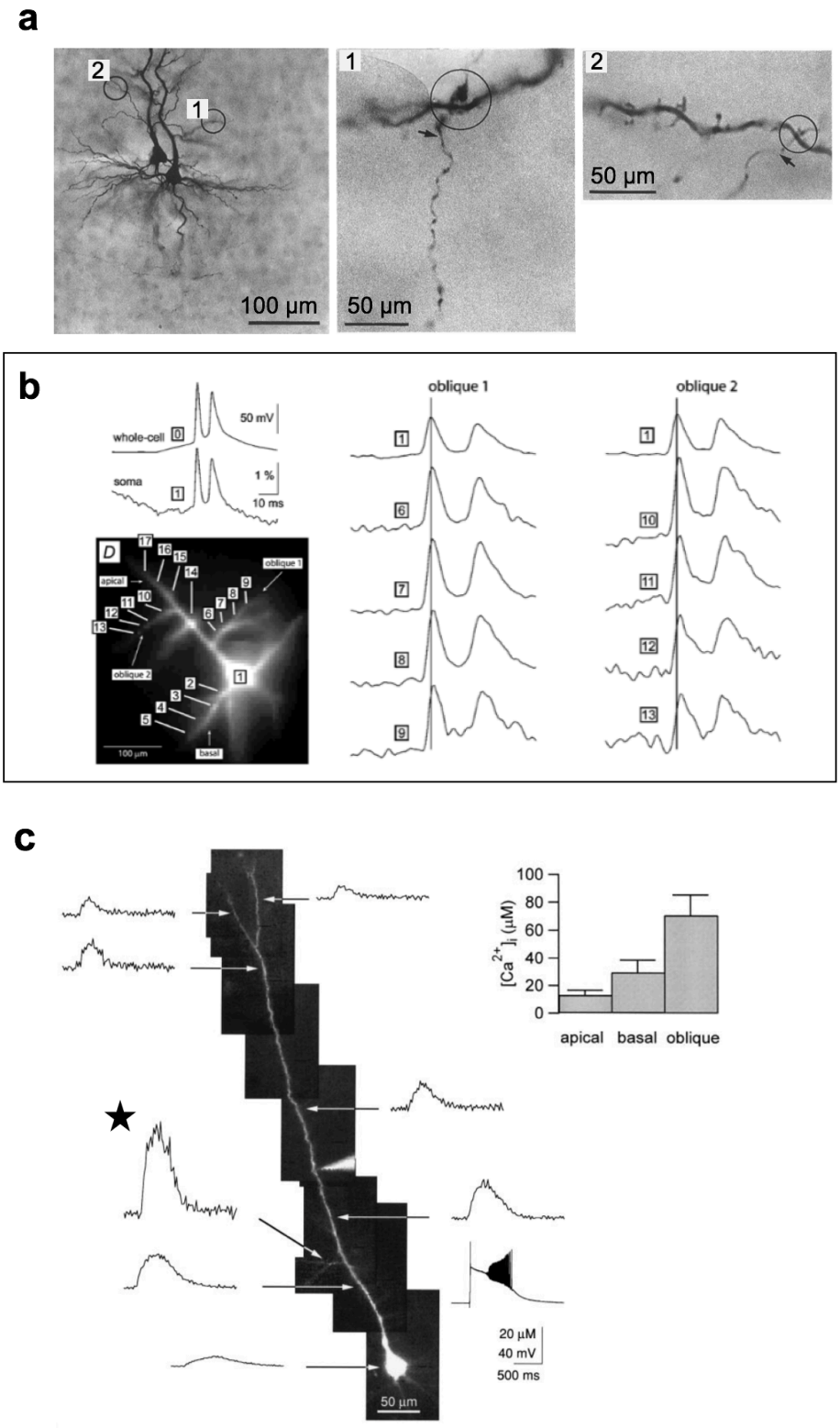

Figure 1.10 Evidence of synaptic contacts and active properties of oblique dendrites of L5PNs. a, The reconstruction of biocytin filled L5PN in vitro highlighting potential synaptic contacts (1 and 2 encircled regions) at oblique dendrites (Markram et al., 1997). **b,** simultaneous voltage imaging recording of bAPs in L5PNs showing efficient invasion of bAPs in proximal oblique branches (Antic, 2003). **c,** Large calcium influx (★) associated with PDS in apical oblique dendrite in L5PN (Schiller, 2002)

Thus, few studies support that apical oblique dendrites of L5PNs are endowed ion channels (e.g., voltage-gated sodium and calcium channels, and NMDA and AMPA receptors) that may play a role in dendritic integration of these branches. However, it remains unknown whether apical oblique dendrites support the generation of local dendritic spikes or oblique branch spikes.

1.8 Summary and general aim of this thesis

Since Cajal (1889), our current knowledge on dendrites has progressed. Dendrites are not just passive membrane structures that conduct synaptic inputs. But, they actively participate in signal transduction and are capable of locally boosting arriving synaptic inputs via the recruitment of regenerative dendritic spikes. Several studies have characterized the mechanisms and condition to generate these dendritic spikes *in vitro* (as discussed in **Section 1.4**). With the strict requirement to elicit the dendritic spikes (i.e., pairing of bAPs with EPSPs, synchronous activation of spines, and a critical frequency of bAP trains), these modalities support that dendrites (structure) play an important role in information processing in the brain, a process called dendritic integration (function).

The general aim of this work is to understand the functional role of a specific set of dendrites, the apical oblique dendrites of L5PNs in the cortex. I pose some questions that would help build on answering the general aim. While a handful of works have shown the active properties of oblique dendrites in CA1 PNs (as discussed in **Section 1.5**), the findings may not necessarily be all translatable L5PNs. **Figure 1.11** illustrates several questions to study regarding the oblique dendrites of L5PNs (some of which were investigated in CA1 PNs). First, how does the branch-point morphology of oblique dendrites of L5PNs modulate forward and back-propagating spikes (**Figure 1.11a-b**) (Migliore et al., 2005; Ferrante et al., 2013)? Schaefer et al. (2003) investigated this problem *in silico* and found that neurons that have more proximal oblique branches (< 140 μm from the soma) exhibited strong coupling between the somatic AP and Ca^{2+}-AP at the nexus. Second, can bAPs recruit dendritic spikes in oblique dendrites of L5PNs (**Figure 1.11c**)? BAPs have been shown to reliably invade proximal oblique branches (Antic, 2003). Another study done by Schiller (2002) showed large calcium influx in oblique dendrites of L5PNS during a PDS or epileptic like discharges at the soma (**Figure 1.11c**). A good follow up on this study would be to systematically characterize whether this large calcium influx can consistently be evoked with trains of bAPs. Third, can pairing of

bAP trains with synaptic inputs (evoked via extracellular stimulation, or 2P glutamate uncaging) induce Alkon (1999)'s theory of branch specific plasticity (**Figure 1.10d**)? This experiment has been done in CA1 PNs in several groups (Gasparini et al., 2007; Canepari et al., 2013) but not intensively in L5PNs (Sjostrom and Hausser, 2006).

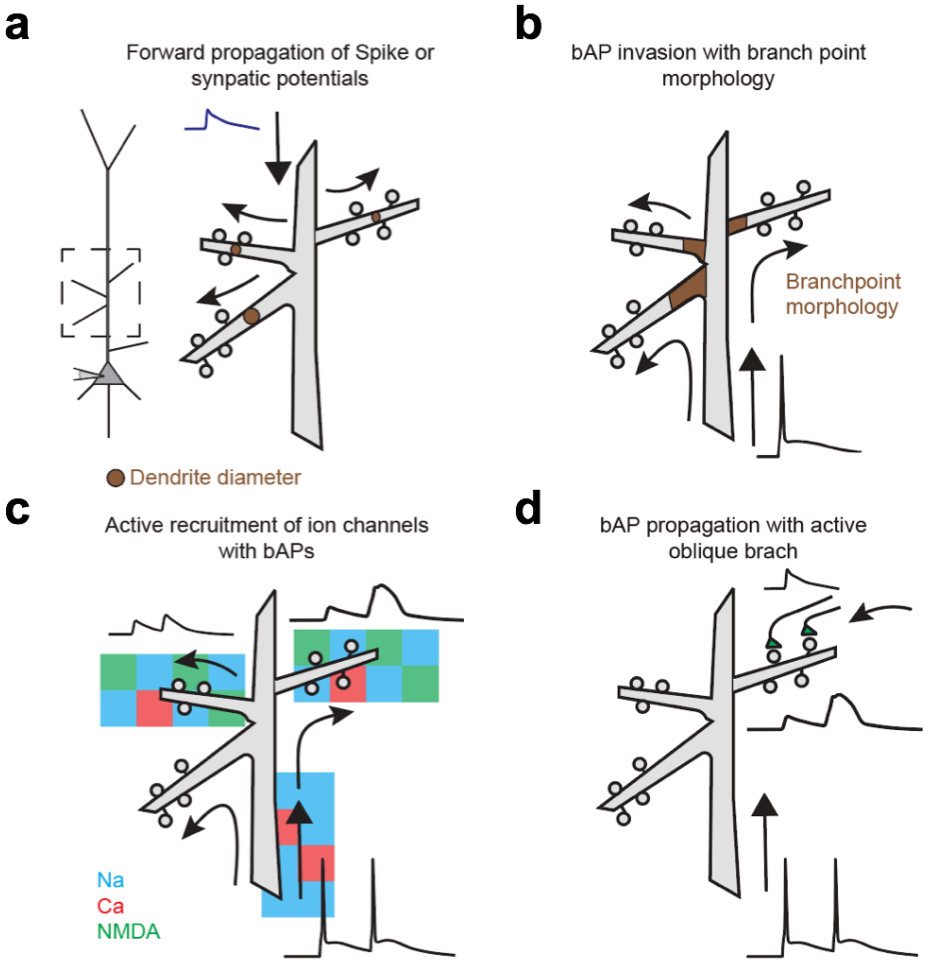

Figure 1.11 Illustration on how oblique dendrites and their properties affect forward and back-propagating spikes. a, Morphological factors (e.g., the number of branch points and dendrite diameter) that determine the attenuation of forward propagating synaptic potentials or spikes. **b,** branch-point morphology and tapering affect the efficacy of bAP invasion. **c,** bAPs activate ion channels at oblique dendrites which may generate regenerative potentials. **d,** Coincidence of bAPs with EPSPs at the oblique branches may strengthen synaptic coonections especially in branches that can generate an oblique branch spike.

The specific aims of this Ph.D. project are the following:

1. **To understand the generation of dendritic spikes in apical oblique dendrites of Layer 5 cortical pyramidal neurons.**

In this aim, we specifically aim to answer the question: Under what conditions can oblique dendrites of cortical L5PNs generate an oblique branch spike? To answer this question, I used a published multi-compartment model of an L5PN by Shai et al. (2015) to investigate how bAPs invade the oblique dendrites. I uniquely show that certain oblique dendrites exhibit dendritic spikes following low frequency train of bAPs. Next, I characterized the generation of a branch-specific dendritic spike and analyzed the ion mechanisms behind its generation in certain apical obliques. The findings in the model served as a guide and starting point for my experimental investigations of the putative oblique spikes in oblique dendrites of L5PNs.

2. **To experimentally generate and observe oblique branch spikes in apical obliques of L5PNs.**

   To achieve this aim, I designed a microscope system to optically record dendritic activity in thin oblique branches of L5PNs with the use of fluorescent calcium indicators. I combined this microscope with the somatic whole-cell patch clamp technique to perform multi-site functional 2P calcium imaging at oblique dendrites of L5PNs *in vitro*.

3. **To improve the signal-to-noise ratio (SNR) of the recorded fluorescent calcium and voltage transients by proposing new optical techniques**.

   I present two methods namely, multi-site functional calcium imaging with temporal gating and voltage imaging via single-photon excitation by scattered photons (1PESP). Preliminary results from these techniques showed promising improvements in the SNR using the multi-site holographic detection system.

1.9 Overview of chapters

This thesis is organized as follows:

Chapter 2: Numerical evidence of putative dendritic spikes in oblique dendrites. Using Shai et al. (2015) L5PN model, I found a putative oblique branch spike with critical frequency of f_{c2} = 35 Hz trains of 2-AP train. I presented the analysis done to classify the oblique branches that exhibit these spikes. I also present the ionic mechanism of this oblique spike and how it affected neighbouring oblique branches. In the L5PN model, I found that the

oblique branch spike is a branch-specific fast sodium spike followed by a broad depolarization due to the activation of high-voltage activated calcium channels.

Chapter 3: General Methods: Two-photon holographic multi-site detection system and sample preparation. In this chapter, I discuss our multi-site functional calcium imaging system and the brain slicing procedure. Among the optical systems that can be used to excite fluorescent calcium and voltage indicators, I used a 2P holographic microscope to enable simultaneous multi-site detection. I used this system to perform calcium imaging in oblique dendrites of L5PNs.

Chapter 4: Experimental evidence of oblique branch spikes in oblique dendrites of L5PNs *in vitro*. In this chapter, I present experimental (matched with numerical) evidence for calcium spikes in oblique dendrites in L5PNs. Calcium imaging, somatic whole-cell recordings of after-depolarizing potentials, local laser-pruning of oblique dendrites, were used to provide evidence that select oblique dendrites can generate oblique branch spikes following a low-frequency burst of bAPs.

Chapter 5: Techniques for enhancing signal-to-noise ratio (SNR) of fluorescent calcium and voltage recordings. I present two techniques namely: multi-site functional calcium imaging with temporal gating, and functional voltage imaging via single-photon excitation via scattered photon (1PESP), that can potentially enhance the SNR of calcium and voltage recordings. Preliminary results showed a ~3-fold enhancement using each of the technique. We envisage future works to refine these techniques which can be useful for recording fast dendritic activities with fluorescent voltage- and calcium indicators.

Chapter 6: General discussion and future directions. I highlight the findings from the multi-compartment model (in Chapter 2), calcium imaging and laser dendrotomy (in Chapter 4), and voltage imaging in dendrites and trunk (in Chapter 5). This work shows that select distal oblique dendrites can generate dendritic oblique spikes during low-frequency bursts of bAPs. **Apical oblique dendrites of L5PNs are not just thin passive membrane structures that receive thalamic inputs and form intracortical connections amongst axons of neighbouring L5PNs; but they may also actively participate in dendritic integration, possibly by coincidence detection, and reinforce the strength of synaptic connections via the recruitment of oblique branch spikes.**

Chapter 2. Numerical evidence of putative dendritic spikes in oblique dendrites

2.1 Introduction

Neuroscientists have long investigated how spikes are generated and conducted in a neuron. Over half a century ago, Hodgkin and Huxley reported the first intracellular electrical recording of action potentials in giant squid axons (Hodgkin and Huxley, 1945). Hodgkin and Huxley (1952) then later established the mathematical foundations on the activation/inactivation of ion channels (i.e., sodium and potassium channels) that generate action potentials (APs). In the same period, Wilfrid Rall pioneered the use of cable theory to understand how current and membrane potentials flow within the complex branching structure of dendrites (Rall, 1959; Rall, 1969; Rall and Rinzel, 1973). Indeed, with the development of patch-clamp technique (Sakmann and Neher, 1984), scientists were able to record membrane potentials along the apical trunk. One important finding was the active back-propagation of action potentials (bAPs) into the dendritic tree (Stuart and Sakmann, 1994), which can offer fast retrograde signal and can set off local dendritic spikes (Stuart and Sakmann, 1994; Larkum et al., 1999a; Larkum et al., 1999b). The complex dendritic morphology influences the propagation of electrical signals in neurons and affects how bAPs invade the neuron's dendritic tree. Relative timing between bAPs and synaptic inputs onto certain dendrites can initiate changes in synaptic strength (Markram et al., 1997; Sjostrom et al., 2001; Kampa et al., 2006). Hence, bAPs have important consequences to synaptic plasticity and understanding how they invade different dendritic domains could provide fundamental basis to learning and memory.

To evaluate how morphology plays a role in the invasion of bAPs, we first attempt to understand back propagation of action potentials via numerical modelling. Multi-compartment models are excellent tools to understand how the distribution of ion channels and dendritic morphology influence spike generation and propagation in neurons. In fact, several studies have shown that membrane morphology and characteristics such as: branching patterns (Mainen and Sejnowski, 1996; Vetter et al., 2001), branch-point tapering (Ferrante et al., 2013), distribution of apical oblique dendrites along the apical trunk (Schaefer et al., 2003), and passive membrane resistance of thin dendrites (Antic, 2003) modulate the forward-propagating

dendritic spikes and bAPs. A seminal work by Mainen and Sejnowski (1996) demonstrated how dendritic morphology influences the firing patterns of neurons. In their work, they modelled a neuron with two regions: soma and dendrites (**Figure 2.1**). The soma had sodium and potassium channels, which are essential to generate action potentials, while the dendrites had voltage-gated and calcium-dependent ion channels. The parameter, ρ, described the ratio of the membrane area between the dendrites to the axo-somatic compartment. A coupling parameter, κ, joined the soma and the dendritic region. Tuning the κ and ρ while maintaining the same ion channel conductance reproduced a spectrum of firing patterns from regular firing of small compact cells to burst firing of L5PNs.

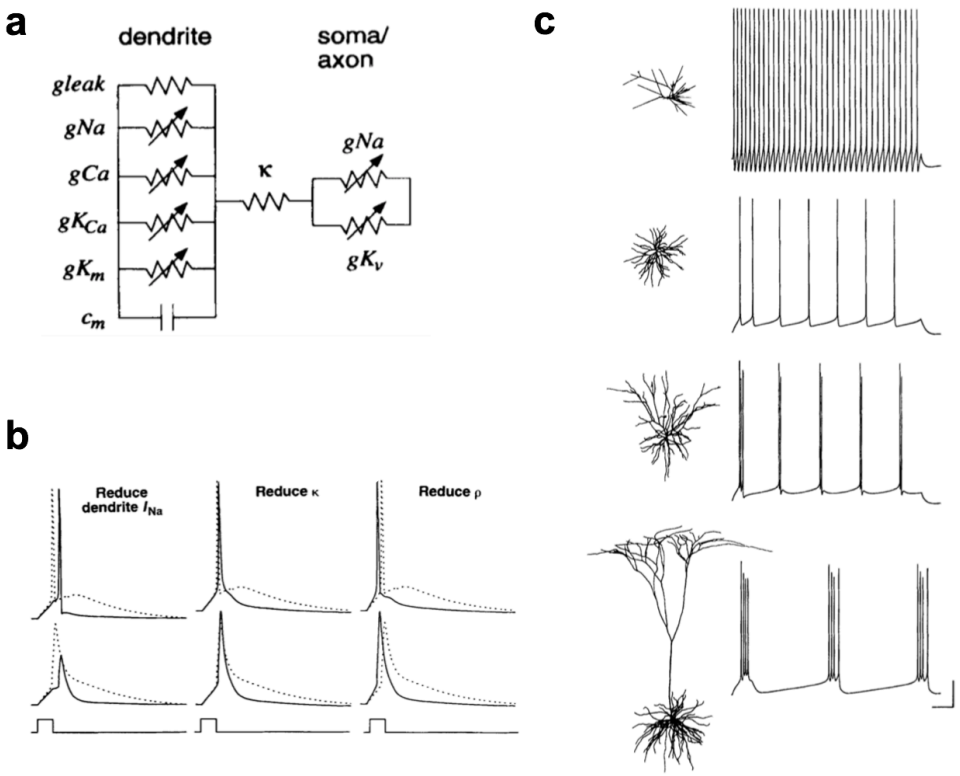

Figure 2.1 Dendritic morphology shapes action potential firing properties of neurons. a, The reduced compartmental model of soma and dendrites. **b**, The electrical origin of after-depolarization dendritic in nature which is influenced by the coupling parameter, κ, and the dendritic, somatic surface area ratio, ρ. **c,** The firing pattern of different multi-compartmental neuron models incorporating the same channel models. Figure taken from (Mainen and Sejnowski, 1996).

Using multi-compartmental models of neurons, scientists can interrogate how distribution of different voltage-gated ion channels determine the generation and propagation of dendritic spikes. These numerical experiments can be confirmed in the laboratory via dendritic recordings in vitro. Intuitive manual tuning (Migliore et al., 2005; Almog and Korngreen, 2014; Shai et al., 2015; Zhou et al., 2015) or computer-assisted multi-parameter search (Hay et al., 2011) of the density of dendritic conductance could aid in generating models that match experimental recordings. These multi-compartment models allow simulation of hypothetical experiments that are not possible with current techniques. Their results give new insights that are yet to be tested.

2.2 Chapter aims

The goals of this chapter are: (1) to investigate bAP invasion along the complex dendritic tree of a L5PN multi-compartment model; and (2) to establish a condition (using the critical frequency protocol) for generating a putative dendritic spike in apical oblique dendrites, or I refer as an oblique branch spike. I use a published multi-compartment model of a L5PN (Shai et al., 2015) and loaded it into the *NEURON-Python* simulation environment (Hines et al., 2009). The results from the simulation served as a guide for my *in vitro* experiments.

2.3 Methods

2.3.1 Active properties of the dendritic tree of the L5PN model

I used a published model of a L5PN (Shai et al., 2015) obtained from ModelDB (accession number: 180373) to investigate the active properties of oblique dendrites in a L5PN (see Figure 2.2 below). In the model, the densities of ion channels are expressed as conductances (*g_bar*) in S/cm^2 and listed in **Table 2.1**. In this study, I used the biophysical mechanism (i.e., ion channels and their distribution) contained in the *L5PCbiophys5.hoc* file from the (Shai et al., 2015) model. Except in the blocking experiment which will be described in **Section 2.3.3**, I kept all the conductance and their distribution along the dendritic tree the same as in the (Shai et al., 2015) model.

The L5PN model (using the morphology file: *cell1.asc*) consists of: the soma, basal dendrites, axon, thick apical trunk and 9 thin apical oblique dendrites (**Figure 2.3a**). Oblique dendrites in L5PN emanate from the main apical trunk starting from proximal regions to the soma. In this study, I refer to oblique branch by their oblique number, O#*n*, with O#1 being the first oblique branch from the soma.

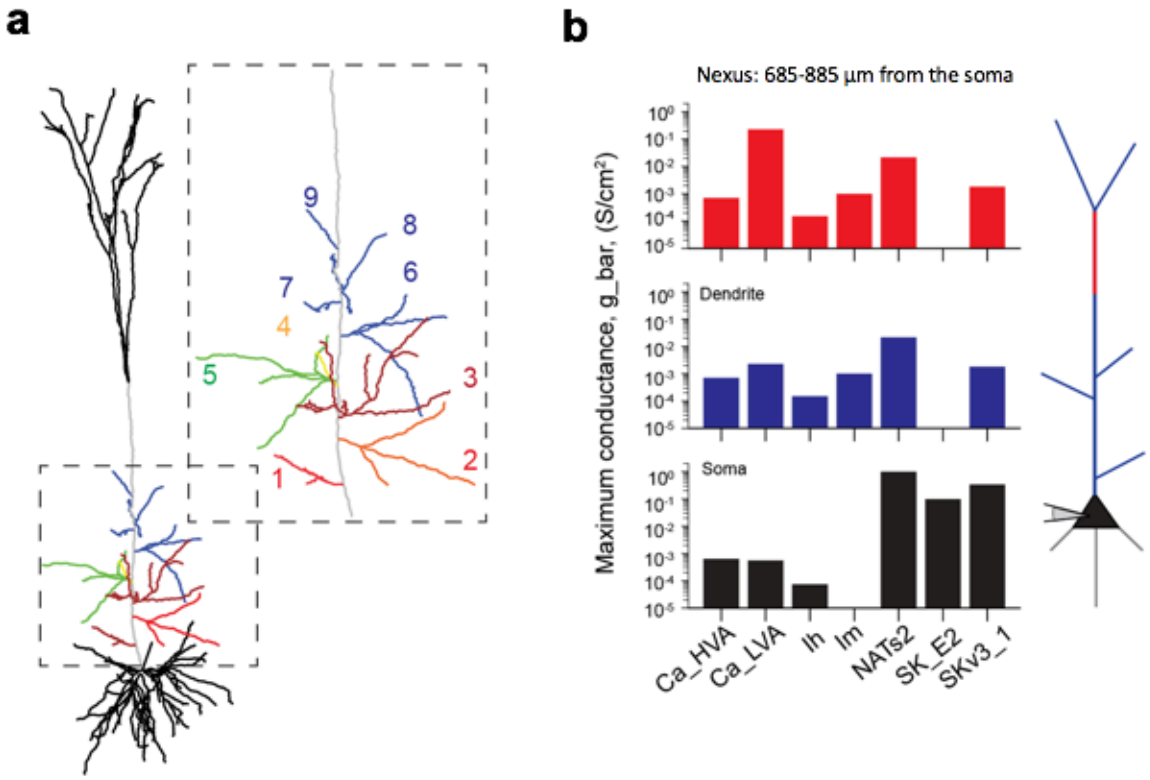

Figure 2.2 Active dendritic properties of the model. a, The morphology ("cell1.asc") of the L5PN neuron (Shai et al., 2015). **b,** Ion channel distribution and active properties of the *NEURON* model. The distribution of different ion channel conductance across the dendritic tree.

Table 2.1 List of parameters used in the published L5PN model

Ion channel	Variable	Conductance (S/cm^2)	Activation/Inactivation parameters	References
Low voltage-activated calcium conductance	*Ca_LVA*	soma: 0.000557 apical: 0.022 nexus: 0.2271264 basal: none axon: 0.000813	somatic: decay = 279.67951, gamma = 0.000509 apical: decay = 35.725651, gamma = 0.000637 axon: decay = 277.300774, gamma = 0.000525	Avery and Johnston (1996)
High voltage-activated calcium conductance	*Ca_HVA*	soma: 0.000644 apical: 0.000701 basal: none axon: 0.000222		Reuveni et al. (1993)
Hyperpolarization-activated cyclic nucleotide–gated conductance	*Ih*	soma: 0.000075 apical: 0.00015 basal: 0.00005 axon: 0.00005		Kole et al. (2006)
M-currents and other potassium conductance	*Im*	soma: 0.000008 apical: 0.00099 basal: none axon: 0.013322		Adams et al. (1982)
Small conductance (SK)-type calcium activated potassium current	*SK_E2*	soma: 0.09965 apical: 0.000002 basal: none axon: 0.000047		Kohler et al. (1996)
Shaw-related potassium channel	*SKv3_1*	soma: 0.338029 apical: 0.001808 basal: none axon: 0.473799		Rettig et al. (1992)
Dendritic voltage-gated sodium channels	*NaTs2*	soma: 0.998912 apical: 0.021489 basal: none axon: none		Colbert and Pan (2002)
Voltage-gated sodium channels for action potential generation: 6x mtau	*Nap_ET2*	axon: 0.005834		Magistretti and Alonso (1999)
	NaTa_t	axon: 3.89618		Colbert and Pan (2002)
Passive properties	*gpas*	soma: 3e-5 apical: 6e-5 basal: 6e-5 axon: 3e-5		
Axial resistance	*Ra*	100 MΩ		
Specific Membrane capacitance	*cm*	1 F/cm^2		

In the Shai et al. (2015) L5PN model, the neuron has different conductance distributed to the axon, soma, apical, and basal dendrites (see **Table 2.1**). For visual presentation, I plotted conductance and grouped them into: soma, dendrite (which is the apical section), and nexus (which are apical segments located 685-885 μm from the soma) (**Figure 2.3**). The maximum conductance for the high voltage-activated calcium (*gCa_HVA*) are the same for all regions. The soma consists of the following maximum conductance: fast inactivating sodium current (*gNaTs2*), small-conductance calcium activated potassium current (*gSK_E2*), fast non-inactivating potassium current (*gSKv3_1*). The dendrites and the nexus have similar densities of sodium, calcium, and potassium currents. At the dendrites and nexus, the calcium activated potassium conductance, g*SK_E2*, is minimal (0.000002 S/cm^2) as compared to the soma with (0.09965 S/cm^2). A step distribution of *Ih* was used in the model with twice the conductance at the apical dendrite as compared to the soma, *gIh_dendrite* = 2**gIh_soma*. A high density of low-voltage activated calcium conductance (*gCa_LVA*) at the nexus allow for the generation of Ca^{2+}-AP (**Figure 2.2b**).

2.3.2 Implementing the critical frequency protocol in the model

I adapted the critical frequency protocol, introduced by Larkum et al. (1999a), to find conditions to generate oblique branch spike in the L5PN model. In my simulation, I injected 2 or 4 current pulse trains (current, $I = 4.1$ nA, pulse width, $\Delta\tau = 2$ ms, frequency range $10 < f <$ 150 Hz) at the soma to evoke a 2-AP or a 4-AP train which evolves into 2-AP and 4-AP train at the dendrites. The after-depolarizing potential (ADP) was measured as the average membrane potential within 10 to 18ms time-window with the time where the peak of the last AP occurs set to t = 0, ADP $= (8)^{-1} \int_{10}^{18} V_m \, dt$.

2.3.3 The program flow of the script and defined functions in *NEURON*

Using the ion-channel distributions and conductance values in the model (see *L5PCbiophys5.hoc*), I added sub-routines in the Shai et al. (2015) *NEURON* script to investigate the generation of oblique branch spikes in apical oblique dendrites with a train of bAPs (see algorithm in **Table 2.2** below). These sub-routines are: oblique tracing, branch dendrotomy, and conductance blocking.

I structured the *NEURON* script into four steps: (A) **Initialization**; (B) **Pre-run**; (C) **Stimulus setup**; and (D) **Run** (see **Table 2.2**). During the Initialization, the adaptive integration (*CVode.active(0)*) is disabled with a fixed integration time step, *h.dt* = 0.025 ms.

The Initialization step loads the morphology file (*cell1.asc*) and biophysics (i.e., the ion channels and their distribution contained in *L5PCbiophys5.hoc*), and allocates recording vectors for the time, voltage, and conductance.

Table 2.2 Script implemented in *NEURON*

A. Initialization

0. Import neuron as *h*
   Disable CVode, *h.CVode.active(0)*
1. Load morphology file and biophysics
2. Call oblique tracing routine
3. Initialize recording vectors: t, voltage, conductance
4. If (dendrotomy), call branch dendrotomy routine

B. Pre-run

5. Pre-run, this step is executed only once to generate the state file, "state_0.dat"
   h.tstop = 3750 ms, h.dt = 0.025 ms
   while (h.t < 3000)
   h.fadvance()
   save state to "*state_0.dat*"
6. Load state file, "*state_0.dat*"
7. If (blocking), call conductance blocking routine

C. Stimulus setup: 4-AP train, Npulse = 4

8. Add current clamp stimulus at the soma
   for i in Npulse:
   *stim[i].delay = 3100 ms + i*1000./frequency*
   stim[i].amp = 4.1 nA
   stim[i].dur = 2 ms

D. Run

9. Continue simulation
   while (h.t < 3000)
   h.fadvance()
10. Export voltage/conductance traces within the 3100-3500 ms time window

Pre-run. To save time when running the numerical experiments, a Pre-run simulation step is initiated starting from $h.t = 0$ up to $h.t = 3000$ ms. At this point, a state file is generated containing the configuration of the model and the status of the membrane potential of the neuron. Note that at $t < 3000$ ms, the resting membrane potential slowly hyperpolarizes to V_m= -85 mV. Saving the status at t =3000 ms ensured that the model has reached a stable state before performing any numerical experiment ono the neuron. The Pre-run took approximately 3-5 mins (using CPU with intel Core i5 2.9GHz with 8GB RAM) and can be performed only once to generate the required state file for a given morphology. When changing the morphology (i.e. dendrotomy) and ion-channel distributions, a new state file needed to be generated. Further numerical experiments only needed the saved state file to load the same state variables into the model.

Stimulus setup adds the pertinent current pulses (2 or 4-pulse trains) at the soma with a given frequency.

Run performs the necessary experiment (i.e. critical frequency protocol), which exports all recording variables upon completion.

I added subroutines into the run script to investigated the effects of dendrotomy and blocking of conductance in a specific branch to the generation of dendritic oblique spike. A main oblique branch was removed (i.e., disconnected from the main apical trunk) and the somatic ADP with critical frequency protocol was recorded. The conductance blocking routine was used to investigate how blocking specific conductance (e.g., *gCA_LVA, gCA_HVA,* or *gNa_Ts2*) in an oblique branch affected the generation of dendritic oblique spikes. The branch dendrotomy routine was used to study how the removal of an oblique branch affected spike propagation.

Oblique tracing routine. I wrote a code using the subtree function in *NEURON* to collect all the sections that belong to the same oblique branch and to output *O*#1 to *O*#9 main oblique branches. An example of the code is shown below,

Code:

```
obl1= h.SectionList()
obl1.subtree(sec=L5PC.apic[104])
```

where the argument of the subtree function is the section of the oblique branch that is connected to the main apical trunk. This function returns a list of sections of that branched from section L5PC.apic[104] inclusive, which are:

Output:

```
L5PC.apic[104], L5PC.apic[105], L5PC.apic[106], L5PC.apic[107],
L5PC.apic[263], L5PC.apic[264], L5PC.apic[265],
L5PC.apic[631], L5PC.apic[632], L5PC.apic[633], L5PC.apic[634], L5PC.apic[635],
L5PC.apic[636], L5PC.apic[637], L5PC.apic[638], L5PC.apic[639]
```

This function was applied for other oblique branches generating a set of lists from *O*#1 to *O*#9, which also corresponds to the oblique number described in **Section 2.3.1**.

Branch dendrotomy. The dendrotomy routine requires the user to input the oblique branch (from *O*#1 to *O*#9 oblique) and disconnects all segments except for the first order branch, i.e. the one that is connected directly to the trunk.

```
Code:
cut_obl = obl5
for i, sec in enumerate(cut_obl):
    if(i==0):
        remove_sec = sec
        cut_obl.remove(sec=remove_sec)
    else:
        break
for sec in cut_obl:
    h.disconnect(sec=sec)
```

Removal of conductance in an oblique branch. I also investigated the influence of removing a specific conductance in an oblique branch. Given a list containing all the segments belonging to an oblique branch (e.g, *O*#1=*Obl1*), I made a code that loops over the sections within the list to set a conductance (e.g., *gCA_HVA*) to zero.

```
Code:
    for seg in obl1:
      seg.gCa_HVAbar_Ca_HVA = 0
```

This changes the specific conductance (*seg.gCa_HVAbar_Ca_HVA*) of *O*#1=*obl1* without affecting the other oblique branches.

2.3.4 Numerical quantification of linear and non-linear responding oblique branches

I classified the membrane potential responses of the oblique branches in the L5PN model into: linear and non-linear response. I devised a procedure to record the membrane potential at each segment following a 2-AP train with frequencies ranging from $20 < f < 150$ Hz. The procedure performs the following: takes the difference of the peaks of the bAPs, ΔbAP_{21}; plots ΔbAP_{21} as a function of frequency; and fits the plot with a sigmoid function,

$$S(f)_{\text{fit}} = \frac{A}{[1 + \exp(-\beta(f - f_{c2}))]} \qquad (\mathbf{2.1})$$

where A is the amplitude of the difference between the two peaks, β is the steepness of the increase with frequency, and f_{c2} is the critical frequency for the 2-AP train. The scatter of the data points plotted between β versus A aided me to identify a threshold for characterising non-linear responding branch segments ($\beta \geq 0.3$ and $A \geq 20$ mV). The other branch segments with

$\beta < 0.3$ and A < 20 mV exhibited a linear response with insignificant difference between the peaks as a function of frequency.

2.4. Results

2.4.1 105 Hz critical frequency for generating Ca^{2+}-AP at the nexus of the apical tuft

With the L5PN model, Ca^{2+}-AP was initiated at the nexus of the apical tuft during a 4-AP train at 105 Hz. **Figure 2.4** shows the *NEURON* model and the membrane potential at the soma and nexus of the apical tuft with the train of bAPs. For a train of 4-bAPs at frequencies above 105 Hz, the dendritic Ca^{2+}-AP was recruited having a broad depolarization of 40 ms. This dendritic Ca^{2+}-AP contributed to the ADP at the soma. This critical frequency for generating Ca^{2+}-AP was higher as compared to the 84 Hz (with 3-AP train) reported by (Shai et al., 2015).

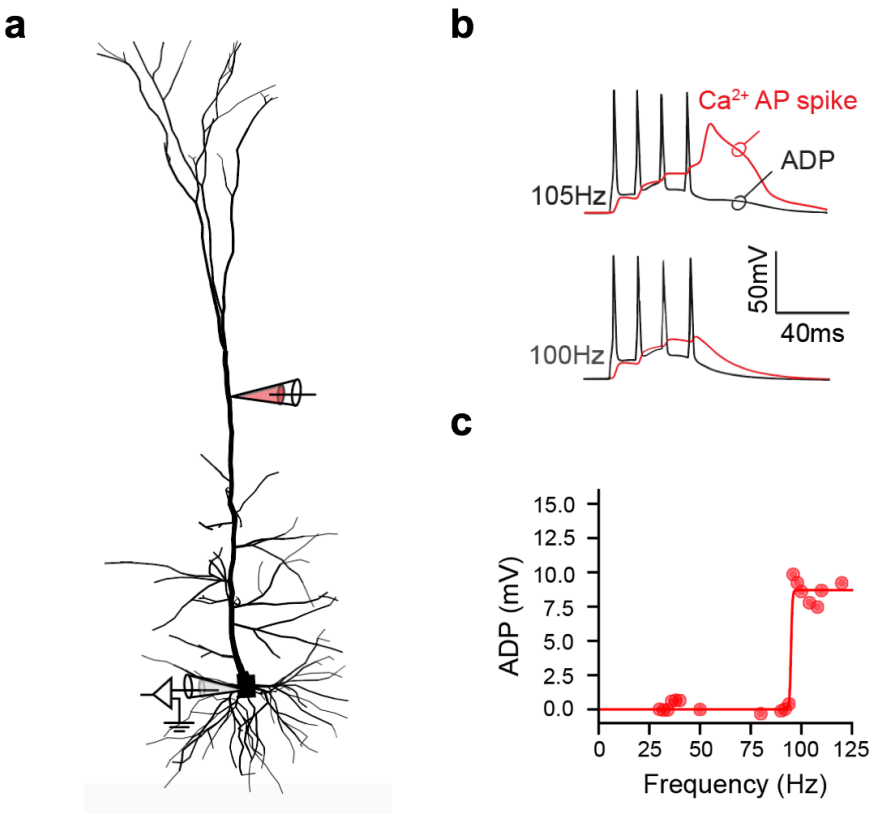

Figure 2.3 The generation of Ca^{2+}-AP in the L5PN model. a, A digital rendering of a stained L5PN with the recordings of the membrane potential at the soma and nexus of the apical tuft (red) in response to a train of bAPs. **b,** The somatic (black) and dendritic (red) recording in response to 4-AP train at 100 and 105 Hz. At 105 Hz, the dendritic Ca^{2+}-AP was recruited. **c,** the ADP with the step-increases at 105 Hz due to the Ca^{2+}-AP.

2.4.2 Shifts in the critical frequency in the model with the amplitude and pulse-width of the injected current

In the model, I found that the critical frequency shifts with the current amplitude, I, and pulse-width, $\Delta\tau$, (**Figure 2.5a**). I mapped out the parameter space (I vs. $\Delta\tau$) with the critical frequency.

In the model, I found a minimum current of 4.1 nA with a 2 ms pulse width to reliably evoke an AP in a 4-AP train. A lower current amplitude resulted to a failure in AP firing. At 4.1 nA and 2 ms, the critical frequency was f_{c4} = 105 Hz. Surprisingly, increasing the amplitude from 4.1-5.0 nA while keeping the pulse with at 2 ms resulted to a lower critical frequency of f_{c4} = 85 Hz as seen from the time-integral, change in the intracellular calcium and ADP (see **Figure 2.5a**). I mapped out the parameter space (I vs. $\Delta\tau$) and observed that "shifts" in the critical frequency were more prominent when increasing the current amplitude of pulse trains with pulse widths of $\Delta\tau$ =1.5-3.0 ms. In the proceeding simulation runs, I fixed the injected current to 4.1 nA and 2 ms.

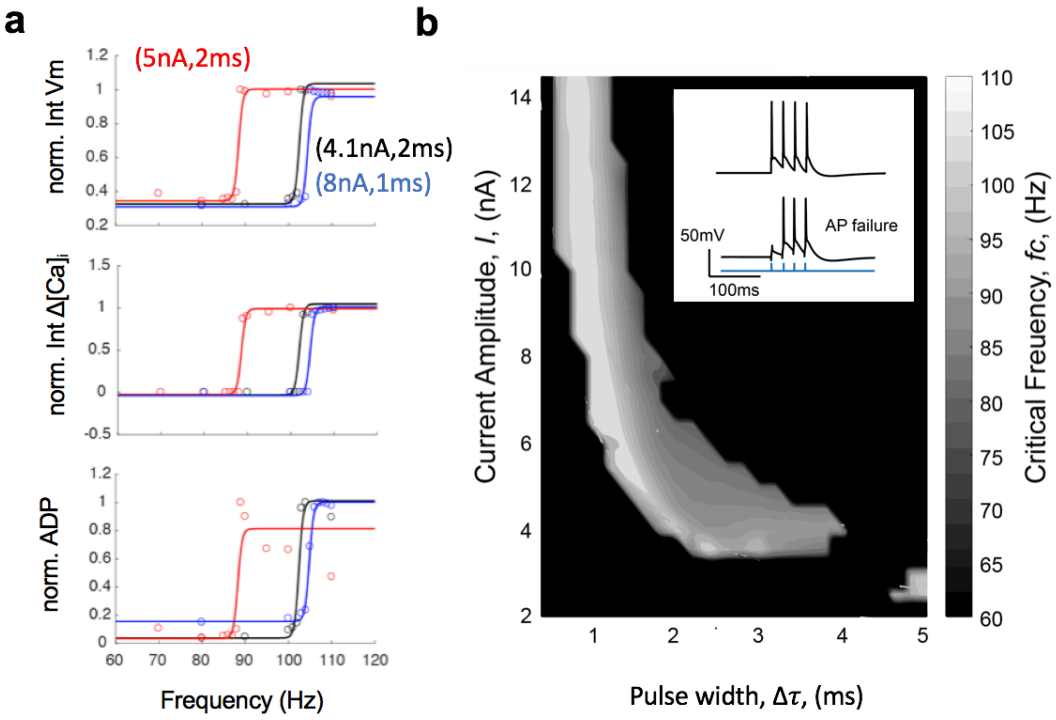

Figure 2.4 The shifts in the critical frequency with the amplitude and pulse width of the injected current in the Shai et al. (2015) model. a, The normalized response with frequency of: the time-integral of the membrane potential, change in the intracellular calcium concentration, and the ADP as measured at the soma. **b,** a parametric plot of I vs tw with z-color as the critical frequency from 60-120 Hz for the pair of I and $\Delta\tau$. The black region indicates current amplitude & pulse width combinations that exhibit AP failure or additional APs.

2.4.3 Invasion of a 4-bAP train in the dendritic tree

In the model, I also investigated the invasion of bAPs in the dendritic tree. Snapshots of AP propagation into the dendritic tree during a 4-AP train at 105 Hz are shown in **Figure 2.6**. The invasion of the bAPs was different in the nexus and in the oblique dendrites. The peak amplitudes the bAPs exponentially decreased as they reach the nexus, whereas at oblique dendrites, the bAP amplitudes increased. For the *O*#3 and *O*#5 oblique dendrites, a large increase in the membrane potential (**Figure 2.6**, green trace) was observed after the second bAP.

Another way to study the bAP invasion is to measure the peak depolarization at each segment by subsequent bAP in a bAP train. **Figure 2.7** shows another visualization of the invasions of bAP in the apical trunk and oblique branches using a 4-AP train at 105 Hz. The depolarization by the bAPs, ΔbAP, is plotted against path distance of segments of the oblique dendrites and the main apical trunk from the cell body, D_soma. The points are scaled to the diameter of the segments. A strong attenuation of the bAP is observed along the main apical trunk (see **Figure 2.7a** and **2.7c**). The first bAP robustly invades oblique dendrites (*O*#1, *O*#2, *O*#3, and *O*#5) with an increasing bAP amplitude towards the sealed end of the oblique consistent with Goldstein and Rall (1974) analytical model. Following the second bAP, there is a 20-40 mV rise in the membrane potential at *O*#5 (green) and *O*#3 oblique which persisted during the third bAP. After the fourth bAP, Ca^{2+}-AP at the nexus of the apical tuft was recruited causing a global depolarisation of the dendritic tree. Thus, the simulation shows a unique and persistent depolarization (i.e., an oblique branch spike) in few oblique dendrites after the second bAP.

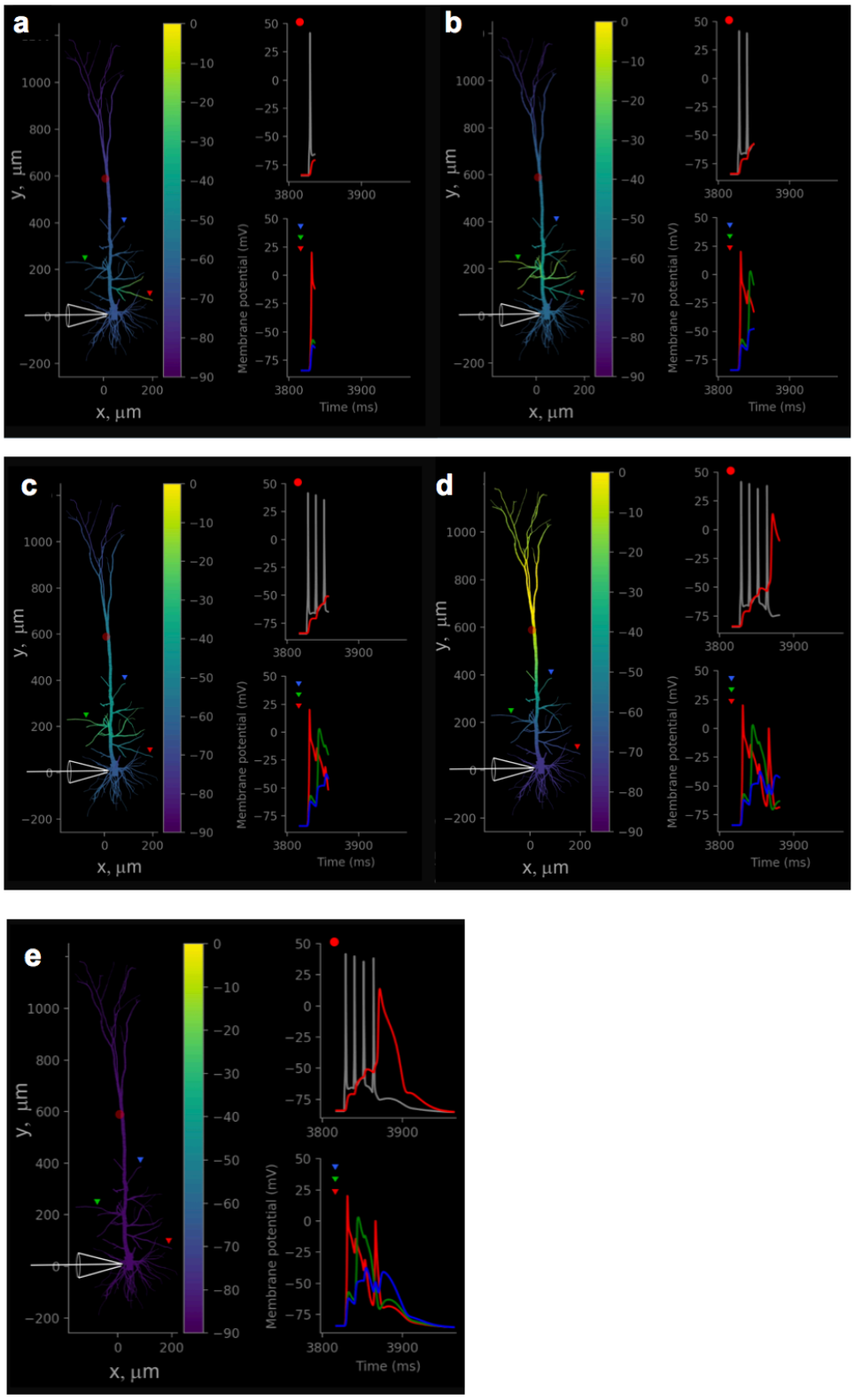

Figure 2.5 Snapshots of the invasion of bAPs in the dendritic tree taken at different times. (left) The multi-compartmental model of a L5PN with z-color is the membrane potential at each compartment in response to a train of 4 current pulses (4.2 nA, 2 ms, 105 Hz) injected at the soma. (right), the recorded membrane potential at the soma, nexus of the apical tuft and selected segments of oblique dendrites from time points a-b-c-d-e.

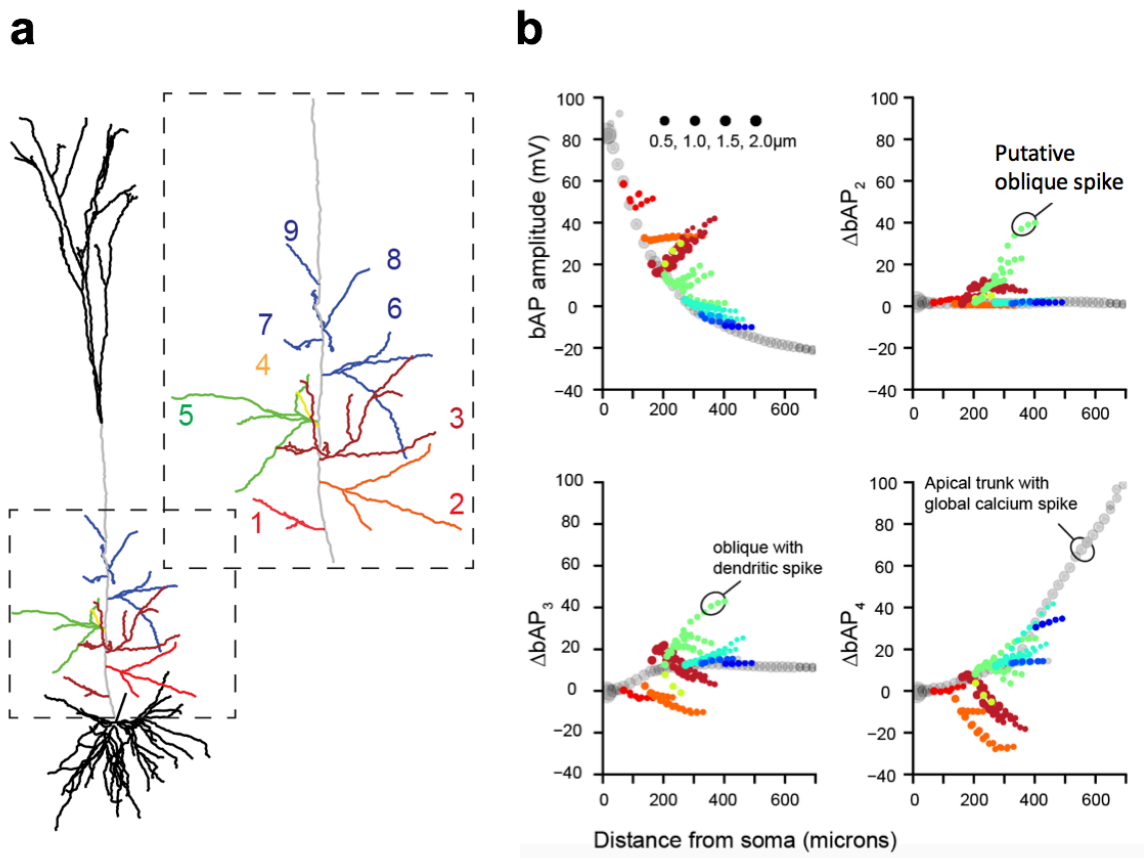

Figure 2.6 The invasion of AP train along the trunk and oblique dendrites in the L5PN model. a, Location of different apical oblique dendrites. **b,** Peak amplitude of the bAP in the obliques for the 1st bAP and the relative difference of the: (c) 2nd; (d) 3rd; and (e) 4th bAP with the 1st bAP. The color assignments for obliques are: O#1 (red), O#2 (orange), O#3 (brown), O#4 (yellow), O#5 (green), and O#6 to O#9 (blue). The main apical trunk is grey.

2.4.4 Dendritic spike in oblique dendrites evoked at low-frequency burst of bAPs

From **Figure 2.7b**, I observed an oblique branch spike generated at an oblique dendrite with a 2-AP train. I then performed the critical frequency protocol and found a critical frequency of f_{c2} = 35 Hz as measured from the ADP at the soma (**Figure 2.8**). On the other hand, the 2-AP train at 105 Hz did not recruit the Ca^{2+}-AP at the nexus of the apical tuft.

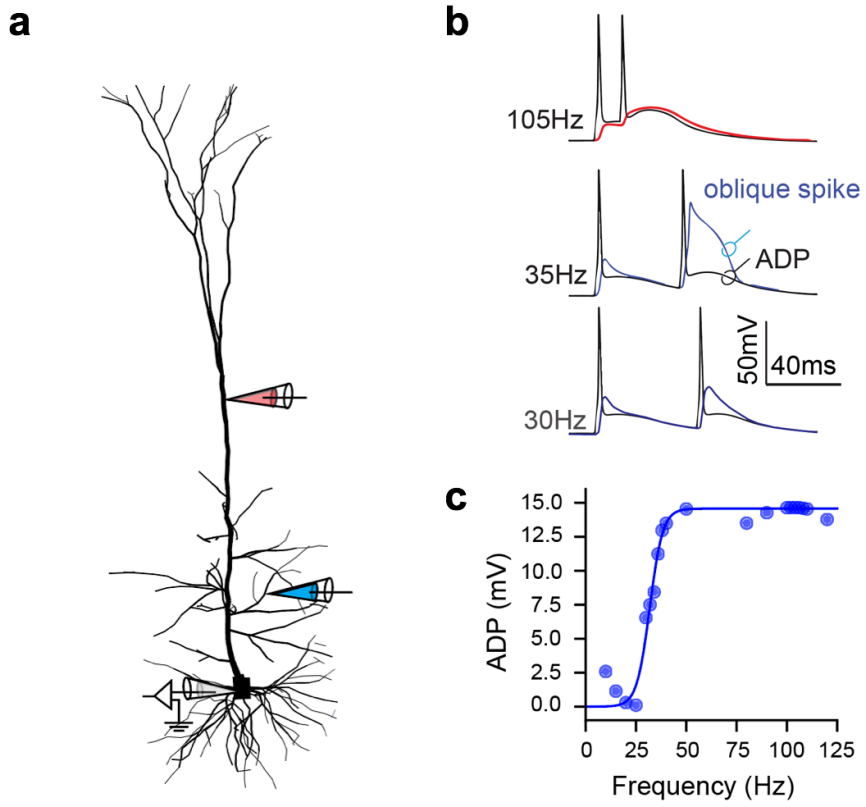

Figure 2.7 The multi-compartment model of L5PN captures an oblique branch spike in oblique dendrites. a, A digital rendering of a stained L5PN with the recordings of the membrane potential at the soma, oblique dendrite (blue), and nexus of the apical tuft (red) in response to a train of bAPs. **b,** The measured after-depolarizing potentials with frequencies for 2-AP train. **c,** The step-increase in the ADP at f_{c2} = 35 Hz following the generation of the oblique branch spike.

2.4.5 Classifying oblique branches that exhibit linear and non-linear membrane potential response with a 2-AP train

While there was a clear non-linear rise in the membrane potential in the *O*#5 oblique branch, I quantified the responses in all the segments of the multi-compartment model into linear and non-linear as described in **Section 2.3.4**. A parametric plot of A and β is shown in **Figure 2.9a** below. The distribution of the data points aided me to separate the responses by a threshold

region defined by: $\beta \geq 0.3$ and $A \geq 20$ mV. The responses equal and above the threshold were non-linear. This classification recovered *O*#3 and *O*#5 oblique as two non-linear responding oblique branches (**Figure 2.9c**). The classification with the voltage response was consistent when measuring the sodium or calcium currents at the oblique segments instead (**Figure 2.9b**).

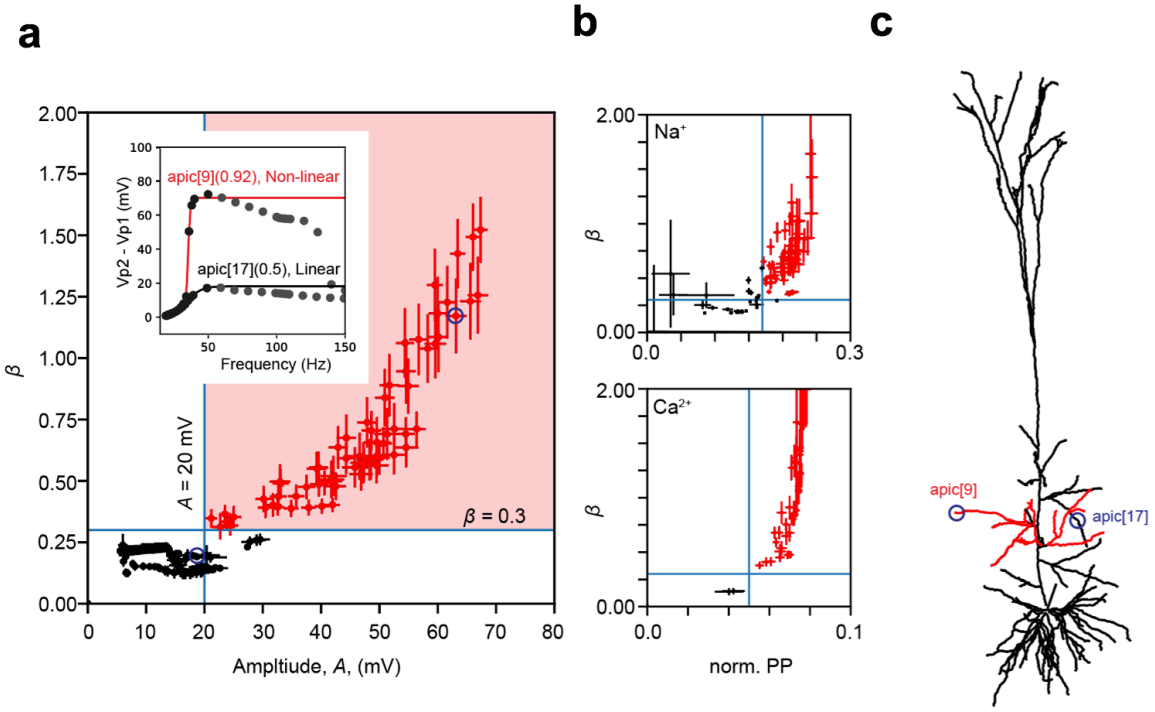

Figure 2.8 Classification of linear and non-linear responding oblique dendrites of a L5PN multi-compartment model. a, The parametric plot of fit parameters β and A of the voltage responses of the segments with AP trains at 20-150 Hz. (**a, inset**), An example of the paired pulse response from segments of two oblique dendrites (i.e., apic[9] and apic[17]) is shown in the inset. A region defined by: $\beta > 0.3$ and $A > 20$ mV, classifies the non-linear from the linear responding segments. **b,** The parametric plot of the normalized paired pulse of the sodium and calcium currents in the model with β. The red points indicate the same segments as classified in the paired pulse voltage response. **c,** The L5PN model with the locations of the non-linear responding segments (highlighted in red) based from the β vs. A classification. Note: A is the differences in the peak amplitude of the membrane potentials for 2- and 1-bAP, and β is the steepness parameter from the sigmoid fit (described in **Equation 2.1**). The vertical and horizontal error bars in **Panel a** are the confidence intervals for A and β based from the fit.

2.4.6 Conductance analysis of the dendritic oblique spike

I investigated the ion channels involved in the generation of the oblique spike in the L5PN model. I blocked specific conductance (i.e., *gCa_LVA*, *gCa_HVA*, and *g_NaTs2,* using the method described in **Section 2.3.3**) and measured the membrane potential of a linear (*O*#2

oblique branch) and two non-linear responding (*O*#3 and *O*#5 oblique branch) oblique dendrites and the soma in response to 30 and 40 Hz AP train (see **Figure 2.10** below).

In the control condition, the non-linear responding obliques (*O*#3 and *O*#5 oblique) as classified in the previous section showed a large depolarization, an oblique branch spike, at 40 Hz consisting of a fast spike followed by a broader depolarization (~50 ms duration) (see **Figure 2.10b**). I investigated the effect of removing the calcium and sodium conductance in a specific branch (**Figure 2.10c-e**). Setting the low-voltage activated calcium conductance to zero, $gCa\_LVA = 0$, did not affect the generation of the oblique branch spike. On the other hand, removing the high-voltage activated calcium conductance, $gCa\_HVA = 0$, abolished the broad 20 ms depolarization but revealed a fast spike (see **Figure 2.10d**) particularly for *O*#5 and *O*#3 non-linear responding oblique branches. This fast spike was confirmed to be mediated by sodium conductance, *gNa_Ts2*. Thus, based from the L5PN model, the oblique branch spike is a fast sodium spike that is followed by a broad depolarization due to recruitment of high-voltage activated calcium channels.

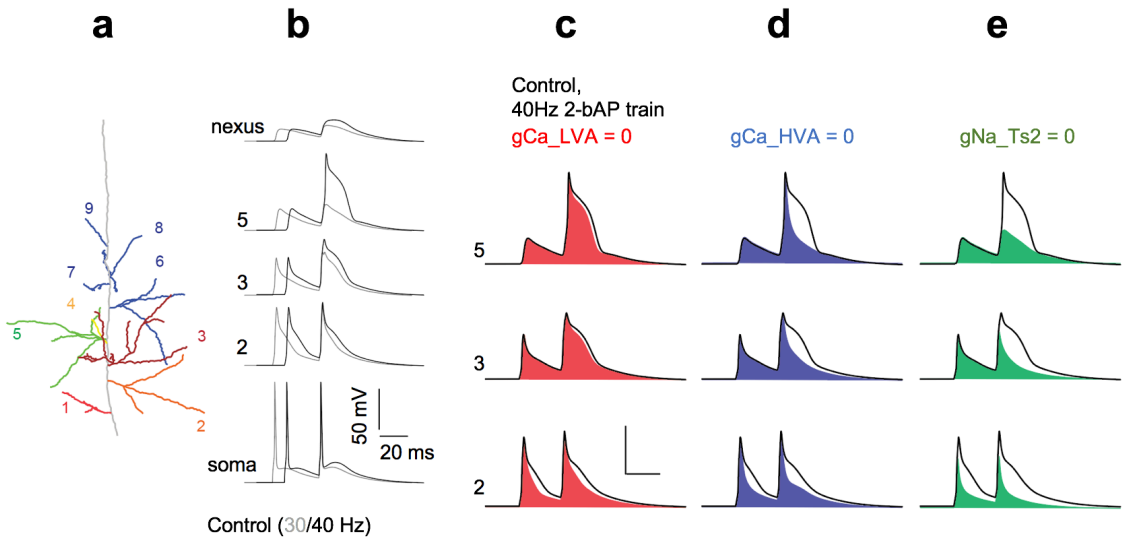

Figure 2.9 The conductance analysis of branches exhibiting the putative oblique spike. a, The L5PN model with the labelled oblique branches according to the number of branch points before it from (from O#1 to O#9). **b,** The membrane potential at different recording sites namely: (O#2, O#3, and O#5) oblique branches, the nexus, and the soma with 30- and 40 Hz AP-trains. **c-e,** The membrane potential in response to 40 Hz AP-train at the recorded sites with the conductance set to zero (removed) in that given oblique branch only. Scale bars indicated 50 mV (vertical) and 20 ms (horizontal).

I tested whether the removal of conductance in a specific branch affected the neighbouring oblique branches during the 2-AP train at 40 Hz (**Figure 2.11**). Extending the analysis made in **Figure 2.10**, I examined the changes in the membrane potential when removing a conductance of an oblique branch (indicated by ★). The removal of conductance in the *O*#5 oblique did not affect the oblique spike in *O*#3 branch. However, the removal of spike in *O*#3 oblique also removed the oblique spike in the *O*#5 oblique (**Figure 2.11c**). In addition, there was a noticeable decrease in the membrane potential at the nexus and the ADP at the soma. Surprisingly, removal of the sodium conductance at *O*#2 linear responding oblique resulted to no oblique spikes at *O*#3 and *O*#5 branch (**Figure 2.11d**). A summary of how the changes in conductance in one oblique affects the spike generation in the neighbouring oblique is shown in **Figure 2.12**. These results suggest that in the L5PN model, the oblique dendrites are coupled with one another such that the activation of conductance in an oblique branch affects the membrane potential of neighbouring oblique branches.

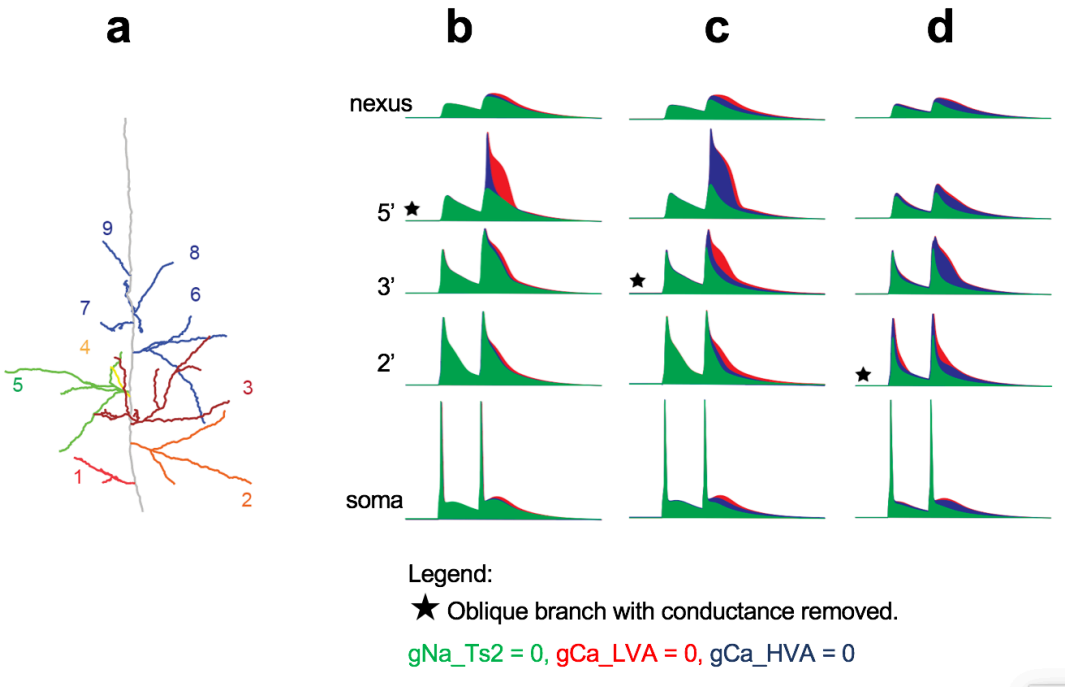

Figure 2.10 Influence of blocking a conductance in a single branch to neighbouring oblique dendrites. a, The L5PN model with the labelled oblique branches according to the number of branch points before it from (from *O*#1 to *O*#9). **b-c,** changes in the membrane potential of the oblique branches when the conductance of obliques: *O*#5, *O*#3, and *O*#2 were removed, respectively.

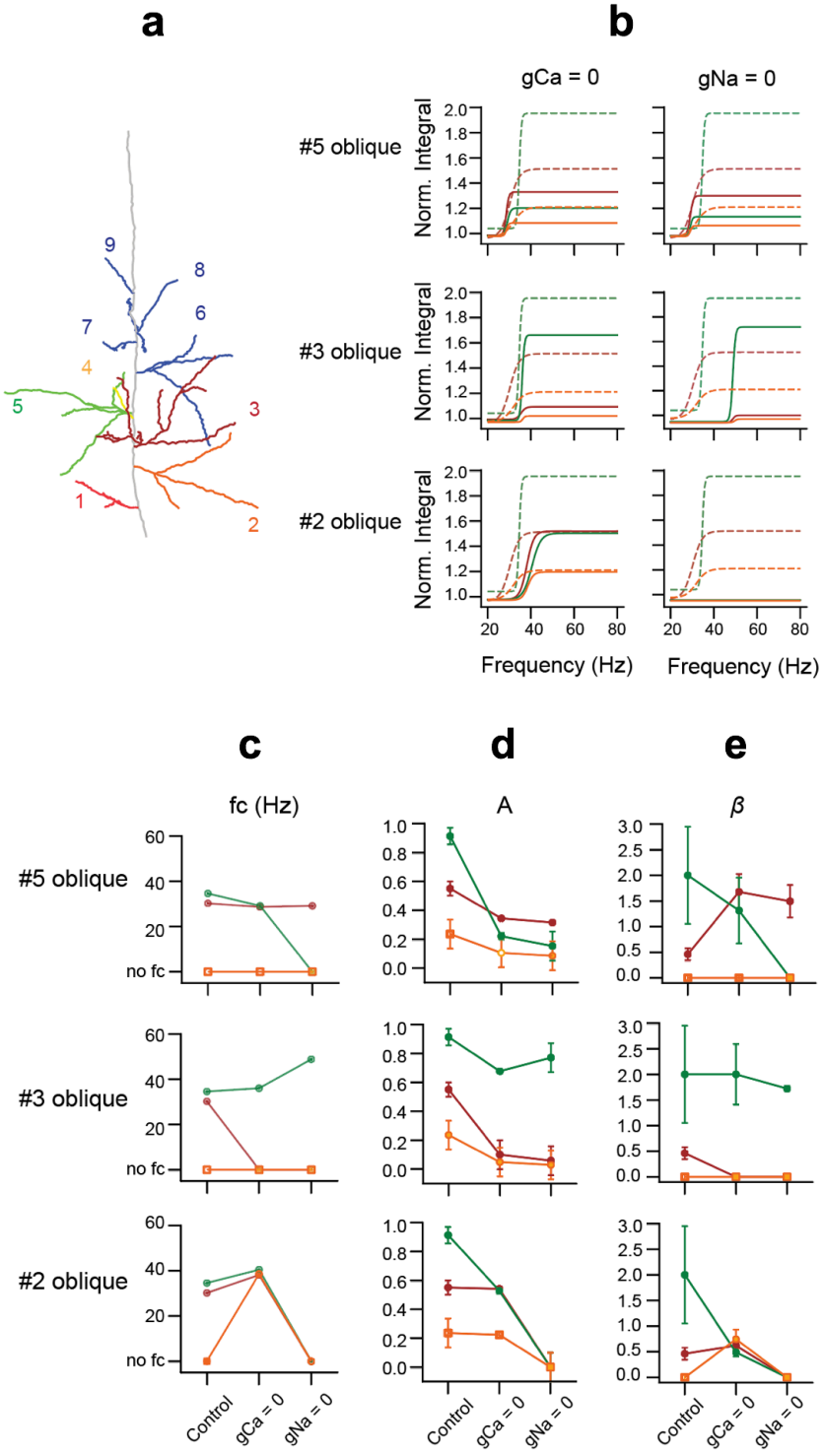

Figure 2.11 The initiation/removal of dendritic oblique spikes with changes in conductance of specific oblique branches. a, The time-integral of the membrane potential with the frequency of 2 bAP-train at the soma, nexus, and oblique dendrites (#5, #3, #1) for a branch where the sodium (*gNa_Ts2*) or calcium (*gCa_LVA, gCa_HVA*) conductance was set to zero. The time-integral is normalized to the time-integral at 20 Hz. **b,** The sigmoid fit parameters (A, β, and critical frequency (fc)) with an abolishment of the critical frequency when *gNa_Ts2* in #2 oblique was set to zero. There error bars are errors in the fit. **c-e,** The sigmoid parameters (f_c, β, A) with the changes in the conductance for a given branch.

2.4.7 Dendrotomy at oblique dendrites in the L5PN model

I tested whether the step-increase in the ADP is due to the recruitment of the oblique branch spike. I selectively removed the oblique branches one at a time and check for changes in the ADP amplitude (**Figure 2.13**). I found that removing *O*#1 and *O*#4 oblique branches, which responded in a linear way did not significantly change the ADP. However, cutting the *O*#3 and *O*#5 (non-linear) oblique dendrites caused the cell to fire an extra spike within 10-40 Hz and significantly reduced the ADP amplitude beyond f_{c2} = 40 Hz. Removing #2 oblique (linear) dendrite also reduced the ADP. The removal of *O*#2 oblique could have altered the bAP propagation as this branch had a large membrane area.

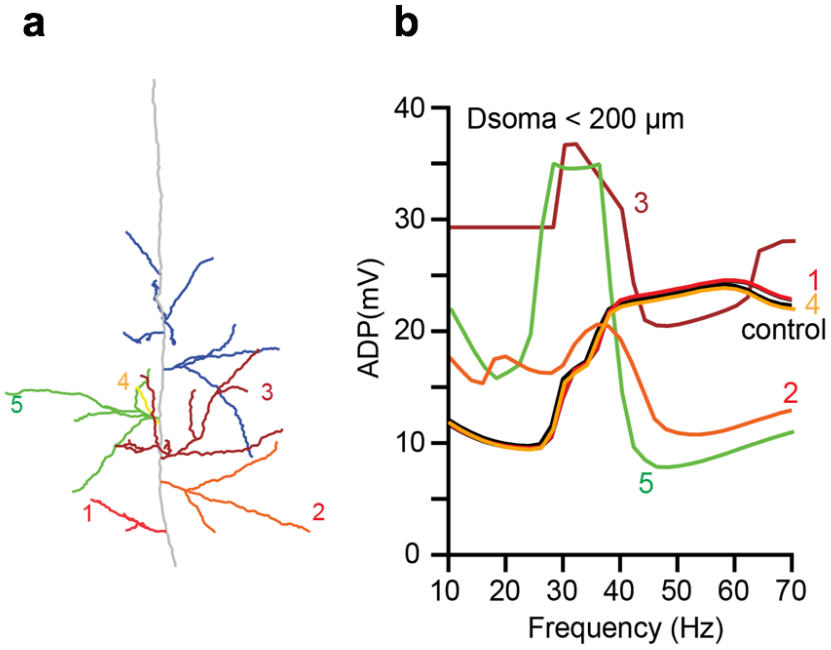

Figure 2.12 Dendrotomy in the *NEURON* model. a, The dendritic section of the L5PN model only showing the O# 1-5 apical oblique branches, **b,** The ADP in response to a two-pulse spike train upon removing a given oblique. The black trace is the ADP response in the control condition when all the oblique dendrites are intact. ADP which were > 30mV showed additional APs at that frequencies.

2.5 Summary

The works of Hodgkin, Huxley and Rall laid the mathematical foundations for modelling how currents and voltage flow within neurons (Hodgkin and Huxley, 1952; Rall, 1959; Rall, 1969; Rall and Rinzel, 1973). Numerical platforms, such as *NEURON*, now enable us to test how dendritic morphology (structure) affects AP firing (function) in single neurons.

Using a published multi-compartment model of a L5PN (Shai et al., 2015), I investigated the propagation of bAPs along the dendritic tree and the generation of dendritic spikes. A 4-AP train at 105 Hz generated a dendritic Ca^{2+}-AP at the nexus. The propagation of bAPs varied in oblique dendrites. A 2-AP train did not elicit Ca^{2+}-AP at the nexus; however, oblique branch spikes were elicited in select oblique branches with a 2-AP train at f_{c2} = 35 Hz. From the parametric plot of A and β, I determined a threshold ($A \geq 20$ mV and $\beta \geq 0.3$) that classified *O*#3 and *O*#5 oblique branches that exhibit this oblique branch spike. Based on my conductance analysis, the oblique branch spike is a fast sodium spike followed by a broad depolarization due to recruitment of high-voltage activated calcium channels.

The generation of dendritic spikes depends highly on the three-dimensional morphology of the dendritic tree. The ability to change dendritic morphology could potentially provide a new way to analyse neuronal function particularly on the generation of dendritic spikes and branch-specific dendritic computation. While dendrotomy is an invasive way to probe neuronal function, it allows for testing the causal relationship between spikes in oblique dendrites and the frequency-dependent step-rise in the ADP. This test could have been performed by highly localised pharmacological approaches such as: focal uncaging of blockers or focal drug application via a sharp pipette (Frick et al., 2003). However, such experimental techniques are challenging to implement especially when the oblique dendrites are very close to each other. In **Chapter 4**, we discuss how we performed highly targeted dendrotomy on specific oblique spikes using a focused femtosecond laser beam isolates the targeted dendrite from the cell while maintaining cell-viability (Go et al., 2016).

In the L5PN model, numerical blocking experiment and dendrotomy reveal that oblique branches are coupled with one another. For example, an oblique spike initiated in the *O*#3 oblique branch depolarized the neighbouring *O*#5 branch enough to set off an oblique spike in *O*#5 branch. The removal of obliques spikes in *O*#5 and *O*#3 branch by either blocking sodium channels in *O*#3 branch or *O*#2 branch resulted in a significant decrease in the ADP at the soma. Furthermore, physically removal branches *O*#2, *O*#3, and *O*#5 via dendrotomy abolished the step response in the ADP. This is consistent with observations in multi-

compartment models of CA1 PNs (Migliore et al., 2005). In hippocampal neuron multi-compartment models, fast sodium spikes did not effectively depolarize the soma due to the unfavourable impedance mismatch (spike propagating from oblique to main apical trunk) at the branch points (Migliore et al., 2005; Ferrante et al., 2013); however, sustained activation of several oblique branches can overcome this loss and add to the ADP at the soma (Migliore et al., 2005). Based from these numerical results, oblique dendrites in L5PNs may function as a coincidence detector with branches that seem to be coupled to one another. A train of APs with frequencies, $f > 35$ Hz, generates an oblique branch spike in a specific branch, which leads to a sustained depolarization of the neighbouring oblique branches via the activation of voltage-gated calcium channels. This sustained dendritic depolarization contributes to the somatic ADP bringing the neuron close to the AP threshold and to fire another AP.

Multi-compartmental models are great tools to visualize how signals, such as bAPs and dendritic spikes, propagate in a single neuron. They provide insights on how signals affect thin dendritic branches, which is hard to access in experiments with current patch-clamp techniques. Using the modelling results as a guide, we can design experimental methods and optical techniques to test these findings. In addition, matching experimental dendritic recordings (via patch clamp and calcium or voltage imaging) with modelling results allow us to infer the distribution of channels in dendrites, which shapes the active properties of the membrane. Indeed, multi-compartment models can be used as a guide to investigate the properties and signal propagation in dendrites. In the next chapters, I test the predictions from this model by investigating the generation of oblique branch spikes in L5PNs *in vitro*.

Chapter 3. General Methods Section: Two-photon holographic multi-site detection system and sample preparation

3.1 Introduction

Functional fluorescence calcium and voltage imaging are indispensable tools in probing membrane activity in thin dendrites. Optical recording of dendritic spikes via voltage imaging requires microscopes with high spatial and temporal resolution. There are several microscope designs that enable fast functional fluorescence imaging. Single-photon (1P) microscope systems such as epifluorescence, confocal, and spinning disk microscopes can achieve high frame rate recording. However, single-photon fluorescence imaging is limited to thin (50-100 μm) samples as blue/green light is strongly scattered by the tissue. On the other hand, two-photon (2P) line-scanning or holographic microscopes can be used to perform functional imaging both in slices and in intact brain preparation.

In this work, we developed a 2P multi-site holographic fluorescence detection system to record calcium activity in neurons. Arbitrarily projecting multiple foci on neuronal segments loaded with calcium indicators allowed simultaneous 2P-excitation, wherein the fluorescence photons from each site are collected by a multi-channel detector (e.g., a camera). Using this system, I performed calcium imaging at oblique dendrites of L5PNs.

The next section provides a background on the different microscope modalities used for functional calcium imaging highlighting the advantages and disadvantages of each optical design. Then, I proceed to present the design of our 2P multi-site system. I also enumerate the procedure used to prepare our tissue samples. Lastly, I give a comparative review of different optical systems used to record fast dendritic spikes *in vitro*.

Background

Functional calcium imaging requires microscopes with sufficient spatiotemporal resolution. **Figure 3.1** shows different microscope modalities to image fluctuations in fluorescence emitted by fluorescent calcium indicators due to changes in intracellular calcium concentration. The discussion focuses on how the excitation beam is delivered and on how the emitted fluorescent photons are recorded.

1P functional imaging can be achieved using a conventional epifluorescence microscope (**Figure 3.1a**) and a two-dimensional multi-channel image sensor (or camera) for video acquisition with a frame rate of at least ~20 frames/s (Connor, 1986; Lasser-Ross et al., 1991). This type of microscope uses 1P excitation with high energy (e.g., light source to excite the calcium indicator. Conventional epifluorescence microscopes have poor axial discrimination and are limited to thin samples such as thin neuronal slices or cultures due to light scattering in the tissue. When imaging neuronal activity within thick (>300 μm) brain slices or from an intact brain (*in vivo*), it is important to discriminate fluorescence photons emitted from different axial planes. Selectively recovering fluorescence photons from a single plane is achieved using a confocal microscope (**Figure 3.1b**). In a confocal microscope, the focused beam scans the sample and the fluorescence photons via a single-channel detector such as a photomultiplier tube (PMT). A pinhole, placed before the detector, restricts the collection in-focus fluorescence to the PMT. The numerical aperture of the lens and the size of the pinhole define the thickness (or depth-of-focus, DOF) of the imaging plane. Raster scanning can be achieved by mechanically scanning the beam via galvanometer-mirrors (slow) and/or resonant scanning mirrors (fast). The speed of scanning and the size of the region-of-interest scanned defines the temporal resolution (frames/s) of the system. Confocal microscopes have been used for functional calcium imaging in a range of preparations (Williams and Fay, 1990; Eilers et al., 1995).

The increased temporal resolution provided by recent camera technologies (e.g. sCMOS and EMCCD) allows high-speed image acquisition at 1000 frames/s or more. High camera frame rate allows for fast imaging in a single focal plane when conventional bright-field microscopy is combined with illumination by a sheet of light along the imaging plane of a bright field microscope (**Figure 3.1c**). Light sheet microscopy, as it is commonly known today, was first referred to as "orthogonal-plane fluorescence optical sectioning microscopy" (Voie et al., 1993), and later as "selective plane illumination microscopy" (Huisken et al., 2004; Huisken and Stainier, 2009). This method is now heavily used in studying calcium dynamics of neuronal circuits in zebrafish (Ahrens et al., 2013; Wolf et al., 2015).

The two-photon (2P) laser-scanning microscope follows the same image acquisition protocol as the confocal microscope where a focused laser beam is raster-scanned across the sample (**Figure 3.1d**) (Denk et al., 1990). The main difference, however, is the use of a non-linear excitation process where a fluorophore absorbs two low-energy photons (λ ~800 nm) as compared to using one high-energy photon (λ ~400 nm) for 1P excitation. The very low probability of two photons to be simultaneously absorbed by a fluorophore requires a highly

focused femtosecond (fs ~10^{-15} s) pulsed laser. The principle can be extended to three or more photons resulting in much lower non-linear excitation probabilities (Horton et al., 2013). Since the probability of multi-photon excitation is highest in the focal plane, the fluorescence emanating from the sample is within the DOF, thereby eliminating the need for a pinhole before the detector.

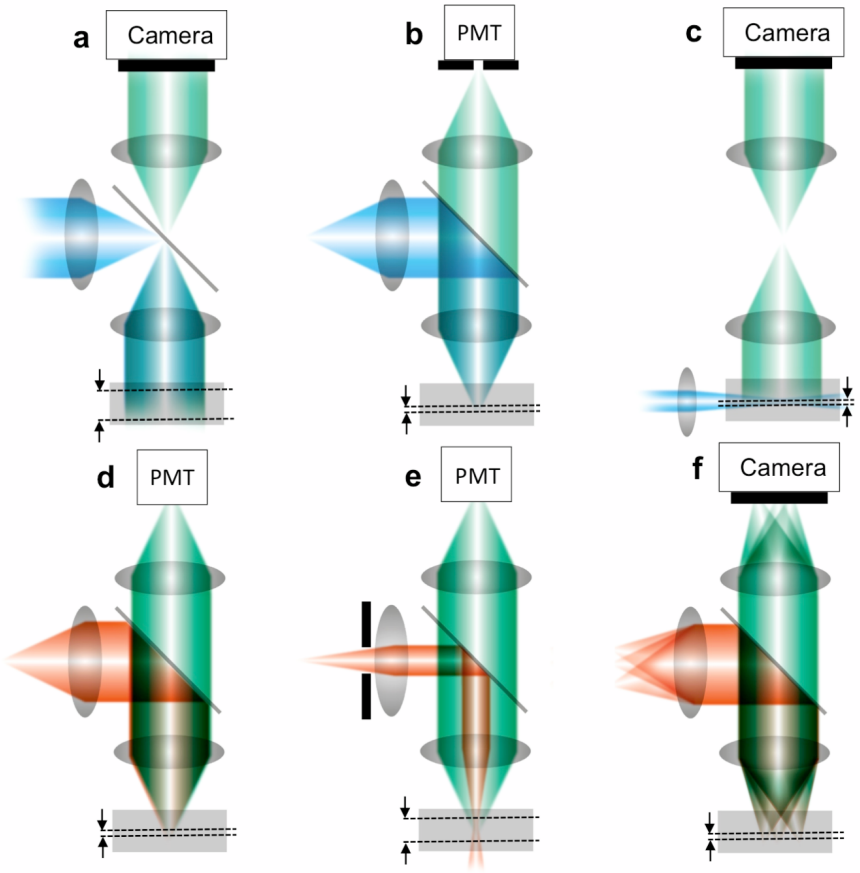

Figure 3.1 Common microscope modalities to perform functional calcium imaging. a, Single- photon (1P) epifluorescence microscope; **b,** 1P confocal microscope; **c,** 1P light-sheet microscope; **d**, Two-photon (2P) microscope; **e**, Extended depth-of-focus 2P microscope; **f**, Patterned illumination via a holographic multi-foci 2P microscope. Relative axial discrimination is shown in dashed lines for the different imaging modalities. Figure taken from (Castanares et al., 2019)

Removal in the use of a pinhole allows more fluorescence photons to be acquired by the detector. An additional advantage of this method is that low-energy photons in the near-infrared (NIR) are scattered less, thereby giving better access to neurons embedded deep within brain tissue (Svoboda et al., 1997; Helmchen et al., 1999; Helmchen and Denk, 2005). Scanning speeds for 2P microscopes have been significantly enhanced with acousto-optic deflectors (AOD) (Saggau et al., 1998), which can randomly position beams in 3D in less than 10 µs

(Katona et al., 2012). AODs have now been commonly used for high-speed functional calcium imaging (Katona et al., 2012). While 2P microscopes have good 3D spatial resolutions, the temporal response suffers when recording neurons in a volume. One way to increase the temporal resolution is to reduce 3D information into 2D by increasing the DOF (Dufour et al., 2006; Katona et al., 2012). **Figure 3.1e** describes a system with extended DOF by reducing the effective numerical aperture of the objective lens. A variant of such extended DOF allows depth discrimination and has been used for fast volumetric calcium imaging (Theriault et al., 2014).

The holographic 2P microscope (**Figure 3.1f**) uses a spatial light modulator (SLM) to shape the incident beam into different patterns (e.g., multiple foci or user-defined patterns) (Nikolenko et al., 2008; Daria et al., 2009; Dal Maschio et al., 2010; Castanares et al., 2016; Bovetti et al., 2017; Song et al., 2017). The fluorescence photons emitted from the multiple excitation sites are recorded simultaneously using a multi-channel detector such as a photodiode-array, linear photo-multiplier tube array, or a camera. Parking the holographic foci at the sites of interest allow longer beam dwell time yielding a better signal-to-noise ratio of the recordings compared to ones acquired with beam-scanning (Bovetti et al., 2017). Individual foci in a multi-focal pattern can also be sequentially illuminated using a digital micro-mirror device (DMD), allowing fluorescence to be sequentially acquired using a single-channel detector (Ducros et al., 2013). With a high-speed DMD (operating at 22,000 samples/second switching speed), the fluorescence signal from 8-11 sites can be decoded with a temporal resolution of 0.72 ms (Ducros et al., 2013). When used without a DMD, holographic projection enables simultaneous illumination of multiple foci and high- speed detection with temporal resolution limited by the frame rate of the camera.

Our 2P multi-site fluorescence detection system utilized the holographic microscope design. We used phase-only holographic projection to shape a single laser beam into arbitrarily positioned multiple foci. These foci were then used to generate 2P excitation at sites of interest. The fluorescence from each site were recorded by a fast camera at the same time.

3.2 Chapter aims

This chapter aims: (1) to review the theory of holographic projection, (2) to describe the techniques used in this thesis such as our novel multi-site fluorescence detection system, and (3) to discuss different optical systems used to detect dendritic spikes.

3.3 Methods

3.3.1 Phase-only holographic projection

The phase-only holographic projection method entails the pre-calculation of a computer-generated hologram (CGH) and encoding the hologram on an optical device such as a phase-only spatial light modulator (SLM). The SLM is a two-dimensional liquid-crystal array of phase-shifting pixels with a nominal phase shift of 2π at its specified operating wavelength. When the SLM is illuminated, the optical transformation in the far field (or at the focus of a lens) projects the optical field pattern suitable for multi-site excitation of calcium indicators (**Figure 3.2a**). Calculation of the appropriate CGH can be achieved by an iterative optimization algorithm or by the superposition of combined prism and lens phase functions to project independently positioned multiple foci (Liesener et al., 2000). For *N* holographically projected foci distributed around the focal volume, the input phase, φ (*u*, *v*), is described by

$$\begin{aligned} \mathrm{h(u,v)} &= \mathrm{a(u,v)exp\big(i\varphi(u,v)\big)} \\ &= \sum_{\mathrm{i}}^{\mathrm{N-1}} \exp\left(\mathrm{i}\frac{2\pi}{\lambda}\left(\frac{\mathrm{NA}}{\mathrm{R}}(\mathrm{ux_i} + \mathrm{vy_i}) + \left(\frac{2\mathrm{NAr}}{\mathrm{R}}\right)^2 \mathrm{z_i}\right)\right) \end{aligned} \quad \textbf{(3.1)}$$

where (u, v) are 2D pixel coordinates at the SLM, *NA* is the numerical aperture of the lens, λ is the wavelength of the laser, *R* is the radius of the operating or illuminated region at the SLM, while (u, v) and $r^2 = u^2 + v^2$ are Cartesian and radial coordinates at the hologram plane, respectively. The 3D spatial coordinate positions of the spots at the output are (x_i, y_i, z_i). In phase-only holographic projection, the SLM encodes only the phase component, $\varphi(u, v)$, discarding the amplitude, $a(u, v)$. To visualize the 3D intensity distribution of the holographically projected multiple foci, Daria et al. (2009) numerically modelled the light propagation from the SLM to the focal volume via the Fresnel diffraction integral. Each focus can be positioned arbitrarily within the focal volume and is bounded by the space-bandwidth product of the optical system. **Figure 3.2b** shows the intensity distribution along the *xz*-plane with two intensity maxima (*N* = 2) of two foci positioned at (±2.25/η, 0, 0). The smaller intensities beside the two foci are high diffraction orders, which account for some losses in the projection (Palima and Daria, 2006). The normalized transverse (*x*,*y*) and axial (*z*) coordinates are related to spatial coordinates by $\eta = NA\lambda^{-1}$ and $\xi = NA^2\lambda^{-1}$.

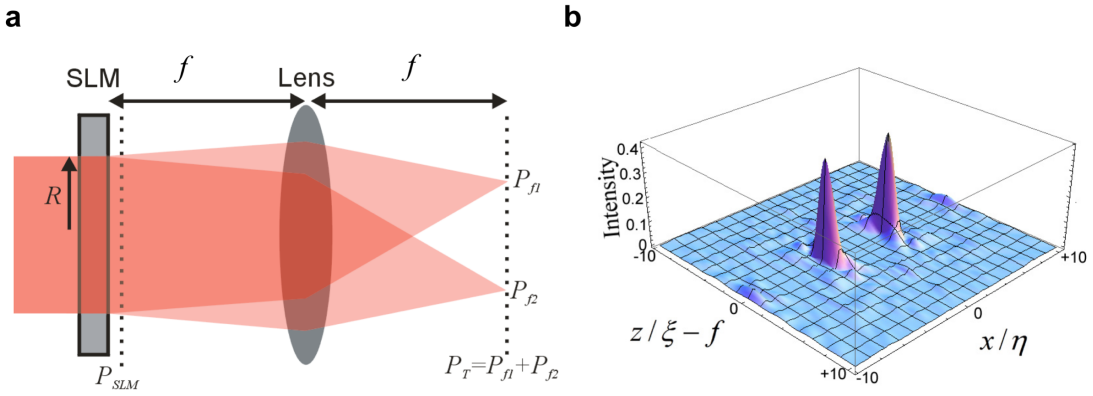

Figure 3.2 Phase-only holographic projection. a, Schematic for phase-only holographic projection. **b**, Numerically evaluated intensity distribution of two foci and high diffraction orders along the *xz*-plane. Note the following: R (beam radius); f is the focal length of the lens; P_{SLM} is the power of the incident beam, P_{f1} and P_{f2} are the normalized power of foci 1 and 2, respectively; P_{T} is the total power at the focal plane. Figure taken from (Castanares et al., 2019).

The profiles of the foci are characterized by the convolution of the Fourier transform of a circular aperture associated with the 3D point-spread function of the optical system and N delta functions. As such, the circularly symmetric two-dimensional (2D) intensity profile of each diffraction-limited spot is described by the normalized Airy pattern.

Daria et al. (2009) evaluated the fundamental optical throughput as the number of foci is increased. First, the intensity distribution at the focal plane of a lens is calculated using two-dimensional Fourier transform (FT), $I(kx, ky) = (\pi R^2)^{-2}|FT\{e(u,v)\}|^2$, where ($k_{\mathrm{x}}$, k_{y}) are spatial frequency coordinates at the Fourier plane. The intensity distribution is then normalized with the square of the illuminated area using Parseval's theorem (Goodman, 2005). **Figure 3.3a** shows the two-dimensional intensity distribution of ten foci ($N = 10$) arbitrarily arranged in the focal plane. To evaluate the fundamental optical throughput, the power at the focal plane was calculated, $P_f = \int I_f \mathrm{dA}$, integrating the intensity over a circular area, A, around each focus (see representative circular area in **Figure 3.3a**). **Figure 3.3b** shows the normalized power per focus, P_f, as N is increased (square markers). Also shown is the total power, $P_T = \sum P_f$ (triangular markers). Note that P_T is slowly decreasing over a range of N indicating that fundamental losses due to higher diffraction orders are maintained even as N is increased. For $N \geq 2$, the normalized power of each focus follows a fit given by,

$$\frac{P_f}{\langle P_{SLM} \rangle} = \frac{\delta(r)}{N} \qquad \textbf{(3.2)}$$

where $\langle P_{SLM} \rangle$ is the average power of the incident beam measured at the SLM and $\delta = 0.84$, radially symmetric measure of the first-order diffraction efficiency (Daria et al., 2009).

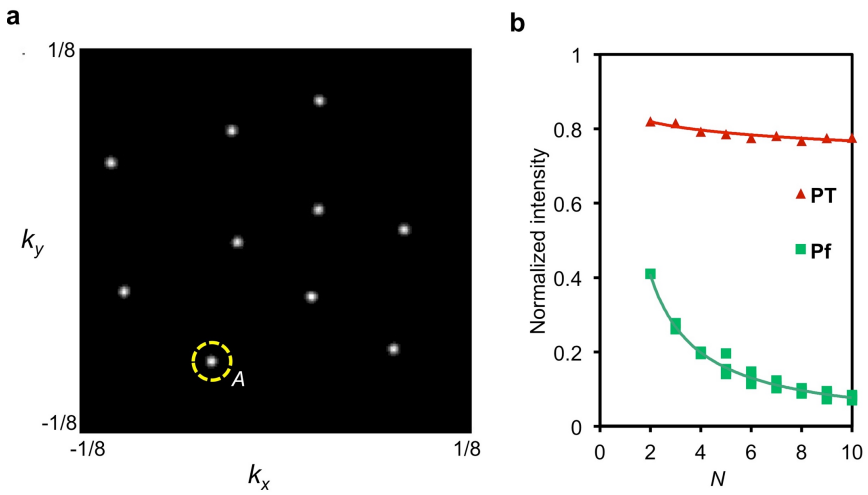

Figure 3.3 Intensity distribution and optical throughput. a, Multi-foci configurations for N = 10 foci derived numerically via two-dimensional Fourier transform using **Equation 3.1** as input. **b**, Plot of the average power per focus (P_f, squares) and total power (P_T, triangles) as the number of foci (N) is increased. Figure taken from (Castanares et al., 2019).

3.3.2 2P multi-site fluorescence detection system

I briefly describe our microscope system shown in **Figure 3.4**. A femtosecond-pulsed Ti:S laser (Chameleon Ultra II, Coherent) is split to a beam scanning and holographic arm via a polarizing beam splitter (PBS1) sending the S-polarized beam to a *xy*-galvanometer-scanning mirrors (GM). The P-polarized laser beam, on the other hand, is directed towards the SLM via a set of beam expansion lenses. A Fourier Transform Lens (FTL) is placed in front of the SLM to produce the multiple foci at its Fourier plane. PBS2 couples the S-polarized beam forming a standard 2P microscope together with tube lenses (TL), dichroic mirror (DM) and the photomultiplier tube (PMT). The P-polarized beam from the SLM is also coupled to the microscope using PBS2. The SLM is used to encode a phase map onto the laser and relayed via a 4f-lens configuration (FTL and TL) to the back aperture of the objective lens (OL). The fluorescence from the sample passes through the DM for imaging to either the photomultiplier tube (PMT) or the electron-multiplied CCD camera (EMCCD, iXon Ultra 897, Andor, Oxford Instruments). Whole-cell patch clamp recordings were performed with a standard patch-clamp system (Penner, 1995) that was integrated in the microscope. Fine glass electrodes (2.0mm Outer Diameter, with open tip pipette resistances of 5-7 MΩ) were pulled using a pipette puller (P-97, Sutter Instruments). A multi-clamp amplifier (Multi-Clamp 700b, Molecular Probes) connected to an A/D converter (ITC-16, Instrutech) injects and records current from the

electrode. The acquisition of current clamp recordings and fluorescence images was synchronized by digital triggering of the camera software (Andor Solis) and multi-clamp acquisition software (Axograph).

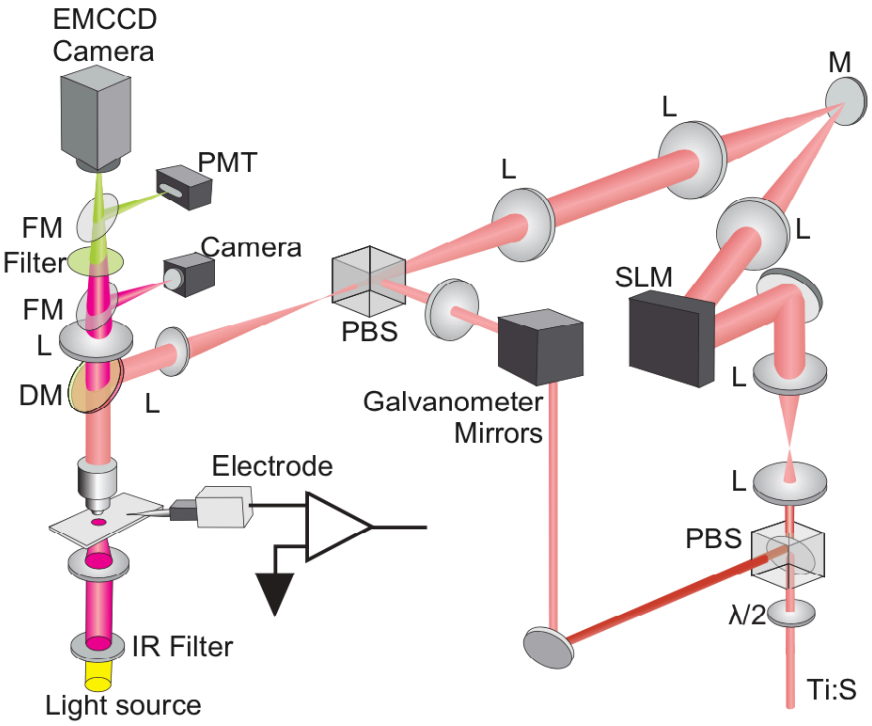

Figure 3.4 Schematic diagram of our custom-built two-photon laser scanning and holographic microscope. The femtosecond laser directed by a polarizing beam splitter (PBS) to the laser scanning arm or the holographic arm by adjusting the polarization angle of the beam relative to the PBS. In laser scanning mode, the beam is deflected using galvanometer mirrors and the fluorescence is collected using a PMT. In holographic mode, the beam is projected onto a spatial light modulator (SLM) where it is shaped into user-positioned multi-foci onto the sample. The fluorescence of each site is simultaneously recorded by an electron-multiplied CCD (EMCCD) camera. Note the following abbreviations: L is convex/focusing lens, DM is dichroic mirror, FM is a flip mirror, M is a mirror, and λ/2 is a half-wave plate polarizer.

3.3.3 Sample preparation

Salt solutions

Before surgery, two types of artificial cerebral spinal fluid solutions: (1) slicing (sACSF) and; (2) normal (nACSF) were prepared (see **Table 3.1** for the recipe). The slicing ACSF contained (in mM): 1.25 NaH_2PO_4, 1.0 $MgCl_2$, 125.0 NaCl, 2.5 KCl, 2.0 $CaCl_2$, 25 $NaHCO_3$, and 10.0 glucose. The high concentration of magnesium blocks NMDA receptor activation of the neurons during the slice preparation. The sACSF is used throughout the surgery and brain collection procedure. On the otherhand, the nACSF is only used during patch-clamp recording. A reservoir of sACSF was prepared in a 100 mL beaker with a custom-made mesh to contain

the brain slices. The sACSF reservoir was heated up to 34 ^{o}C in a water bath. Constant bubbling of carbogen (95% O_2 + 5% CO_2) was maintained in this solution.

Table 3.1 ACSF solution used for slice incubation and recording

10x stock solution: (1L)	73.05g NaCl 1.725g $NaPO_4$ (Mw = 137.99g/mol) 21.0g $NaHCO_2$ (Mw = 84.01g/mol) 2.24g KCl (Mw = 74.55g/mol)
500mL Slicing ACSF (sACSF):	50mL 10x stock solution 3mL 1M $MgCl_2$ 0.5mL 1M $CaCl_2$ 4.5g glucose add deionized water stirred and bubbled with 95% carbogen
1L Normal ACSF (nACSF):	100mL 10x stock solution 1mL 1M $MgCl_2$ 2mL 1M $CaCl_2$ 9.0g glucose add deionized water stirred and bubbled with 95% carbogen

Slice preparation

Whole rat brains were harvested from P26-P34 young adolescent male Wistar (ASD429) Rats following the protocol approved by the Australian National University Animal Ethics Committee (Animal Ethics protocol no: A2018/35). The rats were sedated with 2-4% isoflurane in oxygen (3L/min) by inhalation. As the animal was unconscious, verified by tail pinching, its head was decapitated using a guillotine. The isolated head was submerged to an ice-cold sACSF. The rat brain was carefully removed from the skull. An incision was made of the left hemisphere of the skull (**Figure 3.5a**). The brain was placed in another iced sACSF for 2-3 mins to cool. Then, the rat brain was placed on a glass petri dish with a filter paper to dry out excess solution. With a blade oriented normal to the table, the olfactory bulb was cut from the brain (**Figure 3.5b**). A wedge was inserted at one end of the dish creating a 5-10^{o} tilt (see **Figure 3.5c**). The use of the wedge compensated the natural curve of the brain in the attempt to conserve the dendritic tree of large L5PNs. After the cut, the wedge was removed flattening the dish onto the table and then the cerebellum was cut. The brain was mounted on a filter paper with the cut end of the near the cerebellum facing up. Using another dry filter paper, the brain tissue was held up, the anterior end dried up with another filter paper, and then mounted

on the vibratome stage initially loaded with a super glue (Loctite). The brain tissue was oriented such that the primary somatosensory cortex was parallel to the vibratome blade. The tissue and glue was allowed to bond for 1 min. Then the sACSF was poured onto the bath while maintaining a constant bubbling of carbogen. From the posterior end of the tissue, 1.7-2.0 mm of tissue was remove (this section contains the visual and auditory cortex) to reveal to somatosensory cortex. A key indicator of S1 region is the formation of arc white matter (corpus collosum, axonal projections to S1, indicated by **A** in the image) and the kink (indicated by **K** at the lower right part of the tissue, **Figure 3.5d**). During the cut, the stage was moved 500 µm up then the blade was engaged to cut. As the blade cuts through up to the hippocampus, the vibratome blade was disengaged and the stage was moved down by 200 µm. Using a needle, the cortex was cut-off from the rest of the tissue. With a glass pipette, the sliced tissue was transferred the sACSF bath. This sequence was repeated until 6 coronal slices were recovered. The slices were incubated at 34 °C for 30 mins and kept at room temperature afterward. Healthy neurons can be recorded from the slices in the next 6-8 hours.

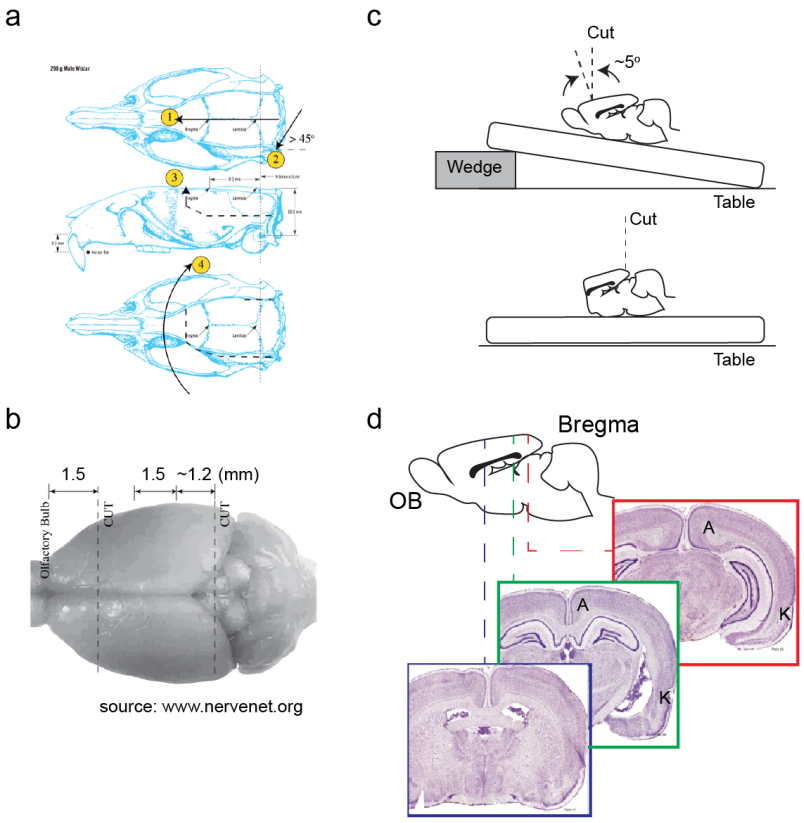

Figure 3.5 Surgery and slice preparation. a, The approach of the cuts to open up skull and expose the brain. **b,** The estimated cut to remove the olfactory bulb and cerebellum. **c,** A slight tilt 5-10^{o} in the angle of cut was used which help orient the dendritic tree of layer 5 pyramidal neurons in a plane avoiding cutting the apical trunk. **d,** Sample images of the coronal slices within the somatosensory cortex region (stained for visualization). Images are taken from the rat brain atlas (Paxinos and Watson, 2006).

Culture preparation

Preparation of cultured primary hippocampal neurons was performed in accordance with the protocol approved by the Australian National University Animal Ethics committee. Hippocampal tissue was dissected and dissociated from the brains of post-natal day 1-2 rats (Wistar). The tissue was then incubated in dissociating Papain solution at 37 °C in a water bath for 20 min. It was then triturated, incubated in DNAase solution at room temperature for 10 min, followed by resuspending in the plating medium (Dulbecco's modified Earl's medium supplemented with 10% fetal bovine serum, 1% L-glutamine, 1% penicillin- streptomycin and 1% B-27 supplement). The cells were then plated onto the pre-treated, poly-L-lysine coated glass coverslips and allowed to grow in an incubator at 37 °C and 5% CO_2.

3.3.4 Electrophysiology and 2P calcium imaging

Calcium imaging was performed on oblique dendrites of L5PNs in the somatosensory cortex of rats *in vitro*. Electrophysiology recordings were done on neurons in brain slices (as presented in the previous **Section 3.3.3**). L5PNs were patched with a glass containing (in mM): 115.0 K-gluconate, 20.0 KCl, 10.0 HEPES, 10.0 phosphocreatine, 4.0 ATP-Mg, 0.3 GTP, 0.13 Alexa-Fluor-488 (Sigma Aldrich), and 0.3 Cal-520 potassium salt (AAT-Bioquest).

The L5PNs were held at -65 mV, a typical resting membrane potential for these neurons. A 30 min to 1 hr loading time before imaging was observed to allow the dye to diffuse into the dendritic tree. In some cases, during the dye loading, the series resistance of the pipette increased to values comparable to the recorded input resistance of the cell, 25-30 MΩ, which introduced measurement errors (e.g., the measured height of APs at the soma). To correct this increase in the series resistance, I applied a brief negative suction to the pipette with the buzz function (50-100 ms) in the multi-clamp amplifier to dislodge the clog at the tip of the electrode. If the brief suction didn't work, I slowly retracted the electrode and repatched the cell with a fresh electrode. Fluorescence imaging was done using the microscope described in **Section 3.3.2**. Fluorescent calcium indicator and tracer (0.3 mM Cal-520 potassium salt and 0.13 mM Alexa-Fluor-488 dissolved in K-gluconate based intracellular solution) were loaded into the L5PNs via a patch pipette in whole-cell patch configuration. While typical fluorescence calcium imaging and structural tracing involved the use of two indicators that have different overlapping spectrum, here I used Alexa-Fluor-488 and Cal-520 indicators. Each indicator emits green fluorescence but have different 2P absorption. I used 810 and 890 nm 2P wavelength to excite Cal-520 and Alexa-Fluor 488, respectively. Cal-520 has a low baseline

fluorescence (Tada et al., 2014). When the neuron was at rest, it was difficult to trace the oblique dendrites from the Cal-520 signal. To overcome this issue, I first acquired a 2P image of the target oblique branch at 890 nm which strongly excited Alexa-Fluor 488 tracer. Then for calcium imaging, then the 2P wavelength was switch to 810 nm which gave strong fluorescence signal from Cal-520 but minimal signal from Alexa-Fluor 488 tracer.

Our 2P microscope has a 150x150 μm^2 field-of-view (FOV) determined by the OL (1.0NA, 40x, water immersion lens, Nikon) (**Figure 3.6a**). However; the size of the imaging area by the EMCCD was determined by the desired frame rate. At full frame (512x512 pixels) acquisition, the camera can capture up to 56 frames per second. For higher frame rates such as 100 frames/s used in my experiment (with acquisition setting in Andor Solis: 0.099ms exposure per frame, frame-transfer mode, 50x gain) was achieved with the optically centred crop mode feature.

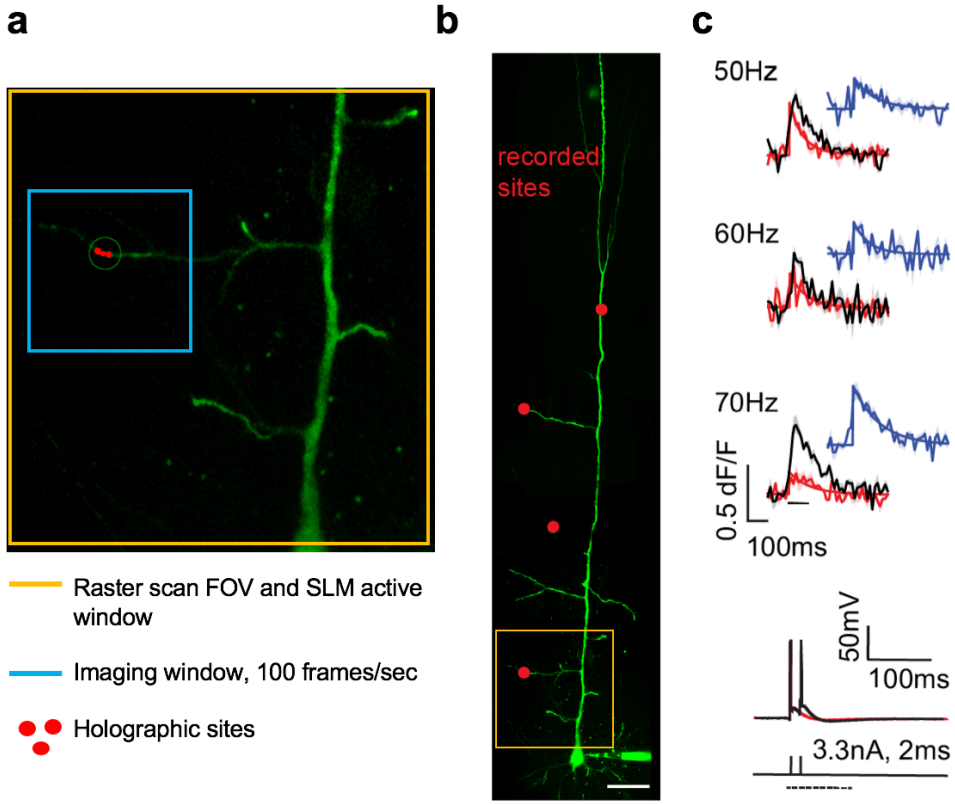

Figure 3.6 The interleaving protocol to measure the differences in the calcium influx between single AP and two AP train. a, The 2P image from the microscope with the 150x150 µm FOV of the scanning mirrors, imaging window of the EMCCD camera, and the positioned holographic sites. **b,** The 2P stitched image of the neuron's dendritic tree. **c,** A sample of recorded fluorescence calcium transients associated with 1- (red) and 2-AP train (black) at train frequencies of f = 50, 60, and 70 Hz. The difference of the traces was calculated (blue) and fitted with an exponential decay. The somatic recording of the membrane voltage is shown in response to current injections (I = 3.3 nA, $\Delta\tau$ = 2 ms). Scale bar is 50 µm.

In the crop mode, acquisition was restricted only to fraction (128x128 pixels) of the camera's total pixels. The unused pixels were shielded from any light using an adjustable circular iris placed in front aperture of the camera. Thus, our imaging area was limited by the camera 128x128 pixel window which translated to an approximately 50x50 μm^2-area at the sample plane. Holographic multi-foci (3-4 sites) were positioned along oblique dendrites within the imaging area (**Figure 3.6b**). I recorded the responses in one region at a time with the critical frequency protocol. In cases where multiple branches were observed within the 50x50 μm^2 imaging window, 1-2 sites were positioned on each branch. Slight movements, particularly along the z-axis, defocused the imaged branch and reduced the fluorescence signals. To account for changes in the baseline fluorescence, we implemented a protocol that interleaved 1- and 2-AP train (see **Figure 3.6c**). Three trials using this interleaving protocol were recorded.

3.4 Results

3.4.1 Imaging dendritic spikes at the nexus of apical tuft dendrites

I experimentally verified the generation of this Ca^{2+}-AP spike and the shift in the critical frequency with the amplitude of the injected current (see **Figure 3.7**). I patched onto the cell body of L5PNs and injected a low (I = 3-5 nA) and high (I = 5-10 nA) current amplitude in the critical frequency protocol with parameters: 4 current pulses, $\Delta\tau$ = 2 ms pulse width, and $20 \leq f \leq 120$ Hz frequency. Calcium responses were recorded at the nexus or the main apical trunk of the L5PNs (**Figure 3.7a**). Only 4 out of 8 of the recorded neurons showed a detectable ($\beta \geq 0.3$) critical frequency. **Figure 3.7b** shows the normalized integral of the calcium transient (measured in dF/F) with increased amplitude or duration of the current pulse. The average critical frequencies with low(2-5nA) and high(5-10nA) amplitude of current injection were f_{c4} = 74±8 Hz and f_{c4} = 76±9 Hz, respectively. With the preliminary recordings (N = 4), no clear conclusion can be made with the difference in the critical frequencies between I = 2-5 nA and I = 5-10 nA current injection. It is possible that this shift in the critical frequency (as discussed in **Chapter 2**, **Section 2.4.2**) could be an artefact in the model. To avoid discrepancy in the results, all simulation run were done with a fixed current amplitude and pulse-width (I = 4.2 nA, $\Delta\tau = 2$ms). Results from the model should be confirmed with experimental data. Future studies can look at resolving this artefact. One approach is to test other multi-compartment models (with different morphology and biophysics file) and check whether the same shift in the critical frequency can be observed.

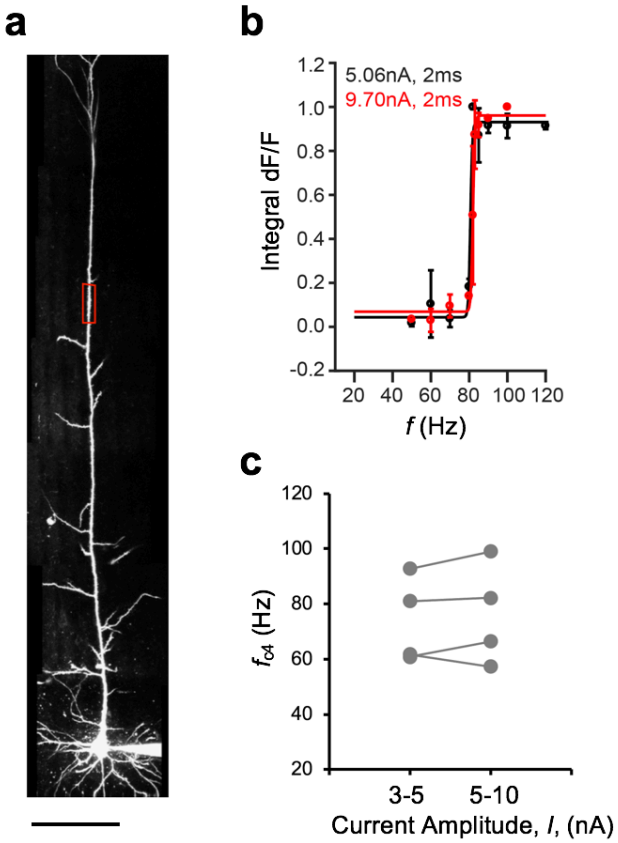

Figure 3.7 Influence of current amplitude with the critical frequency from *in vitro* recordings. a, 2P reconstructed image of L5PN loaded with fluorescent indicators (Alexa-Fluor 488 and Cal-520) with the recorded region indicated by the red ROI. **b,** The normalized peak amplitude of the calcium transients with frequency of somatic AP trains at 5.06 nA (black) and 9.70 nA (red) injected current. **c,** The plot of the critical frequencies of 4-AP train to elicit the Ca^{2+}-AP at the apical trunk with low (3-5 nA) and high (5-10 nA) amplitude of current. The scale bar is 50 µm.

3.4 Summary

In this chapter, I presented our 2P multi-site system to perform fast fluorescence calcium imaging. The arbitrarily multi-foci excitation sites were generated using a spatial light modulator with an encoded phase hologram. The 2D phase-only hologram was calculated as a superposition of prism and lens function to position each focus independently in 3D at the sample plane. The fluorescence from excitation site were recorded at the same time by an EMCCD camera. Depending on the size of the imaging ROI of the camera, the frame rate can be set to capture 50 to 0.5 kHz which can be potentially used for voltage imaging. Several studies have successfully recorded dendritic spikes using 1P and 2P microscope systems. Our multi-site detection system with the use of 2P holographically projected foci presents a novel

optical design for fast 2P calcium and voltage imaging. Our multi-site detection system with the use of 2P holographically projected foci presents a novel optical design for fast 2P calcium and voltage imaging. With the system, we were able to detect Ca^{2+}-AP at the apical trunk of neurons having a critical of f_{c4} = 74±8 Hz (N = 4 neurons).

Chapter 4. Experimental evidence of oblique branch spikes in oblique dendrites of L5PNs *in vitro*

4.1 Introduction

As presented in **Chapter 1**, **Section 1.4**, dendrites have active properties with some dendritic sections capable of generating dendritic spikes that boost the impact of distal synaptic inputs. The strong passive filtering of the membrane and generation of local dendritic spikes enable different dendritic regions to function as independent computational compartments (Larkum et al., 2009; Major et al., 2013). While there is a wealth of information about cortical processing in apical tuft and basal dendrites, the functional role of apical oblique dendrites of L5PNs are less understood.

Oblique dendrites of L5PNs are strategically located in layer 4 of the cortical column, which may potentially receive direct synaptic inputs from thalamocortical projections in layer 4 (Constantinople and Bruno, 2013). In addition, biocytin reconstructions also show that apical oblique dendrites of L5PNs receive nearly 1/3 of all synaptic connections from neighboring L5PNs (Markram et al., 1997). I hypothesize that oblique dendrites of L5PNs may form another independent computational compartment with the generation of oblique branch spike as described numerically in **Chapter 2**.

Dendritic recording together with pharmacology would be the direct approach to identify the generation of dendritic spikes as shown by previous studies (Schiller et al., 1997; Kamondi et al., 1998; Nevian et al., 2007; Larkum et al., 2009). However, oblique dendrites, because of their small diameters, presents a challenge in recording their membrane potential activity with an electrode. To overcome this limitation, I investigate the generation of oblique branch spikes using fluorescence calcium imaging with whole-cell patch. Moreover, **from Chapter 2**, branch-specific generation of dendritic spikes were observed and application of highly localised pharmacological agents could be challenging. To analyse the causal effect of the spikes, I applied laser-dendrotomy on specific obliques. Experimental recordings such as dendritic calcium transients, somatic ADP, and laser dendrotomy, provide consistent evidence that oblique branch spikes are recruited with low-frequency burst of APs firing.

4.2 Chapter aim

This chapter aims to present experimental evidence of oblique branch spikes in apical oblique dendrites of cortical L5PNs in the somatosensory region *in vitro*.

4.3 Methods

4.3.1 Analysis of calcium response and the after-depolarizing potential (ADP)

The critical frequency was measured from: (1) fluorescence calcium transients at oblique dendrites, and (2) ADP recordings at the soma. In probing the non-linearity at oblique dendrites via calcium imaging (with intracellularly loaded 0.3mM Cal-520 (potassium salt, AAT-Bioquest) dissolved in internal solution), I used the interleaving protocol described in **Chapter 3, Section 3.3.4**. Briefly, 2-AP trains of a set of randomly picked frequencies were used. As a reference, a brief single pulse was injected to determine the calcium response associated with 1-AP. The difference between the amplitude of the calcium transients for 2- and 1-AP was assigned as the amplitude of the calcium response, Ca_{21}, at the oblique dendrite at that given frequency.

As for the ADP measurements, I performed the critical frequency protocol with two (2-AP) and four action potential (4-AP) trains on the same cell to test whether the number of pulses influences the generation of a dendritic spike. Note that I use 2-AP when referring to somatic recordings (e.g., ADP measurements) and 2-bAP for dendritic calcium recordings. To reliably fire a train of APs from 4 to 150 Hz, I used current amplitudes from I = 3-5 nA, which was ~1.4x the minimum current required to elicit a single AP. The ADP was measured as the average membrane potential within 5-7 ms after the last AP. Then, I calculated the relative change in the ADP with respect to the mean ADP at low frequencies, $\Delta ADP(f) = ADP(f) - \langle ADP(4\ \text{Hz} \leq f \leq 10\ \text{Hz})\rangle$. Lastly, the relationship of the $\Delta ADP(f)$ or Ca_{21} with frequency was fitted with a sigmoid function described by,

$$S(f)_{\text{fit}} = \frac{A}{[1 + \exp(-\beta(f - f_C))]} \qquad (\mathbf{4.1})$$

with the amplitude, $A = A_{Ca}$ (for calcium response) or A_{ADP} (for ADP response), and the steepness parameter, β.

4.3.2 Classification of linear and non-linear responses in Ca_{21} and ADP

I classified the sigmoid-fitted responses (Ca_{21} vs. f and ΔADP vs f) into linear and non-linear. From the modelling results in **Chapter 2.4.5**, I applied the criteria: $\beta < 0.3$ as a linear and $\beta \geq$

0.3 as a non-linear response. To account for the detection noise in the experiment, I also included a criteria on the amplitudes $A_{Ca} \geq 0.1$dF/F (for calcium imaging) and ΔADP ≥ 1mV (for ADP) as a detectable signal. Note that β tends to saturate (go very large) for small amplitudes (A_{Ca} and ΔADP). I visually inspected the sigmoid fits checking for over-fitting.

4.3.3 Quantification of the recorded sites

From the 2P images, I quantified the locations of the recorded sites as: the distance from the soma to the branch point, *D_soma*; the distance from the branch point to the recorded site, *D_trunk*; and the oblique number, O# (also described in **Chapter 2**). These locations were measured from the 2P z-projected images using Simple Neurite tracer plugin in FIJI (Longair et al., 2011).

4.3.4 Laser dendrotomy

Targeted dendrotomy using a focused femtosecond laser beam can be used to isolate the targeted dendrite from the cell while maintaining cell-viability (Go et al., 2016). The focal incision was within the diffraction limit (~1 μm) matching that of typical diameters of apical obliques. First, I identified neurons that exhibited a step-wise increase in the ADP at around f_{c2} ~60 Hz. I then randomly target oblique dendrites. The cell was held in voltage clamp at typical resting membrane potential, (V_{hold} = -65 mV). The laser intensity and shutters were configured to deliver an average power $\langle P \rangle$ = 80 mW, with 0.5 to 3-sec laser exposures at λ = 890 nm. The 2P image of the target oblique dendrites were captured before dendrotomy to verify that the branches were in-focus. A slight defocus of the beam reduced the efficiency of the cut. During dendrotomy, a successful cut was directly followed by large inward currents at the soma, indicative of action potential firing due to membrane opening at the incision site. The membrane potential decayed back to a stable, but a depolarised potential after 10 mins (requiring -50 to -200 pA holding current to maintain the cell at -65mV).

4.3.5 Analysis

Linear regression analysis was used to test for correlations of calcium responses with the location of recorded sites, with the strength of the correlation described by the Pearson correlation coefficient, R^2. Paired student t-test was used to assess statistically significant differences of the data for a given *p*-value ($p < 0.01$, * $p < 0.1$, ** $p < 0.01$, *** $p < 0.001$). The standard error, ε, for the experimentally determined critical frequencies from calcium imaging and ADP measurements are expressed as $\varepsilon = \pm \sqrt{(\text{var}[fcn]/N}$ and N is the number of L5PNs.

4.4 Results

4.4.1 Calcium imaging at oblique branches of L5PNs

I performed calcium imaging at oblique dendrites of L5PNs (N = 13 cells) with the critical frequency protocol. The increase in the amplitude of the calcium transients with the frequency of AP trains was variable at different oblique branches (see **Figure 4.1** for representative traces). Some oblique branches (represented with blue trace in **Figure 4.1b**) and a few recordings at the apical trunk (represented with red trace in in **Figure 4.1b**) showed a linear response ($\beta < 0.3$) for the relation of Ca_{21} vs. f of the AP train. In some obliques, I observed a non-linear increase in the calcium transient (represented with green trace in **Figure 4.1b**) that was set-off after the second AP at f = 70Hz AP train. This large increase in the amplitude of the calcium transients persisted at higher frequencies as observed in the relation of Ca_{21} vs. f **(Figure 4.1e-Top)**. A large fraction of recorded cells (16 cells, 13 rats) exhibited a spikelet after the 2nd AP and were not included in this analysis, as the added spike induced large changes in the intracellular calcium and changed the effective frequency of the AP train (see **Table 4.1** for summary of the recordings).

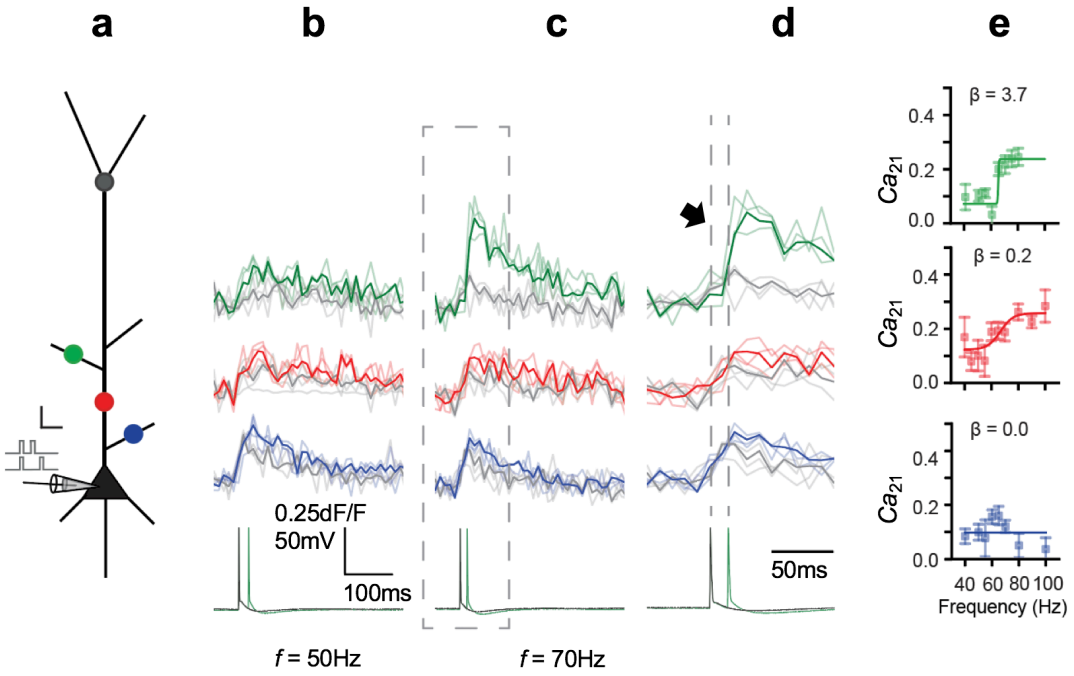

Figure 4.1. Variable calcium influx on different oblique branches. a, The schematic of an L5PN with its apical oblique dendrites. **b-d,** Representative traces of the calcium transients recorded at different oblique dendrites (blue and green) and apical trunk (red) from a L5PN following a train of 2-APs at 50 Hz (**b**) and 70 Hz (**c**). A non-linear increase in the calcium transient recorded in an oblique branch (green) after the second bAP (**d,** indicated by an arrow). The traces of calcium transients associated with a single bAP is also shown (grey). **e,** The amplitude difference between the two calcium transients, Ca_{21}, from 40 Hz to 100 Hz two AP trains fitted with a sigmoid function.

An aggregate of the fitted responses is shown by the parametric plot of A and β in **Figure 4.2**. The noise floor observed in the recording was ~0.1 dF/F. A fraction of the recorded neurons (8 out of 13 cells) showed non-linear increase in intracellular calcium at a critical frequency of f_{c2} = 57±5 Hz (N = 8 neurons) for the 2-AP train. Fitting a linear regression lines, there were no correlations of A_{Ca} with the oblique number (O#, R^2 = 0.039) and location of the recorded sites (*D_soma*: R^2 = 0.020, *D_trunk*: R^2 = 0.001) (**Figure 4.2b-d**). **Figure 4.3** shows the calcium responses versus the frequency of 2-AP train of neurons that exhibited an oblique branch spike.

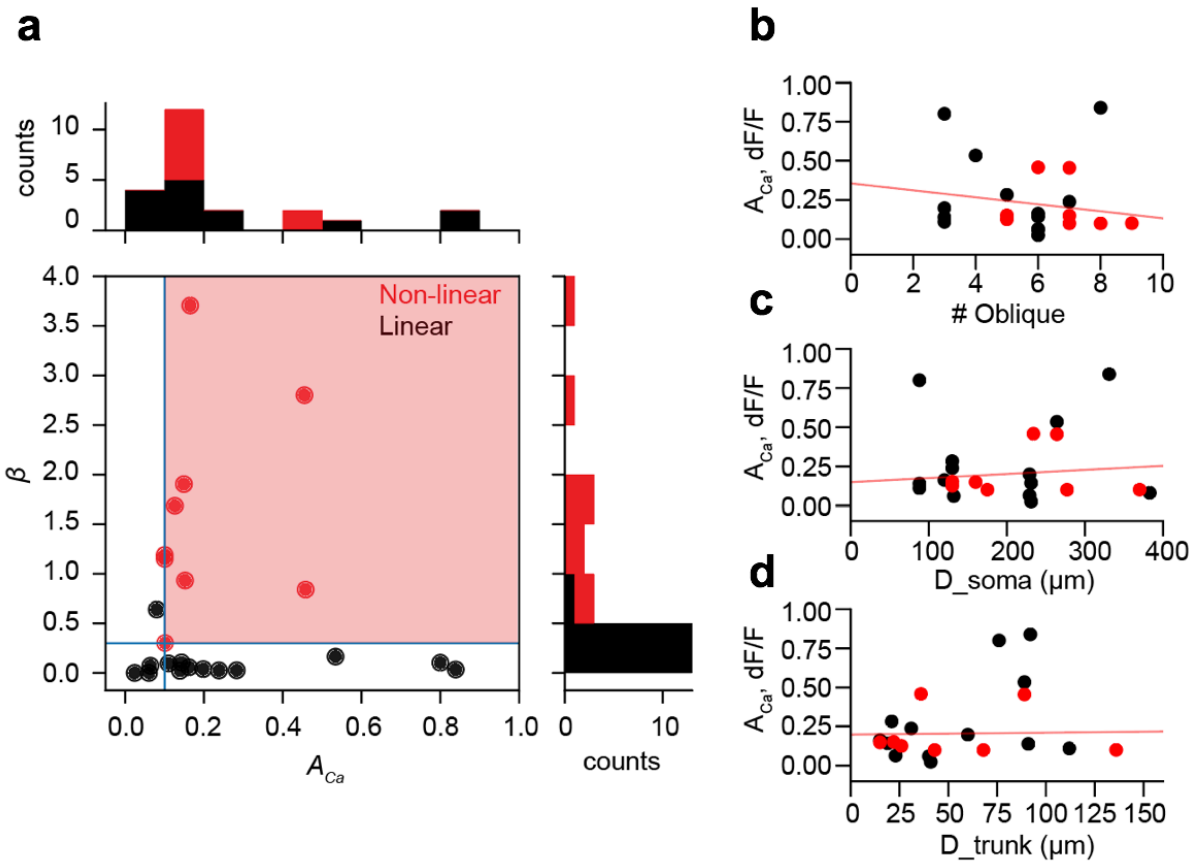

Figure 4.2 Pooled summary of the recorded responses from oblique dendrites. a, A parametric plot of the non-linear parameter, β, and A_{Ca}. The red region, described by $A_{Ca} \geq$ 0.1dF/F and $\beta \geq 0.3$, indicates the set of A_{Ca} and β parameters in which I considered the response as non-linear. **b,** The oblique number (O#) with A_{Ca}. **c,** The path distance of the recorded sites from the main apical trunk, *D_trunk*, for the classified linear (black) and non-linear (red) responding oblique dendrites. **d,** The distance from the branch point of the recorded oblique dendrites to the soma.

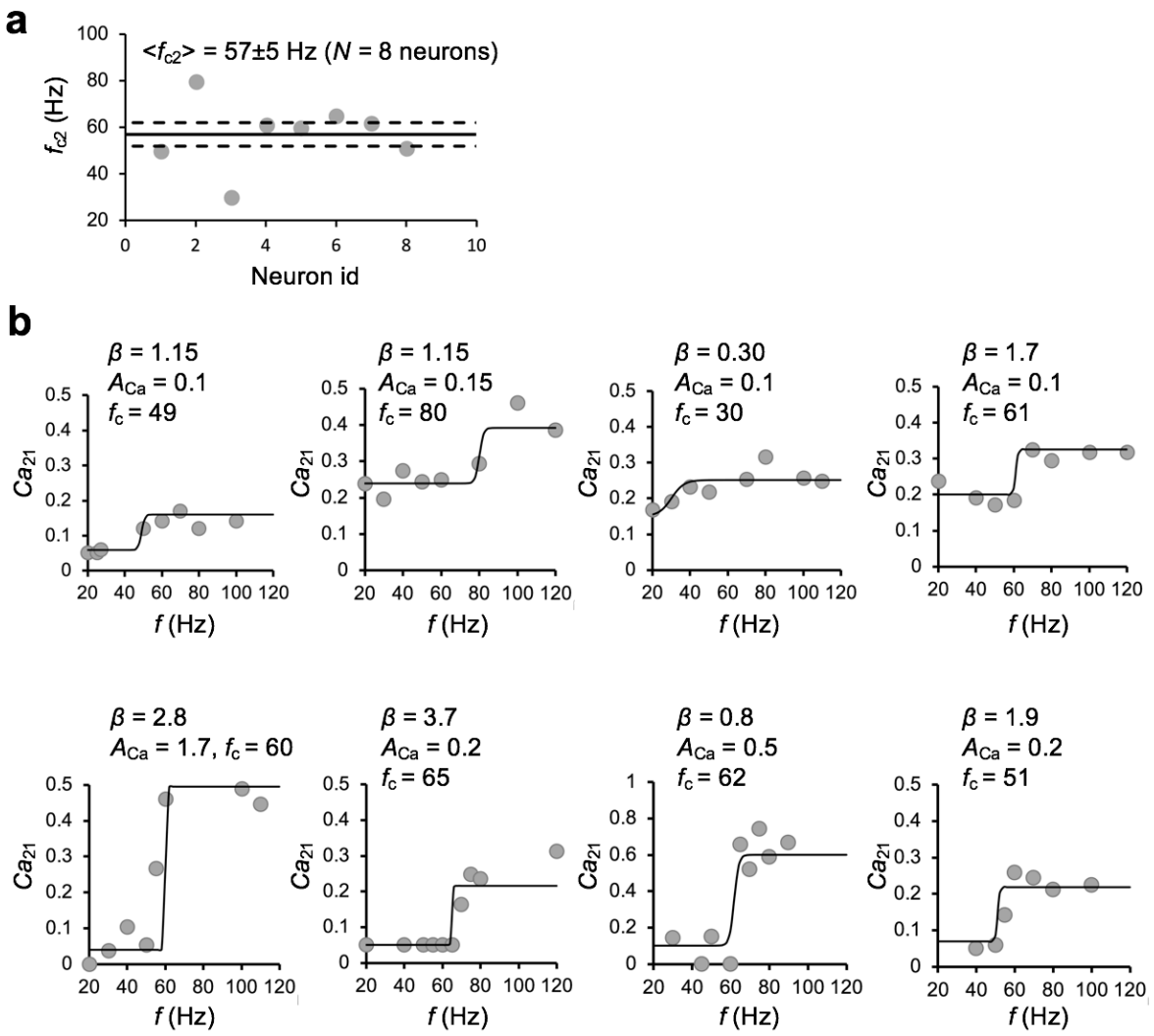

Figure 4.3. The calcium transients vs. frequency with the sigmoid fit from neurons that exhibited an oblique branch spike. a, The critical frequency with 2-AP train and **b,** The Ca_{21} vs. *f* of neurons with the generation of oblique branch spikes.

4.4.2 Morphologies of the responding neurons and the location of the recorded sites

Representative 2P fluorescence images of L5 pyramidal neurons are shown in **Figure 4.4**, with oblique dendrites showing non-linear responses indicated. These neurons had large dendritic trees that span ~1 mm of the cortex. It was important to verify that the nexus of the apical tuft was intact in the recorded neurons. A neuron with a cut apical trunk would exhibit different active properties (e.g., the threshold of AP initiation and propagation of bAP) as a large capacitive load is removed from the neuron (Bekkers and Hausser, 2007), which could potentially affect the critical frequency of AP train required to set-off an oblique branch spike.

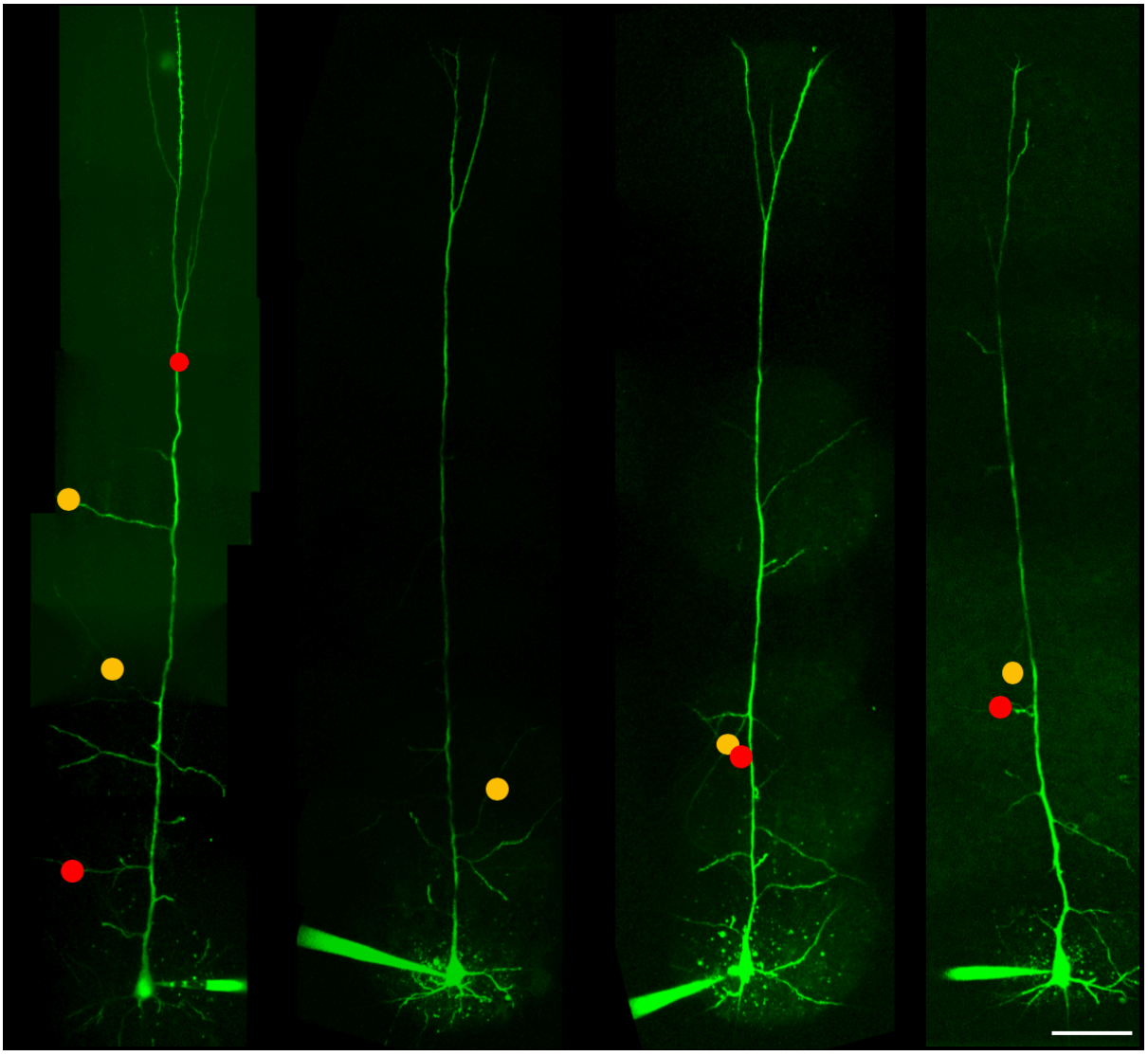

Figure 4.4 Representative two-photon images of neurons loaded with Cal-520 and Alexa-Fluor 488 indicators. The dendrites are marked with the recorded sites (red and yellow circles). The yellow circles are segments with a non-linear rise in the calcium transient, while the red circles are segments that exhibited a linear increase in the calcium transient. The scale bar is 50 μm.

Table 4.1. L5PNs recorded in calcium imaging experiment

Total (27)	NL response (8)	Linear (3)	with spikelet (16)
080218_cell3	051018_cell1	051518_cell1	052818_cell1
051018_cell1	061218_cell5	060418_cell4	052418_cell3
051518_cell1	062118_cell4	080218_cell2	052818_cell2
052418_cell3	072618_cell3		053018_cell1
052818_cell1	073018_cell2		053118_cell1
052818_cell2	081418_cell1		053118_cell2
053018_cell1	090618_cell2		061218_cell2
053118_cell1	100418_cell1		061218_cell4
053118_cell2			073118_cell1
060418_cell4			073118_cell3
061218_cell2			080218_cell3
061218_cell4			080218_cell5
061218_cell5			080818_cell1
062118_cell4			081418_cell5
072618_cell3			082718_cell7
073018_cell2			082918_cell3
073118_cell1			
073118_cell3			
080218_cell2			
080218_cell5			
080818_cell1			
081418_cell1			
081418_cell5			
082718_cell7			
082918_cell3			
090618_cell2			
100418_cell1			

Note: L5PNs with spikelets were not included in the analysis as the frequency of the AP train was not controlled.

4.4.3 The influence of oblique spike to the ADP

I investigated whether the dendritic oblique spike contributes to the ADP at the soma and tested whether the non-linearity in the ADP could serve as an indicator of an oblique branch spike. A total of 144 neurons were patched establishing a whole-cell configuration and their ADP were examined with the critical frequency protocol of 2-AP and 4-AP train. However, only 100 neurons were included in the analysis (see **Table 4.2**). The remaining 45 cells (31.2%) exhibited no clear ADP or additional spikelet which made them unusable for the ADP analysis. Non-linear increase in the *ΔADP* were observed starting with critical frequencies ≥ 50 Hz (**Figure 4.5**). A sample somatic recordings, with traces aligned to the peak of the last AP, of an L5PN in response to 2-AP and 4-AP train is shown in **Figure 4.5a**. The ADP was measured as the average membrane potential within t = 0.510-0.518s time window (indicated as a dotted rectangle in **Figure 4.5a**).

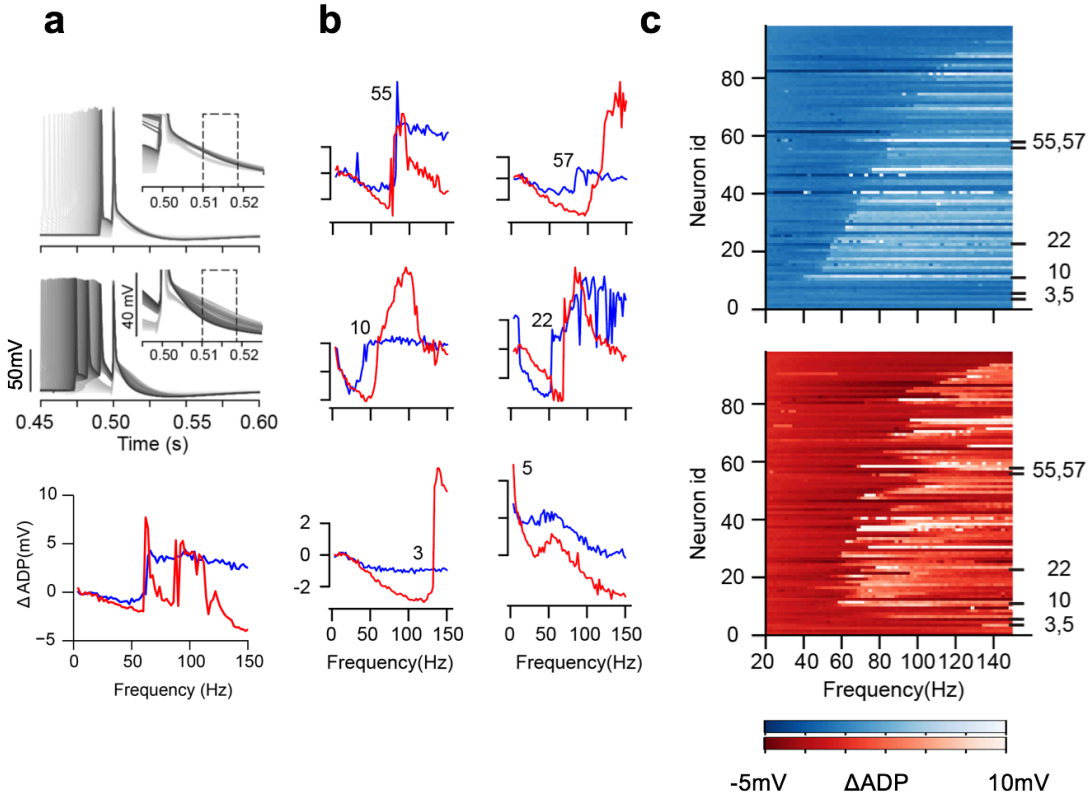

Figure 4.5 Measured after-depolarising potentials in neurons at different frequencies for two- and four-AP trains. a, A representative somatic recordings with the two (2-AP, light grey) and four (4-AP, dark grey) AP train with the traces aligned at the last AP. The corresponding ADP is shown at the bottom. **b,** The varied ADP responses of different neuron with 2-AP (blue) and 4-AP (red) trains. The scale bars for the amplitude for all cells is the same as that shown in neuron 3(**b** – Neuron id 3). **c,** the heat map visualization of the ADP responses from a large neuron sample (100 cells, 29 rats) sorted with increasing critical frequency for the 2-AP train.

With the aligned somatic traces, two distinct bands in the time window indicating a step increase in the ADP. The corresponding changes in the *ΔADP* with frequency of 2-AP (blue) and 4-AP (red) train are shown in **Figure 4.5a-bottom**. This L5PN exhibited critical frequencies, f_{c2} = 62 Hz and f_{c4} = 62, 92 Hz (two inflection points with 4-AP train). Recordings from other L5PNs showed varied critical frequencies with some (neuron id: 55 and 5) having the same critical frequencies for 2-AP and 4-AP trains and others (neuron id: 10, 57, and 22) with a lower critical frequency with 2-AP than the 4-AP train (see **Figure 4.5b**). A summary of all the ADP recordings is shown in the heat map with the responses arranged according the increasing critical frequency for 2-AP train (**Figure 4.5c**).

The responses in the ADP were grouped into 4 categories namely: no detectable non-linear increase in the ADP (*no f_c,* 27 neurons), with critical frequency only with 2-AP train (f_{c2}, 2 neurons), with critical frequency only with 4-AP train (f_{c4}, 35 neurons), and with critical frequencies with 2- and 4-AP trains (f_{c2} and f_{c4}, 36 neurons) (**Figure 4.6a**). There were 27% of the sample recorded L5PNs did not show any critical frequency, which could be due to either: cut-off apical trunk from the slicing preparation, or the under expression of voltage-gated ion channels at the apical trunk in developing young adolescent mouse (~P30 day old). There were neurons that exhibit only one critical frequency for 2-AP or 4-AP train. There were 35% of the recorded neurons exhibited critical frequencies with 4-AP train, f_{c4} = 98±4 Hz, which due to the recruitment of Ca^{2+}-AP at the nexus of the apical tuft (Larkum et al., 1999). Interestingly, there were 36% of neurons that exhibit critical frequencies with the 2- and 4-AP train. The two critical frequencies were significantly different (p = 0.0013 <0.01, paired student t-test, 36 neurons) (**Figure 4.6b**). On average, the critical frequencies for 2- and 4-AP trains were: f_{c2} = 72±4 Hz and f_{c4} = 82±3 Hz, respectively. The critical frequencies for 2-AP train from calcium imaging and ADP were similar: f_{c2} = 57±5 Hz (for calcium imaging) to f_{c2} = 72±4 Hz (for ADP).

I investigated the critical frequency for the 2-AP train in the presence of NMDA receptor antagonist. L5PNs were patched and their critical frequencies for 2-AP trains were measured under normal ACSF (control) (**Figure 4.6c**). Then, 25 μM of DL-APV (DL-2-Amino-5-phophonopentanoic acid sodium salt dissolved in ACSF, Tocris) was bath applied in the recording chamber for 15 mins. A sample recording of the ADP responses from a neuron before (control ACSF) and after 15min bath application of APV is shown in **Figure 4.6d**. There was no significant change (p = 0.375, paired t-test, 4 neurons) in the: ADP, nonlinearity, and critical frequencies in the presence of DL-APV (**Figure 4.6e-g**). Thus, the step-increase in the ADP was not due to the activation of NMDA receptors.

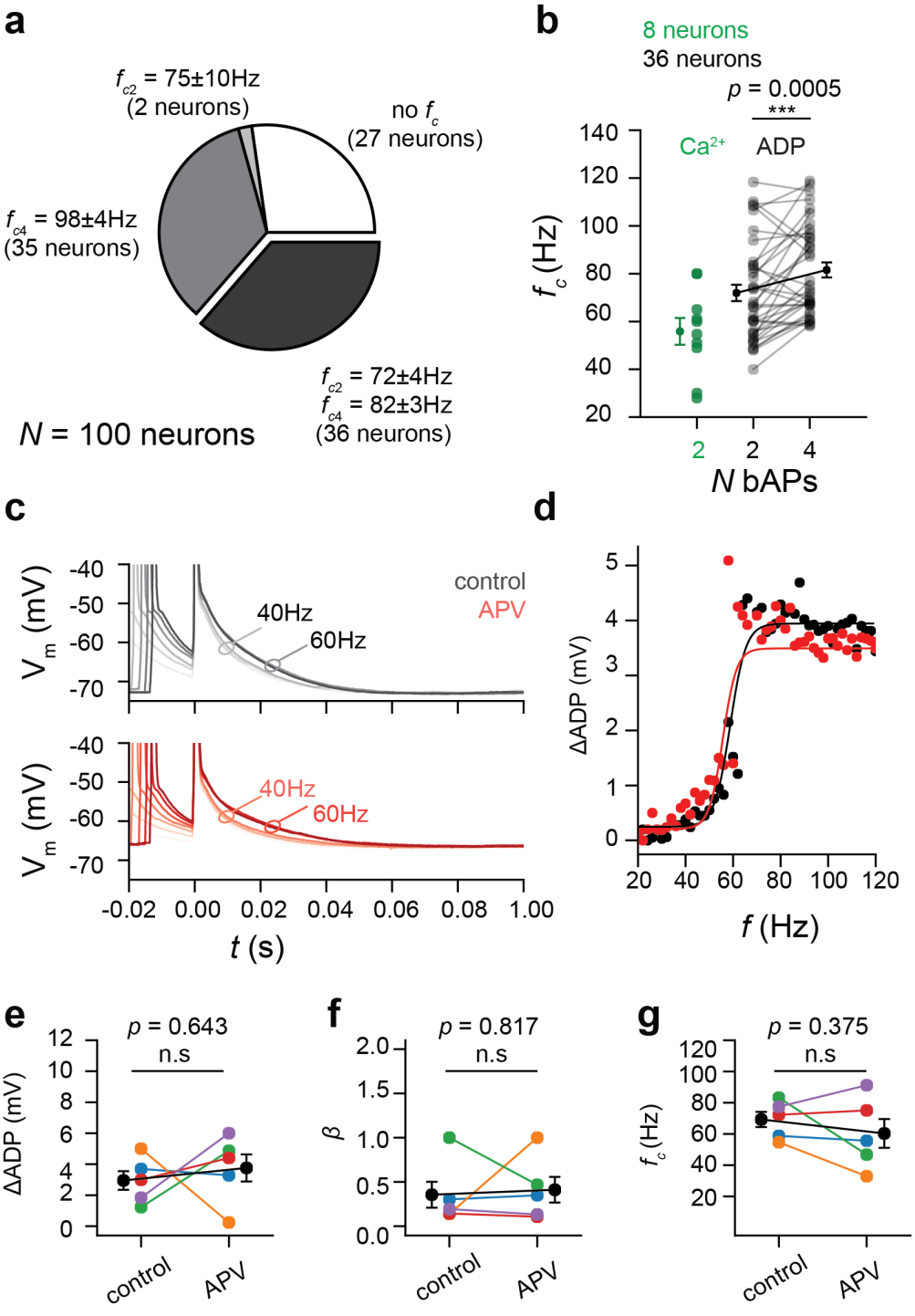

Figure 4.6 Summary of the critical frequencies of large neuronal sample and the effect of APV with the ADP with an oblique branch spike. a, A sample 2P images of the neuron with the corresponding after-depolarizing potentials (from 4 Hz to 100Hz, light blue to dark blue traces) before and after laser ablation of an oblique dendrite. **b,** A voltage-clamp recording of the membrane current with the laser ablation showing a decay of holding current to a new set value after 10 mins indicating that the membrane of the incised site has partially resealed.

Table 4.2. Recordings in the ADP experiment

Date	Upon break-in (144)	Included in the Analysis (100)
062118	4	2
021819	6	6
021919	6	5
022119	3	3
022219	8	8
072618	4	2
073018	5	2
073118	3	3
080218	5	3
080818	5	2
082618	6	2
082718	6	4
082918	3	3
090318	6	4
090418	6	1
090618	4	3
091718	2	2
092718	4	1
092818	2	1
100218	5	5
100402	2	2
100818	4	2
100918	2	2
101718	5	4
101818	6	3
102418	5	4
102518	6	6
112118	6	4
112218	5	5
112818	5	4
112918	5	2

Note: L5PNs that did not show a clear ADP were not included in the analysis.

4.4.4 Targeted Pruning of thin oblique dendrites

So far in **Section 4.4.3**, I reported that the critical frequency from calcium imaging was similar to critical frequency from the ADP. I further verified that this rise in the ADP was not mediated by NMDA receptor activation. However, it remains unknown whether oblique branch spikes triggered the step increase in the ADP. To test for a causal link between oblique branch spikes and the step-rise in the ADP, I removed oblique dendrites via laser dendrotomy (as described in **Section 4.3.4**).

Four L5PNs with critical frequencies f_{c2} < 100Hz were examined (see **Figure 4.7a** for ADP recordings from two neurons). Before dendrotomy, the extent of the oblique branch was imaged using 2P scanning. Segments 10-20μm bifurcating from the main apical trunk were cutted. Just after 3-sec exposure of the focused beam (dendrotomy), the AP firing was recorded at the soma and the holding current gradually decayed back to a set value (-30 to -200pA, **Figure 4.7b**), which indicated resealing of the membrane at the incision site. The cut site was also verified with 2P imaging with no fluorescence signal from segments beyond the incision site (**Figure 4.7a**). From the changes in the holding current (**Figure4.7c**) and the shift in AP threshold from the phase-plots(**Figure 4.7d-e**), dendrotomy affected the excitability of the neurons.

The ADP responses were monitored before and after dendrotomy. For two of the cells (yellow and blue), cutting their distal oblique dendrites (237 and 170 μm from soma) removed the step-rise in the ADP. For the other two cells (red and green), cutting the proximal oblique dendrites (*D_soma* = 20 and 140 μm from the soma) did not remove the step-rise in the ADP (**Figure 4.7a-top and Figure 4.7f-h)**. The variability in the removal of the step-increase in the ADP when cutting the oblique branches indicate that specific oblique dendrites contributed to the ADP. While more recordings are needed to draw conclusions, preliminary recordings indicate that cutting one or two oblique branches was potentially enough to abolish the step-rise in the ADP. It remains to be verified whether the cut branches which led to a removal of the step-rise in the ADP were also the ones that generated the oblique branch spike.

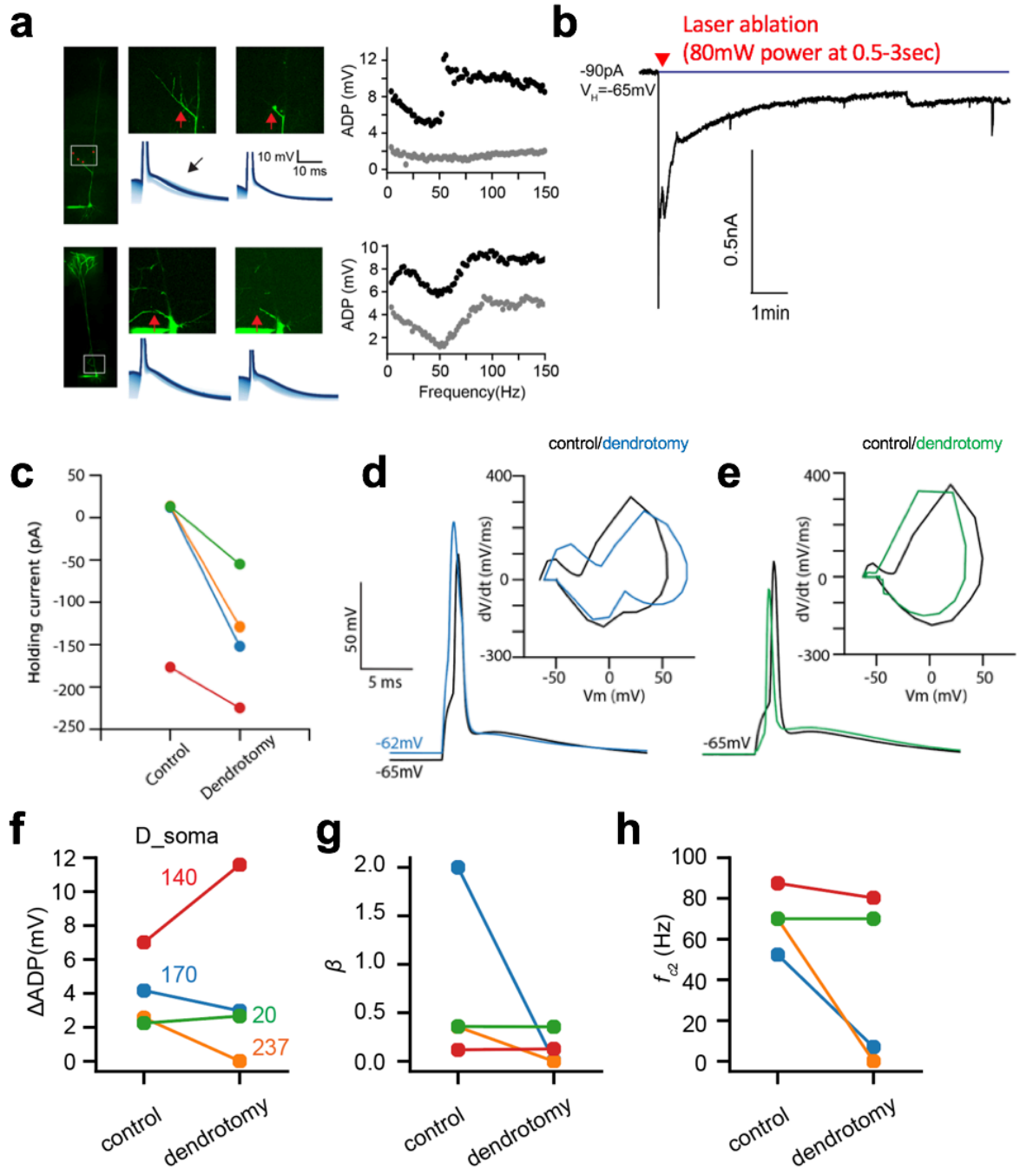

Figure 4.7 The effect of cutting oblique dendrites with the after-depolarizing potentials. **a,** The sample two-photon images of the neuron with the corresponding after-depolarizing potential before and after laser ablation of an oblique dendrite. **b,** The changes in the holding current, AP, and AP threshold of the recorded neuron before and after dendrotomy. **c,** The voltage-clamp recording of the membrane current with the laser ablation showing resealing of the membrane after 10mins. **c,** A pair plot of the amplitude, β, and critical frequencies of the ADP of four neurons (red, green, blue, and yellow) before and after dendrotomy. The distance of the targeted oblique from the soma is indicated next to the data.

4.5 Discussion and summary

Fast sodium spikes have been reported in the apical obliques of CA1 pyramidal neurons (Losonczy and Magee, 2006); however, whether oblique branch spikes could be generated in L5PNs is unknown. The thin diameter of oblique dendrites makes it difficult to probe the presence of oblique branch spikes with conventional patch-clamp recordings (although see Figure 3 in Kamondi et al. (1998)). I investigated the generation of oblique branch spikes in thin oblique dendrites of L5PNs *in vitro* using our 2P multi-site detection system.

Non-linear increase in the fluorescence calcium signals at oblique dendrites and after-depolarizing potentials were observed with low frequency bursts of bAPs using the critical frequency protocol. Calcium imaging showed non-linear ($\beta > 0.3$) increases in intracellular calcium with f_{c2} = 57±5 Hz burst of a 2-bAP in select oblique branches, indicating of an oblique branch spike (as also captured in the multi-compartment model presented in Chapter 2). The occurrence of this oblique branch spike was heterogeneous did not show any relation with O#, D_soma, or D_trunk. ADP measurements at the soma also recovered two distinct critical frequencies, with f_{c2} = 72±4 Hz and f_{c4} = 82±3 Hz for 2- and 4-AP trains, respectively. The step increase in the ADP was not mediated by NMDA receptors. Taken together, these results provide experimental evidence of oblique branch spikes in L5PNs *in vitro*. Furthermore, there is 1/3 probability that an L5PN would exhibit an oblique branch spike and a Ca^{2+}-AP at the nexus of the apical trunk which would be seen in its critical frequency (f_{c2} and f_{c4}).

With dendrotomy, the removal of oblique branches may have been enough to abolish the step-increase in the ADP. From the preliminary recordings (N = 4), it remains uncertain if dendrotomy of oblique branches indeed caused changes in the ADP considering dendrotomy also altered the excitability and health of some cells (i.e., cells became more depolarized). With fine tuning of optical parameters to keep the changes in the holding current to a minimum and additional experiments, dendrotomy can be a potential tool to interrogate a possible causal link of oblique branch spikes with the ADP as discussed in **Chapter 2**.

Calcium imaging, dendrotomy, and multi-compartment modelling revealed that this oblique branch spike occurs only in a few (1 to 2) oblique branches. Based on the L5PN model in **Chapter 2**, the branch-specific response can be attributed to the efficacy of bAP invasion in oblique dendrites. One factor that affects bAP propagation along the dendritic tree is the dendritic morphology. *In vitro* patch-clamp recordings (Kim and Connors, 1993; Stuart and Sakmann, 1994; Williams and Stuart, 2000; Gasparini, 2011) and voltage imaging (Antic, 2003; Grewe et al., 2010) in L5PNs show activity, morphology, and distance-dependent

attenuation of bAPs. Studies using multi-compartmental models indicate that this attenuation is due several factors such as: extent of dendritic branching, number of branch points, branch point tapering, changes in dendritic diameter, and leaking of currents from the main apical trunk to the oblique dendrites (Vetter et al., 2001; Migliore et al., 2005; Ferrante et al., 2013). Aside from branching patterns, other works have also shown that the heterogeneous distribution of A-type potassium channels, which opposes membrane excitability and are expressed at high levels in the dendritic tree, impact on bAP invasion of oblique dendrites (Hoffman et al., 1997; Frick et al., 2003; Gasparini et al., 2007; Zhou et al., 2015). Thus, regulation of bAP invasion at the obliques by dendritic branching pattern and heterogeneous expression of A-type potassium channels may explain branch specificity of dendritic spikes in different oblique dendrites in L5PNs.

In summary, the result of this chapter adds to the set of frequency-dependent activation of dendritic spikes across different parts of the neuron (**Figure 4.7** on the next page). The Ca^{2+}-AP at the nexus of the apical tuft are recruited via a train of bAPs with f_{c4} ~100 Hz (Larkum et al., 1999). Calcium spikes at distal segments of the basal dendrites are generated with AP trains at critical frequencies of f_{c3} ~120 Hz (Kampa and Stuart, 2006). In this Chapter, I reported that low frequency (f_{c2} = 57±5 Hz, from calcium imaging, or f_{c2} = 72±4 Hz, from ADP) 2-AP train generated an oblique branch spike in L5PNs. These critical frequencies are well within the frequencies of high-frequency (f = 330±10 Hz) burst firing of action potentials in these thick-tufted L5PNs (Chagnac-Amitai et al., 1990; Amitai et al., 1993; Williams and Stuart, 1999). Oblique branch spikes could well be another computational tool that participate in the dendritic processing inputs (possibly the thalamic inputs in layer 4 and intercortical inputs from neighbouring L5PNs) arriving at the proximal (oblique regions) of L5PNs.

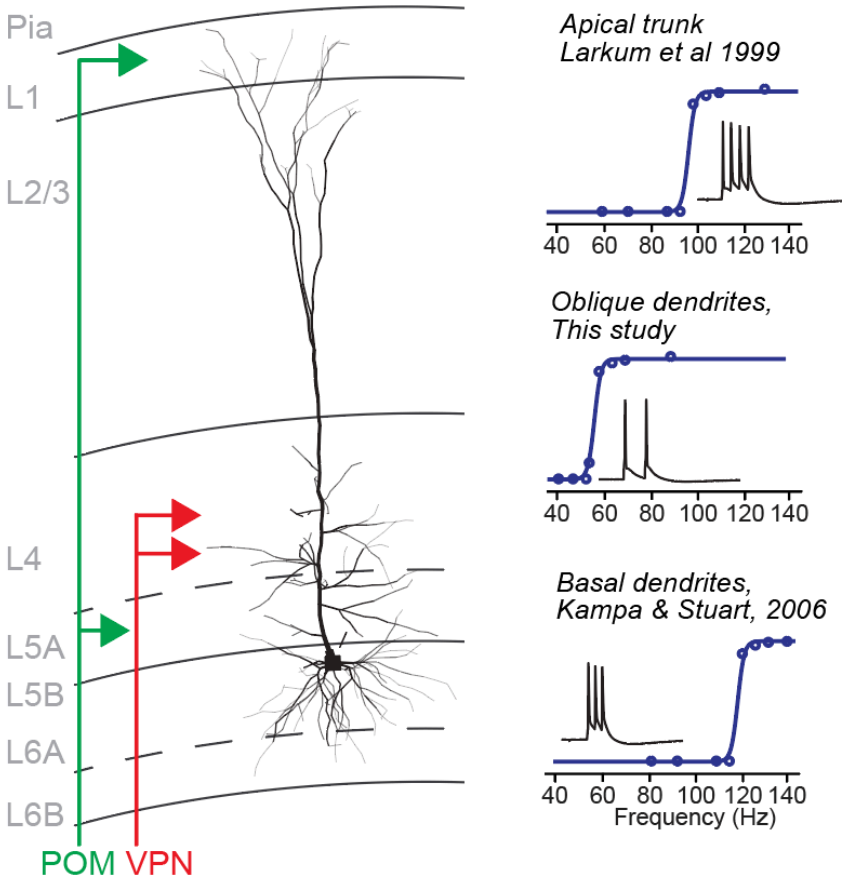

Figure 4.8. Critical frequency responses at different dendritic regions. Previous works showed a critical frequency response at the basal and nexus of the apical tuft dendrites. The critical frequency protocol showed that a f_{c4} ~100 Hz AP train recruits a dendritic Ca^{2+}-AP at the nexus (Larkum et al., 1999). A critical frequency response was also reported to be exhibited at distal segments basal dendrites at f_{c3} = 120-200 Hz AP train recruiting a mix of sodium (Nevian et al., 2007) and calcium spikes (Kampa and Stuart, 2006). This work shows that oblique branch spikes are evoked at select oblique branches at f_{c2} ~60 Hz train of APs.

Chapter 5. Development of techniques to enhance calcium and voltage imaging on dendrites.

5.1 Introduction

Functional imaging using voltage and calcium indicators facilitates optical readout of dendritic activity of thin dendrites. As discussed in **Chapter 3**, several works using calcium and/or voltage imaging have been used to record dendritic spikes and bAPs at the apical trunk as well at thin basal and oblique dendrites (Larkum et al., 1999; Antic, 2003; Kampa and Stuart, 2006; Canepari et al., 2007; Katona et al., 2012; Popovic et al., 2015). Calcium imaging offers high signal-to-noise ratio (SNR) by reporting the changes in the intracellular calcium (Grienberger and Konnerth, 2012). Unfortunately, the combination of multiple intracellular calcium sources and slow changes in calcium concentration (~200 ms) requires interpolation techniques (e.g., shift-mean algorithm (Rama, 2015)) to correlate calcium transients with bAPs. On the other hand, the temporal resolution of voltage imaging can report the time course of fast changes in the membrane potential (such as bAPs), but suffers from a low SNR. The thin membrane (~4 nm) makes it challenging to pack or co-locate a sufficient number of fluorescent voltage indicators that sense changes in the electric field across the membrane (Peterka et al., 2011). Thus, there is a continuing development of more sensitive indicators as well as optical approaches to perform calcium and voltage imaging of small neuronal structures (such as spines and dendrites) or neuronal populations (Fromherz et al., 2008; Yan et al., 2012; St-Pierre et al., 2014; Gong et al., 2015; Popovic et al., 2015; Antic et al., 2016; Roome and Kuhn, 2018).

In line with these developments, we initially proposed a 2P multi-site fluorescence detection system (as described in **Chapter 3**), which offers simultaneous illumination onto the sample and parallel detection of fluorescence from different sites. The technique has proven useful to analyse the generation of oblique branch spikes along apical obliques (as presented in **Chapter 4**). Such patterned illumination/detection can therefore be used for functional imaging either via calcium or voltage indicators. However, by conservation of energy, the intensity of each focus decreases as the number of foci is increased (Daria et al., 2009). Due to the non-linearity of 2P excitation, the fluorescence per site drops by a factor of $\sim 1/N^2$, where

N is the number of sites. Another factor to consider is the exposure of the sample to the laser beam. Unlike in laser-scanning microscopes where the beam's focus illuminates a point on the sample for a short dwell time (~ 4µs with resonant scanner coupled with regular galvo mirror at 30 frames/sec, (Schultz et al., 2017)), the multi-foci pattern in holographic projection constantly exposes the sites on the sample throughout the recording. Increasing the incident laser power can provide higher fluorescence intensity from each focus, but higher power also increases the photon flux and local heating, which can cause photo-damage on the tissue (Podgorski and Ranganathan, 2016). Thus, there is a need to efficiently excite fluorescence from each site while maintaining low photon flux to minimize photo-damage.

In this chapter, I present two spatio-temporal excitation modalities to improve the SNR namely: (1) temporal gating of the excitation laser for multi-site 2P functional calcium imaging; and (2) voltage imaging single-photon excitation by scattered photons (1PESP). These two techniques are currently under development in our laboratory. The aim is to characterize and implement these techniques for future functional imaging on dendrites. To improve the SNR in the multi-site functional calcium imaging method, I incorporated a temporal gating technique as an approach to improve the fluorescence yield of our 2P multi-foci excitation. As a proof-of-principle experiment, we tested the temporal gating technique by recording calcium transients in neuronal cultures. To improve the SNR in the functional voltage imaging, I describe the 1PESP technique, which is a unique excitation protocol that resulted in a 1.8fold SNR enhancement in the recorded voltage transients.

5.2 Chapter aims

This chapter aims to: (1) characterize the enhancement in the SNR of multi-site functional calcium imaging via temporal gating; and (2) present a novel oblique illumination technique, 1PESP, as applied to functional voltage imaging to analyse the invasion of bAPs in thin oblique and basal dendrites.

5.3. Temporal gating for efficient calcium imaging

An approach to improve the fluorescence yield in 2P excitation is via temporal gating where the excitation beam is modulated at a lower gating rate (~0.5 MHz) to maintain a low average power but with a compensatory increase in the peak power. Aside from the high-peak powers,

delaying the pulsed excitation of fluorophores long enough for its triplet state to relax between two pulses has been shown to enhance fluorescence yield and prevent photo bleaching as applied in 1P (Donnert et al., 2009) and 2P excitation (Donnert et al., 2007). Here, we utilized the temporal gating technique with 2P excitation to improve the fluorescence yield and SNR of recorded calcium transients using the 2P multi-site holographic fluorescence detection system (Castanares et al., 2016).

5.4 Method for implementing multi-site functional calcium imaging with temporal gating

5.4.1 Mathematical basis of fluorescence enhancement with temporal gating

In this section, I present a mathematical derivation of the improvement in the fluorescence yield with temporal gating. Multiple foci in a single *z*-plane are generated using prism phase maps encoded on the SLM (see **Equation 3.1**). The 2P fluorescence, $F(r)$, generated from each focus at radial distance r from the optical centre is given by,

$$F(r) = \alpha P(r)^2, \tag{5.1}$$

where α accounts for all the relevant quantities (*e.g.* dye concentration, 2P cross-section, numerical aperture of the focusing lens, etc) for generating 2P fluorescence from a single foci (Xu and Webb, 1996).

With a temporally gated beam, we set an incident beam with an "on" state within a bunch width, τ, while the "off" state is given by $f_R^{-1} - \tau$, where f_R is the gating frequency. From **Equation 5.1**, the time-averaged 2P fluorescence per foci, $\langle F(r) \rangle$, within an exposure time, T_O, is given by

$$\begin{aligned} \langle F(r) \rangle &= \frac{1}{T_0} \int_0^{T_0} F(r)dt \\ &= \frac{1}{T_0} \left(\int_0^{\tau} F(r)dt + \int_{\tau}^{T_o} F(r)dt \right) \\ &= f_R(\tau \cdot F(r)) + 0 \end{aligned} \tag{5.2}$$

where $f_R^{-1} = T_O$. Since light is only gated within 0 to τ, the second term vanishes and the fluorescence from temporally gated beam observes a linear relationship with the duty cycle, τf_R .

Prior to holographically dividing the beam, the laser is temporally gated and from conservation of energy, the time-average laser power, $\langle P_{\text{out}} \rangle$, (within f_R of the temporally gated beam is given by:

$$\langle P_{\text{out}} \rangle f_R^{-1} = \tau \langle P_{\text{in}} \rangle \quad \textbf{(5.3)}$$

where $\langle P_{in} \rangle$ is the average power within the "on" state, τ, used for generating 2P fluorescence. For an ungated beam, $\tau = f_R^{-1}$ sets $\langle P_{out} \rangle = \langle P_{in} \rangle$. On the other hand, for $\tau << f_R^{-1}$ then $\langle P_{out} \rangle << \langle P_{in} \rangle$, which results in a low average power but with high $\langle F(r) \rangle$ set by $\langle P_{in} \rangle$. Therefore, within the exposure time T_O, the average excitation laser before holographically dividing the beam is $\langle P_{out} \rangle$ and its relation with $\langle F(r) \rangle$ is derived by combining **Equations 5.2** and **5.3**, which results to

$$\langle F(r) \rangle = \alpha \left(\frac{1}{\tau f_R} \right) \left[\delta(r) \frac{\langle P_{\text{out}} \rangle}{N} \right]^2 . \quad \textbf{(5.4)}$$

Because of the non-linear relationship of the fluorescence with the input power $\langle P_{in} \rangle$ described in **Equation 5.1**, we see an improvement in the fluorescence by a factor of $1/(\tau f_R)$. In the experiments, we enhance the average fluorescence, $\langle F(r) \rangle$, by maintaining a low average output power per site, $\langle P_{\text{out}} \rangle / N$, using different gating frequencies, f_R.

5.4.2 Holographic 2P microscope with an acousto-optic modulator (AOM)

As proof-of-principle experiment, we constructed a simpler version of the microscope presented **Chapter 3** (**Figure 5.1**) without electrophysiological capabilities. This holographic system is equipped with an AOM device to temporally gate the excitation laser and a blue LED source for wide-field 1P epifluorescence imaging.

The system utilized a femtosecond Ti:S laser (Coherent MIRA 900 pumped with a 12 W Coherent Verdi G) for 2P excitation set at λ = 800 nm. An AOM (AA Opto ST110-A1-B4) driven by a radio-frequency driver (AA Opto-MODA110-B4-33, τ = 140 ns pulse width, and a gating frequency, f_R, set to 0.8 and 1.6 MHz) modulated the pulsed NIR beam. The temporal gating frequencies were chosen from prior work of Gautam et al. (2015), which showed minimal photo-damage (as indicated by < 10% change in the input resistance of the neurons). The laser beam was expanded 4x ($L2/L1$ = 200mm/50mm) and was projected to a reflective phase-only SLM (Meadowlark Optics XY-512). A half-wave plate was placed before the beam

expander to align the beam polarization with the preferred polarization angle of the SLM to achieve the maximum diffraction efficiency. The SLM was encoded with a phase-only hologram, which shaped the beam's wavefront to produce multiple foci at the Fourier plane of lens, *L3* (f = 150 mm). Lens *L4* (f = 300 mm) and the objective lens (*OL*, Carl Zeiss 20x, *NA* = 1.0) formed a 4f-lens configuration to relay the optical field at the Fourier plane (of *L3*) to the sample plane of *OL*. A dichroic mirror, *DM1*(Thorlabs FM202), reflected the NIR excitation laser towards the *OL* and transmitted the collected fluorescence towards the tube lens (*L5*, f =200mm) and the CMOS camera (Thorlabs DCC3240M, ~60% quantum efficiency at λ = 550 nm). A short-pass filter (FES700, Thorlabs) was placed before the camera to filter the laser beam. We also incorporated a single-photon epifluorescence path that consisted of an LED operating at a wavelength of λ = 470 nm (Thorlabs M470L3), lens (*L6*, f = 125 mm), and a dichroic mirror (DM2, Thorlabs DMLP490R). Due to slight systematic optical misalignments, we encoded aberration corrections represented by Zernike polynomials, $Z(n, m)$, (2nd-order astigmatism, $Z(2, 4) = 8$, and spherical aberration, $Z(0, 4) = 6$).

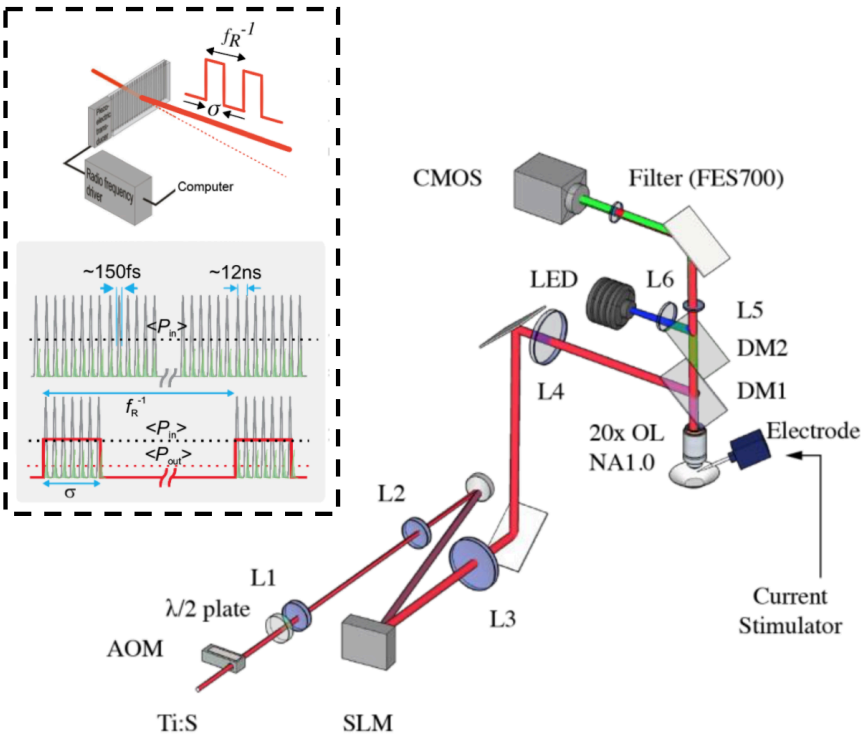

Figure 5.1 A two-photon holographic microscope with an acousto-optic modulator for temporal gating. The schematic diagram shows a custom-built two-photon holographic microscope with an epifluorescence capability to allow for either 2P multi-site or wide-field 1P imaging. Inset, an illustration of how the femtosecond pulses (80 MHz cycle) are bunched into an envelope wave with a period of f_R^{-1} using an AOM. We define the following as follows: L1-L6 are lenses, Ti:S is the titanium Sapphire femto-second laser, SLM is the spatial light modulator, DM1-DM2 are dichroic mirrors, CMOS is the camera, OL is the objective lens.

5.4.3 Calibration with Fluorescein dye

We prepared 10 mM of Fluorescein dye solution in a 100 μm-thick well mounted on a glass slide to measure the relationship of the fluorescence with the average power per focus using an ungated and temporally gated beam (f_R = 0.8 and 1.6 MHz). The holographically projected multiple foci were positioned at the sample plane. The fluorescence was captured at 20 frames per second with 50 ms exposure time. The CMOS camera (DCC3240C, Thorlabs) was set with 3.0x sensor gain, 2x2 binning, 120 black level offset and a region of interest (480x336 pixels) covering the area where the spots are projected. The fluorescence images as a function of time were analysed using a script in ImageJ (National Institute of Health). Within each image, we selected 5x5 pixels to measure the average grey levels of each focus as a function of time. The signal to noise (SNR) per spot was determined for the ungated and temporally gated beam with 2 to 6 mW average power per focus. The average power under the objective was measured with a power meter (PM100A with S130C sensor, Thorlabs).

5.4.4 Calcium imaging on cultured hippocampal neurons

We performed fluorescence calcium imaging on primary hippocampal neuronal cultures (Days In Vitro, DIV 26-33) using temporally gated beam (see **Chapter 3**, **Section 3.3.3** for the culture preparation). On the day of imaging, the cultures were bathed in 10 μM Cal-520 (AAT Bioquest, CA) in culture medium for 15 mins. The cultures were then washed with culture external medium, consisting of (in mM): 125 NaCl, 3 KCl, 2 $CaCl_2$, 1 $MgCl_2$, 25 HEPES and 10 D-Glucose, for 30 mins.

To determine the locations of the neurons, the sample was first imaged with blue light via the single-photon epifluorescence path of the microscope. Neurons were identified as elongated cells about 10 μm in diameter and exhibit higher levels of baseline fluorescence compared to their glial neighbours. Based from the wide-field image, eight foci were positioned on the somas and dendrites of neurons. An extracellular bipolar electrode was placed near the recorded region to stimulate neuronal activity and correspondingly trigger calcium transients from the neurons. A train of current pulses (15 μA, 100 ms pulse at 0.5 Hz) was delivered by a custom-built current stimulator. The stimulator and acousto-optic modulator were triggered using a digital acquisition (DAQ) device (PCI-6363, National Instruments). The fluorescence from the holographically projected sites was captured at 20 Hz (50 ms exposure time) for 10 seconds with the CMOS camera (DCC3240C, Thorlabs).

5.4.5 Data Analysis

The raw fluorescence signals were analysed in MATLAB (Mathworks). The signal-to-noise ratio of each site was calculated as,

$$SNR(r) = \langle F(r) \rangle / \sigma \qquad (5.5)$$

where $<F(r)>$ was measured from the camera's grey level (8-bit) readings after background subtraction and $\sigma = ({\sigma_{on}}^2 + {\sigma_{off}}^2)^{1/2}$ is the quadrature of the standard deviation of the fluorescence, σ_{on}, and the dark noise, σ_{off}, following a normal distribution. The noise fluctuation distribution was verified to follow a normal distribution (chi-square goodness of fit test at 5% significance level of rejection, MATLAB).

The SNR and slope ($<P>/N$, average power per site) values are sample averages (mean ± S.E). The improvement in SNR was determined by taking the normalized value of the SNR at a given gating frequency relative to the ungated beam. The SNR with temporal gating were compared to that of an ungated beam using paired sample t-test (ns, $p > 0.05$; *, $p \leq 0.05$; **, $p \leq 0.01$, ***, $p \leq 0.001$, in *R* programming language).

The calcium activity was visualized with the relative change in the fluorescence, which is calculated as,

$$\frac{\Delta F}{F} = \frac{F(t) - \langle F_b \rangle}{\langle F_b \rangle_{\max}} \qquad (5.6)$$

where $<F_b>$ was the baseline fluorescence just before the first triggered fluorescence activity, $<F_b>_{\max}$ was the maximum of the pooled baseline fluorescence from all sites. The relative change in the fluorescence traces were further filtered with wavelet denoising (first order db1 wavelet, Matlab).

5.5 Preliminary results showing improved fluorescence yield and SNR with temporal gating

We first compared the fluorescence yield of eight holographically generated foci of temporally gated and ungated beam incident in a chamber with Fluorescein dye for a pre-set average power per site. A time-series and histogram of the fluorescence at $<P_{out}>/N$ = 2 to 6 mW for temporally gated and ungated beam are shown in **Figure 5.2a**. Note that $<P_{out}>/N$ is an approximate measure of the average power per focus. Also, note that the spread of $<F(r)>$ measured for each $<P_{out}>/N$ considers differences in excitation average power per focus due

to $\delta(r)$ in (**Equation 3.2 in Chapter 3**). **Figure 5.2b** shows the relationship of the fluorescence with $\langle P_{out} \rangle / N$ in a log-log plot with base 2. The slopes (1.9±0.1, 1.79±0.08, 1.82±0.05 for 0.8 MHz, 1.6 MHz, and ungated beam, respectively) are in good agreement with a two-photon excitation process (slope = 2.0). The fluorescence signals from 0.8 MHz and 1.6 MHz temporally gated beam were 6.7 ($p < 0.001$) and 3.7 ($p < 0.001$) fold higher compared to the ungated beam. Using chi-square goodness of fit test (at 5% significance level of rejection, Matlab), we verified that 93% (167/180) of the fluctuation in the fluorescence followed a normal distribution (**Figure 5.2c**).

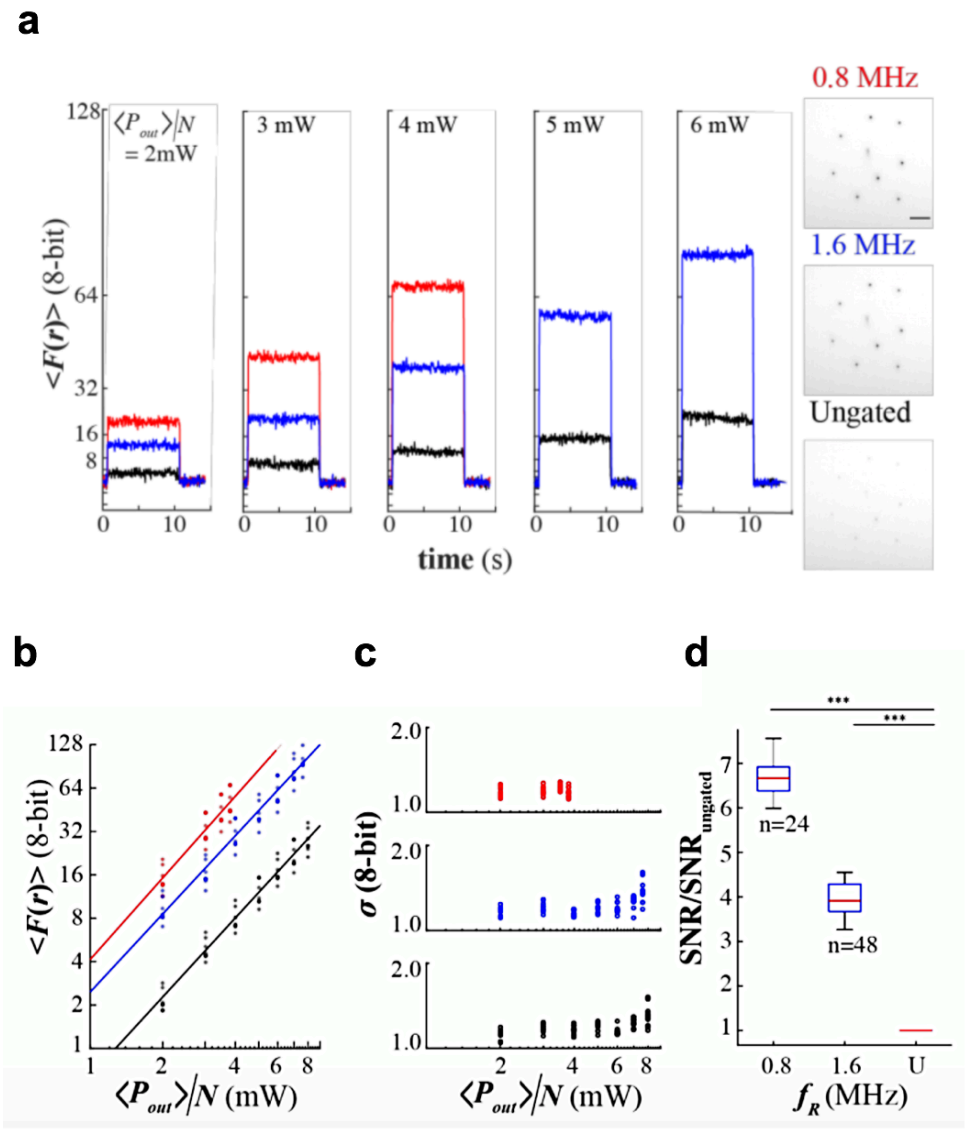

Figure 5.2 The increase in fluorescence yield from holographic sites with temporal gating. **a,** Sample time-series across $\langle Pout \rangle / N$ ~2 to 6 mW for ungated and temporally gated beam and sample negative images of the fluorescence from the holographic sites at $\langle P \rangle / N$ = 4 mW. **b,** The plot of fluorescence of each site with power. **c,** The fluctuations of the fluorescence with power. **d,** The pooled SNR of each site for gated beam (f_R = 0.8 and 1.6 MHz) relative to the SNR of the ungated beam (U). Figure taken from Castanares et al. (2016).

We used Gaussian statistics to describe the fluctuations in the fluorescence. It was observed that the standard deviation showed a weak correlation (max slope 0.17±0.02, ungated beam) with power, which may be due to the laser noise. Next, we determined the pooled ratio SNR of the temporally gated beam with respect to the ungated beam shown in **Figure 5.2d**. We observed 6.6±0.1 and 3.9±0.1fold increase in the SNR for 0.8 and 1.6 MHz, respectively.

We then applied temporal gating for imaging calcium activity of cultured hippocampal neurons loaded with Cal-520 AM dye. Triggered activity was evoked by applying a train of current pulses using an extracellular bipolar electrode near two neurons of interest (**Figure 5.3a**). Eight foci were positioned at the somas and dendrites of two neurons. Site one was placed outside the two neurons and its fluorescence was used to subtract the correlated noise with the other sites. The raw traces in **Figure 5.3b** shows that the temporally gated beam yielded higher fluorescence than the ungated. In addition, triggered calcium activity was observed. A sample trace of the triggered calcium activity with 0.8 MHz temporally gated beam is shown in **Figure 5.3c**. Except for site 4, the six other sites showed fast fluorescent transients (~500 ms time constant) that were well timed with the current. The pooled SNR (48 samples from $\langle P_{out} \rangle / N$ ~3, 4, and 6 mW) increased by 3.9±0.4 ($p < 0.0001$) and 3.7±0.3 ($p < 0.0001$) for 0.8 and 1.6 MHz temporally gated beam, respectively (**Figure 5.3d**).

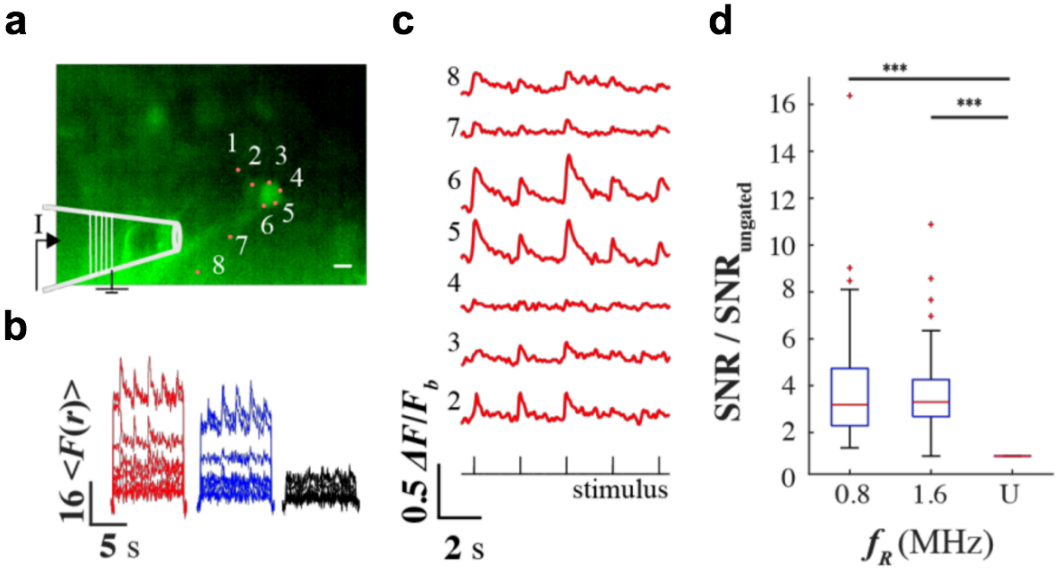

Figure 5.3 Enhancement of SNR with temporal gating. a, Fluorescence image of the neuronal cultures loaded with Cal-520 dye with eight holographically projected two-photon sites. **b,** Time-series plot of the fluorescence of each site for ungated and temporally gated beam at 4 mW average power. **c,** $\Delta F/F$ under 0.8 MHz and 4 mW temporally gated beam. **d,** Pooled SNR ratio of the temporally gated beam relative to the ungated beam. The scale bar is 10 μm. Figure taken from Castanares et al. (2016).

5.6 Voltage imaging using single-photon via scattered photon illumination (1PESP)

Voltage imaging is a promising tool to record rapid changes in the membrane potential and can be useful to understand the generation and propagation of dendritic spikes. However, the low SNR of voltage indicators limits its applications. For example, electrochromic voltage-sensitive dyes exhibit ~1% dF/F optical response from the shift in absorption and emission spectrum during a voltage spike. These electrochromic voltage-sensitive dyes (VSDs) exhibit fast temporal response which can record fast spikes waveform such as APs and dendritic spikes.

While temporal gating could effectively improve the SNR as discussed in the previous section, the main issue with using VSDs is not due to low fluorescence yield. In fact, VSDs produce bright fluorescence but the low optical readout (dF/F) is due to the following issues: (1) the small Stark shift in most electrochromic VSDs; and (2) the small fraction of VSD molecules that are bound to the cellular membrane that report changes in the electric field. The first issue makes it difficult to find an appropriate 2P excitation wavelength to observe the small Stark shift in the VSD's spectral response with changes in membrane potential. However, by 1P excitation using a monochromatic light with appropriate energy specifically tuned to the rising or downward curve the VSD's absorption spectrum, the Stark shift associated with changes in membrane potential can be observed. The second issue results in low SNR due to the fact that only a small fraction of the molecules reports the changes in membrane potential. The responding VSDs, those that bind to the 4nm plasma membrane, respond to the changes in the electric field during a voltage transient and report the membrane activity. On the other hand, bulk of the fluorescence comes from non-responding VSDs or those that bind to intracellular structures, which do not respond to voltage transients in the membrane. Non-responding VSDs contribute to the overall baseline fluorescence and shot noise in the recording. The small fraction of VSDs that are responding to changes in membrane potential results in a high background fluorescence signal and minimal transient response of ~1% dF/F.

We hypothesize that a way to improve the SNR is to limit the excitation only to the responding VSDs and lessen the fluorescence of non-responding VSDs. Direct single-photon illumination on neurons loaded with VSDs produces a high background fluorescence signal which can saturate the sensor. We propose a unique method to reduce the baseline fluorescence and increase the response by restricting the illumination only at the edge or boundary of the neuron (see **Figure 5.4** below). Instead of direct illumination, the beam focus is placed on the

neuropil beside the cell of interest. The scattered photons from the focus of excite the VSDs that are situated at the membrane boundary. Indirect oblique illumination of the sample also reduces the probability of photo-damage or heating as the light is only illuminating the neighbouring tissue. In addition, the reduced fluorescence from the unresponsive VSDs lowers the baseline fluorescence which then maximizes the use of the gain of a multi-channel sensor such as an EMCCD camera. From here on, I refer to this indirect oblique illumination as "single-photon excitation by scattered photons (1PESP)".

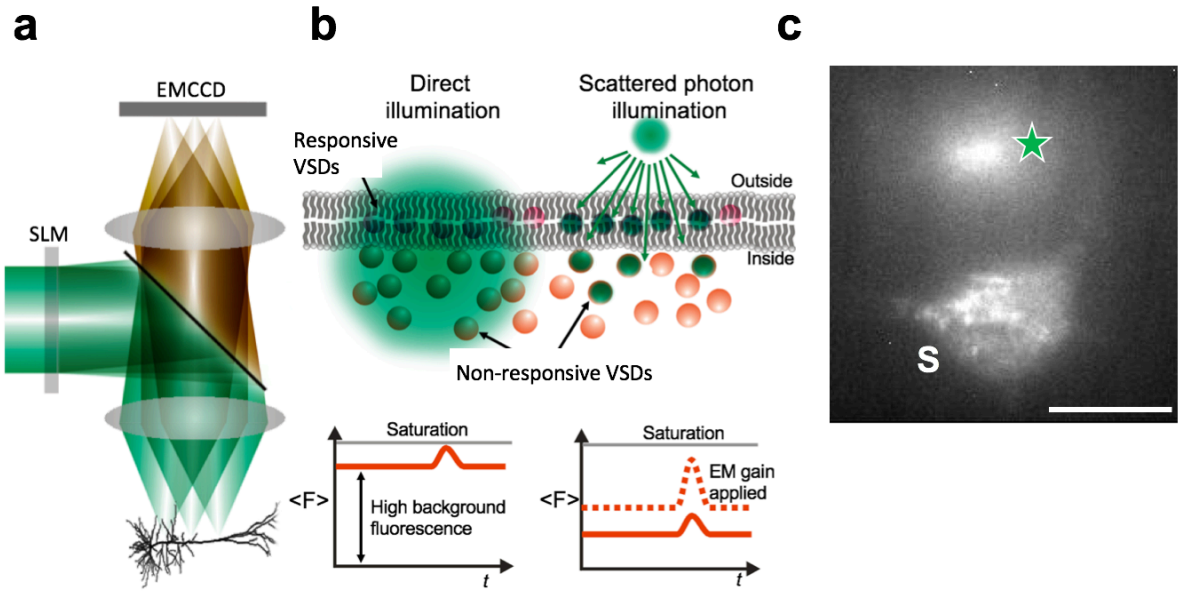

Figure 5.4 An illustration of the 1P-ESP. a, The scattered photon excitation uses a single- or patterned illumination of the excitation beam. The fluorescence is recorded by a fast EMCCD camera. **b,** An illustration of the proposed enhancement with 1P-ESP by reducing the background fluorescence from non-responsive voltage-sensitive dye molecules (VSDs) and limiting mostly to exciting the responsive VSDs with the scattered photon illumination on the neighbouring neuropil. Enhancement is made with the use of the EM gain of the camera. **c,** A sample image of the oblique illumination where the 532 nm beam focus (★) was positioned at ~5 µm from the soma (S) of the neuron loaded with JPW-1114 VSD. The scattered light produced highly heterogeneous fluorescence at the membrane surface of the soma which could be the responsive VSDs. Scale bar is 5µm.

5.7 Method for implementing 1P-ESP

5.7.1 Intracellular loading of JPW-1114 voltage indicator

We prepared 300-µm thick coronal slices at the primary somatosensory cortex as described in **Chapter 3, Section 3.3.3**. A voltage indicator JPW-1114 was intracellularly loaded in L5PNs via a patch pipette following previous loading protocols (Stuart and Palmer, 2006; Popovic et

al., 2012). JPW-1114 are large molecules relative to the ions present in the intracellular solution. They tend to clump at the tip of the pipette which blocks the flow and causes undesirable pressure build-up. I paid close attention to two steps in the loading procedure to circumvent this problem. The first step was to prepare a stout pipette tip (with ~ 5-6MΩ open pipette resistance), which allowed good control of pressure in the pipette especially when the dye molecules start to clump at the tip (see **Table 5.1** for the micro-pipette puller settings). The stout pipette did not provide stable electrophysiological recordings but maintained good loading of the VSD into the cell. The second step was to introduce a small volume of dye-free intracellular solution at the tip to help form a good seal when setting up the patch. The intracellular solution was front-loaded first using a 20-mL syringe (pulling 1-5 mL air pocket) for 20 seconds. Then, the same electrode was back-filled with 0.8 mM JPW-1114 in intracellular solution. Microbubbles were carefully cleared inside the tip to avoid undesirable pressure build-up.

Table 5.1 Glass puller settings for 2.0mm OD glass capillaries

Time between pull: ~30mins, Heat ramp: 580 units				
Loop	Heat	Pull	Velocity	Time
1-3	580	-	31	250
4	572*	10	23	250
			Heat on	15.45-15.80s

Note: *Add to the heat ±3 units to make the tip size (smaller, +, or bigger, -)

Using micromanipulators, the dye-filled micro-pipette was quickly made to contact with the neuron to minimize spillage of the dye onto the neuropil. A whole-cell patch was established and the dye was allowed to diffuse into the soma for 30-45 mins. In some cases, during the loading, the series resistance substantially increased. This increase in the series resistance was often due to the clumping of the VSD at the tip changing the series resistance. To check for cell viability, 100 ms voltage-step was injected to see if action potential currents can still be evoked at the soma. If so, the patch was maintained until sufficient loading at the soma was observed. Otherwise, large clumps of the VSD prevented good dye loading into the cell, which made the cell unusable for voltage imaging. With successfully loaded cells, the electrode was retracted after one hour and the cell was incubated at 34 ^{o}C for 1-2 hours before repatching it with a standard pipette (not stout) loaded with intracellular solution without VSD.

During the incubation, I went on to load neighbouring neurons with the VSD using the same procedure.

To compare the extent of VSD loading into the dendrites, I present 2P reconstructed images of L5PNs. One L5PN was loaded with JPW-1114 while another L5PN was loaded with Alexa-Fluor 488 using the same loading procedure described above. VSD molecules are heavier than standard fluorescent morphology tracer dyes limiting the spatial extent of the loading (**Figure 5.5**). Alexa-Fluor 488 labelled the whole dendritic tree of the L5PN extending up to ~1 mm from the soma. On the other hand, the VSD (JPW-1114) labelled the soma and dendrites extending only up to 150-200 µm away from the soma. The VSDs bound to the membrane yield brighter fluorescence compared to the intracellular regions.

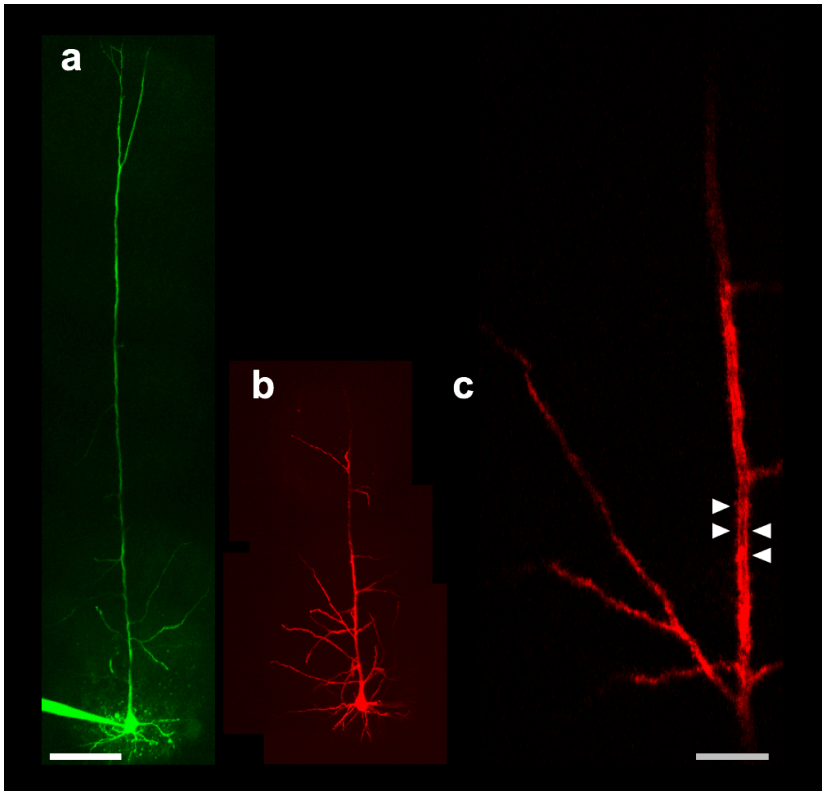

Figure 5.5 Comparison of the extent of loading of calcium and voltage indicators. Two-photon z-project image of the dendritic tree of L5PNs loaded with: (**a**) Cal-520 and Alexa Fluor-488, and (**b**) JPW-1114. Both were imaged at 890 nm and were taken at >1hr of loading. (**c**) Magnified view of the 2P image at the apical trunk showing strong fluorescence signal of JPW-1114 at the membrane. The scale bars on the left and right are 50, and 5 µm, respectively.

5.7.2 Integrated two-photon and single-photon holographic microscope

To perform voltage imaging via 1PESP, we integrated a 1P holographic projector into our existing holographic 2P multi-site detection system (**Figure 5.6**). A 1W diode-pumped solid state (DPSS) laser (λ = 532 nm) was expanded and projected onto a spatial light modulator (SLM, Hamamatsu) for encoding with a computer-generated phase hologram. Using 4f relay lenses, the phase-encoded beam is reduced back to its initial diameter (~2 mm) and coupled onto the system via the NIR scanning beam path for 2P microscopy.

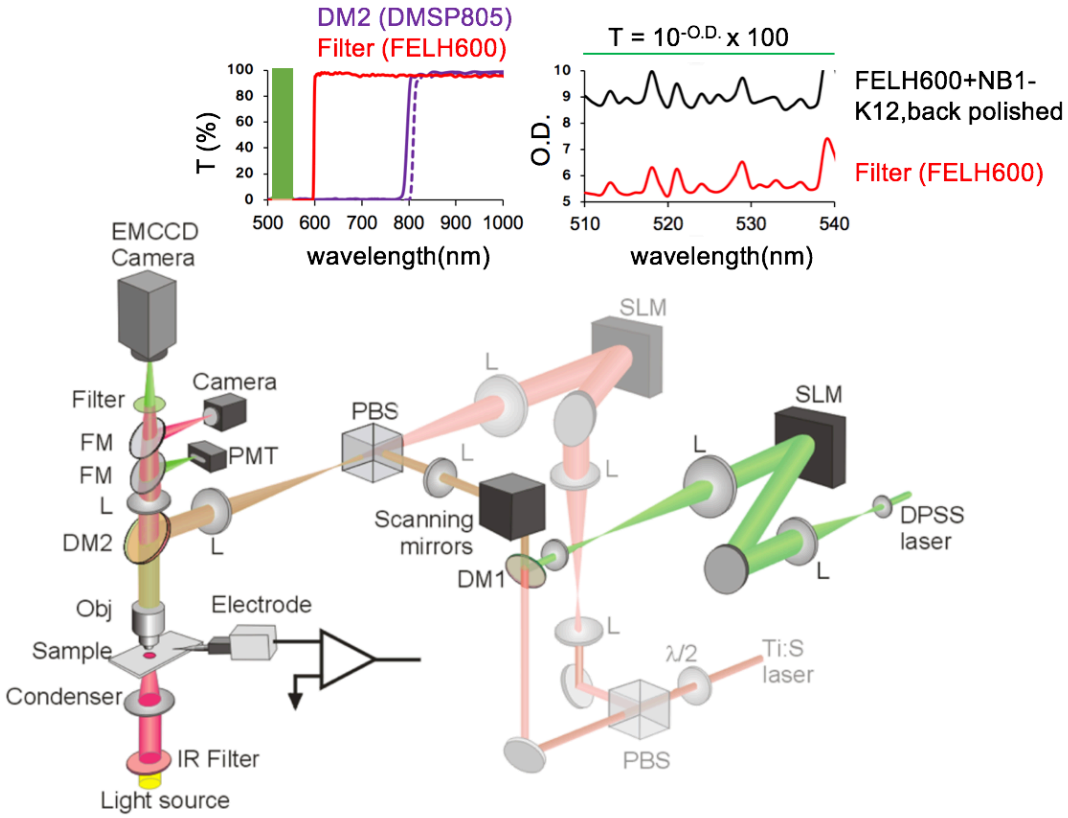

Figure 5.6 The single-photon holographic attachment integrated with our existing two-photon holographic and laser-scanning microscope. The use of a dichroic mirror (DMLP805) and a cascade of long-pass (FEHL600) and laser-line green filter (NB1-K12) was crucial in the design. The inset shows the transmission profile of dichroic mirrors and filters.

Coupling is achieved via a dichroic mirror, while the relay lenses set a conjugate image of the phase hologram onto the scanning mirrors. From the scanning mirrors, both the NIR and 532 nm beams were projected onto the objective lens with a short-pass dichroic mirror DM2 (DMSP805, Thorlabs) for optimal reflection of the NIR laser for 2P microscopy. Since DM2 is not optimized to reflect the 532 nm laser, rotating the polarization of the 532-nm beam with a half-wave plate maximized the reflection up to some extent (~10%). Since DM2 has been chosen to provide optimized illumination for 2P imaging, the 1P holographic module has an

overall power output of 0.4% onto the sample ($P_{objective}/P_{laser}$ = 0.8mW/200mW). This power was nonetheless was sufficient to excite the VSDs. On the detection side, several filters were used, which consisted of a back-polished laser-line mirror (NB1-K12 1064/532, Thorlabs) and 600 nm long-pass filter (FELH600, Thorlabs) to completely filter out the green excitation laser. The laser-line mirror results in an overall extinction of T~$1x10^{-9}$ % for 510-540 nm which strongly blocked the 532-nm beam. The fluorescence was acquired using an EMCCD camera (Ixon Ultra 897, Andor) with parameters: 0.0022 s (400 frames per second) exposure time, 50x EM gain, 128x128 pixel optically centred crop mode.

5.8 Preliminary results showing improved SNR with 1PESP

5.8.1 Signal-to-noise ratio with different regions-of-interest (ROIs)

To improve the SNR of the voltage responses, I first need to establish an appropriate ROI to use when extracting the time-series fluorescence data from the image sequence. From the setup, the camera captures the image containing fluorescence signals of the responding and non-responding VSDs. I compared the SNR with different sized ROIs namely: whole-field, user-defined covering a region of fluorescence (ROI1), user-defined tracing only the fluorescent segment (ROI2).

Figure 5.7 shows 2P images of two neurons loaded with JPW-1114 and the optically recorded membrane potential at the soma and oblique dendrites. The EMCCD camera acquired in- and out-of-focus fluorescence from the single-photon green excitation. For the same data, three different ROIs were drawn (e.g., whole-field: blue, ROI1: red, ROI2: green). Time-series data containing APs, bAPs, and 100 ms long hyperpolarization were observed. I compare the SNRs of the AP, bAPs, and the hyperpolarization extracted from the different ROIs (e.g., whole field, ROI1, ROI2). For large structures such as the soma, taking the whole-field ROI extracted the optical transient with the best SNR (SNR=16.1, **Figure 5.7a**). For thin dendritic structures where the fluorescence only fell on to a fraction of the total camera pixels, taking the whole-field (SNR = 15.3, **Figure 5.7b**) smoothened out the signal. In this case, a defined ROI that traced out the fluorescent regions yielded a better result (SNR = 22). Across different data sets, the average SNR were 8.22±0.7 (for a single bAP) and 0.94±0.08 (for the hyperpolarization) as shown in **Figure 5.7c**. The recovered SNR from different user-defined ROIs were similar to whole-field ROI (single bAP: $p = 0.47 > 0.5$, $p = 0.27 > 0.5$, hyperpolarization: $p = 0.10 > 0.05$, 1.5 >0.05, paired t-test). ROI2 yielded a slightly better SNR for responses in dendrites. In the

succeeding measurements, a user-defined ROI2 (a region tracing only the fluorescent segment) was used in extracting the responses from the image sequence.

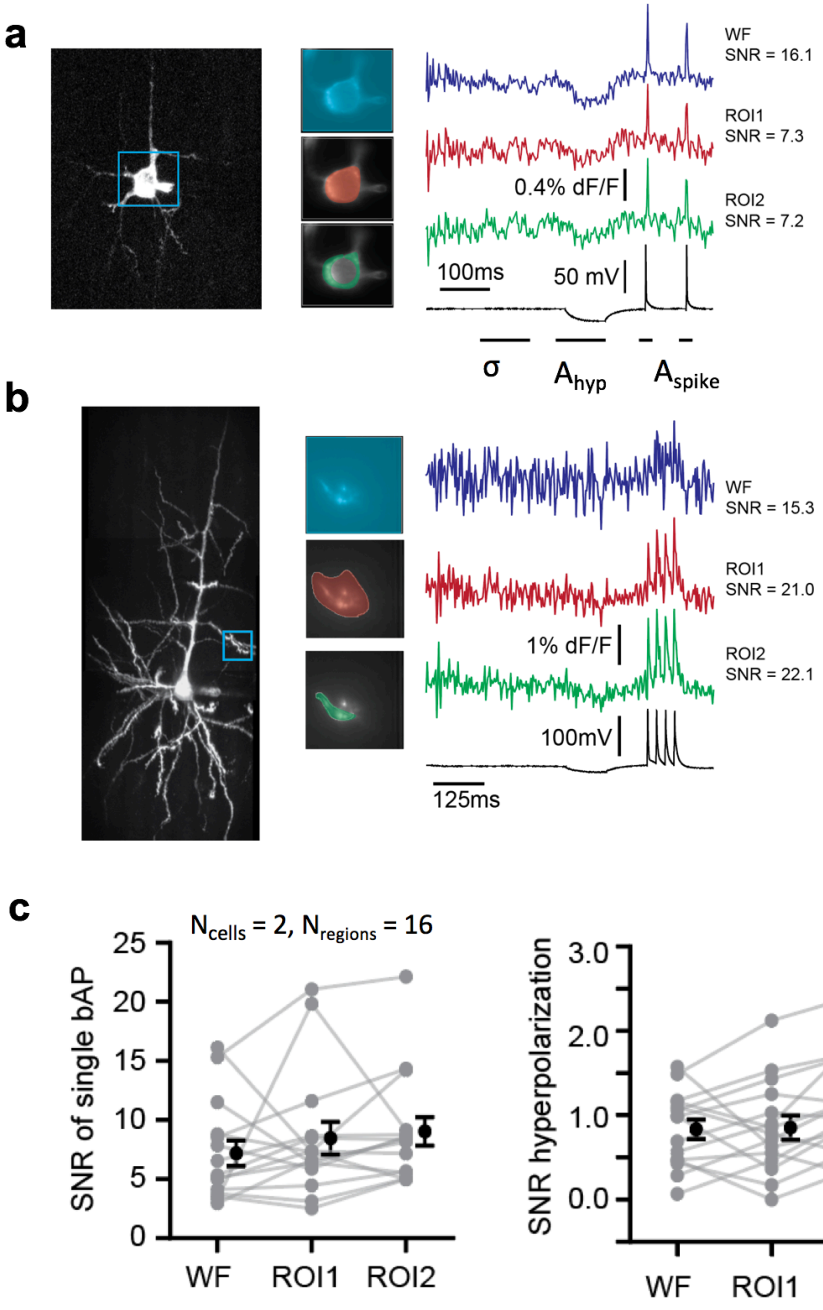

Figure 5.7 The recovered optical transients and the SNR of the spike and hyperpolarization for different regions-of-interest. a-b, The two-photon image of neurons loaded with VSD (0.8mM JPW-1114 via a patch pipette). Three different regions of interest namely: whole-field (blue), user-defined1 (ROI1, red) and user-defined2 (ROI2, green) were used and the resulting optical transient is plotted.**c,** Plots of the signal-to-noise ratio of a single bAP and hyperpolarization for the different drawn ROIs.

5.8.2 Improvement of SNR in the optical voltage recordings by 1P-ESP

Optical voltage recordings of bAPs along the apical trunk were made with different beam positions with respect to the dendrite. The position of the laser site was inferred by the line profiles of the fluorescence along the dendrite (see **Figure 5.8**). Locating the beam > |±2 µm| from the trunk produced uniform fluorescence signal; whereas, locating the beam close to the trunk (< |±2 µm|) produced a strong fluorescence signal from the boundary (see **Figure 5.8b**). The optical voltage transients were recovered from a fixed ROI (highlighted in yield box), which maintained the same mean fluorescence signal for different beam positions.

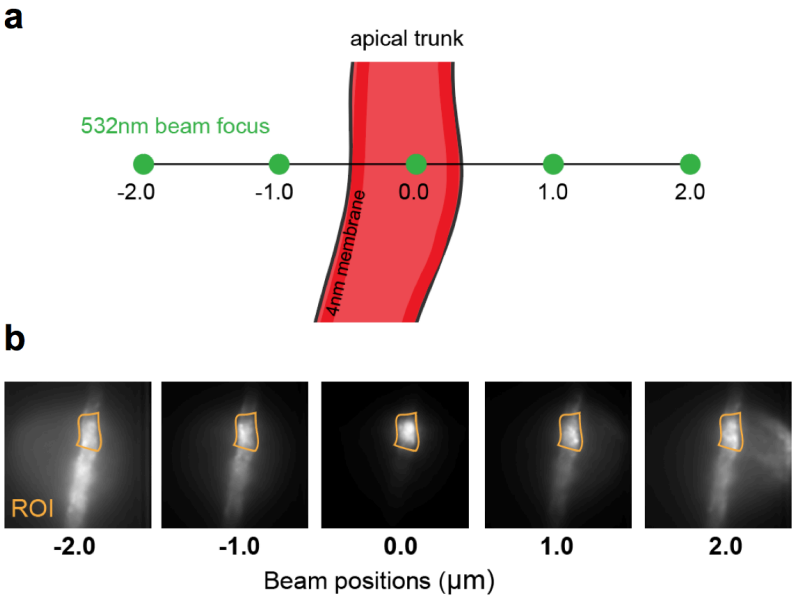

Figure 5.8 Differences in the fluorescence signal from apical trunk of a neuron loaded with VSDs with beam positions. a, A diagram of the line scan made across the apical trunk of the neuron loaded with JPW-1114 VSD. **b,** Images of an apical trunk with the 532-nm beam positioned at different locations at a time.

I compared the SNR of the optical traces recovered with different beam positions. **Figure 5.9** shows a 5-trial average response for different beam positions capturing bAPs along the trunk. A characteristic artefact was observed at the start of every recording possibly due to mechanical vibrations via opening of the beam shutters. A sufficient delay introduced before the current stimulus (t > 0.3 s) avoided the contamination of the artefact with the optical voltage spikes. The SNR is the ratio of the amplitude and baseline noise (SD) of the optically recorded voltage traces. When the beam is located at the centre of the dendrite (beam position = 0), the amplitude of the spike was low compared to that when the beam was located at +1 µm from the dendrite (see **Figure 5.10**). Moreover, SD in *win2* was minimal when the beam was positioned (< |±1 µm|) from the trunk. Taking the ratio, *A/(2*SD)*, the SNR is highest at 1 µm

position from the trunk, which shows a 1.8fold improvement in the SNR (i.e., *win2* = 6.58/3.53, see **Figure 5.10d**). With 1PESP, I found that the SNR was maximum when the beam was positioned ~1 µm away from the trunk (see **Figure 5.10e**).

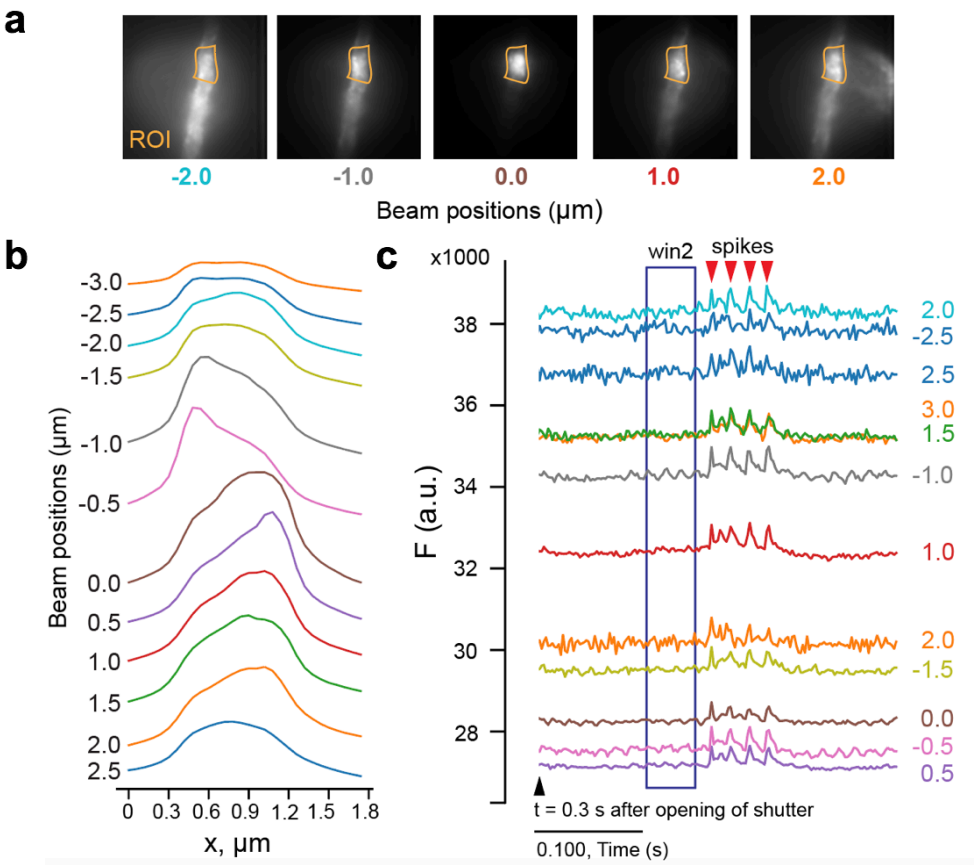

Figure 5.9 The optically recorded voltage spikes from different beam positions. a, The single photon image of the dendrite loaded with VSDs for different laser positions. **b,** Transverse profiles of the fluorescence along the dendrites with beam positions. **c,** The corresponding optical voltage transients (16-bit Fluorescence signal, *F*, as read from the EMCCD) at the apical trunk with AP firing.

As expected, the SNR was low when the beam focus was located at the centre of the trunk. While, positioning the beam directly on the trunk excited more VSDs on that segment. The low SNR is due to recording of VSDs that did not report changes in the membrane potential. Instead, the SNR was maximum when the laser spot was positioned 1.0 µm away from the apical trunk. Positioning the beam away from the dendrite illuminates one side of the branch exciting the edge-bound responsive VSDs while reducing the fluorescence from the non-responsive VSDs. While these preliminary analysis provided good results, more experiments are required. to investigate dye saturation and photo-damage comparing voltage imaging via 1PESP and direct illumination.

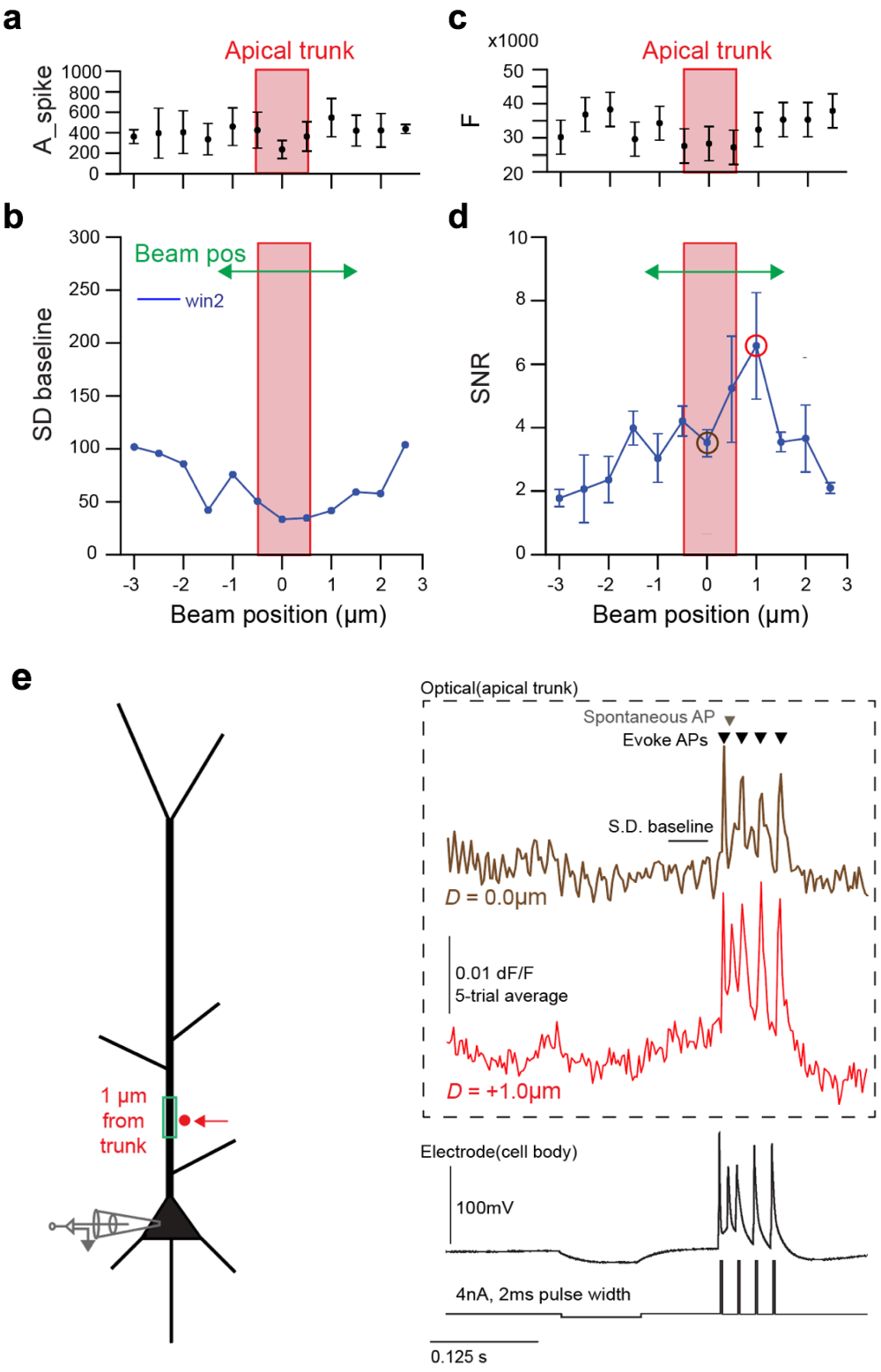

Figure 5.10 SNR enhancement with 1P-ESP. a, The average amplitude of the optical spike recorded relative to the baseline. **b,** The standard deviation of the baseline measured just before the spikes (*win2*). **c,** The mean fluorescence at the recorded trunk for different beam position. **d,** The signal-to-noise ratio for different beam position. **e,** The optical trace of the membrane potential at beams positions: D = 0 µm (brown) and D = 1 µm (red) with the electrical recording from the cell body.

5.8.3 Multi-site 1P-ESP

I also performed multi-site 1PESP where three foci were positioned to illuminate a distal basal dendrite (dend1) and an axon (dend2) (see **Figure 5.11a**). The corresponding time-series trace recovered by taking ROIs (dend1, background, and dend2) is shown in **Figure 5.11b**. We see that the Dend1 showed two bAPs that were above the background signal. Dend 2 did not show any response possible because the branch was previously damaged before the recording as indicated by the blebbing. 1PESP illumination can be extended from a single to multi-foci illumination sites to record membrane activity of several dendrites simultaneously.

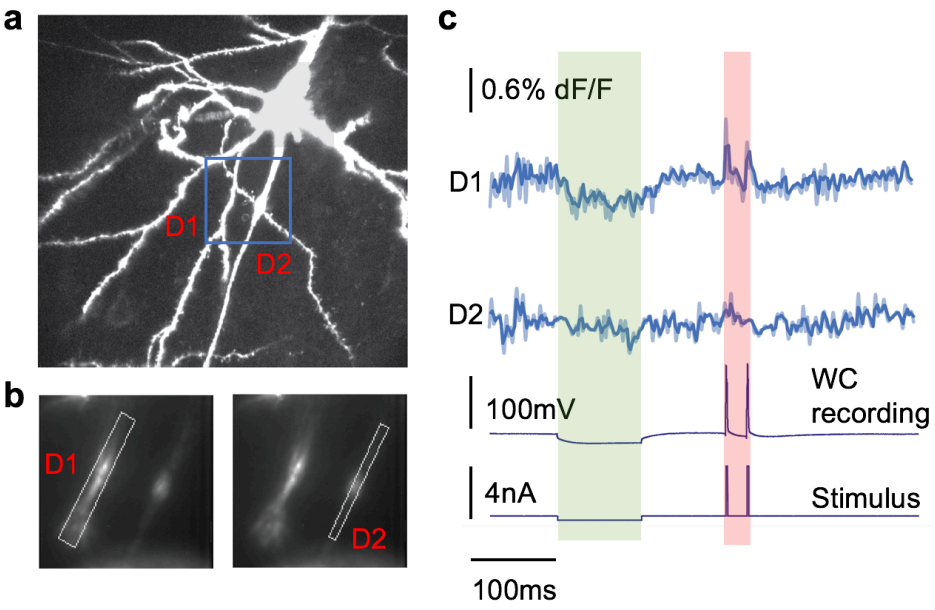

Figure 5.11 Multi-site 1P-ESP. a, Two-photon image a neuron loaded with JPW-1114 with the EMCCD active window (blue box) and two dendrites to record the voltage transient (D1-basal dendrite and D2-axon). **b,** The ROI drawn for each dendrite. **c,** The optical voltage-transient (average of 10 trials – light blue line and after 2-point moving average – solid line) showing bAPs (in red region) and hyperpolarization (in green region) at the basal dendrite D. BAPs were elicited by a 40Hz AP firing with the current injection at the soma. D2, although showed fluorescence, did not exhibit a response possibly due to previous photo-damage as observed from the axon blebbing.

5.8.4 Optical recordings at thin oblique and basal dendrites

Voltage imaging via 1PESP captured the invasion of back-propagating action potentials invasion at thin basal and oblique dendrites of L5PNs. Dendritic responses of thin basal and oblique dendrites are shown in **Figure 5.12**. The AP train were at 50- and 100 Hz invaded these segments. Broadening of the optical response after the 3rd bAP in the 100 Hz train was observed

at the distal segment of the basal dendrite (B2b) and along the apical trunk (1) indicative of a dendritic Ca^{2+} spike either from the nexus or locally at the basal segment (see **Figure 5.12**, sites 3, B2a and B2b).

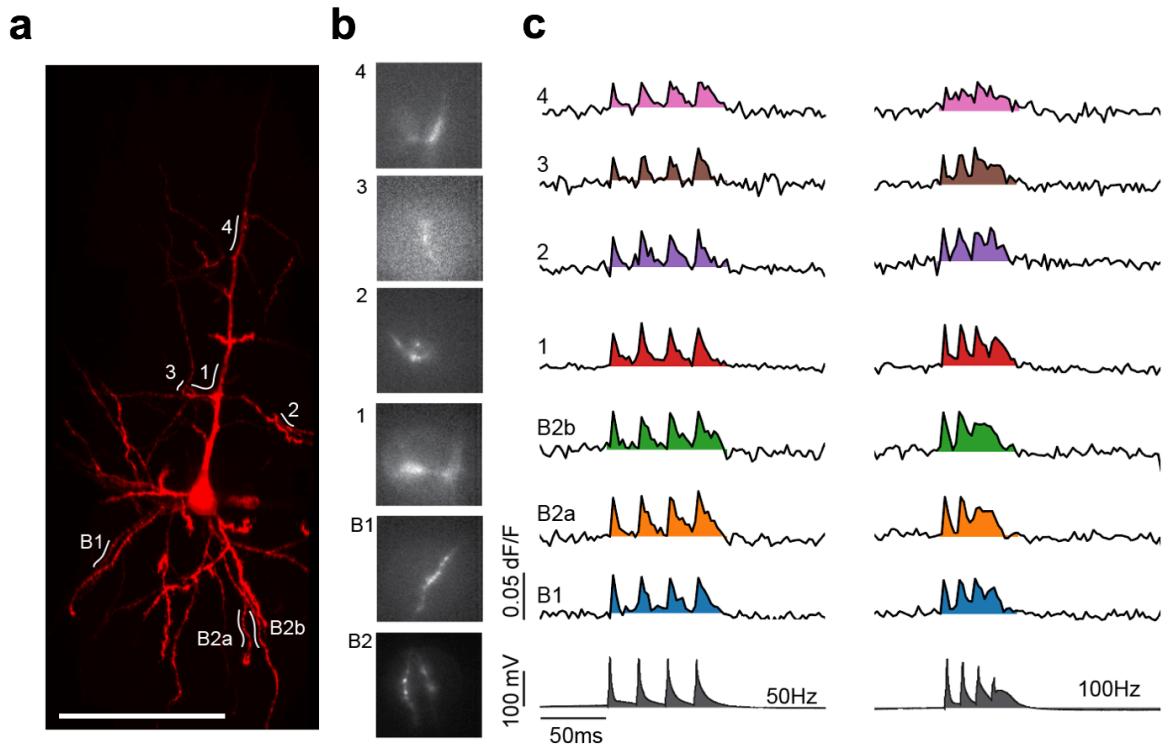

Figure 5.12 Back-propagating action potentials reliably invades trunk, oblique dendrites and basal dendrites. a, Two-photon image of a L5 pyramidal neuron loaded with the VSD showing targeted sites for voltage imaging. **b,** Fluorescence images corresponding to the sites in **a** excited via 1P excitation with fluorescence acquired via the EMCCD camera. **c,** The electrophysiological recording (bottom trace) and voltage-imaging traces (average of 5 trials) for 50 Hz and 100 Hz 4-AP train. Scale bar is 50 μm.

I also probed for the generation of an oblique branch spike in apical oblique dendrites with the 2-AP train for a set of frequencies (**Figure 5.14**). The optical traces were then aligned with the 2nd AP and the integral of the optical transients were calculated. Based on the *NEURON* model (in **Chapter 2**), the oblique branch spike would be followed by a broad 20-50 ms depolarization due to the activation of high-voltage activated calcium channels. Unfortunately, no broadening of the membrane potential was observed in this branch (N=1 cell). The recorded branch could possibly be a dendrite that does not exhibit an oblique branch spike.

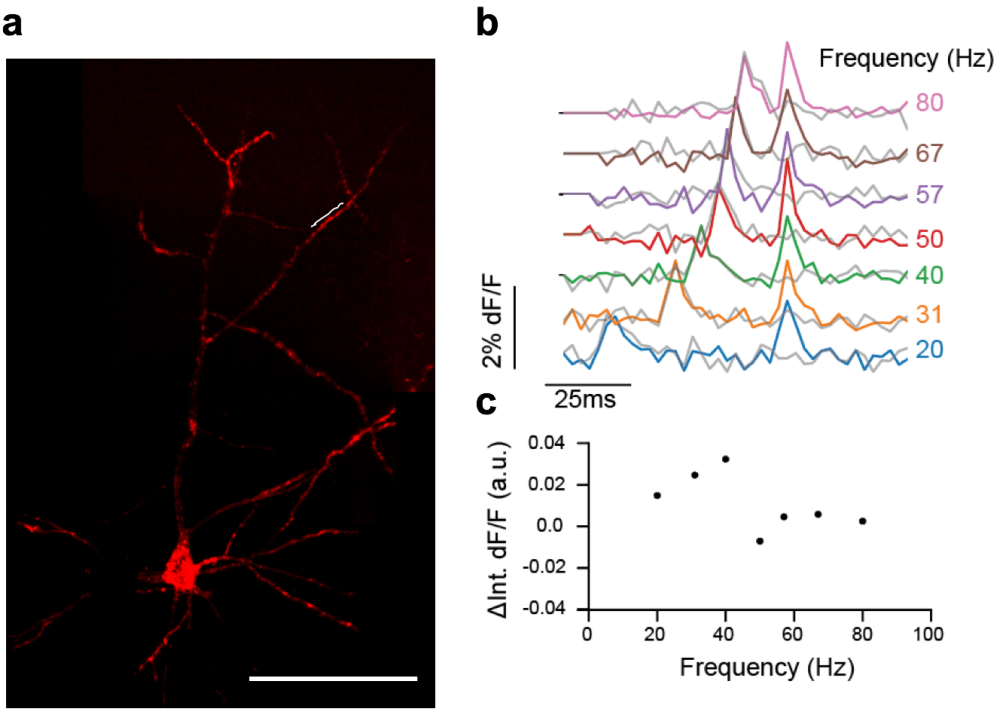

Figure 5.13 Sample optical voltage recordings at oblique dendrites. a, Two-photon fluorescence image of neuron loaded with 0.8mM JPW-1114. **b,** Optical voltage transients at a segment of an oblique dendrites in response to 2-AP train. The transients were aligned at the peak of the second bAP. The optical transient associated with single bAP is shown in grey as a reference. **c,** The difference of the integral of the optical voltage response for 2- and 1-bAP. Scale bar is 50 μm.

5.9 Discussion

5.9.1. Multi-site functional calcium imaging with temporal gating

With temporal gating, the overall fluorescence yield by 2P holographic multi-foci sites was increased while maintaining a low average power on the sample by modulating the 80 MHz femtosecond pulses with an AOM driven at 0.8 and 1.6 MHz gating frequencies. At the off-states, the AOM dumped the beam thereby throwing away most of the laser power. This limits the maximum laser power and consequently the number of foci that can be generated. Alternatively, one can use an expensive regenerative amplifier (RegA) which is capable of delivering 200 kHz pulse repetition rate without significant loss of average power (Theer et al., 2003). However, a RegA operates at a pre-set wavelength adding complexity when tuning the excitation to different wavelengths. Nevertheless, temporal gating with an AOM and a

femtosecond pulse laser (e.g., Ti:S) with an average output power of >2 W presents a flexible alternative to achieve an enhancement in fluorescence.

In a previous work in our lab, Gautam et al. (2015) showed that the increase in fluorescence with temporal gating with beam scanning translates to improvements in penetration depth and minimal photo-damage, as indicated by the change in the input resistance of the cell. I extended this work by applying it to 2P multi-site holographic illumination (Castanares et al., 2015). Our results showed up to 3.9±0.4 increase in the fluorescence yield with temporally gated beam while observing triggered calcium transients from the neurons.

A limitation of this study is that lack of characterization with penetration depth and signal cross-talk between neighbouring holographic sites. Temporal gating may enhance penetration depth as previous reports were able to image deeper with lower repetition rates by a factor of 2.0x (40μm/20μm, f_R = 1.2 MHz) in brain slices (Gautam et al., 2015) and ~1.4x (860μm/600μm, f_R = 200 kHz) in living intact brain (Theer et al., 2003). Another potential limitation with the detection of 2P multi-site fluorescence is cross talk from scattered fluorescence from each focus, especially when imaging through deep opaque tissue. Characterization of the scattering of holographic sites with depth will provide a benchmark on the allowable distance between sites to minimize the cross-talk. Bovetti et al. (2017) , with their 2P holographic system, performed scattering calibration of two neighbouring (10 μm apart) neurons at different depths and found that a parameter *S*, which measures ability to separate the two peak signals, dropped to 50% at 300 μm depth (see supplementary Figure S6 in (Bovetti et al., 2017)). Lastly, a potential concern with 2P holographic patterned illumination is local heating due to long beam dwell time. While long dwell-times allow higher time-averaged fluorescence per site, it may also induce local heating and cell damage (Podgorski and Ranganathan, 2016; Picot et al., 2018). Picot et al. (2018) provides a theoretical estimation with experimental verification of the temperature rise in 2P laser scanning and holographic illumination. Researchers can utilize Picot et al. (2018)'s numerical model to find optimal parameters of the a holographically projected patterned illumination (e.g., average laser power and dwell time) to reduced photo damage.

High fluorescence yield and SNR are crucial for imaging fast changes in fluorescence (~1 ms), where the number of fluorescence photons ($\Delta F/F$) is low. When imaging with rapidly changing fluorescence, an EMCCD camera can be used and can be set near camera saturation by applying gain or reducing the frame rate to overcome imaging noise. An increase in fluorescence from temporal gating offers high SNR while maintaining high frame rates (>1

kHz). As a proof-of-principle demonstration, we used a standard CMOS camera (max QE 60%, 3x Gain) to capture enhancement of the fluorescence with temporally gated excitation. Further improvement can be made in detection by using a more sensitive camera (e.g., sCMOS or EMCCD). In **Figure 5.14**, we extrapolate the enhancement in fluorescence when using an EMCCD camera, to allow for high-speed detection of fast changes in fluorescent signals. We consider the relation of the photo-electrons with time via photo-conversion, $N(t) \sim QE \cdot G \cdot photons(t)$, where G is the electronic gain from the camera. With temporal gating, the increase in the number of photo-electrons is due to the higher number of photons generated from a higher fluorescence yield. Since there are more photo-electrons with a 0.8 MHz temporally gated beam with respect to the ungated beam, the exposure time of the camera can be reduced to collect the same total number of photo-electrons, $N_{0.8\text{MHz}}/N_{\text{ungated}} = 1$, (see point B in **Figure 5.15**). In this case, the resulting exposure time of the CMOS camera with the temporally gated beam is 7.58 ms, allowing 130 Hz frame rate.

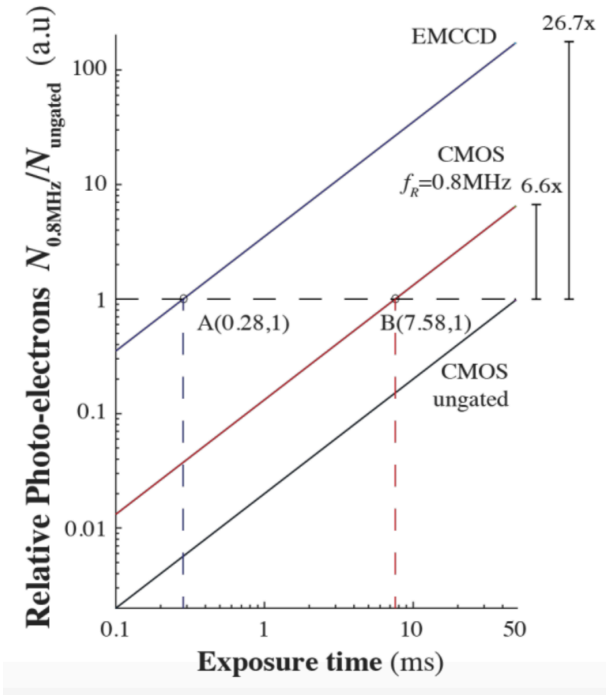

Figure 5.14 Further signal enhancement of SNR with the use of an EMCCD camera. Diagram of the relative number of photoelectrons with exposure time for 0.8 MHz (red line) temporally gated and ungated beam (black line) captured by the CMOS camera, and for 0.8 MHz temporally gated beam using an EMCCD (blue line). The exposure time can be reduced down to 7.58 ms (red broken line) with 0.8 MHz temporally gated beam for collecting the same number of photo-electrons ($N_{0.8\text{MHz}}/N_{\text{ungated}} = 1$, horizontal broken line) as that of the ungated beam at 50 ms exposure. Using an EMCCD with temporal gating, the exposure time can be further reduced to ~0.28 ms (blue broken line). Figure taken from Castanares et al. (2016).

Furthermore, using an EMCCD camera for the detection (max QE 96%, 50x EM Gain), the relative number of photo-electrons generated increases by 26.7-fold ($[QE \cdot G]_{EMCCD}/[QE \cdot G]_{CMOS}$) allowing a much shorter exposure time for collecting the same number of photo-electrons compared to the ungated beam (i.e., 0.28 ms corresponding to 3.6 kHz frame rate see point A in **Figure 5.14**). By substituting the CMOS with an Electron-Multiplied CCD (~96% QE at 550 nm and 50x EM Gain), higher image acquisition with a descent SNR can be achieved. This enhancement can then be applied to image responses from fast voltage indicators.

Initially, I performed two-photon voltage imaging with the temporal gating technique however, the longer 2P excitation wavelength of the JPW-1114 VSD limited the experiment. Fluorescence signal was observed from neurons loaded with JPW-1114 at 920 nm NIR beam. At 920-nm 2P excitation, I initially chose the to excite the dye at the rising edge of its absorption spectrum. However, it was difficult to find an appropriate 2P excitation wavelength to demonstrate the necessary Stark shift following changes in the membrane potential. With 2P excitation, I was not able to observe neuronal spikes at the soma (data not shown). One possible explanation for this is that optimal 2P excitation wavelength for JPW-1114 is not within the operating wavelength of our laser and optical system. The 1P excitation wavelength of JPW-1114 is optimal at the downward edge of its absorption spectrum (~532 nm) and for 2P it is estimated to be at λ>1060 nm. Other labs have developed and characterized the spectral characteristics of their stark-shift VSDs in HEK and hippocampal neuronal cultures (Kuhn and Fromherz, 2003; Kuhn et al., 2004; Yan et al., 2012; Acker and Loew, 2013) and slices (Acker et al., 2011; Acker and Loew, 2013). Kuhn et al. (2004) found that the maximal fluorescence response of ANNINE-6 was recorded when illuminating the dye at the downward edge with -0.35%/mV at 514 nm (for 1P excitation) and -0.52% at 1040 nm (for 2P excitation). Fluorinated variants of VSDs also exhibit optimal 2P excitation wavelengths from 1160-1290 nm with changes in fluorescence of 8-14%/ 100 mV (Yan et al., 2012). I tried increasing the 2P excitation wavelength; however, the output power of our NIR laser significantly decreased at longer wavelengths (from 4W at 800 nm down to ~500 mW at 1000 nm) limiting the intensity of the excitation beam. With very low power output, it was not possible to demonstrate temporal gating at wavelengths higher than 1050nm using our existing laser. Instead, I used single-photon voltage imaging with 532 nm laser. While tissue scattering is one of the main problems in using a short-wavelength light source, I investigated whether scattered photons could be sufficient indirectly excite the VSDs.

5.9.2 Voltage imaging with 1P-ESP

Integrating 1P (532 nm laser beam) excitation in our current multi-site detection system, I was able to optically record APs at the soma and bAPs along thin dendrites using JPW-1114 VSD. First, by scanning the illumination transverse to the dendrite, I observed a 1.8fold improvement in the SNR of the optically recorded voltage transients by offsetting the position of the beam focus ~1µm from the target dendrite. We hypothesized that the improvement is due to excitation of responding VSDs at the membrane and fluorescence signal amplification by the EMCCD gain. Second, the voltage imaging via 1P-ESP can be extended to use multi-foci illumination enabling the recording of multiple dendrites at the same time. Foust et al (2015) proposed using computer generated holography with patterned illumination that took shape of the neuronal structures (e.g. dendrites and soma) to deliver direct 1P excitation of the VSD (Foust et al., 2015). In our case, we used holographic patterned illumination to deliver indirect or scattered photon illumination to improve the SNR. We have shown that voltage imaging via 1PESP revealed that bAPs invade thin oblique dendrites of L5PNs. Future follow-up experiments utilizing 1PESP are envisaged to optically capture the oblique spikes with voltage imaging.

5.10 Summary

In conclusion, I presented the development of two techniques: (1) multi-site functional calcium imaging with temporal gating; and (2) voltage imaging with 1PESP. These two techniques aim to enhance the SNR of the optical recordings of dendritic activity. By temporal modulation of holographically projected multi-foci, the SNR increases up to 3.9±0.4 fold (at f_R = 1.6 MHz) of the recorded calcium transients. By extrapolation of the enhancement, we predict that coupling temporal gating with an EMCCD camera allows for fast (kHz) acquisition while maintaining a descent SNR suitable for high-speed 2P imaging. While temporal gating has been proven to effectively improve the SNR, its applicability to 2P voltage imaging is still limited. The low SNR associated with voltage imaging is not due to low fluorescence yield but due to a small number of voltage indicators that are bound to the thin membrane (~4nm). Moreover, it is difficult to find an appropriate 2P excitation wavelength to excite electrochromic voltage indicators to exhibit a Stark shift associated with changes in membrane potential. Hence, in an attempt to improve the SNR of voltage imaging, I presented a new oblique illumination technique, 1PESP, that exhibits an SNR enhancement in the optical voltage transients. By off-

setting the position of the beam (~1 μm) to the structure of interest (apical trunk), we recorded 1.8fold improvement in the SNR. The 1PESP can be extended with 1P multi-foci excitation allowing for recording of multiple dendrites at the same time. With the preliminary results, these two techniques can potentially be applied to optically probe membrane activity of thin dendrites that will potentially offer better spatial and temporal resolution.

Chapter 6. General discussion and future directions

6.1 Summary

The general aim of this thesis is to understand to functional role of thin apical oblique dendrites of L5PNs in the cortex. Specifically, I aim to identify specific characteristics of apical oblique dendrites that influence neuronal computation. To carry out this aim, I started with numerical modelling of a L5PN and found unique characteristics, such as dendritic spikes evoked on select apical oblique dendrites following low frequency trains of back-propagating action potentials. The numerical results guided my experiments where I used functional calcium imaging to confirm the existence of dendritic spikes in apical obliques of cortical L5PNs, which I refer to as oblique branch spikes, of cortical L5PNs *in vitro*. In addition to studying oblique branch spikes, the experience I gained while performing the experiments pushed me to develop new protocols to improve the optical recording techniques of dendritic activity. Overall, this work provides novel insights on the function of apical obliques of L5PNs and at the same time proposed new approaches to improve the SNR of the optically recorded neuronal activity.

6.2 Discussion of specific findings

Aim 1: The first aim of this thesis is to understand the generation of dendritic spikes in apical oblique dendrites of L5PNs. *Using multi-compartment model of a L5PN published by Shai et al. (2015), branch specific dendritic spikes were generated with a 2-AP train at a critical frequency of f_{c2} = 35 Hz. By analysing the ionic mechanisms numerically, I conclude that the oblique branch spike is a fast sodium spike followed by a broad 20 ms depolarization due to the recruitment of high voltage-activated calcium channels.*

The Shai et al. (2015) model exhibits dendritic active properties such as the Ca^{2+}-AP spike at the nexus of the apical tuft. In **Chapter 2**, I studied the extent of bAP invasion at oblique dendrites of the L5PN model. I used the critical frequency protocol to establish the conditions to generate dendritic spikes. I observed a strong attenuation of the bAPs in the model as they propagate back to the dendritic tree. As control, I injected current pulses (current, I = 4.2 nA, pulse duration, $\Delta\tau$ = 2 ms) at the soma to produce a 4-AP train, which evolves as 4-AP train to the apical dendrites and evokes a Ca^{2+}-AP at the nexus of the apical tufts at a critical

frequency of f_{c4} = 105 Hz of the 4-AP train. Surprisingly, I found that a 2-AP train generated with the same stimulation parameters as the 4-AP train sets off a dendritic spike at f_{c2} = 35 Hz at specific apical oblique branches. The 2-AP train with the same parameters were not enough to evoke a Ca^{2+}-AP spike at the nexus of the apical tufts.

I systematically quantified the dendritic segments that exhibits an oblique branch spike by analysing the relative changes of the peak membrane potential with varying frequencies of the 2-AP train. I used a sigmoid function to fit the curve of the changes in the peak membrane potentials as a function of frequency. From the sigmoid fit, I recovered a threshold of $A \geq 20$ mV and $\beta \geq 0.3$, where A is the change in the amplitude of the membrane potential and β is the slope parameter. I classified the responses into linear, $\beta < 0.3$, and non-linear, $\beta \geq 0.3$. In the model, the non-linear responding segments are observed only in oblique dendrites (referred to as their oblique number O#) O#3 and O#5, which suggest that the oblique branch spike is branch-specific. Moreover, the critical frequency is specific to certain branches around a nominal f_{c2} = 35±5 Hz.

I investigated the ionic mechanisms of the oblique branch spike in the L5PN model by blocking (or setting the conductance to zero) the calcium (*gCa_LVA, gCa_HVA*) and sodium (*g_NaTs2*) conductance of a linear responding branch (O#2) and two non-linear responding branches (O#3 and O#5). Blocking the *gCa_HVA*, or the high-voltage activated calcium conductance, removed the broad 20 ms depolarization but maintained a fast spike. The fast spike is due to the activation of *g_NaTs2* conductance. *From the results in the simulation, I conclude that the oblique branch spike is a fast sodium spike followed by a broad 20 ms depolarization due to the recruitment of high voltage-activated calcium channels.*

An active (depolarized) oblique branch boosted the excitability of the neighbouring branches and the added an after-depolarizing potential (ADP) at the soma. Plot of the ADP as a function of frequency also produced step increase at f_{c2} = 35 Hz. In **Chapter 2**, **Section 2.4.6**, I studied how blocking the conductance of an oblique dendrite affected the neighbouring branches and the ADP at the soma. Blocking the conductance of O#5 did not alter the dendritic spike in O#3. However, blocking the sodium conductance in O#3 shifted the critical frequency of O#5 to a higher frequency. Moreover, blocking the conductance in O#2 completely removed the oblique branch spikes in O#3 and O#5 and significantly reduced the ADP at the soma. I also altered the morphology of the neuron by physically removing an oblique branch (via dendrotomy). Removing the non-linear responding branches O#3 and O#5 and the linear O#2 branch led to a reduction in the ADP. The results suggest that the activity of an oblique dendrite

provided an added sustained depolarization, which helped neighbouring oblique dendrites to reach the threshold of generating an oblique branch spike.

Aim 2: The second aim is to experimentally generate and observe dendritic spikes in apical obliques of cortical L5PNs. *I experimentally verified the occurrence of oblique branch spikes in L5PNs as presented in Chapter 4. I developed and used our 2P multi-site detection microscope coupled with patch-clamp recording system to perform functional calcium imaging in oblique dendrites and electrophysiology of L5PNs in the somatosensory cortex (as presented in Chapter 3). Oblique branch spikes occur at a higher critical frequency (f_{c2} = 57±5 Hz, from calcium imaging) as compared to that measured in the model. When dendritic spikes are evoked in certain oblique branches, they manifest as an ADP from the whole-cell patch-clamp recordings at the soma. I conclude that the dendritic spikes predicted in silico occur experimentally.*

From the experiment, select oblique branches exhibited a non-linear increase in the intracellular calcium with a 2-AP train beyond a certain critical frequency. The critical frequencies of the oblique branch spikes were f_{c2} = 57±5 Hz (8 out of 13 neurons from calcium imaging). Adapting the criteria ($\beta \geq 0.3$) for classifying linear and non-linear responses (see **Chapter 2**, **Section 2.4.5**), I recovered neurons whose oblique dendrites exhibited a non-linear increase intracellular calcium. The locations of these non-linear responding segments were from O#4 to O#7 oblique branches. Plotting the ADP as a function of frequency sets of a step increase in the ADP at the same critical frequency observed at the branches. Recordings from 17 neurons were not included in the analysis as they exhibited an extra spikelet after the 2nd bAP which altered the efficacy of the critical frequency analysis. In contrast to the model, the average critical frequencies of oblique branch spike were higher, f_{c2} = 57±5 Hz (from calcium imaging) and f_{c2} = 72±4 Hz (from ADP), suggesting that the oblique branches were less excitable (or depolarized by a more attenuated bAPs) in the experiment.

The plot of the ADP as a function of frequency showed a distribution of critical frequencies with 2- and 4-AP train. From the L5PN model, the oblique branch spike has a lower critical frequency compared to the Ca^{2+}-AP at the nexus of the apical tuft. In the experiment, I found that 2% (2/100 neurons) and 35% (35/100 neurons) exhibited a single critical frequency at 2- and 4-AP train, respectively. Interestingly, similar fraction (36%) of recorded neurons exhibited two different critical frequencies of: f_{c2} = 72±4 Hz and f_{c4} = 82±3 Hz (**, p = 0.0013< 0.01). Furthermore, application of 0.25 μM DL-APV, an NMDA

antagonist, did not change the critical frequency in the ADP vs frequency plot. These blocking experiment results support that the oblique branch spike and Ca^{2+}-AP in the nexus of the apical tufts were recruited by bAPs and not by synaptic events.

Lastly, preliminary results with dendrotomy showed that cutting oblique branches changes the ADP at the soma. Using a tightly focused femto-second laser with reasonably higher power, I precisely severed an oblique branch from the neuron. After dendrotomy, the site of the severed oblique sealed as verified with 2P fluorescence imaging; however, the cut site might have partially sealed (also indicative of an unhealthy cell) as observed by an increase in the required holding current (from -100 to -200 pA) to keep the cell at -65mV and shifts in the action potential-threshold. The critical frequency protocol was performed before and after dendrotomy. Neurons showing a non-linear step increase in the ADP were selected for dendrotomy experiments. No calcium imaging was performed before dendrotomy which allowed for large number of neurons to be recorded. Hence, choosing dendrites to severe was done randomly and based on the location from the soma. When oblique branches O#3 and O#7 located 170 μm and 237 μm from the soma were cut, the neuron no longer produce a non-linear step increase in the ADP. On the other hand, cutting O#1 and O#6 branches situated 20 μm and 140 μm from the soma still maintained a step increase in the ADP at the same critical frequency as before the dendrite was cut. Indeed, there is a heterogeneity in the responses of the ADP when cutting specific oblique branches.

Overall, the evidence from calcium imaging, ADP measurements, and dendrotomy support to a dendritic oblique spike in L5PNs *in vitro* recruited with 2-AP train. Similar to what was observed in the model, the oblique spike was found to be in select oblique branches. Although I have not investigated what factors determine the location of the oblique spike, I observed that the dendritic spike occurred between branches O#4 to O#7 (experimentally), and O#3 and O#5 (model). Cutting the branches close to the soma (20 and 140 μm) did not affect the ADP. On the other hand, cutting branches suspected to evoke a dendritic spike no longer produced a step increase in the ADP at the specified critical frequency measured before dendrotomy.

Aim 3. The third aim is to improve the signal-to-noise ratio (SNR) of the recorded fluorescent calcium and voltage transients by proposing new optical techniques. *I presented novel techniques namely: (1) multi-site functional calcium imaging with temporally gated excitation laser; and (2) functional voltage imaging via single-photon excitation by scattered photons (1PESP). Functional calcium imaging with temporally gated excitation laser*

produced a 3-fold improvement in the SNR, while and functional voltage imaging via 1P ESP enhanced the SNR by 1.8-fold. I conclude that these two techniques can improve the SNR of the recorded calcium and voltage transients and can be applied to record and analyse dendritic spikes in apical oblique dendrites in the future.

Temporally gating the excitation fs-laser holds promise of enhancement in the generated 2P fluorescence as determined by the modulation parameters (τ – duration of the modulating pulse and f_R – the gating frequency). We initially derived the mathematical theory that showed a $1/(\tau f_R)$ factor enhancement in the recorded fluorescence signal (see **Equation 5.4**) due to the non-linearity of the 2P-excitation process. We experimentally implemented the temporal gating technique using an AOM. We characterized the enhancement by recording electrically triggered transients from hippocampal neuronal cultures loaded with fluorescent calcium indicator (Cal-520AM). The SNR increased by 3.9±0.4 and 3.7±0.3-fold relative to the ungated beam using f_R = 0.8 MHz and f_R = 1.6 MHz, respectively. Extrapolating from these results, we estimated that the use of an EMCCD camera and temporally gated beam (f_R = 0.8 MHz) allows for a 3-fold increase in photo-electrons collected within a 1 ms exposure compared to using an ungated beam. This modality will be suitable for 2P imaging fast fluorescent voltage transients.

When I shifted and attempted to perform functional voltage imaging, I discovered another technique to improve the SNR of optically recorded voltage transients. I discovered that using scattered photons to excite VSDs can reduce the background fluorescence and limit the excitation only to VSDs that report voltage changes in the membrane. I refer this technique as functional voltage imaging via single-photon excitation by scattered photons (1PESP). As observed in previous studies (Antic, 2003; Stuart and Palmer, 2006) and in this work, neurons loaded with VSDs exhibit high baseline fluorescence (resulting to a typical <1% dF/F response) due to the binding of VSDs with intracellular lipid compartments that do not respond to changes in membrane potential. I hypothesized that a way to improve the SNR is to limit the excitation only to the responding VSDs and lessen the fluorescence of non-responding VSDs, which produces a large background signal. With reduced background, the SNR is improved by increasing the gain of the sensor, such as an EMCCD camera. I experimentally verified the theory by integrating a 1P excitation into our existing 2P microscope and performed 1P voltage imaging with 532 nm laser spot illumination on L5PNs intracellularly loaded with VSD (JPW-1114). I optically recorded action potentials along the main apical trunk and at thin basal and

oblique dendrites and resulted in an SNR ~3.8 using an EMCCD camera (with parameters 50x EM gain, 0.0022s exposure time, 400 frames per second). By deliberately offsetting the position of the laser focus from the dendrite (~1.0 μm) of interest, I found a 1.8-fold improvement, with SNR from 3.5 to 6.6.

Thus, temporal gating and 1PESP are approaches to enhance the SNR of fluorescent voltage and calcium recordings. These techniques can be implemented in current microscope systems either by addition of an AOM or using a low-repetition rate fs-laser (for temporal gating) or off-setting the position of laser focus (for 1PESP). Future works are envisaged to use these techniques.

6.3 Implications of my results

The role of apical oblique dendrites of cortical L5PNs is still not fully understood. While several studies have investigated the apical obliques of hippocampal CA1 PNs (as presented in **Chapter 1**, **Section 1.7**), only few studies have investigated the oblique dendrites of L5PNs. Findings made in hippocampal CA1 PNs may not all be translatable to cortical L5PNs.

In silico and *in vitro* studies of L5PNs have investigated how the distribution of oblique branches modulate forward- and back- propagating spikes (Vetter et al., 2001; Antic, 2003; Schaefer et al., 2003; Zhou et al., 2015). Vetter et al. (2001) showed that dendritic branching and density of sodium channels modulate the forward propagation of dendritic Na+ APs initiated at the apical trunk and oblique dendrites. Invasion of bAPs in proximal oblique dendrites was observed to be reliable with less filtering (maintained bAP width) at the oblique branches (Antic, 2003); however, bAPs failed to invade a few distal oblique branches (higher oblique number) due to attenuation at branch points, minute differences in dendritic diameter, and to the non-uniform distribution of A-type K+ conductance in oblique dendrites (Zhou et al., 2015). Furthermore, simulation studies show that the addition of oblique branches in close proximity to the soma (d < 140 μm) can increase the coupling of the nexus Ca^{2+}-AP and the somatic-AP from 35% to 60% (Schaefer et al., 2003). These studies suggest that bAPs, modulated by dendritic branching and dendritic conductance, can drive strong depolarization in oblique dendrites to recruit dendritic non-linearity such as an oblique branch spike. Schiller (2002) reported large calcium influx in a select oblique branch during a PDS (epileptic-like) discharge at the soma (see **Figure 1.9c**). This could be a first evidence of an oblique branch spike in L5PNs; however, the conditions of reliably eliciting this oblique branch spike was not established.

Several studies have also investigated the anatomical and functional synaptic connections at the apical oblique dendrites (Markram et al., 1997; Sjostrom and Hausser, 2006; Oberlaender et al., 2012). Biocytin reconstructions and paired-patch clamp recordings have shown that L5PNs form intracortical connections among each other via axon-oblique connection (Markram et al., 1997; Oberlaender et al., 2012). Furthermore, repetitive somatic AP-firing have shown to induce the activity dependent LTP in the axon-oblique connections (Sjostrom and Hausser, 2006). It remains unknown as to the mechanism for the increased level of intracellular calcium as required for LTP induction. One possible mechanism can be a prolonged activation of calcium channels due to an oblique branch spike. In basal dendrites, calcium spikes are implicated to play a role in spike-timing dependent plasticity (Kampa et al., 2006). A similar mechanism may exist with an oblique branch spike in oblique dendrites.

In this study, I found that apical obliques of L5PNs do exhibit branch-specific oblique branch spikes with a lower critical frequency of f_{c2} = 57±5 Hz (from Calcium imaging) and f_{c2} = 72±4 Hz (from ADP) as compared to the f_{c4} = 82±3 Hz (from ADP) critical frequency for recruiting Ca^{2+}-AP at the nexus of the apical tuft. Previous works showed a critical frequency response at the basal and nexus of the apical tuft dendrites (Schiller et al., 1997; Larkum et al., 1999; Kampa and Stuart, 2006; Nevian et al., 2007) (see **Figure 6a**). The critical frequency protocol showed that bAPs recruited a Ca^{2+}-AP at the nexus at f_{c4} = 98±6 Hz Larkum et al. (1999). On the other hand, a critical frequency of f_{c3} > 100 Hz (120-200 Hz) with 3-AP train also recruited calcium spikes in distal segments of the basal dendrites (Kampa and Stuart, 2006). Some studies also reported that basal dendrites support sodium and NMDA spikes (Schiller et al., 2000; Nevian et al., 2007). This work has shown that dendritic spikes could be evoked at select oblique branches with a 2-AP train at f_{c2} ~60 Hz train. Conductance analysis in the Shai et al. (2015) L5PN model showed that the oblique branch spike is a fast sodium spike followed by a broad depolarization due to the activation of high-voltage activated calcium channels. To verify ionic mechanisms experimentally, future work will involve the design of pharmacological experiments onto specific oblique branches such as the use of caged ion-blockers or by puff application or iontophoresis.

The discrepancy in the critical frequencies of the oblique branch spike from the experiment and model. The critical frequency of this oblique spike was higher in the experiment (f_{c2} = 57±5 Hz, from Calcium imaging) than in the model (f_{c2} = 35 Hz, from ADP). This suggests that the oblique dendrites of L5PNs *in vitro* were less excitable (or depolarized by a more attenuated bAPs) compared to oblique dendrites in the model. Hyperpolarizing

voltage-gated ion channels such as A-type potassium channels could play a role in dampening the excitability of oblique dendrites of L5PNs like the findings in CA1 PNs (Frick et al., 2003; Gasparini et al., 2007). Future studies can investigate the influence of hyperpolarizing channels by local application of channels blockers on an oblique branch either by puff application or iontophoresis.

The discrepancy in the critical frequencies of the oblique branch spike as measured with calcium imaging and the step-increase of the ADP at the soma. The critical frequencies in the ADP measurement were higher as compared to the ones recovered from calcium imaging. A possible explanation for this is that the oblique spikes do not effectively propagate to the soma due to the unfavourable mismatch at the branch points. This ineffective forward propagation of oblique spikes to the soma has also been studied multi-compartment models of CA1 PN (Migliore et al., 2005). Migliore et al. (2005) also found that a sustained activity in the obliques in the CA1 PN model was required to influence the soma. Consistent with this finding, I also observed in the Shai et al. (2015) L5PN model that removing the oblique spikes in two non-linear branches (O#3 and O#5) significant decreased the ADP at the soma.

Likelihood of generating a dendritic spike in apical oblique dendrites of L5PNs. L5PNs exhibit intrinsic burst firing making it likely to recruit oblique branch spikes in apical obliques. *In vitro* recordings have shown that L5bPNs fire in burst of 3-4 APs at frequencies up to 300 Hz (Agmon and Connors, 1989; Chagnac-Amitai et al., 1990; Connors and Gutnick, 1990; Kim and Connors, 1993; Williams and Stuart, 2000). Bursting of L5bPNs in the barrel cortex have also been documented in awake rats ~17% of the time during a whisker stimulus (de Kock and Sakmann, 2008). The origin of the ADP leading to burst AP firing is due to the recruitment of nickel-sensitive calcium channels along the apical trunk (Amitai et al., 1993; Williams and Stuart, 1999). This work shows that non-linear responses of oblique branches contribute to an additional ADP at the soma. Plotting the ADP as a function of frequency reflected two distinct critical frequencies of f_{c2} = 72±4 Hz and f_{c4} = 82±3 Hz. Considering that the oblique branch spike presented in this study occurs at a much lower critical frequency (f_{c2} ~60 Hz, from experiments), oblique branch spikes are likely to be recruited first before the Ca^{2+}-AP at the nexus of the apical tuft. Future *in vivo* studies can focus on quantifying the occurrence of the oblique branch spike when the rodent is at rest or is actively performing a certain task.

Voltage imaging in oblique dendrites. The results from calcium imaging showed a non-linear increase in the intracellular calcium in a few oblique dendrites. However, calcium imaging is an indirect measure of membrane activity as there are many other sources of Calcium (see review, Grienberger and Konnerth (2012)). Voltage imaging is a better approach to verify the generation of dendritic (fast sodium) spikes in oblique dendrites. Several studies that used intracellularly loaded VSD (e.g., JPW-1114) have optically recorded dendritic spikes in dendrites and APs in axons with 1P excitation (Antic, 2003; Stuart and Palmer, 2006; Foust et al., 2010; Popovic et al., 2011; Popovic et al., 2015). It would be interesting to apply the same recording modalities and investigate the generation oblique spikes with 2-AP train above $f_{c2} \sim$ 60 Hz. In general, voltage imaging requires a fair number of trials to obtain a good SNR of the voltage traces. The 1PESP technique can then be utilized to enhance the SNR of the recordings using only few trials.

On the other hand, 2P voltage imaging is a promising tool to investigate the dendritic spikes such as the oblique spike presented in this study. 2P imaging should be performed with VSDs that have 2P excitation spectra that matches the operating wavelength of the femto-second laser available. There are few promising studies that have successfully recorded dendritic spikes with 2P microscope systems *in vivo* (Acker et al., 2011; Tran-Van-Minh et al., 2016; Roome and Kuhn, 2018). A notable study by Roome and Kuhn (2018), where they recorded dendritic activity of Purkinje neurons in an awake mouse, reported the following: (1) voltage spikelets where generated during a dendritic complex spikes but had no direct correlation with somatic activity, (2) bAPs were highly attenuated at the dendritic tree, and (3) variable voltage hotspots were locally observed but did not evoked corresponding calcium signals. Roome and Kuhn (2018) provided evidence for dendritic integration and compartmentalization of dendritic from somatic activity *in vivo* and awake condition.

With 2P line-scan voltage imaging as in the study by Roome and Kuhn (2018), rigid filtering of traces and data analysis has to be made recover the true voltage signals. We propose that temporal gating could be another "active" technique to improve the SNR of the recorded voltage transients. One potential issue with temporal gating is the possibility of inducing artefacts in the recording due to the "gating" of the beam. This would appear as a sharp frequency and its harmonics in the frequency spectrum of the voltage signal. A solution around this problem is to use lock-in detection to synchronize the acquisition of the voltage transients with the gating of laser beam. This approach has been done with 1P single-channel recording with a balanced detection (Bullen et al., 1997).

6.4 Limitations of the study

Oblique dendrites in a L5PN are sparsely distributed along its trunk (50-300 μm from the soma) and extend laterally ~50 μm. In order to get good statistics as to which oblique dendrites exhibit a dendritic calcium spike, multiple oblique branches have to be recorded at the same time. In this study, I was only able to perform two-photon calcium imaging on a few oblique branches at a time due to the limited imaging window of the camera to achieve a descent frame rate (~ 100 fps) to capture the calcium transients at oblique dendrites.

A fast two-photon microscope with a larger imaging ROI would increase the throughput of the recording. Single-photon epifluorescence microscope can offer a high throughput approach to simultaneously imaging multiple oblique branches at the same time and with large field-of-view (Antic, 2003; Zhou et al., 2015). However, signal cross-talk can be a problem especially when the dendrites overlap (along the z-axis) with each other. Single-photon epifluorescence microscopes have poor axial discrimination of the fluorescence photons. In contrast, two-photon microscopes offer minimal cross-talk with the localized excitation volume and allow imaging multiple dendrites along a single z-plane (Hill et al., 2013).

The use of an improved EMCCD camera or coupling the holographically projected beam into a galvanometric scanning mirrors can increase the throughput of the recording. First, the development of faster EMCCD cameras with large imaging window operating at higher frame-rates may cover more regions of interest. Along with this development are hardware-specific firmware that enable fast multiple-ROI recording while keeping the required frame rate (such as the PCO prime multi-ROI function). This limits the recording to the ROIs and minimizes the file size of the acquired image sequences. Another way to extend the field-of-view to increase the throughput of the experiment is to couple the holographic beam with the galvanometric scanning mirrors (GM) (Go et al., 2019). We have successfully characterized the robustness of this design using our collaborator's existing 2P GM scanning microscope. The holographic active region will still be determined by the SLM and the relay lenses used; however, the pattern can be move across the sample using the galvanometric mirror instead of moving the sample stage. In the future, we plan to integrate the design to our system here at ANU.

6.5 Future Directions

Investigate the increased excitability of oblique dendrites. Thin oblique dendrites are susceptible targets for branch-specific plasticity. These dendrites have high-impedance due to their thin diameters relative to the apical trunk. As such, they yield large depolarizations when bAPs invade causing voltage-gated conductance (i.e., voltage-gated calcium and potassium channels) to open up and lead to the generation of spikes. The increased levels of intracellular calcium paired with synaptic inputs can promote induction of spike-timing-dependent plasticity (STDP) (Kampa et al., 2006; Sjostrom and Hausser, 2006), Long-term potentiation (LTP) (Magee and Johnston, 1997; Canepari et al., 2007), branch-specific plasticity (Cichon and Gan, 2015) or excitotoxicity (Morse et al., 2010). An LTP experiment on thin basal dendrites, by pairing single AP firing of a pre-synaptic neuron with a burst of APs (3 APs at f $\geq$ 200 Hz, generating a dendritic calcium spike in the basal dendrite of the post-synaptic neuron) showed an increase in the average EPSP amplitude (Kampa et al., 2006). Another interesting study is to perform the experiments done by Sjostrom and Hausser (2006) that paired APs and EPSPs while imaging the calcium or voltage activity at the oblique dendrites. This would validate whether oblique branch spikes participated in the induction of LTP in the oblique branches.

Another important aspect is to test whether oblique branch spikes affect sensory inputs. Several works have shown that dendritic Ca^{2+}-AP at the nexus and NMDA at the apical tuft branches spikes enhances sensory inputs (Lavzin et al., 2012; Xu et al., 2012; Smith et al., 2013; Palmer et al., 2014; Ranganathan et al., 2018). Future experiments can investigate the membrane activity of oblique dendrites of L5PNs while the rodent is performing a whisking task. Chemical and optical modulation of voltage-gated potassium channels (K_v) in oblique dendrites *in vivo* would also be a good experiment to assess how branch-specific modulation of K_v channels affect sensory processing.

The excitability of oblique dendrites can be regulated by the dense expression of hyperpolarizing voltage-gated channels (e.g., potassium channels). CA1 PNs show normalization of the calcium influx due to the reduction in the bAP amplitude in the oblique dendrites by the activation of Barium sensitive voltage-gated A-type potassium channels (Frick et al., 2003; Gasparini et al., 2007). Drawing insights from a multi-compartment model, Zhou et al. (2015) suggested a heterogeneous density distribution of A-type potassium channels in the oblique dendrites which could explain their findings of branch-specific efficacy of bAP

invasion at the oblique of L5PNs *in vitro*. Blocking A-type potassium channels may lead to hyper-excitability of oblique dendrites.

An increase in excitability of oblique dendrites can potentially be linked to neurodegenerative disease. A few studies have also shown that oblique dendrites became "hyper-excitable" in the presence of amyloid beta proteins, which blocks voltage-gated potassium channels (Good and Murphy, 1996; Chen, 2005; Morse et al., 2010). Also, large calcium events in oblique dendrites are observed during epileptic discharges (Schiller, 2002). Future works can focus on how oblique branch spikes play a role in plasticity and disease. This adds to the growing interest on how abnormalities of dendritic excitability may be linked to brain disease (for review, see Palmer (2014)).

Thus, the excitability of oblique dendrites can be a feature or a bug in neuronal computation. Excitability of oblique dendrites with the generation of dendritic spikes can be an important component for the induction of branch-plasticity. In contrast, hyper-excitability of oblique dendrites can be an abnormality in the dendritic activity which could be linked with neurodegenerative disease. Voltage-gated A-type potassium channels regulate this excitability. A study of post-status epilepticus (post-SE) mouse model showed that potassium currents decreased after 1 hour of post-seizure due to the internalization of potassium channels from the membrane surface (Lugo et al., 2008). The mechanisms behind the up- and down-regulation of voltage-gated potassium channels that regulates the excitability of oblique dendrites remains to be studied.

6.6 Conclusion: The role of apical oblique dendrites in information processing

Taking a big picture view of this thesis, I go back to the main aim of this research, "What is the functional role of apical oblique dendrites in information processing?" While this work has shown the intrinsic property that select apical oblique dendrites in L5PNs can generate oblique branch spikes, it provided evidence that apical oblique dendrites may potentially participate in dendritic integration which opens up exciting research questions. How do oblique branch spikes interact with other dendritic spikes in the apical trunk and basal dendrites? Do they enhance processing of sensory inputs? Do they play a role in learning and memory?

Apical oblique dendrites of L5PNs play a role in relaying sensory inputs and integrating active-sensing and passive whisker representation (see **Figure 6b**). Oblique dendrites of L5PNs

are strategically located across layers 2/3 to layer 4 which are densely innervated by axon terminals from neurons in the VPM. 3D reconstructions of the density of VPM axon-dendrite overlap have shown a unimodal peak at layer 4 for slender-tufted L5PNs (or layer 5a pyramidal neurons, L5PN-a) suggesting VPM innervations at the apical oblique dendrites (Oberlaender et al., 2012). The overlap between axons from VPM neurons and dendrites of thick-tufted L5PNs (or layer 5b pyramidal neurons, L5PN-b) indicate a bimodal distribution at the boundaries of: layer 4-5 and layer 5-6 suggesting that synaptic connections are formed at the apical oblique and basal dendrites of these thick-tufted pyramidal neurons (Oberlaender et al., 2012). The slender-tufted L5PNs are active during active-sensing whisking tasks such as object localization but inactive during quiet or non-whisking states (de Kock and Sakmann, 2009). Layer 5b (or the thick-tufted) neurons exhibit burst firing during quite period and are more involved in passive whisker touch, inputs via VPM thalamic afferents. Connections formed among apical tuft and oblique dendrites of L5PNs gave rise to cell-specific intracortical micro-circuit. Pairs of L5PNs form unidirectional and bidirectional with axon-dendritic synaptic connections: at the apical tuft (for layer 5a to layer 5b neurons) (Oberlaender et al., 2011) and at apical oblique dendrites (layer 5b to layer 5b) (Markram et al., 1997). A recent work by Ranganathan et al. (2018) using calcium imaging *in vivo* have shown that a non-linear mixed representation of neuronal activity in the barrel cortex was produced during an adaptive active-sensing whisker task, where the mouse was tested to track a moving object with its whisker (see **Figure 6c**). This representation involved the activation of a set of L5PNs that exhibited unique selectivity of touch magnitude and location to represent a given task. Ranganathan et al. (2018) suggested that non-linear mixed representation could potentially be mediated by plateau potentials (e.g. NMDA and calcium spikes) in the apical tuft dendrites and apical trunk of L5PNs. It is possible that oblique branch spikes can strengthen the intracortical activity within L5PN-L5PN connections.

In conclusion, this work has shown that select apical oblique dendrites in L5PNs can carry out the generation of oblique branch spikes following a lower frequency of a train of bAPs as compared to the the Ca^{2+}-AP at the nexus of the apical tuft. My findings expand our understanding of the passive and active function of oblique dendrites of L5PNs. (Schaefer et al., 2003) reported that the distribution of oblique dendrites along the apical trunk passively tunes to coupling between the firing of Na^{+}-AP at the soma and Ca^{2+}-AP at the nexus of the apical tuft. This work, along with the work of Losonczy and Magee (2006), reveal that sodium mediated dendritic spikes are generated in apical oblique dendrites by either low-frequency burst of back-propagating action potentials or clustered and distributed synaptic activation

along an oblique branch. These spikes can be a mechanism to significantly raise the intracellular calcium levels which promotes local-branch plasticity, a theory proposed by Alkon (1999). Thus, apical oblique dendrites of L5PNs are not just thin passive membrane structures that receive thalamic inputs and provide intracortical connections amongst L5PNs; but they may also actively participate in dendritic integration and reinforce the strength of these axon-oblique connections with the recruitment of the oblique branch spikes.

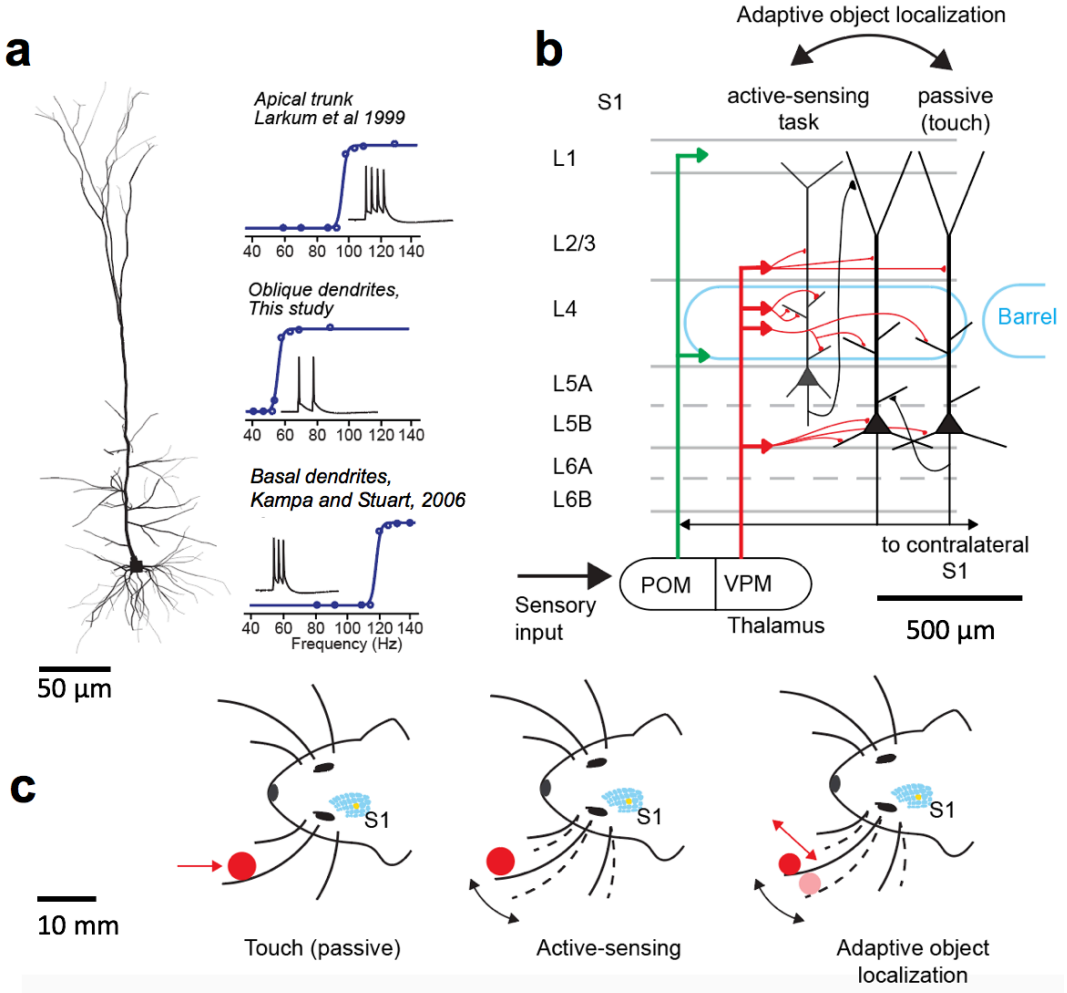

Figure 6. Role of apical oblique dendrites of L5PNs. a, Illustration showing different critical frequencies of generation calcium spikes in the apical tuft dendrites (Larkum et al., 1999), basal dendrites (Kampa and Stuart, 2006), and oblique branch spikes in oblique dendrites (this study). **b,** A diagram of the intracortical layer 5 micro-circuit in the primary somatosensory cortex, S1, that are active during a passive and active whisking task. Note that a fraction of VPM terminals synapse onto the apical oblique dendrites and basal dendrites of layer 5a (or slender tufted) and layer 5b (or thick-tufted) pyramidal neurons. Note that this circuit diagram only highlights connections of VPM axons to layer 5 pyramidal neurons. There also exists synaptic connections of different cells types (e.g. layer 4 and L2/3 pyramidal neurons and interneurons) to layer 5 pyramidal neurons. **c,** Different sensing modes, touch(passive), active-sensing, and adaptive-object localization, that correlates with the activity of layer 5 microcircuit in a column of the barrel cortex. **Figure 6c** is modified from Xu et al. (2012) and Ranganathan et al. (2018).

References:

Abraham, W. C. & Bear, M. F. 1996. Metaplasticity: the plasticity of synaptic plasticity. Trends Neurosci, 19, 126-30.

Acker, C. D., Yan, P. & Loew, L. M. 2011. Single-voxel recording of voltage transients in dendritic spines. Biophys J, 101, L11-3.

Adams, P. R., Brown, D. A. & Constanti, A. 1982. M-currents and other potassium currents in bullfrog sympathetic neurones. J Physiol, 330, 537-72.

Agmon, A. & Connors, B. W. 1989. Repetitive Burst-Firing Neurons in the Deep Layers of Mouse Somatosensory Cortex. Neuroscience Letters, 99, 137-141.

Ahrens, M. B., Orger, M. B., Robson, D. N., Li, J. M. & Keller, P. J. 2013. Whole-brain functional imaging at cellular resolution using light-sheet microscopy. Nat Methods, 10, 413-20.

Akemann, W., Mutoh, H. & Knöpfel, T. 2014. Fluorescent Indicators for Functional Optical Imaging. In: WEBER, B. & HELMCHEN, F. (eds.) Optical Imaging of Neocortical Dynamics. Humana Press.

Akemann, W., Mutoh, H., Perron, A., Park, Y. K., Iwamoto, Y. & Knopfel, T. 2012. Imaging neural circuit dynamics with a voltage-sensitive fluorescent protein. Journal of Neurophysiology, 108, 2323-2337.

Akerboom, J., Chen, T. W., Wardill, T. J., Tian, L., Marvin, J. S., Mutlu, S., Calderon, N. C., Esposti, F., Borghuis, B. G., Sun, X. R., Gordus, A., Orger, M. B., Portugues, R., Engert, F., Macklin, J. J., Filosa, A., Aggarwal, A., Kerr, R. A., Takagi, R., Kracun, S., Shigetomi, E., Khakh, B. S., Baier, H., Lagnado, L., Wang, S. S., Bargmann, C. I., Kimmel, B. E., Jayaraman, V., Svoboda, K., Kim, D. S., Schreiter, E. R. & Looger, L. L. 2012. Optimization of a GCaMP calcium indicator for neural activity imaging. J Neurosci, 32, 13819-40.

Alkon, D. L. 1999. Ionic conductance determinants of synaptic memory nets and their implications for Alzheimer's disease. J Neurosci Res, 58, 24-32.

Almog, M. & Korngreen, A. 2014. A quantitative description of dendritic conductances and its application to dendritic excitation in layer 5 pyramidal neurons. J Neurosci, 34, 182-96.

Amitai, Y., Friedman, A., Connors, B. W. & Gutnick, M. J. 1993. Regenerative activity in apical dendrites of pyramidal cells in neocortex. Cereb Cortex, 3, 26-38.

Antic, S. D. 2003. Action potentials in basal and oblique dendrites of rat neocortical pyramidal neurons. Journal of Physiology-London, 550, 35-50.

Antic, S. D., Empson, R. M. & Knopfel, T. 2016. Voltage imaging to understand connections and functions of neuronal circuits. J Neurophysiol, 116, 135-52.

Antic, S. D., Zhou, W. L., Moore, A. R., Short, S. M. & Ikonomu, K. D. 2010a. The Decade of the Dendritic NMDA Spike. Journal of Neuroscience Research, 88, 2991-3001.

Antic, S. D., Zhou, W. L., Moore, A. R., Short, S. M. & Ikonomu, K. D. 2010b. The decade of the dendritic NMDA spike. J Neurosci Res, 88, 2991-3001.

Bando, Y., Grimm, C., Cornejo, V. H. & Yuste, R. 2019. Genetic voltage indicators. BMC Biol, 17, 71.

Barreto-Chang, O. L. & Dolmetsch, R. E. 2009. Calcium imaging of cortical neurons using Fura-2 AM. Journal of visualized experiments : JoVE, 1067.

Barth, A. M., Vizi, E. S., Zelles, T. & Lendvai, B. 2008. Alpha2-adrenergic receptors modify dendritic spike generation via HCN channels in the prefrontal cortex. J Neurophysiol, 99, 394-401.

Behabadi, B. F., Polsky, A., Jadi, M., Schiller, J. & Mel, B. W. 2012. Location-dependent excitatory synaptic interactions in pyramidal neuron dendrites. PLoS Comput Biol, 8, e1002599.

Bekkers, J. M. & Hausser, M. 2007. Targeted dendrotomy reveals active and passive contributions of the dendritic tree to synaptic integration and neuronal output. Proc Natl Acad Sci U S A, 104, 11447-52.

Benyus, J. 2002. Biomimicry: Innovation Inspired by Nature, Harper Perennial.

Berger, T., Borgdorff, A., Chrochet, S., Neubauer, F. B., Lefort, S., Fauvet, B., Ferezou, I., Carleton, A., Lüscher, H.-R. & Petersen, C. C. H. 2007. Combined Voltage and Calcium Epifluorescence Imaging In Vitro and In Vivo Reveal. Journal of Neurophysiology, 97, 3751-3762.

Bernard, C. & Johnston, D. 2003. Distance-dependent modifiable threshold for action potential back-propagation in hippocampal dendrites. J Neurophysiol, 90, 1807-16.

Berridge, M. J., Lipp, P. & Bootman, M. D. 2000. The versatility and universality of calcium signalling. Nat Rev Mol Cell Biol, 1, 11-21.

Bliss, T. V. & Collingridge, G. L. 1993. A synaptic model of memory: long-term potentiation in the hippocampus. Nature, 361, 31-9.

Bradley, J., Luo, R., Otis, T. S. & DiGregorio, D. A. 2009. Submillisecond Optical Reporting of Membrane Potential In Situ Using a Neuronal Tracer Dye. Journal of Neuroscience, 29, 9197-9209.

Branco, T., Clark, B. A. & Hausser, M. 2010. Dendritic discrimination of temporal input sequences in cortical neurons. Science, 329, 1671-5.

Brock, L. G., Coombs, J. S. & Eccles, J. C. 1952. The recording of potentials from motoneurones with an intracellular electrode. The Journal of Physiology, 117, 431-460.

Bullen, A. & Saggau, P. 1998. Indicators and optical configuration for simultaneous high-resolution recording of membrane potential and intracellular calcium using laser scanning microscopy. Pflugers Arch, 436, 788-96.
Bullen, A., Patel, S. S. & Saggau, P. 1997. High-speed, random-access fluorescence microscopy: I. High-resolution optical recording with voltage-sensitive dyes and ion indicators. Biophys J, 73, 477-91.
Cajal, S. R. y. 1889. Contribución al estudio de la estructura de la médula espinal. Rev.
Cameron, M., Kekesi, O., Morley, J. W., Tapson, J., Breen, P. P., van Schaik, A. & Buskila, Y. 2016. Calcium Imaging of AM Dyes Following Prolonged Incubation in Acute Neuronal Tissue. PLoS One, 11, e0155468.
Canepari, M., Djurisic, M. & Zecevic, D. 2007. Dendritic signals from rat hippocampal CA1 pyramidal neurons during coincident pre- and post-synaptic activity: a combined voltage- and calcium-imaging study. J Physiol, 580, 463-84.
Canepari, M., Vogt, K. E., De Waard, M. & Zecevic, D. 2013. Combining Ca2+ and membrane potential imaging in single neurons. Cold Spring Harb Protoc, 2013, 1161-4.
Carafoli, E. 1991. Calcium pump of the plasma membrane. Physiol Rev, 71, 129-53.
Carandini, M., Shimaoka, D., Rossi, L. F., Sato, T. K., Benucci, A. & Knopfel, T. 2015. Imaging the Awake Visual Cortex with a Genetically Encoded Voltage Indicator. Journal of Neuroscience, 35, 53-63.
Castanares, M. L., Gautam, V., Drury, J., Bachor, H. & Daria, V. R. 2016. Efficient multi-site two-photon functional imaging of neuronal circuits. Biomedical Optics Express, 7, 5325-5334.
Castanares, M. L., Stuart, G. J. & Daria, V. R. 2019. Holographic Functional Calcium Imaging of Neuronal Circuit Activity. In: KAO, F.-J., KEISER, G. & GOGOI, A. (eds.) Advanced Optical Methods for Brain Imaging. Singapore: Springer.
Castanares, M., Gautam, V., Drury, J., Bachor, H. A. & Daria, V. R. 2015. Improving holographic multi-site fluorescence excitation via temporal gating. Australian and New Zealand Conference on Optics and Photonics. Adelaide, South Australia.
Catterall, W. A. 2000. Structure and regulation of voltage-gated Ca2+ channels. Annu Rev Cell Dev Biol, 16, 521-55.
Chagnac-Amitai, Y., Luhmann, H. J. & Prince, D. A. 1990. Burst Generating and Regular Spiking Layer-5 Pyramidal Neurons of Rat Neocortex Have Different Morphological Features. Journal of Comparative Neurology, 296, 598-613.
Chamberland, S., Yang, H. H., Pan, M. M., Evans, S. W., Guan, S., Chavarha, M., Yang, Y., Salesse, C., Wu, H., Wu, J. C., Clandinin, T. R., Toth, K., Lin, M. Z. & St-Pierre, F. 2017. Fast two-photon imaging of subcellular voltage dynamics in neuronal tissue with genetically encoded indicators. Elife, 6.
Chen, C. 2005. beta-Amyloid increases dendritic Ca2+ influx by inhibiting the A-type K+ current in hippocampal CA1 pyramidal neurons. Biochem Biophys Res Commun, 338, 1913-9.
Chen, T. W., Wardill, T. J., Sun, Y., Pulver, S. R., Renninger, S. L., Baohan, A., Schreiter, E. R., Kerr, R. A., Orger, M. B., Jayaraman, V., Looger, L. L., Svoboda, K. & Kim, D. S. 2013. Ultrasensitive fluorescent proteins for imaging neuronal activity. Nature, 499, 295-300.
Christie, B. R., Eliot, L. S., Ito, K., Miyakawa, H. & Johnston, D. 1995. Different Ca2+ channels in soma and dendrites of hippocampal pyramidal neurons mediate spike-induced Ca2+ influx. J Neurophysiol, 73, 2553-7.
Clapham, D. E. 2007. Calcium Signaling. Cell, 131, 1047-1058.
Clements, J. D., Lester, R. A., Tong, G., Jahr, C. E. & Westbrook, G. L. 1992. The time course of glutamate in the synaptic cleft. Science, 258, 1498-501.
Colbert, C. M. & Pan, E. 2002. Ion channel properties underlying axonal action potential initiation in pyramidal neurons. Nat Neurosci, 5, 533-8.
Connor, J. A. 1986. Digital imaging of free calcium changes and of spatial gradients in growing processes in single, mammalian central nervous system cells. Proc Natl Acad Sci U S A, 83, 6179-83.
Dal Maschio, M., Difato, F., Beltramo, R., Blau, A., Benfenati, F. & Fellin, T. 2010. Simultaneous two-photon imaging and photo-stimulation with structured light illumination. Opt Express, 18, 18720-31.
Dale, H. H. 1906. On some physiological actions of ergot. J Physiol, 34, 163-206.
Daria, V. R. & Bachor, H.-A. 2015. Using light to probe neuronal function. EPL (Europhysics Letters), 111, 38001.
Daria, V. R., Stricker, C., Bowman, R., Redman, S. & Bachor, H. A. 2009. Arbitrary multisite two-photon excitation in four dimensions. Applied Physics Letters, 95.
de Kock, C. P. & Sakmann, B. 2008. High frequency action potential bursts (>or= 100 Hz) in L2/3 and L5B thick tufted neurons in anaesthetized and awake rat primary somatosensory cortex. J Physiol, 586, 3353-64.
de Kock, C. P. & Sakmann, B. 2009. Spiking in primary somatosensory cortex during natural whisking in awake head-restrained rats is cell-type specific. Proc Natl Acad Sci U S A, 106, 16446-50.

de Kock, C. P., Bruno, R. M., Spors, H. & Sakmann, B. 2007. Layer- and cell-type-specific suprathreshold stimulus representation in rat primary somatosensory cortex. J Physiol, 581, 139-54.
DeFelipe, J. & Farinas, I. 1992. The pyramidal neuron of the cerebral cortex: morphological and chemical characteristics of the synaptic inputs. Prog Neurobiol, 39, 563-607.
Dempsey, B., Turner, A. J., Le, S., Sun, Q. J., Bou Farah, L., Allen, A. M., Goodchild, A. K. & McMullan, S. 2015. Recording, labeling, and transfection of single neurons in deep brain structures. Physiol Rep, 3.
Denk, W., Strickler, J. H. & Webb, W. W. 1990. Two-photon laser scanning fluorescence microscopy. Science, 248, 73-6.
Dombeck, D. A., Sacconi, L., Blanchard-Desce, M. & Webb, W. W. 2005. Optical recording of fast neuronal membrane potential transients in acute mammalian brain slices by second-harmonic generation microscopy. Journal of Neurophysiology, 94, 3628-3636.
Donnert, G., Eggeling, C. & Hell, S. W. 2007. Major signal increase in fluorescence microscopy through dark-state relaxation. Nature Methods, 4, 81-86.
Donnert, G., Eggeling, C. & Hell, S. W. 2009. Triplet-relaxation microscopy with bunched pulsed excitation. Photochemical & Photobiological Sciences, 8, 481-485.
Ducros, M., Houssen, Y. G., Bradley, J., de Sars, V. & Charpak, S. 2013. Encoded multisite two-photon microscopy. Proceedings of the National Academy of Sciences of the United States of America, 110, 13138-13143.
Eccles, J. C. 1972. The ionic mechanism of postsynaptic inhibition. Nobel Lecture, December 11,
Egger, V., Nevian, T. & Bruno, R. M. 2008. Subcolumnar dendritic and axonal organization of spiny stellate and star pyramid neurons within a barrel in rat somatosensory cortex. Cereb Cortex, 18, 876-89.
Eilers, J. & Konnerth, A. 2009. Dye loading with patch pipettes. Cold Spring Harb Protoc, 2009, pdb prot5201.
Emiliani, V., Cohen, A. E., Deisseroth, K. & Hausser, M. 2015. All-Optical Interrogation of Neural Circuits. J Neurosci, 35, 13917-26.
Etherington, S. J., Atkinson, S. E., Stuart, G. J. & Williams, S. R. 2001. Synaptic Integration. eLS. John Wiley & Sons, Ltd.
Felleman, D. J. & Van Essen, D. C. 1991. Distributed Hierarchical Processing in the Primate Cerebral Cortex. Cerebral Cortex, 1, 1-47.
Ferrante, M., Migliore, M. & Ascoli, G. A. 2013. Functional Impact of Dendritic Branch-Point Morphology. Journal of Neuroscience, 33, 2156-2165.
Ferrer, I., Fabregues, I. & Condom, E. 1986. A Golgi study of the sixth layer of the cerebral cortex. I. The lissencephalic brain of Rodentia, Lagomorpha, Insectivora and Chiroptera. J Anat, 145, 217-34.
Fink, A. E., Bender, K. J., Trussell, L. O., Otis, T. S. & DiGregorio, D. A. 2012. Two-Photon Compatibility and Single-Voxel, Single-Trial Detection of Subthreshold Neuronal Activity by a Two-Component Optical Voltage Sensor. Plos One, 7.
Fishman, M. C. 1972. Sir Henry Hallett Dale and acetylcholine story. Yale J Biol Med, 45, 104-18.
Fluhler, E., Burnham, V. G. & Loew, L. M. 1985. Spectra, membrane binding, and potentiometric responses of new charge shift probes. Biochemistry, 24, 5749-55.
Foust, A. J., Zampini, V., Tanese, D., Papagiakoumou, E. & Emiliani, V. 2015. Computer-generated holography enhances voltage dye fluorescence discrimination in adjacent neuronal structures. Neurophotonics, 2, 021007-021007.
Foust, A., Popovic, M., Zecevic, D. & McCormick, D. A. 2010. Action potentials initiate in the axon initial segment and propagate through axon collaterals reliably in cerebellar Purkinje neurons. J Neurosci, 30, 6891-902.
Frick, A., Magee, J., Koester, H. J., Migliore, M. & Johnston, D. 2003. Normalization of Ca2+ signals by small oblique dendrites of CA1 pyramidal neurons. Journal of Neuroscience, 23, 3243-3250.
Fromherz, P., Hubener, G., Kuhn, B. & Hinner, M. J. 2008. ANNINE-6plus, a voltage-sensitive dye with good solubility, strong membrane binding and high sensitivity. European Biophysics Journal with Biophysics Letters, 37, 509-514.
Gambino, F., Pages, S., Kehayas, V., Baptista, D., Tatti, R., Carleton, A. & Holtmaat, A. 2014. Sensory-evoked LTP driven by dendritic plateau potentials in vivo. Nature, 515, 116-9.
Gasparini, S. 2011. Distance- and activity-dependent modulation of spike back-propagation in layer V pyramidal neurons of the medial entorhinal cortex. J Neurophysiol, 105, 1372-9.
Gasparini, S., Losonczy, A., Chen, X., Johnston, D. & Magee, J. C. 2007. Associative pairing enhances action potential back-propagation in radial oblique branches of CA1 pyramidal neurons. J Physiol, 580, 787-800.
Gasparini, S., Migliore, M. & Magee, J. C. 2004. On the initiation and propagation of dendritic spikes in CA1 pyramidal neurons. Journal of Neuroscience, 24, 11046-11056.
Go, M. A., Choy, J. M., Colibaba, A. S., Redman, S., Bachor, H. A., Stricker, C. & Daria, V. R. 2016. Targeted pruning of a neuron's dendritic tree via femtosecond laser dendrotomy. Sci Rep, 6, 19078.

Go, M. A., Mueller, M., Castanares, M. L., Egger, V. & Daria, V. R. 2019. A compact holographic projector module for high-resolution 3D multi-site two-photon photostimulation. PLoS One, 14, e0210564.
Golding, N. L. & Spruston, N. 1998. Dendritic sodium spikes are variable triggers of axonal action potentials in hippocampal CA1 pyramidal neurons. Neuron, 21, 1189-200.
Golding, N. L., Jung, H. Y., Mickus, T. & Spruston, N. 1999. Dendritic calcium spike initiation and repolarization are controlled by distinct potassium channel subtypes in CA1 pyramidal neurons. J Neurosci, 19, 8789-98.
Golding, N. L., Staff, N. P. & Spruston, N. 2002. Dendritic spikes as a mechanism for cooperative long-term potentiation. Nature, 418, 326-331.
Goldstein, S. S. & Rall, W. 1974. Changes of action potential shape and velocity for changing core conductor geometry. Biophys J, 14, 731-57.
Golgi, C. 1906. The neuron doctrine—theory and facts. Nobel Lecture, December 11, *1906.,* New York, Elsevier Publishing.
Gong, Y., Huang, C., Li, J. Z., Grewe, B. F., Zhang, Y., Eismann, S. & Schnitzer, M. J. 2015. High-speed recording of neural spikes in awake mice and flies with a fluorescent voltage sensor. Science, 350, 1361-6.
Gong, Y., Wagner, M. J., Zhong Li, J. & Schnitzer, M. J. 2014. Imaging neural spiking in brain tissue using FRET-opsin protein voltage sensors. Nat Commun, 5, 3674.
Grewe, B. F., Bonnan, A. & Frick, A. 2010. Back-propagation of physiological action potential output in dendrites of slender-tufted L5A pyramidal neurons. Frontiers in Cellular Neuroscience, 4.
Grewe, B., Helmchen, F. & Kampa, B. 2014. Two-Photon Imaging of Neuronal Network Dynamics in Neocortex. In: WEBER, B. & HELMCHEN, F. (eds.) Optical Imaging of Neocortical Dynamics. Humana Press.
Grienberger, C. & Konnerth, A. 2012. Imaging calcium in neurons. Neuron, 73, 862-85.
Groh, A., Meyer, H. S., Schmidt, E. F., Heintz, N., Sakmann, B. & Krieger, P. 2010. Cell-Type Specific Properties of Pyramidal Neurons in Neocortex Underlying a Layout that Is Modifiable Depending on the Cortical Area. Cerebral Cortex, 20, 826-836.
Grynkiewicz, G., Poenie, M. & Tsien, R. Y. 1985. A New Generation of Ca-2+ Indicators with Greatly Improved Fluorescence Properties. Journal of Biological Chemistry, 260, 3440-3450.
Haas, K., Sin, W. C., Javaherian, A., Li, Z. & Cline, H. T. 2001. Single-cell electroporation for gene transfer in vivo. Neuron, 29, 583-591.
Hattox, A. M. & Nelson, S. B. 2007. Layer V neurons in mouse cortex projecting to different targets have distinct physiological properties. Journal of Neurophysiology, 98, 3330-3340.
Hausser, M. 2014. Optogenetics: the age of light. Nat Methods, 11, 1012-4.
Hay, E., Hill, S., Schurmann, F., Markram, H. & Segev, I. 2011. Models of Neocortical Layer 5b Pyramidal Cells Capturing a Wide Range of Dendritic and Perisomatic Active Properties. Plos Computational Biology, 7.
Heim, N., Garaschuk, O., Friedrich, M. W., Mank, M., Milos, R. I., Kovalchuk, Y., Konnerth, A. & Griesbeck, O. 2007. Improved calcium imaging in transgenic mice expressing a troponin C-based biosensor. Nat Methods, 4, 127-9.
Helmchen, F. & Tank, D. W. 2015. A single-compartment model of calcium dynamics in nerve terminals and dendrites. Cold Spring Harb Protoc, 2015, 155-67.
Higley, M. J. & Sabatini, B. L. 2008. Calcium signaling in dendrites and spines: practical and functional considerations. Neuron, 59, 902-13.
Hill, D. N., Varga, Z., Jia, H., Sakmann, B. & Konnerth, A. 2013. Multibranch activity in basal and tuft dendrites during firing of layer 5 cortical neurons in vivo. Proc Natl Acad Sci U S A, 110, 13618-23.
Hille, B. 2001. Ion Channels of Excitable Membranes, 23 Plumtree Road, Sunderland, MA 01375, U.S.A, Sinauer Associates, Inc.
Hochbaum, D. R., Zhao, Y., Farhi, S. L., Klapoetke, N., Werley, C. A., Kapoor, V., Zou, P., Kralj, J. M., Maclaurin, D., Smedemark-Margulies, N., Saulnier, J. L., Boulting, G. L., Straub, C., Cho, Y. K., Melkonian, M., Wong, G. K., Harrison, D. J., Murthy, V. N., Sabatini, B. L., Boyden, E. S., Campbell, R. E. & Cohen, A. E. 2014. All-optical electrophysiology in mammalian neurons using engineered microbial rhodopsins. Nat Methods, 11, 825-33.
Hodgkin, A. L. & Huxley, A. F. 1952. A quantitative description of membrane current and its application to conduction and excitation in nerve. J Physiol, 117, 500-44.
Hoffman, D. A., Magee, J. C., Colbert, C. M. & Johnston, D. 1997. K+ channel regulation of signal propagation in dendrites of hippocampal pyramidal neurons. Nature, 387, 869-75.
Holthoff, K., Zecevic, D. & Konnerth, A. 2010. Rapid time course of action potentials in spines and remote dendrites of mouse visual cortex neurons. J Physiol, 588, 1085-96.
Huisken, J. & Stainier, D. Y. 2009. Selective plane illumination microscopy techniques in developmental biology. Development, 136, 1963-75.
Huisken, J., Swoger, J., Del Bene, F., Wittbrodt, J. & Stelzer, E. H. 2004. Optical sectioning deep inside live embryos by selective plane illumination microscopy. Science, 305, 1007-9.

Jiang, X., Shen, S., Cadwell, C. R., Berens, P., Sinz, F., Ecker, A. S., Patel, S. & Tolias, A. S. 2015. Principles of connectivity among morphologically defined cell types in adult neocortex. Science, 350, aac9462.
Judkewitz, B., Rizzi, M., Kitamura, K. & Hausser, M. 2009. Targeted single-cell electroporation of mammalian neurons in vivo. Nature Protocols, 4, 862-869.
Kamondi, A., Acsady, L. & Buzsaki, G. 1998. Dendritic spikes are enhanced by cooperative network activity in the intact hippocampus. J Neurosci, 18, 3919-28.
Kampa, B. M. & Stuart, G. J. 2006. Calcium spikes in basal dendrites of layer 5 pyramidal neurons during action potential bursts. Journal of Neuroscience, 26, 7424-7432.
Kampa, B. M., Letzkus, J. J. & Stuart, G. J. 2006. Requirement of dendritic calcium spikes for induction of spike-timing-dependent synaptic plasticity. Journal of Physiology-London, 574, 283-290.
Katona, G., Kaszas, A., Turi, G. F., Hajos, N., Tamas, G., Vizi, E. S. & Rozsa, B. 2011. Roller Coaster Scanning reveals spontaneous triggering of dendritic spikes in CA1 interneurons. Proc Natl Acad Sci U S A, 108, 2148-53.
Katona, G., Szalay, G., Maak, P., Kaszas, A., Veress, M., Hillier, D., Chiovini, B., Vizi, E. S., Roska, B. & Rozsa, B. 2012. Fast two-photon in vivo imaging with three-dimensional random-access scanning in large tissue volumes. Nat Methods, 9, 201-8.
Kim, H. G. & Connors, B. W. 1993. Apical dendrites of the neocortex: correlation between sodium- and calcium-dependent spiking and pyramidal cell morphology. J Neurosci, 13, 5301-11.
Koester, H. J. & Sakmann, B. 1998. Calcium dynamics in single spines during coincident pre- and postsynaptic activity depend on relative timing of back-propagating action potentials and subthreshold excitatory postsynaptic potentials. Proc Natl Acad Sci U S A, 95, 9596-601.
Kohler, M., Hirschberg, B., Bond, C. T., Kinzie, J. M., Marrion, N. V., Maylie, J. & Adelman, J. P. 1996. Small-conductance, calcium-activated potassium channels from mammalian brain. Science, 273, 1709-14.
Kole, M. H., Hallermann, S. & Stuart, G. J. 2006. Single Ih channels in pyramidal neuron dendrites: properties, distribution, and impact on action potential output. J Neurosci, 26, 1677-87.
Kralj, J. M., Douglass, A. D., Hochbaum, D. R., Maclaurin, D. & Cohen, A. E. 2012. Optical recording of action potentials in mammalian neurons using a microbial rhodopsin. Nat Meth, 9, 90-95.
Kuhn, B., Fromherz, P. & Denk, W. 2004. High sensitivity of stark-shift voltage-sensing dyes by one- or two-photon excitation near the red spectral edge. Biophysical Journal, 87, 631-639.
Larkum, M. 2013. A cellular mechanism for cortical associations: an organizing principle for the cerebral cortex. Trends in Neurosciences, 36, 141-151.
Larkum, M. E., Kaiser, K. M. M. & Sakmann, B. 1999. Calcium electrogenesis in distal apical dendrites of layer 5 pyramidal cells at a critical frequency of back-propagating action potentials. Proceedings of the National Academy of Sciences of the United States of America, 96, 14600-14604.
Larkum, M. E., Kaiser, K. M. M. & Sakmann, B. 1999a. Calcium electrogenesis in distal apical dendrites of layer 5 pyramidal cells at a critical frequency of back-propagating action potentials. Proceedings of the National Academy of Sciences of the United States of America, 96, 14600-14604.
Larkum, M. E., Nevian, T., Sandler, M., Polsky, A. & Schiller, J. 2009. Synaptic integration in tuft dendrites of layer 5 pyramidal neurons: a new unifying principle. Science, 325, 756-60.
Larkum, M. E., Waters, J., Sakmann, B. & Helmchen, F. 2007. Dendritic spikes in apical dendrites of neocortical layer 2/3 pyramidal neurons. J Neurosci, 27, 8999-9008.
Larkum, M. E., Zhu, J. J. & Sakmann, B. 1999b. A new cellular mechanism for coupling inputs arriving at different cortical layers. Nature, 398, 338-341.
Lasser-Ross, N., Miyakawa, H., Lev-Ram, V., Young, S. R. & Ross, W. N. 1991. High time resolution fluorescence imaging with a CCD camera. J Neurosci Methods, 36, 253-61.
Lavzin, M., Rapoport, S., Polsky, A., Garion, L. & Schiller, J. 2012. Nonlinear dendritic processing determines angular tuning of barrel cortex neurons in vivo. Nature, 490, 397-401.
Ledergerber, D. & Larkum, M. E. 2010. Properties of Layer 6 Pyramidal Neuron Apical Dendrites. Journal of Neuroscience, 30, 13031-13044.
Lichtman, J. W. & Denk, W. 2011. The big and the small: challenges of imaging the brain's circuits. Science, 334, 618-23.
Loew, L. 2010. Design and Use of Organic Voltage sensitive Dyes. In: CANEPARI, M. & ZECEVIC, D. (eds.) Membrane Potential Imaging in the Nervous system. Springer
Loew, L. 2011. Design and Use of Organic Voltage Sensitive Dyes. In: CANEPARI, M. & ZECEVIC, D. (eds.) Membrane Potential Imaging in the Nervous System. Springer New York.
Loew, L. M., Cohen, L. B., Dix, J., Fluhler, E. N., Montana, V., Salama, G. & Wu, J. Y. 1992. A naphthyl analog of the aminostyryl pyridinium class of potentiometric membrane dyes shows consistent sensitivity in a variety of tissue, cell, and model membrane preparations. J Membr Biol, 130, 1-10.
Loew, L. M., Scully, S., Simpson, L. & Waggoner, A. S. 1979. Evidence for a charge-shift electrochromic mechanism in a probe of membrane potential. Nature, 281, 497-9.

London, M. & Hausser, M. 2005. Dendritic computation. Annu Rev Neurosci, 28, 503-32.
Longair, M. H., Baker, D. A. & Armstrong, J. D. 2011. Simple Neurite Tracer: open source software for reconstruction, visualization and analysis of neuronal processes. Bioinformatics, 27, 2453-4.
Losonczy, A. & Magee, J. C. 2006. Integrative properties of radial oblique dendrites in hippocampal CA1 pyramidal neurons. Neuron, 50, 291-307.
Lubke, J., Egger, V., Sakmann, B. & Feldmeyer, D. 2000. Columnar organization of dendrites and axons of single and synaptically coupled excitatory spiny neurons in layer 4 of the rat barrel cortex. J Neurosci, 20, 5300-11.
Magee, J. C. & Johnston, D. 1997. A synaptically controlled, associative signal for Hebbian plasticity in hippocampal neurons. Science, 275, 209-13.
Magistretti, J. & Alonso, A. 1999. Biophysical properties and slow voltage-dependent inactivation of a sustained sodium current in entorhinal cortex layer-II principal neurons: a whole-cell and single-channel study. J Gen Physiol, 114, 491-509.
Major, G., Larkum, M. E. & Schiller, J. 2013. Active properties of neocortical pyramidal neuron dendrites. Annu Rev Neurosci, 36, 1-24.
Major, G., Polsky, A., Denk, W., Schiller, J. & Tank, D. W. 2008. Spatiotemporally graded NMDA spike/plateau potentials in basal dendrites of neocortical pyramidal neurons. Journal of Neurophysiology, 99, 2584-2601.
Manita, S., Miyakawa, H., Kitamura, K. & Murayama, M. 2017. Dendritic Spikes in Sensory Perception. Front Cell Neurosci, 11, 29.
Markram, H. & Sakmann, B. 1994. Calcium transients in dendrites of neocortical neurons evoked by single subthreshold excitatory postsynaptic potentials via low-voltage-activated calcium channels. Proceedings of the National Academy of Sciences, 91, 5207.
Markram, H., Lubke, J., Frotscher, M. & Sakmann, B. 1997. Regulation of synaptic efficacy by coincidence of postsynaptic APs and EPSPs. Science, 275, 213-5.
Markram, H., Lubke, J., Frotscher, M., Roth, A. & Sakmann, B. 1997. Physiology and anatomy of synaptic connections between thick tufted pyramidal neurones in the developing rat neocortex. J Physiol, 500 (Pt 2), 409-40.
Markram, H., Muller, E., Ramaswamy, S., Reimann, M. W., Abdellah, M., Sanchez, C. A., Ailamaki, A., Alonso-Nanclares, L., Antille, N., Arsever, S., Kahou, G. A. A., Berger, T. K., Bilgili, A., Buncic, N., Chalimourda, A., Chindemi, G., Courcol, J. D., Delalondre, F., Delattre, V., Druckmann, S., Dumusc, R., Dynes, J., Eilemann, S., Gal, E., Gevaert, M. E., Ghobril, J. P., Gidon, A., Graham, J. W., Gupta, A., Haenel, V., Hay, E., Heinis, T., Hernando, J. B., Hines, M., Kanari, L., Keller, D., Kenyon, J., Khazen, G., Kim, Y., King, J. G., Kisvarday, Z., Kumbhar, P., Lasserre, S., Le Be, J. V., Magalhaes, B. R. C., Merchan-Perez, A., Meystre, J., Morrice, B. R., Muller, J., Munoz-Cespedes, A., Muralidhar, S., Muthurasa, K., Nachbaur, D., Newton, T. H., Nolte, M., Ovcharenko, A., Palacios, J., Pastor, L., Perin, R., Ranjan, R., Riachi, I., Rodriguez, J. R., Riquelme, J. L., Rossert, C., Sfyrakis, K., Shi, Y., Shillcock, J. C., Silberberg, G., Silva, R., Tauheed, F., Telefont, M., Toledo-Rodriguez, M., Trankler, T., Van Geit, W., Diaz, J. V., Walker, R., Wang, Y., Zaninetta, S. M., DeFelipe, J., Hill, S. L., Segev, I. & Schurmann, F. 2015. Reconstruction and Simulation of Neocortical Microcircuitry. Cell, 163, 456-492.
Mel, B. W. 1993. Synaptic integration in an excitable dendritic tree. J Neurophysiol, 70, 1086-101.
Mel, B. W. 1994. Information-Processing in Dendritic Trees. Neural Computation, 6, 1031-1085.
Migliore, M., Ferrante, M. & Ascoli, G. A. 2005. Signal propagation in oblique dendrites of CA1 pyramidal cells. J Neurophysiol, 94, 4145-55.
Milojkovic, B. A., Radojicic, M. S., Goldman-Rakic, P. S. & Antic, S. D. 2004. Burst generation in rat pyramidal neurones by regenerative potentials elicited in a restricted part of the basilar dendritic tree. J Physiol, 558, 193-211.
Minta, A., Kao, J. P. Y. & Tsien, R. Y. 1989. Fluorescent Indicators for Cytosolic Calcium Based on Rhodamine and Fluorescein Chromophores. Journal of Biological Chemistry, 264, 8171-8178.
Miyakawa, H., Ross, W. N., Jaffe, D., Callaway, J. C., Lasser-Ross, N., Lisman, J. E. & Johnston, D. 1992. Synaptically activated increases in Ca2+ concentration in hippocampal CA1 pyramidal cells are primarily due to voltage-gated Ca2+ channels. Neuron, 9, 1163-1173.
Miyawaki, A., Llopis, J., Heim, R., McCaffery, J. M., Adams, J. A., Ikura, M. & Tsien, R. Y. 1997. Fluorescent indicators for Ca2+ based on green fluorescent proteins and calmodulin. Nature, 388, 882-7.
Moreaux, L., Blanchard-Desce, M. & Mertz, J. 2002. Second harmonic generation microscopy and membrane potential imaging. Biophysical Journal, 82, 499a-499a.
Moreaux, L., Sandre, O., Blanchard-Desce, M. & Mertz, J. 2000. Membrane imaging by simultaneous second-harmonic generation and two-photon microscopy. Opt Lett, 25, 320-2.
Mountcastle, V. B. 1997. The columnar organization of the neocortex. Brain, 120 (Pt 4), 701-22.
Nakai, J., Ohkura, M. & Imoto, K. 2001. A high signal-to-noise Ca2+ probe composed of a single green fluorescent protein. Nature Biotechnology, 19, 137.

Nevian, T. & Helmchen, F. 2007. Calcium indicator loading of neurons using single-cell electroporation. Pflugers Archiv-European Journal of Physiology, 454, 675-688.
Nevian, T., Larkum, M. E., Polsky, A. & Schiller, J. 2007. Properties of basal dendrites of layer 5 pyramidal neurons: a direct patch-clamp recording study. Nat Neurosci, 10, 206-14.
Nikolenko, V., Watson, B. O., Araya, R., Woodruff, A., Peterka, D. S. & Yuste, R. 2008. SLM Microscopy: Scanless Two-Photon Imaging and Photostimulation with Spatial Light Modulators. Front Neural Circuits, 2, 5.
Oberlaender, M., Boudewijns, Z. S., Kleele, T., Mansvelder, H. D., Sakmann, B. & de Kock, C. P. 2011. Three-dimensional axon morphologies of individual layer 5 neurons indicate cell type-specific intracortical pathways for whisker motion and touch. Proc Natl Acad Sci U S A, 108, 4188-93.
Oberlaender, M., de Kock, C. P., Bruno, R. M., Ramirez, A., Meyer, H. S., Dercksen, V. J., Helmstaedter, M. & Sakmann, B. 2012. Cell type-specific three-dimensional structure of thalamocortical circuits in a column of rat vibrissal cortex. Cereb Cortex, 22, 2375-91.
Palima, D. & Daria, V. R. 2006. Effect of spurious diffraction orders in arbitrary multifoci patterns produced via phase-only holograms. Applied Optics, 45, 6689-6693.
Palmer, L. M. & Stuart, G. J. 2006. Site of action potential initiation in layer 5 pyramidal neurons. Journal of Neuroscience, 26, 1854-1863.
Palmer, L. M. & Stuart, G. J. 2009. Membrane potential changes in dendritic spines during action potentials and synaptic input. J Neurosci, 29, 6897-903.
Palmer, L. M., Shai, A. S., Reeve, J. E., Anderson, H. L., Paulsen, O. & Larkum, M. E. 2014. NMDA spikes enhance action potential generation during sensory input. Nat Neurosci, 17, 383-90.
Paxinos, G. & Watson, C. 2006. The Rat Brain in Stereotaxic Coordinates, US, Elsevier Science Publishing Co Inc.
Penner, R. 1995. A Practical Guide to Patch Clamping. In: SAKMANN, B. & NEHER, E. (eds.) Single-Channel Recording. 2nd ed. New York: Springer Science+Business Media.
Peterka, D. S., Takahashi, H. & Yuste, R. 2011. Imaging voltage in neurons. Neuron, 69, 9-21.
Petersen, C. C. 2007. The functional organization of the barrel cortex. Neuron, 56, 339-55.
Picot, A., Dominguez, S., Liu, C., Chen, I. W., Tanese, D., Ronzitti, E., Berto, P., Papagiakoumou, E., Oron, D., Tessier, G., Forget, B. C. & Emiliani, V. 2018. Temperature Rise under Two-Photon Optogenetic Brain Stimulation. Cell Rep, 24, 1243-1253 e5.
Podgorski, K. & Ranganathan, G. 2016. Brain heating induced by near-infrared lasers during multiphoton microscopy. J Neurophysiol, 116, 1012-23.
Popovic, M. A., Foust, A. J., McCormick, D. A. & Zecevic, D. 2011. The spatio-temporal characteristics of action potential initiation in layer 5 pyramidal neurons: a voltage imaging study. J Physiol, 589, 4167-87.
Popovic, M. A., Gao, X., Carnevale, N. T. & Zecevic, D. 2014. Cortical dendritic spine heads are not electrically isolated by the spine neck from membrane potential signals in parent dendrites. Cereb Cortex, 24, 385-95.
Popovic, M., Gao, X. & Zecevic, D. 2012. Voltage-sensitive Dye Recording from Axons, Dendrites and Dendritic Spines of Individual Neurons in Brain Slices. Jove-Journal of Visualized Experiments.
Popovic, M., Vogt, K., Holthoff, K., Konnerth, A., Salzberg, B. M., Grinvald, A., Antic, S. D., Canepari, M. & Zecevic, D. 2015. Imaging Submillisecond Membrane Potential Changes from Individual Regions of Single Axons, Dendrites and Spines. Adv Exp Med Biol, 859, 57-101.
Purves, D. 2004. Synaptic transmission. In: PURVES, D., AUGUSTINE, G. J., FITZPATRICK, D., HALL, W. C., LAMANTIA, A.-S., MCNAMARA, J. O. & MARK WILLIAMS, S. (eds.) Neuroscience. 3rd ed. Sunderland, Massachusetts, U.S.A: Sinauer Associates, Inc.
Rall, W. 1959. Branching Dendritic Trees and Motoneuron Membrane Resistivity. Experimental Neurology, 1, 491-527.
Rama, S. 2015. Shift and Mean Algorithm for Functional Imaging with High Spatio-Temporal Resolution. Front Cell Neurosci, 9, 446.
Ranganathan, G. N., Apostolides, P. F., Harnett, M. T., Xu, N. L., Druckmann, S. & Magee, J. C. 2018. Active dendritic integration and mixed neocortical network representations during an adaptive sensing behavior. Nat Neurosci, 21, 1583-1590.
Reuveni, I., Friedman, A., Amitai, Y. & Gutnick, M. J. 1993. Stepwise repolarization from Ca2+ plateaus in neocortical pyramidal cells: evidence for nonhomogeneous distribution of HVA Ca2+ channels in dendrites. J Neurosci, 13, 4609-21.
Rojo, C., Leguey, I., Kastanauskaite, A., Bielza, C., Larranaga, P., DeFelipe, J. & Benavides-Piccione, R. 2016. Laminar Differences in Dendritic Structure of Pyramidal Neurons in the Juvenile Rat Somatosensory Cortex. Cereb Cortex, 26, 2811-2822.
Roome, C. J. & Kuhn, B. 2018. Simultaneous dendritic voltage and calcium imaging and somatic recording from Purkinje neurons in awake mice. Nat Commun, 9, 3388.

Saggau, P., Bullen, A. & Patel, S. S. 1998. Acousto-optic random-access laser scanning microscopy: fundamentals and applications to optical recording of neuronal activity. Cell Mol Biol (Noisy-le-grand), 44, 827-46.
Sakmann, B. & Neher, E. 1984. Patch clamp techniques for studying ionic channels in excitable membranes. Annu Rev Physiol, 46, 455-72.
Schaefer, A. T., Larkum, M. E., Sakmann, B. & Roth, A. 2003. Coincidence detection in pyramidal neurons is tuned by their dendritic branching pattern. J Neurophysiol, 89, 3143-54.
Schiller, J., Major, G., Koester, H. J. & Schiller, Y. 2000. NMDA spikes in basal dendrites of cortical pyramidal neurons. Nature, 404, 285-9.
Schiller, J., Schiller, Y., Stuart, G. & Sakmann, B. 1997. Calcium action potentials restricted to distal apical dendrites of rat neocortical pyramidal neurons. J Physiol, 505 (Pt 3), 605-16.
Schiller, Y. 2002. Inter-ictal- and ictal-like epileptic discharges in the dendritic tree of neocortical pyramidal neurons. Journal of Neurophysiology, 88, 2954-2962.
Schuck, R., Go, M. A., Garasto, S., Reynolds, S., Dragotti, P. L. & Schultz, S. R. 2018. Multiphoton minimal inertia scanning for fast acquisition of neural activity signals. J Neural Eng, 15, 025003.
Shai, A. S., Anastassiou, C. A., Larkum, M. E. & Koch, C. 2015. Physiology of Layer 5 Pyramidal Neurons in Mouse Primary Visual Cortex: Coincidence Detection through Bursting. Plos Computational Biology, 11.
Shepherd, G. M. 2015a. From the Beginnings to the Cell Theory. Foundations of the Neuron Doctrine. 25th Anniversary Edition ed.: Oxford University Press.
Shepherd, G. M. 2015b. Joining the Mainstream. Foundations of the Neuron Doctrine. 25th Anniversary Edition ed.: Oxford University Press.
Sjostrom, P. J. & Hausser, M. 2006. A cooperative switch determines the sign of synaptic plasticity in distal dendrites of neocortical pyramidal neurons. Neuron, 51, 227-38.
Sjostrom, P. J., Turrigiano, G. G. & Nelson, S. B. 2001. Rate, timing, and cooperativity jointly determine cortical synaptic plasticity. Neuron, 32, 1149-64.
Smith, S. J. & Augustine, G. J. 1988. Calcium ions, active zones and synaptic transmitter release. Trends Neurosci, 11, 458-64.
Smith, S. L., Smith, I. T., Branco, T. & Häusser, M. 2013. Dendritic spikes enhance stimulus selectivity in cortical neurons in vivo. Nature, 503, 115-120.
Song, A., Charles, A. S., Koay, S. A., Gauthier, J. L., Thiberge, S. Y., Pillow, J. W. & Tank, D. W. 2017. Volumetric two-photon imaging of neurons using stereoscopy (vTwINS). Nat Methods, 14, 420-426.
Spruston, N. 2008. Pyramidal neurons: dendritic structure and synaptic integration. Nat Rev Neurosci, 9, 206-21.
St-Pierre, F., Marshall, J. D., Yang, Y., Gong, Y., Schnitzer, M. J. & Lin, M. Z. 2014. High-fidelity optical reporting of neuronal electrical activity with an ultrafast fluorescent voltage sensor. Nat Neurosci, 17, 884-9.
Stosiek, C., Garaschuk, O., Holthoff, K. & Konnerth, A. 2003. In vivo two-photon calcium imaging of neuronal networks. Proc Natl Acad Sci U S A, 100, 7319-24.
Stuart, G. & Spruston, N. 1998. Determinants of voltage attenuation in neocortical pyramidal neuron dendrites. J Neurosci, 18, 3501-10.
Stuart, G. J. & Sakmann, B. 1994. Active Propagation of Somatic Action-Potentials into Neocortical Pyramidal Cell Dendrites. Nature, 367, 69-72.
Stuart, G. J. & Spruston, N. 2015. Dendritic integration: 60 years of progress. Nature Neuroscience, 18, 1713-1721.
Svoboda, K., Denk, W., Kleinfeld, D. & Tank, D. W. 1997. In vivo dendritic calcium dynamics in neocortical pyramidal neurons. Nature, 385, 161-5.
Swanson, L. & Newman, E. 2016. Beautiful Brain: The Drawings of Ramon y Cajal, US, Harry N Abrams Inc.
Tada, M., Takeuchi, A., Hashizume, M., Kitamura, K. & Kano, M. 2014. A highly sensitive fluorescent indicator dye for calcium imaging of neural activity in vitro and in vivo. Eur J Neurosci, 39, 1720-8.
Tank, D. W., Sugimori, M., Connor, J. A. & Llinas, R. R. 1988. Spatially resolved calcium dynamics of mammalian Purkinje cells in cerebellar slice. Science, 242, 773-7.
Theer, P., Hasan, M. T. & Denk, W. 2003. Two-photon imaging to a depth of 1000 microm in living brains by use of a Ti:Al2O3 regenerative amplifier. Opt Lett, 28, 1022-4.
Theriault, G., Cottet, M., Castonguay, A., McCarthy, N. & De Koninck, Y. 2014. Extended two-photon microscopy in live samples with Bessel beams: steadier focus, faster volume scans, and simpler stereoscopic imaging. Front Cell Neurosci, 8, 139.
Tian, L., Hires, S. A., Mao, T., Huber, D., Chiappe, M. E., Chalasani, S. H., Petreanu, L., Akerboom, J., McKinney, S. A., Schreiter, E. R., Bargmann, C. I., Jayaraman, V., Svoboda, K. & Looger, L. L. 2009. Imaging neural activity in worms, flies and mice with improved GCaMP calcium indicators. Nat Methods, 6, 875-81.
Tischbirek, C., Birkner, A., Jia, H., Sakmann, B. & Konnerth, A. 2015. Deep two-photon brain imaging with a red-shifted fluorometric Ca2+ indicator. Proc Natl Acad Sci U S A, 112, 11377-82.

Todman, D. 2008. Henry Dale and the discovery of chemical synaptic transmission. Eur Neurol, 60, 162-4.
Tran-Van-Minh, A., Abrahamsson, T., Cathala, L. & DiGregorio, D. A. 2016. Differential Dendritic Integration of Synaptic Potentials and Calcium in Cerebellar Interneurons. Neuron, 91, 837-850.
trim. Histol. norm, patol, 1, 79-106.
Tsien, R. Y. 1980. New Calcium Indicators and Buffers with High Selectivity against Magnesium and Protons - Design, Synthesis, and Properties of Prototype Structures. Biochemistry, 19, 2396-2404.
Tsien, R. Y. 1981. A Non-Disruptive Technique for Loading Calcium Buffers and Indicators into Cells. Nature, 290, 527-528.
Tsien, R. Y., Pozzan, T. & Rink, T. J. 1982. T-Cell Mitogens Cause Early Changes in Cytoplasmic Free Ca(2+) and Membrane-Potential in Lymphocytes. Nature, 295, 68-71.
Verkhratsky, A. J. & Petersen, O. H. 1998. Neuronal calcium stores. Cell Calcium, 24, 333-43.
Vetter, P., Roth, A. & Hausser, M. 2001. Propagation of action potentials in dendrites depends on dendritic morphology. J Neurophysiol, 85, 926-37.
Voie, A. H., Burns, D. H. & Spelman, F. A. 1993. Orthogonal-plane fluorescence optical sectioning: three-dimensional imaging of macroscopic biological specimens. J Microsc, 170, 229-36.
Waggoner, A. S., Wang, C. H. & Tolles, R. L. 1977. Mechanism of potential-dependent light absorption changes of lipid bilayer membranes in the presence of cyanine and oxonol dyes. J Membr Biol, 33, 109-40.
Watkins, J. C. & Evans, R. H. 1981. Excitatory amino acid transmitters. Annu Rev Pharmacol Toxicol, 21, 165-204.
Whitaker, M. 2010. Genetically encoded probes for measurement of intracellular calcium. Methods Cell Biol, 99, 153-82.
Williams, D. A. & Fay, F. S. 1990. Intracellular calibration of the fluorescent calcium indicator Fura-2. Cell Calcium, 11, 75-83.
Williams, S. R. & Stuart, G. J. 1999. Mechanisms and consequences of action potential burst firing in rat neocortical pyramidal neurons. J Physiol, 521 Pt 2, 467-82.
Williams, S. R. & Stuart, G. J. 2000. Backpropagation of physiological spike trains in neocortical pyramidal neurons: Implications for temporal coding in dendrites. Journal of Neuroscience, 20, 8238-8246.
Williams, S. R. & Stuart, G. J. 2002. Dependence of EPSP efficacy on synapse location in neocortical pyramidal neurons. Science, 295, 1907-1910.
Wolf, S., Supatto, W., Debregeas, G., Mahou, P., Kruglik, S. G., Sintes, J. M., Beaurepaire, E. & Candelier, R. 2015. Whole-brain functional imaging with two-photon light-sheet microscopy. Nat Methods, 12, 379-80.
Xu, N. L., Harnett, M. T., Williams, S. R., Huber, D., O'Connor, D. H., Svoboda, K. & Magee, J. C. 2012. Nonlinear dendritic integration of sensory and motor input during an active sensing task. Nature, 492, 247-251.
Yan, P., Acker, C. D., Zhou, W. L., Lee, P., Bollensdorff, C., Negrean, A., Lotti, J., Sacconi, L., Antic, S. D., Kohl, P., Mansvelder, H. D., Pavone, F. S. & Loew, L. M. 2012. Palette of fluorinated voltage-sensitive hemicyanine dyes. Proc Natl Acad Sci U S A, 109, 20443-8.
Zeng, H. & Madisen, L. 2012. Mouse transgenic approaches in optogenetics. Prog Brain Res, 196, 193-213.
Zhou, W. L., Short, S. M., Rich, M. T., Oikonomou, K. D., Singh, M. B., Sterjanaj, E. V. & Antic, S. D. 2015. Branch specific and spike-order specific action potential invasion in basal, oblique, and apical dendrites of cortical pyramidal neurons. Neurophotonics, 2.
Zhou, W. L., Yan, P., Wuskell, J. P., Loew, L. M. & Antic, S. D. 2007. Intracellular long-wavelength voltage-sensitive dyes for studying the dynamics of action potentials in axons and thin dendrites. J Neurosci Methods, 164, 225-39.
Zhou, W. L., Yan, P., Wuskell, J. P., Loew, L. M. & Antic, S. D. 2008a. Dynamics of action potential backpropagation in basal dendrites of prefrontal cortical pyramidal neurons. Eur J Neurosci, 27, 923-36.
Zhou, W. L., Yan, P., Wuskell, J. P., Loew, L. M. & Antic, S. D. 2008b. Dynamics of action potential backpropagation in basal dendrites of prefrontal cortical pyramidal neurons. European Journal of Neuroscience, 27, 923-936.
Zipfel, W. R., Williams, R. M. & Webb, W. W. 2003. Nonlinear magic: multiphoton microscopy in the biosciences. Nature Biotechnology, 21, 1368-1376.